The magnetic properties of ultrathin cobalt multilayers symmetrically and antisymmetrically sandwiched between layers of platinum and iridium

Dissertation

zur Erlangung des Doktorgrades

an der Fakultät für Mathematik, Informatik und

Naturwissenschaften

Fachbereich Physik

der Universität Hamburg

vorgelegt von

Jochen Wagner
aus Karlsruhe

Hamburg
Oktober 2018

Gutachter/innen der Dissertation:	Prof. Dr. Hans Peter Oepen *Universität Hamburg, Germany* Prof. Dr. Ralf Röhlsberger *DESY, Germany*
Zusammensetzung der Prüfungskommission:	Prof. Dr. Hans Peter Oepen *Universität Hamburg, Germany* Prof. Dr. Ralf Röhlsberger *DESY, Germany* Prof. Dr. Gerhard Grübel *DESY, Germany* Prof. Dr. Daniela Pfannkuche *Universität Hamburg, Germany* Prof. Dr. Nils Huse *Universität Hamburg, Germany*
Vorsitzende der Prüfungskommission:	Prof. Dr. Daniela Pfannkuche
Datum der Disputation:	21.02.2019
Vorsitzender Fach-Promotionsausschusses Physik:	Prof. Dr. Wolfgang Hansen
Leiter des Fachbereichs Physik:	Prof. Dr. Michael Potthoff
Dekan der Fakultät MIN:	Prof. Dr. Heinrich Graener

Abstract

This thesis deals with a systematic study of magnetic properties, i.e. saturation magnetization, exchange stiffness, anisotropy, interlayer exchange coupling, and average domains size, of ultrathin Co-based multilayer systems. The multilayers were prepared by DC-magnetron sputtering and the Co-layers are sandwiched either symmetrically or antisymmetrically between nonmagnetic spacer layers of Pt or Ir.

Various experimental techniques were employed to study the different properties and their Co-thickness-driven evolution. The saturation magnetization was measured using ferromagnetic resonance spectroscopy (FMR), while anisotropies and interlayer exchange coupling were determined from measurements of the magneto-optic Kerr effect (MOKE). The exchange stiffness is extracted from domain wall profiles acquired with X-ray holographic microscopy (XHM). To this end, the fabrication scheme of the X-ray optics used in the microscope was improved and a lateral resolution of sub-12 nm experimentally proven. The average domain size was obtained from intensity profiles acquired via X-ray resonant magnetic scattering (XRMS). From the comparison of measured domain sizes to ones calculated from domain spacing models, the strength of the Dzyaloshinskii-Moriya interaction (DMI) can be estimated. It is shown that this method, which is frequently applied in literature, is prone to problems, such as the strong dependence on all other magnetic parameters, as well as on the geometry of the domain pattern, the influence of domain wall pinning, and the various models producing differing results. This aggravates the comparison of values between different groups and strongly limits the applicability.

Unlike in recent publications concerning similar multilayer systems, the values measured for the saturation magnetization down to layer thicknesses of 2 nm are in line with the literature value for bulk Co. MOKE data suggest that bulk-like values persist down to ≈ 1 nm. The exchange stiffness was found to be considerably reduced in ultrathin layers compared to the bulk value of fcc Co. The reduction is attributed to interdiffusion at the interfaces and a model is developed that describes the reduction in dependence of the Co thickness and thewidth of the interdiffusion zone.

A spin reorientation transition (SRT) from perpendicular to easy-plane magnetization was observed, which is driven by the Co thickness. The transition, however, is strongly influenced by the number of repetitions N and the thickness of the non-magnetic spacer layers. Perpendicular magnetization was observed far beyond the zero crossing of the effective anisotropy for $N \geq 6$, which is attributed to the formation of a three-dimensional magnetic microstructure, the so-called vortex state.

In the antisymmetric systems, the stacking sequence plays a crucial role. Both, anisotropy and interlayer exchange coupling are altered by inversion of the sequence. The interlayer exchange coupling changes from a strictly ferromagnetic to an oscillatory behavior, like it is found for a pure Ir spacer layer, but with a longer period length, which is dependent on the thickness of both spacer layers. Finally, perpendicular domains were observed also in antiferromagnetically coupled multilayers, starting from a specific Co-layer thickness, and extending far beyond the zero crossing of the effective anisotropy. While such domains were proposed and observed in such systems for weak effective anisotropies favoring perpendicular magnetization, their presence beyond the zero crossing has not been described before.

Zusammenfassung

Diese Doktorarbeit befasst sich mit der systematischen Untersuchung von sehr dünnen kobaltbasierten Multilagensystemen im Hinblick auf ihre magnetischen Eigenschaften, d.h. Sättigungsmagnetisierung, Austauschsteiffigkeit, magnetische Anisotropie, Zwischenlagenaustauschkopplung und mittlere Domänengröße. Die Kobaltlagen sind symmetrisch oder antisymmetrisch von nichtmagnetischen Zwischenlagen aus Platin oder Iridium eingefasst und wurden mittels Gleichspannungs-Kathodenzerstäubung präpariert.

Die verschiedenen Eigenschaften wurden mittels unterschiedlicher experimenteller Techniken auf ihre kobaltschichtdickenabhängige Entwicklung untersucht. Für die Untersuchung der Sättigungsmagnetisierung wurde ferromagnetische Resonanzspektroskopie eingesetzt, während Anisotropie und Zwischenlagenkopplung durch Messung des magnetooptischen Kerr-Effektes (MOKE) untersucht wurden. Die Austauschsteiffigkeit wurde aus Domänenwandprofilen extrahiert, welche mit röntgenholographischer Mikroskopie (XHM) aufgenommen wurden. Um dies zu ermöglichen wurde der Herstellungsprozess eines für dieses Mikroskop essentiellen röntgenoptischen Bauteils verbessert und eine räumliche Auflösung von unter 12 nm experimentell nachgewiesen. Die Bestimmung der mittleren Domänengröße erfolgte aus Intensitätsprofilen, welche mittels resonanter Röntgen-Kleinwinkelstreuung (XRMS) gemessen wurden. Aus dem Vergleich der experimentell bestimmten und mit Modellen berechneten Domänengrößen kann die Stärke der Dzyaloshinskii-Moriya Wechselwirkung (DMI) bestimmt werden. Es wird gezeigt, dass diese häufig in der Literatur verwendete Methode sehr problemanfällig ist, was den Vergleich von Werten zwischen verschidenen Arbeitsgruppen erschwert und die Verlässlichkeit so gewonnener Ergebnisse in Frage stellt. Diese Anfälligkeit ist der starken Abhängigkeit von den übrigen magnetischen Parametern sowie dem Einfluss von Pinning, der Geometrie des Domänenmusters, sowie abweichenden Vorhersagen der unterschiedlichen verwendeten Modelle geschuldet.

Im Gegensatz zu mehreren kürzlich erschienen Publikationen zu ähnlichen Multilagensystemen, wurden für Kobaltschichtdicken bis zu 2 nm Sättigungsmagnetisierungswerte gemessen die in Übereinstimmung mit dem Literaturwert für Kobaltvolumenkristalle sind. Aus MOKE Messungen wurde abgeschätzt, dass volumenartige Werte bis Schichtdicken von 1 nm vorherschen. Für die Austauschsteiffigkeit wurde ein im Vergleich zu fcc Volumenkobalt stark verringerter Wert gemessen. Die Reduktion wird auf Durchmischung an den Grenzflächen zurückgeführt und ein Modell entwickelt, welches die Reduktion in Abhängigkeit der Kobaltschichtdicke und der Breite der Durchmischungszone an der Grenzfläche beschreibt.

Es wurde ein kobaltdickengetriebener Spinreorientierungsübergang (SRT) beobachtet, bei welchem sich die Vorzugsrichtung der Magnetisierung von senkrecht zu in der Ebene verändert. Die Art des Übergangs ist allerdings stark von der Anzahl der Multilagen N und der Dicke der nichtmagnetischen Zwischenlagen abhängig. Auch noch in Bereichen jenseits des Null-durchgangs der effektiven Anisotropiewurden für $N \geq 6$ senkrechte Domänen beobachtet, welche der Entstehung einer dreidimensionalen Magnetisierungsverteilung zugeschrieben wird.

Es hat sich gezeigt, dass in den antisymmetrischen Systemen die Reihenfolge der Schichten eine entscheidende Rolle für die resultierenden Eigenschaften spielt. Sowohl die Anisotropie wie auch die Zwischenlagenaustauschkopplung werden davon entscheidend beeinflusst. Durch die Umkehrung der Schichtenfolge wird ein Wechsel von ausschließlich ferromagnetischer Kopplung zu einem periodisch zwischen ferro- und antiferromagnetisch oszillierenden Verhalten hervorgerufen – ein Verhalten, welches bereitsvon Zwischenlagen aus reinem Iridium bekannt ist. Die Oszillation erfolgt jedoch mit einer längeren Periodenlänge welche sowohl von der Dicke wie auch der Zusammensetzung der Zwischenlagen abhängig ist. Des Weiteren wurden senkrecht magnetisierte Domänen auch in antiferromagnetisch gekoppelten Multilagen oberhalb einer spezifischen Kobaltschichtdicke beobachtet, die sich bis weit über den Nulldurchgang der effektiven Anisotropie hinaus beobachteten ließen. Während derartige Domänen für solche Systeme im Bereich von schwacher senkrechter Anisotropie vorhergesagt und bereits beobachtet wurden, ist deren Präsenz jenseits des Nulldurchgangs bisher nicht berichtet worden.

Content

List of Figures

List of Equations

Introduction

Magnetism is a quantum physical phenomenon that can be directly experienced in our everyday life. Thus by attaching our latest travel-souvenir magnet to the fridge, we directly observe the workings of quantum physics. Magnetism is a highly worthwhile field for research from both a fundamental point of view as well as for technological application, of which magnetism has many. E.g., magnetic nanoparticles are used as contrast agent in magnetic resonance imaging or for the pinpoint delivery of drugs into tumors in medicine (*1*). Even more strongly, magnetism is linked to applications in sensors, actuators and data storage (*2–9*).

Magnetic data storage has come a long way since the pioneering works of Oberlin Smith in 1878 and Valdemar Poulsen in 1898 (*10*). Smith envisioned an apparatus to store and read sound as electrical information in magnetic wires. Twenty years later, the so-called telegraphone was realized by Poulsen, which was capable of storing 30 minutes of sound on a steel wire. Due to the lack of electronic amplification, the reproduced sounds were very faint and noisy, thus magnetic data storage lay dormant for almost three decades to follow. This changed with the invention of magnetic tapes by J.A. O'Neill in 1927(*11*), the introduction of biasing recording techniques and electronic amplification (*10*). From that point on, magnetic recording thrived and found many other applications besides the recording of sounds, especially in the storage of digital data.

In 1956, IBM released the first magnetic hard disk drive (HDD) with a capacity of 5 MB and a data density of 2 kb/in²; the information was stored in homogenously magnetized in-plane regions (bits). Since then, an incredible increase in both storage capacity and density was enabled by ever-growing understanding of the magnetic systems and their properties, discovery of new effects and improved preparation techniques. One important milestone was the discovery of oscillatory interlayer exchange coupling (IEC) and the resulting giant magnetoresistance effect (GMR), which occurred independently in the working groups of Peter Grünberg (*12*) and Albert Fert (*13*) in 1988. They observed a giant change in the electrical resistance of two magnetic layers dependent on whether the relative alignment of the magnetization in both layers was parallel or antiparallel. The discovery was enabled by new technologies making the preparation of thin films of few atomic layers with high-quality interfaces feasible (*14, 15*) and in 2007 was awarded with the Nobel Prize in physics. The GMR was subsequently used in the read/write heads of HDDs where it enabled the miniaturization of the bits. Furthermore, it sparked intense research in the field of "spintronics"(*16–19*) and "spin-orbitronics" (*20, 21*), which deal with the role of the spin magnetic moment of electrons on the electrical transport.

Nowadays, most large-scale data storage is based on HDDs and state of the art devices achieve data densities of 1 Tb/in² The information is stored in granular thin-film systems with perpendicular magnetization anisotropy (PMA), so-called perpendicular recording media, where several grains form a sub-100 nm-sized magnetic region (bit). The bits are written and read by magnetic thin-film heads making use of the tunneling magnetoresistance (TMR), where two magnetic layers are separated by an insulator. The probability for electrons to tunnel through the nanometer thick layer is dependent on the relative alignment of the magnetization in the layers (*22–25*).

In order to keep up with the vastly growing demand for data storage, e.g. driven by the ubiquity of smartphones, cameras, social media and cloud storage, new generations of devices have to further increase the areal storage density, access speed and energy efficiency. The main issue limiting further miniaturization of the bits in conventional HDDs is the superparamagnetic limit, where the thermal energy is sufficient to initiate an uncontrolled switching of the bits, thus corrupting the stored information. For general application, a ratio of the energy barrier KV, with the anisotropy K and the volume V, to thermal energy $k_B T$, with the Boltzmann constant k_B and the temperature T, has to be larger than 60. In order to maintain this ratio while decreasing the volume, the anisotropy has to increase. Subsequently, the writing fields of the bits, linked to K, increases to an extent that current writing heads cannot produce the spatially localized fields of required strength (*26*). One proposed solution is the heat-assisted magnetic recording (HAMR), where a laser heats up a bit to lower its writing field (*27*). Other new concepts required a two- or even three dimensional structuring of the recording media, e.g. bit patterned media, magnetic random access memory (MRAM) (*28*) or the racetrack memory (*29, 30*).

In a racetrack memory, the information is stored in the form of domain walls (DWs) in arbitrarily shaped ferromagnetic nanowires (*29*). Using an electric current, the DWs can be moved along the wire by spin-transfer torque (STT) (*31–35*) to a stationary reading head. Thus, no movable parts are required. Usually, magnetic materials with PMA, e.g. Pt\Co\Pt layers, are used in these devices as they host narrower Bloch walls compared to easy-plane systems, thus the STT can act more effectively (*36*). Furthermore, the narrower walls enable a higher DW density. Three major improvements have been proposed in recent years: (i) in 2012, it was shown that in ultrathin films the interfacial Dzyaloshinkii-Moriya interaction (iDMI) can stabilize narrow Néel DWs with fixed rotational sense that can be moved even more efficiently with currents by STT (*37*). (ii) only one year later, in 2013, followed the suggestion of replacing DWs for skyrmions stabilized by iDMI (*38*) for their various advantages, e.g. theoretically requiring 10^5– 10^6 lower current densities to move them, having lower depinning currents and being repelled by each other, defects and edges. (iii) in 2015

it was observed that DWs can be moved with up to 1000 m/s and five time more efficiently in racetracks formed of two magnetic layers with antiferromagnetic IEC (*39*).

The DMI, the effect at the heart of the first two propositions, is an asymmetric exchange interaction that favors non-collinear spin-alignments with fixed rotational sense and arises due to the lack or breaking of symmetry in crystal lattices (bulk DMI) or at interfaces (iDMI). Dzyaloshinkii proposed it in 1957 (*40*) for bulk oxides and Moriya derived the interaction in 1960 analytically (*41*). Its interfacial counterpart was predicted thirty years later, in 1990 (*42*) and the first experimental observation of the resulting Néel DWs with fixed rotational sense occurred in 2007 using spin-polarized scanning tunneling microscopy (SP-STM) (*43*).

The key to the second proposal, skyrmions, are named after nuclear physicist Tony Skyrme for his development of a non-linear field theory of interacting pions in 1960 (*44*) that showed that topologically stable field configurations occur as particle-like solutions. The term is used nowadays in various contexts. Magnetic skyrmions were first proposed in 1989 by A.N. Bogdanov as the smallest conceivable micromagnetic spin configuration (*45*) and are currently topic of intense research activities. They are topologically protected, chiral spin structures with whirling configurations of fixed rotational sense that are usually stabilized by DMI[1] (*38, 52, 53*). In 2009, they were first observed in bulk MnSi where they form lattices with six-fold symmetry (*54*). Two years later, in 2011, atomic scale skyrmions stabilized by iDMI were found in a monolayer Fe on Ir(111) at high fields (2 T) and low temperature (11 K) using SP-STM (*55*). And in 2015, micron-sized so-called "skyrmionic bubbles" with iDMI stabilized Néel DWs were reported at RT (*56*). For the application in racetrack memory devices more relevant sub-100 nm RT skyrmions were first observed in 2016 in Ir\Co\Pt multilayers at RT, stabilized by small fields, and their current-induced mobility demonstrated.

Many experimental reports of skyrmions followed thereafter (*57–62*), confirming the predicted velocity component perpendicular to the current direction, the so-called skyrmion Hall effect (*63*). Two possibilities to evade this adverse effect for application have been proposed: (a) it was shown in 2018 that using ferrimagnetic alloys, like GdFeCo, with compounds that have opposite skyrmion Hall angles inhibits the undesired sideward motion (*64*). (b) in 2016 it was proposed that in two magnetic layers with antiferromagnetic IEC the skyrmion Hall effect of each layer cancels with the

[1] Other mechanisms for the stabilizations involve RKKY interactions (*46*), dipole stabilization (*47*), anisotropic frustration (*48*), interlayer exchange coupling (*49*), or confinement through patterning (*50, 51*).

other (*65*). Thus, we have come full circle to the third proposed improvement for the racetrack memory. However, skyrmions in such systems have yet to be experimentally confirmed.

With the surging activity in the research on the racetrack memory and skyrmions, many new material systems are proposed and tested for their applicability. Yet systematic studies on their magnetic properties are rare, despite their tremendous influence on features like the average domain size, width of DWs, and diameter of skyrmions. The most frequently used method to determine the strength of the DMI[2] in multilayer samples relies on the comparison of experimentally observed domain patterns to domain spacing models (*70, 71*). For accurate results, the magnetic properties of the investigated system need to be very well understood. Furthermore, static and dynamic investigations of the magnetic microstructure in these complex thin-film systems, elementally resolved and with sufficient spatial and temporal resolution are still a non-trivial task. The relevant length scales are the widths of domain walls and the diameter of skyrmions, both of which are typically in the range of few tens of nanometers.

Several well-established techniques exist to study nanometer-sized magnetic nanostructure. Magnetic force microscopy (MFM) is one of these techniques, where a few-nm-sized magnetic tip scans closely over the sample surface and interacts with the stray field generated by the domain structure (*72–74*). Typically, spatial resolutions of around 30 nm are achieved (*73*), with extensive effort 10 nm can be reached (*74, 75*). The time resolution is limited by the duration of the scanning process (several minutes). The technique is highly susceptible to external fields, the domain structure can be altered by the magnetic tip and neither depth nor element-selective information can be obtained. A previously mentioned scanning probe technique is the spin-polarized scanning tunneling microscope (SP-STM), which is capable of atomic resolution (*76*). The technique measures the current caused by electrons tunneling between tip and sample surface to obtain information on the local magnetization on the sample and is sensitive only to the top-most atomic layer. Furthermore, only samples with high quality, ordered surfaces can be investigated.

Another scanning technique is scanning electron microscopy with polarization analysis (SEMPA) which probes the spin-polarization of the low-energy secondary electrons (SE) (*77, 78*). Spatial resolutions down to 3 nm are reported (*79*) and a time resolution of 700 ps is feasible (*80*). A major advantage of this technique is its capability of measuring two components of the magnetization simultaneously, thus the rotational sense of DWs is accessible (*81*). Due to measuring low-energy

[2] Other techniques involve Brillouin light scattering (BLS) (*66*), asymmetric DW creep (*67, 68*), and asymmetric hysteresis in patterned structures (*69*).

SEs, only information from near-surface layers (< 2 nm) is accessible and the technique is not suited for studies requiring strong magnetic fields. A related technique is transmission electron microscopy in Lorentz mode (Lorentz TEM). The illuminating electrons are deflected by the Lorentz force of the samples magnetic field while transmitting through the sample (*82, 83*). Due to the high-energy electrons used, it can be performed in the presence of magnetic fields and on samples with thicknesses of several tens to hundreds of nanometer. Spatial resolutions below 1 nm (*84*) and temporal resolutions of 10 ns (*85*) are feasible.

A photon based technique is the full-field Kerr microscopy, based on the magneto-optic Kerr-effect (MOKE) (*82, 86–88*). The effect occurs when light is reflected on a ferromagnetic sample, changing the polarization of the light. The spin-orbit coupling causes a dependence of the dielectric tensor on the orientation of the magnetization (*86*). The resolution is diffraction limited (*89*), thus with blue light ($\lambda = 460$ nm) around 250 nm is achievable. Using ultra-short intense laser pulses in pump-probe geometry, magnetization dynamics in the fs-regime are accessible, where the time resolution is limited by the pulse length (*90*).

Of special interest in this thesis are synchrotron-based techniques utilizing the X-ray circular dichroism (XMCD) that occurs at element-specific photon energies. As the energy of the X-rays is adjustable, this enables element-specific imaging. Full-field X-ray transmission microscopy (TXM) uses Fresnel zone plates (FZP) as lenses for the image projection and resolutions of (12– 20) nm were achieved (*91–93*). A closely related technique is the scanning TXM (STXM) (*94*), where the beam is focused with a FZP onto the sample and the image is obtained by scanning the sample[3]. Here, resolutions down to 7 nm at 700 eV are reported (*95*). Both, TXM and STXM, achieve time resolutions of 70 ps (*96, 97*). Unlike for visible light, X-ray lenses cannot be produced aberration free, thus the resolution is aberration limited. In X-ray photoelectron emission microscopy (X-PEEM), the intensity of X-ray induced photoelectrons is measured which depends on the local X-ray absorption. This surface sensitive technique achieves a spatial resolution of 20 nm and 15 ps time resolution (*98, 99*) and is highly susceptible to magnetic fields.

Promising techniques based on coherent X-ray scattering are X-ray resonant magnetic scattering (XRMS), coherent diffraction imaging (CDI) and Fourier transform holography (FTH). XRMS is used to acquire ensemble-averaged information from a magnetic microstructure in Fourier-space, where the magnetic diffraction pattern caused by scattering from magnetic domains is detected by a charge-coupled device (CCD). The technique requires no special optics, thus the spatial resolution

[3] Unlike other scanning techniques, the probe (X-ray beam) is fixed in space and the sample is moved in STXM.

is solely limited by the wavelength and detectable maximum momentum transfer q. Using free electron laser (FEL) sources and pump-probe geometry, magnetization dynamics in the fs-regime are accessible, where the time resolution is limited by the pulse length (*100–104*). CDI faces the problem that the phase information required to reconstruct the real-space information is lost in a scattering image. However, by acquiring several spatially overlapping scattering patterns (ptychography) and employing complex phase-retrieval algorithms, the real space image can be reconstructed. Spatial resolutions of 10 nm have been achieved (*105, 106*). A major advantage of CDI is the capability of using it for tomography, thus obtaining three-dimensional information where resolutions below 20 nm were demonstrated (*107*). Using hard X-rays, a resolution of 100 nm was achieved on a few-micron-sized sample (*108*). However, CDI is quite time consuming and the time resolution is limited by the time it takes to acquire a whole set of scattering patterns.

One way to circumvent the phase problem is FTH, where a reference wave is superimposed onto the scattering pattern and the phase is encoded in the resulting interference pattern, the so-called hologram. It is recorded with a CCD and the real-space information can be retrieved using a simple two-dimensional Fourier transformation. This technique requires one optical component, the holographic mask. The mask is opaque and contains an object hole, defining the field of view, and a reference hole, which provides the reference wave. The experimental resolution is defined by the diameter of the reference hole and the detectable maximum momentum transfer q. With reference holes of 30 nm diameter, a resolution of 20 nm was demonstrated(*109*). In pump-probe experiments at FEL sources, a time resolution of 15 ps was achieved (*110, 111*).

This thesis addresses the lack of systematic studies of magnetic properties in some of the most frequently used Co-based multilayer systems within the research on racetrack memory and skyrmions. The ultrathin Co layers are sandwiched symmetrically or antisymmetrically between Pt and/or Ir layers and both, single and multilayers are investigated.

Chapter 1 briefly introduces the basics of micromagnetism that are relevant for this thesis, the formation of magnetic domains, and the image formation in soft X-ray holographic microscopy **Chapter 2** describes the main experimental setups used for the fabrication of the samples and holographic masks, as well as for the investigation of the magnetic properties.

In order to guarantee sufficient spatial resolution to resolve the relevant length scales with X-ray holographic microscopy, an optimized fabrication scheme of the holographic masks is introduced in **chapter 3**. The improved masks are experimentally tested and a magnetic resolution of $\lesssim 12$ nm is demonstrated.

In **chapter 4**, the sample systems are investigated regarding their saturation magnetization (M_S), anisotropy, exchange stiffness, and interlayer exchange coupling. The saturation magnetization in Co-layers of moderate thickness is investigated by ferromagnetic resonance (FMR). The anisotropy and interlayer exchange coupling are studied by MOKE, which is also used to extrapolate M_S to ultrathin layers. It is shown that the IEC depends on the stacking order of the sample and exhibits peculiar features in the antisymmetric systems. The exchange stiffness is extracted from domain wall widths imaged by X-ray holographic microscopy. Furthermore, a model is developed to explain the observed reduction in ultrathin Co-layers with structural disorder at the interfaces.

The average domain size is studied by XRMS in **chapter 5** and domain spacing models are employed to extract the strength of the DMI. It is shown that the domain spacing models are insufficient to describe the observed behavior of the domain sizes, especially close to and after the transition from perpendicular magnetization anisotropy to easy-plane behavior. In this region, a three-dimensional magnetic microstructure forms.

1 Fundamentals

The first chapter deals with the theoretical principles and terminology of the thesis. First in section 1.1, the basic concepts of micromagnetism are discussed. The magnetic energy terms, which determine the magnetic properties of ferromagnetic materials and thus are responsible for the formation of the magnetic microstructure, are briefly introduced. Subsequently in section 1.2, the most prominent of these distributions are introduced, namely magnetic domains with their transition region in-between individual domains, the domain walls. Finally, in section 1.3, the X-ray techniques used to study nanometer-sized magnetic domain structures and domain walls are presented. These are X-ray magnetic X-ray resonant magnetic scattering (XRMS) (section 1.3.2), and X-ray holographic microscopy (XHM) (section 1.3.3).

1.1 Micromagnetism

The theory of micromagnetism is a continuum theory and defines the gap between quantum theory, dealing with atomic dimensions, and the Maxwell theory dealing with macroscopic dimensions. Micromagnetism has developed to an indispensable theory to describe and understand fundamental aspects of magnetic domain configuration, interplay between microstructure and magnetization as well as magnetization processes. The main principles of the theory originate from Landau and Lifshitz (*112*) and the variational principle. Under certain assumptions, it allows for an accurate description of the magnetic system in the range of the nano- and microscale. Hence, it involves typical dimensions of domain structures and domain walls found in ultrathin magnetic layers. The main idea of micromagnetism is to present a formalism where the macroscopic properties are described with the best approximation to the fundamental atomic behavior. In this way, the discrete magnetic moments in the atomistic theory are replaced by an averaged quantity and a continuous vector field, the magnetization **M**. Thus, the atomistic summations are replaced by volume integrals. Consequently, the resulting micromagnetic equations can be solved numerically even for relatively large systems in comparison to atomistic approaches. In static micromagnetism, the magnetization distribution at equilibrium is calculated via minimizing the total magnetic energy of the system given by:

$$E = E_{\mathrm{ex}} + E_{\mathrm{MC}} + E_{\mathrm{Z}} + E_{\mathrm{d}} + E_{\mathrm{DMI}} + E_{\mathrm{IEC}}. \qquad \text{Eq. 1-1}$$

Some of the energy terms of the total energy are described classically, e.g., the Zeeman energy E_{Z} and the demagnetization energy E_{d}. Other energy terms like the exchange E_{ex}, Dzyialoshinkii-Moriya E_{DMI}, anisotropy E_{MC} or interlayer exchange energy E_{IEC} have a quantum mechanical origin.

The local or global minimum of the total energy functional of the magnetic system gives rise to a stable magnetic microstructure, also called magnetic domain pattern. Thus, the magnetic behavior and structure are mainly determined by the balance between the aforementioned energy terms. In the following, the magnetic energy terms are introduced and discussed in detail.

1.1.1 Exchange energy

The exchange interaction between electrons is the origin of long-range magnetic order. It does not result from a direct electron-electron coupling; phenomenologically it can be expressed by the atomistic Heisenberg Hamiltonian (*113, 114*):

$$H_{\mathrm{ex}} = -\sum_{i \neq j} J_{ij} \mathbf{S}_i \cdot \mathbf{S}_j \,. \qquad \text{Eq. 1-2}$$

J_{ij} is the so-called exchange integral and has its quantum-mechanical origin in the Pauli principle. $\mathbf{S}_i$ and $\mathbf{S}_j$ are the spins of atom i and j. For $J_{ij} \neq 0$, a collective spin arrangement is preferred with either parallel (ferromagnetic, FM) alignment of neighboring spins ($J_{ij} > 0$) or antiparallel (antiferromagnetic, AFM) alignment ($J_{ij} < 0$). The short-range exchange interaction prevents strong inhomogeinities as non-parallel alignment of spins creating an excess energy. In the micromagnetic approximation, individual spins and sums are replaced by an average magnetization and integrals. The exchange energy is obtained by expanding Eq. 1-2 into a Taylor series for small-angle deviations (*78, 115–117*) and given by

$$E_{\mathrm{ex}} = A_{\mathrm{ex}} \int \left(\nabla \frac{\mathbf{M}}{M_{\mathrm{S}}} \right)^2 dV \,. \qquad \text{Eq. 1-3}$$

A_{ex} is the material specific exchange constant and $\mathbf{M}/M_{\mathrm{S}}$ the magnetization unit vector with the saturation magnetization M_{S}. A_{ex} can be expressed as a function of M_{S} and the second spatial moment of the exchange integral $J^{(2)}$ via the spin wave stiffness D_{Spin} .For fcc lattices the exchange constant is described by (*118*) follows

$$A_{\mathrm{ex}} = \frac{M_{\mathrm{S}}}{2g\mu_{\mathrm{B}}} D_{\mathrm{Spin}} = \frac{M_{\mathrm{S}}}{2g\mu_{\mathrm{B}}} \left(\frac{1}{6} a^2 Z J^{(2)} S \right) = \frac{a^2 S M_{\mathrm{s}} J^{(2)}}{12 g \mu_{\mathrm{B}}} Z, \qquad \text{Eq. 1-4}$$

With a, the lattice constant (for hcp a^2 is replaced by the basal lattice constant $2a^2$), the coordination number Z (number of next-neighbors), the Landé-Factor g and the Bohr magneton μ_{B}. The nth spatial moment of the exchange integral is given by (*118*):

$$J^{(n)} = \frac{1}{Z}\sum_{\mathbf{r}} J(r)\left(\frac{\sqrt{2}}{a}\mathbf{r}\right)^{n}. \qquad \text{Eq. 1-5}$$

It should be noted that M_S and D_{spin} are in general temperature dependent. Thus, A_{ex} is also implicitly dependent on the temperature T (*119, 120*).

1.1.2 Magnetic field energy

The magnetic field (or magnetostatic) energy E_{MS} can be expressed as the sum of the Zeeman energy E_Z and the stray field energy E_d. The former originates from the interaction of the magnetization $\mathbf{M}$ with an applied field $\mathbf{H}_a$ and is given by

$$E_Z = -\mu_0 \int \mathbf{M}\cdot\mathbf{H}_a \, dV\,. \qquad \text{Eq. 1-6}$$

The stray field energy is caused by the magnetization itself as each magnetic moment represents a magnetic dipole contributing to a total magnetic field $\mathbf{H}_d$ inside the sample. $\mathbf{H}_d$ is called the demagnetization or magnetic dipolar field and arises from the long-range magnetostatic interaction between magnetic moments. Starting from Maxwell's second equation div $\mathbf{B} = \mu_0$ div $(\mathbf{M} + \mathbf{H}_d) = 0$, we define the stray field as div $\mathbf{H}_d = -\mu_0$ div $\mathbf{M}$. The sinks and sources of the magnetization act like magnetic charges for the stray field. Thus, the field can be calculated like a field in electrostatics with the difference that magnetic charges never appear isolated). The stray field energy of a ferromagnetic sample is given by

$$E_d = -\frac{\mu_0}{2}\int \mathbf{M}\cdot\mathbf{H}_d \, dV\,. \qquad \text{Eq. 1-7}$$

Thus, while E_Z is associated with the interaction of $\mathbf{M}$ with an external field, E_d is the self-energy of the interaction of $\mathbf{M}$ with the field created by the magnetization distribution itself. It should be noted that since $\mathbf{M}$ vanishes outside a sample, the integrals of Eq. 1-6 and 1-7 are only carried out over the volume V. Nevertheless, E_d implicitly includes the energy outside of the ferromagnet associated with $\mathbf{H}_d$.

The stray field can be calculated from the magnetostatic potential generated by surface charges $\rho_S = \mathbf{M}\cdot\mathbf{n}$ and volume charge $\rho_V =$ - div $\mathbf{M}$, with $\mathbf{n}$ the outward oriented surface normal (*117, 121*). The determination is quite complicated and can only be carried out analytically in a few cases. In the case of homogenously magnetized ellipsoids, however, $\mathbf{H}_d$ is uniform and depends linearly on its origin, $\mathbf{M}$ (*117, 121*):

$$\mathbf{H}_\mathrm{d} = -\overleftrightarrow{N} \cdot \mathbf{M}. \qquad \text{Eq. 1-8}$$

The second-rank tensor $\overleftrightarrow{N}$ is called demagnetization factor. It can be diagonalized when its coordinate system is in accordance with the main axes (a, b, c) of the ellipsoid. For thin films ($a = b = \infty$, $c \ll a$), it takes the form (*122*):

$$\overleftrightarrow{N} = \begin{pmatrix} 0 & 0 & 0 \\ 0 & 0 & 0 \\ 0 & 0 & 1 \end{pmatrix}. \qquad \text{Eq. 1-9}$$

The stray field energy density $(E/V)_\mathrm{d}$ can thus be calculated for thin films by inserting Eq. 1-8 and 1-9 into Eq. 1-7:

$$\left(\frac{E}{V}\right)_\mathrm{d} = \frac{\mu_0}{2}\left(\overleftrightarrow{N} \cdot \mathbf{M}\right) \cdot \mathbf{M} = \frac{\mu_0}{2} M_z^2 = \frac{\mu_0}{2} M_\mathrm{S}^2 \cdot \cos^2\Theta, \qquad \text{Eq. 1-10}$$

with Θ, the angle between film normal and $\mathbf{M}$. $(E/V)_\mathrm{d}$ is anisotropic as it is at its maximum for $\Theta = 0°$ and minimum for $\Theta = 90°$. The difference in energy density between the direction of easiest and hardest magnetizability is called the shape anisotropy K_d

$$K_\mathrm{d} = \frac{\mu_0}{2} M_\mathrm{S}^2. \qquad \text{Eq. 1-11}$$

For Co films with $M_\mathrm{S} = 1.4\,\mathrm{MA/m}$ (*123*), a shape anisotropy of $K_\mathrm{d} = 1.23\,\mathrm{MJ/m^3}$ is obtained.

1.1.3 Magnetocrystalline and surface anisotropy energy

While the shape of a ferromagnet causes the shape anisotropy, the magnetocrystalline (or volume) anisotropy originates from the lattice structure. It arises due to the spin-orbit interaction (SOI), which couples the electron spin $\mathbf{S}$ to the orbital angular momentum $\mathbf{L}$. The latter is strongly linked to the crystal lattice (*114*). The SOI is expressed as the Hamiltonian $H_\mathrm{SOI} = A_\mathrm{SOI}\ \mathbf{L} \cdot \mathbf{S}$, with the constant A_SOI indicating the strength of the interaction (*117*). For crystal lattices with a single preferred direction of magnetization (uniaxial), the energy density is only a function of the angle Θ between this axis and $\mathbf{M}$. For fcc Co this is the (111) direction (*124*). The uniaxial energy density can then be expanded into a power series (*114*):

$$\left(\frac{E}{V}\right)_\mathrm{MC,V} = K_\mathrm{1V} \sin^2\Theta + K_\mathrm{2V} \sin^4\Theta + \cdots. \qquad \text{Eq. 1-12}$$

For $K_\mathrm{(i+1)V} \ll K_\mathrm{iV}$, the power series is usually terminated after the first or second order. The coefficients K_1V and K_2V are the magnetocrystalline anisotropy constants of the respective order. Values reported in literature are usually expressed as the sum $K_\mathrm{V} = K_\mathrm{1V} + K_\mathrm{2V}$, because both quantities

cannot be distinguished by the area method, which is the most widely used experimental method (see chapter 4.3.2.2). For bulk fcc Co (111), K_V is in the order of single-digit kJ/m³, so one order of magnitude smaller than for hcp Co with K_V = 0.53 MJ/m³ (*125*). For thin films, however, the reported values cover a wide range K_V = 0– 0.9 MJ/m³ (*126*). Few studies attempted to separate the first and second order contribution and found a constant value of K_{2V} = (0.07 ± 0.03) MJ/m³ (*127–131*).

The crystal lattice is interrupted at surfaces and interfaces, causing a breaking of the translational symmetry. Compared to a bulk atom, a surface or interface atom has less next-neighbors of the same kind. This causes a surface or interface anisotropy, first formulated in Néel's pair interaction model (*132, 133*):

$$\left(\frac{E}{V}\right)_{MC,S} = \frac{2K_S \sin^2\Theta}{t}. \qquad \text{Eq. 1-13}$$

Due to the $1/t$ dependence, for ultrathin films the surface and interface contribution can become of equal magnitude and even surpass the shape anisotropy, resulting in a preferred orientantion of magnetization (easy axis) perpendicular to the surface plane (perpendicular magnetization anisotropy (PMA)). Since the theoretical description, K_{1S} has first been experimentally observed for CoNi films on Cu(111) (*134*) resulting in PMA for t < 1.8 ML (monolayers). Some Co-based systems exhibiting PMA are Pd\Co\Pd (*135*), Pt\Co\Pt (*136*), Au\Co\Au (*137*), Ru\Co\Ru (*126*), and Ir\Co\Ir (*126*). In these systems K_{1S} is typically in the order of K_{1S} = 0.07– 1.29 mJ/m²(*126, 138*) or about 1 meV per interface atom. Néel's model fails in the attempt to produce accurate values for K_{1S} (*139*). Latest improvements (*140–142, 142*) enabled the calculation for Pd\Co\Pd and Pt\Co\Pt, further predicting a strong influence of strain on K_{1S}.

Strain acts on the lattice. In the case of an elastic and isotropic crystal, this results in the magnetoelastic energy density (*143*)

$$\left(\frac{E}{V}\right)_{ME} = \underbrace{\frac{3}{2}\lambda_m E\varepsilon}_{K_{ME}} \cdot \cos^2(\Theta_{ME}), \qquad \text{Eq. 1-14}$$

with the dimensionless magnetostriction coefficient λ_m, the elasticity module E, the strain ε, the angle Θ_{ME} between $\mathbf{M}$ and ε, and the magnetoelastic anisotropy constant K_{ME}. In layered structures ε mostly stems from the lattice mismatch η of the materials. For Co on Pt(111) η is 11%, on Ir(111) 8% (*128, 129, 144*). There are two distinct thickness or growth regimes in which the strain acts differently (*126, 137, 145, 146*), with a transition from one regime to the other at a critical thickness

t_C. In the coherent regime ($t < t_C$), η is relaxed by strain on both sides of the interface, altering the lattice constant, and thus effectively changing the volume term

$$K_S = K_{MC,S}\,, \qquad K_V = K_{MC,V} + K_{ME}. \tag{Eq. 1-15}$$

In the second so-called incoherent regime ($t > t_C$), η is relaxed by incorporating lattice misfit dislocations at the interfaces, altering the symmetry at the interfaces and thus acting as an interface term:

$$K_S = K_{MC,S} + K_{ME}\,, \;\; K_V = K_{MC,V}\,. \tag{Eq. 1-16}$$

In order to experimentally disentangle the individual anisotropy contributions (chapter 1.1.3.1, Eq. 1-18), the sum of all anisotropy contributions multiplied by thickness of the magnetic layer is plotted over the magnetic layer-thickness. In this kind of plot, a distinctive kink is expected at t_C.

All contributions are uniaxial with respect to the stacking order in polycrystalline fcc Co (111) and sum up to the henceforth-called total anisotropy K_{tot}

$$K_{tot} = \underbrace{K_{1V} - K_d + \frac{2K_{1S}}{t_{Co}}}_{K_{1,eff}} + K_{2V}. \tag{Eq. 1-17}$$

There are no higher orders to the shape anisotropy and K_{2S} was experimentally found to be negligible, at least for Pt\Co\Pt samples (*131, 147*). Therefore, the second order contribution consists only of a volume-like term K_{2V}. A method to disentangle the individual contributions is presented in the following.

1.1.3.1 Experimentally disentangling the total magnetic anisotropy

There are several contributions to the magnetic anisotropy as described above. Experimentally, only the superposition of the individual contributions is accessible. For the samples investigated in this thesis, each anisotropy term can be treated as uniaxial with respect to the stacking order (polycrystalline fcc Co (111) layers) and hence sum up to a total anisotropy K_{tot}. No higher orders of the shape anisotropy K_d exist. Additionally, K_{2S} was experimentally found to be negligible, at least for Pt\Co\Pt layers (*131, 147*). Therefore, the second order contribution consists only of a volume-like term K_{2V}.

By varying the thickness t_{Co}, the surface term $2K_{1S}$ can be disentangled from K_{tot}. This is commonly done by plotting $K_{tot} \cdot t_{Co}$ versus t_{Co}:

$$K_{\mathrm{tot}} \cdot t_{\mathrm{Co}} = \underbrace{(K_{1\mathrm{V}} + K_{2\mathrm{V}} - K_{\mathrm{d}})}_{K_{\mathrm{V,eff}}} \cdot t_{\mathrm{Co}} + 2K_{1\mathrm{S}}. \qquad \text{Eq. 1-18}$$

With M_{S} = 1.4 MA/m being constant for $t_{\mathrm{Co}} \gtrsim 1$ nm (this is discussed in chapter 4.2), and assuming a constant $K_{2\mathrm{V}}$ = (0.07 ± 0.03) MJ/m³ for Pt\Co\Pt layered structures (*127, 129*), $K_{1\mathrm{V}}$ and $K_{1\mathrm{S}}$ can be determined from the linear behavior of measured data plotted according to Eq. 1-18. $2K_{1\mathrm{S}}$ corresponds to the intersection with the ordinate and $K_{\mathrm{V,eff}}$ resembles the slope. The shape anisotropy dominates $K_{\mathrm{V,eff}}$, thus the slope is, in this case, always negative. For the other systems investigated in this thesis, however, $K_{2\mathrm{V}}$ is unknown and its determination is beyond the scope of this thesis. While it might be equal in all systems due to the fact that it is a volume term, the distinction between $K_{1\mathrm{V}}$ and $K_{2\mathrm{V}}$ is avoided if possible by using the sum $K_{\mathrm{V}} = K_{1\mathrm{V}} + K_{2\mathrm{V}}$ instead.

If t_{Co} is small enough, $K_{1,\mathrm{eff}} \geq 0$ kJ/m³ is fulfilled as $K_{1\mathrm{S}}$ dominates in this case. This results in an easy axis of magnetization perpendicular to the sample plane. For thicker samples, $K_{1,\mathrm{eff}}$ is dominated by the shape anisotropy, changes sign and the easy axis is parallel to the sample plane (easy plane). The transition from one regime to another is called spin-reorientation transition (SRT). In systems with $K_{2\mathrm{V}} > 0$ kJ/m³, like Pt\Co\Pt, the SRT takes place via a gradual canting of the easy axis from perpendicular to parallel to the sample plane (*147–151*). The angle between easy axis and sample normal Θ_{C} is given by

$$\theta_{\mathrm{C}} = \sin^{-1}\sqrt{\frac{-K_{1,\mathrm{eff}}}{2K_{2\mathrm{V}}}}. \qquad \text{Eq. 1-19}$$

The "easy axis" is then lying on two cones with the opening angle Θ_{C}, which is why this region is frequently called cone state region. The cone state region ($K_{2\mathrm{V}} > 0$, $-2K_{2\mathrm{V}} < K_{1,\mathrm{eff}} < 0$) is usually limited to a narrow thickness range of approximately 0.1 nm. For Co based systems, the region appears for $t_{\mathrm{Co}} \leq 2$ nm (*139*). This two-dimensional description (co-linear orientation of magnetization along z-direction), however, is not valid for multilayers with number of layers $N \gtrsim 4$. This is due to the formation of three-dimensional magnetic microstructures (see chapter 5.2). For $K_{2\mathrm{V}} < 0$ and $-2K_{2\mathrm{V}} > K_{1,\mathrm{eff}} > 0$, e.g. Au\Co\Au (111) the SRT proceeds via a phase of coexistence of easy-plane and perpendicularly magnetized domains (*152–154*).

1.1.4 Dzyaloshinskii-Moriya interaction

The breaking or lack of inversion symmetry in crystal lattices combined with SOI gives rise to the chiral Dzyaloshinskii-Moriya interaction (DMI). DMI favors the canting of adjacent spins and is

the interaction at the heart of the stabilization of magnetic skyrmions (*45, 50, 53–55, 70*). Dzyaloshinskii first proposed the antisymmetric exchange interaction in 1957 to explain weak ferromagnetism in antiferromagnetic bulk oxides (*40*). In 1960, Moriya derived the interaction analytically from the relativistic SOI Hamiltonian (*41*). In atomistic description, the corresponding Hamiltonian is given by (*40, 41*)

$$H_{\mathrm{DMI}} = -\mathbf{D}_{12}(\mathbf{S}_1 \times \mathbf{S}_2), \qquad \text{Eq. 1-20}$$

with the two ferromagnetic spins $\mathbf{S}_1$ and $\mathbf{S}_2$, and the DMI vector $\mathbf{D}_{12}$[4]. In 1980, interfacial DMI was predicted for interfaces of a ferromagnetic material to one with strong SOI, such as Pt or Ir (*155*). Fig. 1-1 shows the three-site indirect super-exchange mechanism between to atomic interface spins $\mathbf{S}_1$ and $\mathbf{S}_2$ mediated via a neighboring atom having a large SOI. The resulting $\mathbf{D}_{12}$ vector is perpendicular to the plane defined by the triangle, and favors a canting or spiraling of the spins around $\mathbf{D}_{12}$ with fixed rotational sense (*38*).

Within the micromagnetic formalism the iDMI energy is given by (*156*)

$$E_{\mathrm{DMI}} = D_{\mathrm{DMI}}\left(\left(M_{\mathrm{z}}\frac{\partial M_{\mathrm{x}}}{\partial x} - M_{\mathrm{x}}\frac{\partial M_{\mathrm{z}}}{\partial x}\right) + \left(M_{\mathrm{z}}\frac{\partial M_{\mathrm{y}}}{\partial y} - M_{\mathrm{y}}\frac{\partial M_{\mathrm{z}}}{\partial y}\right)\right), \qquad \text{Eq. 1-21}$$

with the magnetization components M_i, and the continuous effective DMI constant D_{DMI}. The latter is proportional to $1/t$, due to its interface character.

1.1.5 Interlayer exchange coupling

The coupling of two ferromagnetic layers through a non-magnetic spacer layer is called the interlayer exchange coupling (IEC). It was first observed in 1986 in Dy and Gd films separated by Y and Fe films separated by Cr (*157–159*). In its simplest form

$$\left(\frac{E}{A}\right)_{\mathrm{IEC}} = -J_{\mathrm{IEC}}\,\mathbf{M}_1 \cdot \mathbf{M}_2, \qquad \text{Eq. 1-22}$$

the energy per area of the IEC is called bilinear, as it is linear with respect to the directions of both magnetizations $\mathbf{M}_i$. Positive values of the coupling constant J_{IEC}[5] favor parallel alignment or ferromagnetic IEC (FIC), while negative values favor an antiparallel one or antiferromagnetic IEC (AIC). In literature the latter case is also called synthetic or artificial antiferromagnetic (sAFM or

[4] In literature, the DMI vector is often also defined without the minus sign. Thus, a DMI of opposite sign is obtained.

[5] In literature, the sign of J_{IEC} is often changed, as Eq. 1-22 is defined without a minus sign.

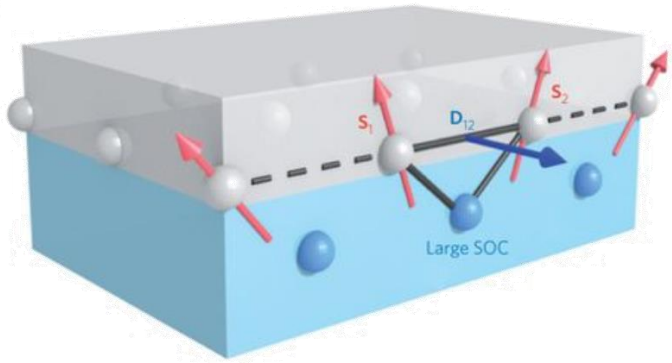

Figure 1-1: Sketch of a DMI at the interface between a ferromagnetic metal (grey) and a metal with strong SOI (blue). The DMI vector $\mathbf{D}_{12}$ related to the triangle composed of two magnetic sites and atom with large SOI is perpendicular to the plane of the triangle. Because the a large SOI exists only in the bottom metal layer, this DMI is not compensated by a DMI coming from a symmetric triangle (*38*).

aAFM). Subsequent discoveries of resulting effects such as the giant magnetoresistance (GMR) in 1988 (*12, 13*) led to enhanced research efforts in the area of interlayer exchange coupling. In 1990 it was discovered that for some spacer materials the sign of J_{IEC} oscillates with the thickness of the non-magnetic layer t_{NM} (*160*) with the magnitude decaying asymptotically. Up to 60 oscillations were observed for t_{NM} = 0– 80 monolayers (ML) (*161*). Systematic studies for sputtered Co-based multilayers revealed oscillation periods of 0.9– 1.2 nm for V, Cu, Mo, Ru, Rh, Re and Ir spacer layers (*162–166*) while longer periods of 1.5 nm were observed for Os (*167*) and 1.8 nm for Cr (*162*). More complicated behaviors were observed in MBE-grown lattice-matched systems, e.g. Co\Cu\Co (*168*).

In 1993, a consensus on the origin of IEC was reached by the development of a model capable of unifying the previous ones (*169–171*), e.g. RKKY- and the free-electron model. The model describes IEC by using quantum well states due to spin-dependent reflections at interfaces. A detailed description of the model can be found in the review articles (*172, 173*). The interface between a ferromagnetic (FM) and a non-magnetic (NM) layer acts as a spin-dependent potential step for free electrons at which they are reflected. In a FM\NM\FM trilayer, electrons are reflected from both interfaces and interfere with each other, like in a quantum well. Constructive interference of the reflected waves leads to bound states of discrete energy, called quantum well states. They are shifted with the NM-layer thickness and an oscillation of the coupling occurs each time a bound state passes the Fermi energy. The period π/q_F is determined by the critical spanning vectors of the spacer layer q_F. A spanning vector, shown in Fig. 1-2, of the Fermi surface is parallel to the interface normal that connects two points on the Fermi surface, one point has a positive component of velocity, and the other has a negative component in the interface direction. A critical spanning

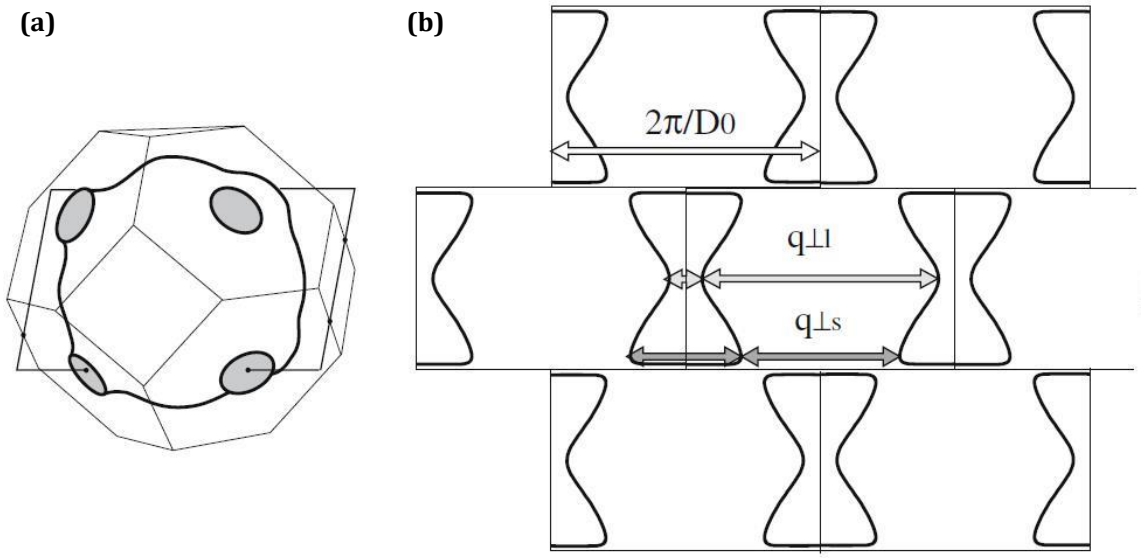

Figure 1-2: (a) Representation of the Fermi surface of Cu. The necks in (111) direction are indicated in gray. (b) Periodically repeated rectangular slice through the Fermi surface in (a) using the extended zone scheme. The bold lines represent the Fermi surface; the white arrow shows a one-dimensional reciprocal lattice vector in the interface direction. Two critical spanning vectors are indicated as light and dark gray arrows. (*172*)

vector is a spanning vector that connects two sheets of the Fermi surface at a point where they are parallel to each other (*172*).

In the same year, the influence of the ferromagnetic-layer thickness on the oscillatory coupling strength was investigated (*174*). They found that interference also occurs in the magnetic layer and results in a change of the electron density. This influences the spin-dependent reflections at the interfaces.

For spacer materials like Pt and Pd, only FIC coupling without oscillations was observed until much later. In 2004 and 2005 oscillations on top of a ferromagnetic background were observed for Pt\Co\Pt multilayers with PMA (*175, 176*). The background is attributed to magnetostatic coupling of surface charges due to the presence of a correlated roughness, the so-called orange peel coupling (*133*). Within a few years, several studies reported AFC for Pt\Co\Pt multilayer in spin-valve geometry with PMA (*177–179*) for $t_{NM} > 2.4\,\text{nm}$ and J_{IEC} two orders of magnitude smaller than for Ir or Ru. AIC for multilayers using Pd as spacer layer has not been reported yet.

Next to the bilinear term, there is also a biquadratic contribution to the IEC. It originates from disorder at the interfaces and favors an orthogonal alignment of $\mathbf{M}_i$ for $J_{IEC} \approx 0$. It is not considered in the following. For a detailed description, the interested reader is referred to (*172, 173, 180*).

Experimental determination of J_{IEC} in the case of AIC

Fig. 1-3 shows idealized easy-axis remagnetization curves for samples with AIC. In the absence of external magnetic fields, the magnetization of adjacent layers is aligned antiparallel. In the presence of fields, three general cases have to be distinguished:

First, the case of strong PMA and two identical ferromagnetic Co-layers of thickness t_{Co}, and $K_{tot} > -J_{IEC}/t_{Co}$ is considered. Above the so-called switching Field H_{SF}, the magnetization of the layer with magnetization direction antiparallel to the external field is reoriented and aligned parallel to it (see Fig. 1-3(a)). At the switching field H_{SF}, both energy contributions are equal and the coupling constant J_{IEC} can be estimated by (*181, 182*)

$$J_{IEC} = -\mu_0 t_{Co} M_S |H_{SF}|. \qquad \text{Eq. 1-23}$$

The remagnetization curve is shown in Fig. 1-3(a) (blue line).

In case of more than two (but even number) of identical Co-layers, a second switching field H_{SF2} is occurs. For a sample consisting of $N = 4$ identical Co-layers, shown as red dashed line in Fig. 1-3(a), the two outer layers are both coupled to only one adjacent magnetic layer while the inner layers are coupled to two layers (above and below). Thus, the inner layers experience twice the coupling. Due to this fact, two magnetization switching processes occur, where the second switching field is $H_{SF2} = 2\,H_{SF}$ (*181*) and

$$J_{IEC} = -\frac{\mu_0 t_{Co} M_S |H_{SF2}|}{2}. \qquad \text{Eq. 1-24}$$

It should be noted that Eq. 1-23 and Eq. 1-24 are only valid for samples possessing no coercivity. For samples with non-vanishing coercivity, the coercivity of the individual layers cause a deviation of the switching fields for the forward and backward sweep (c.f. Fig. 4-23(b)). Although it is technically not correct, averaging of switching fields in both sweeps is common practice, as no better way to treat the presence of coercivity in real samples has been found or proposed (*181*).

In the second case, a multilayer consisting of N Co-layers each with an in-plane easy-axis of magnetization is considered ($K_{tot} \leq 0$). An ideal in-plane easy-axis remagnetization loop is shown in

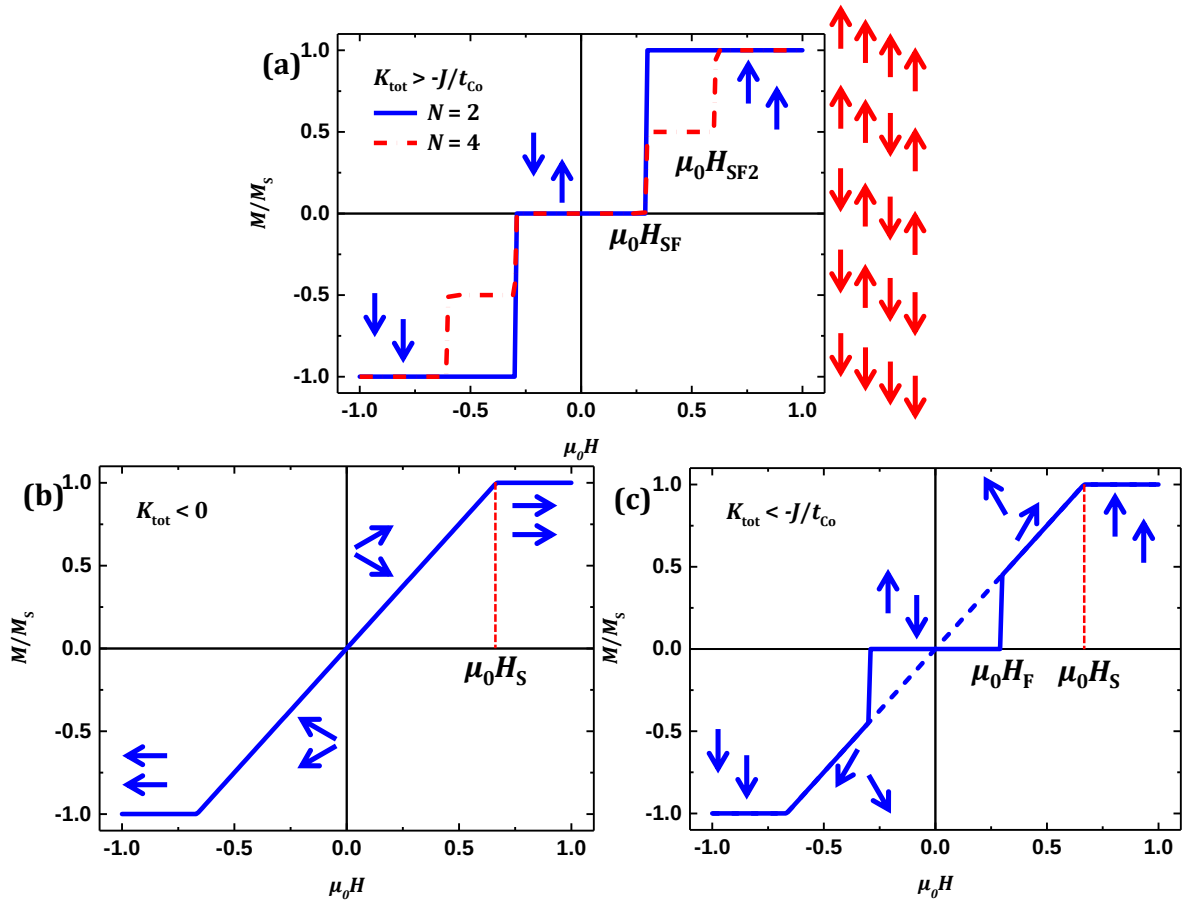

Figure 1-3: Theoretical remagnetization curves for identical antiferromagnetically coupled ferromagnetic layers for the cases (a) perpendicular anisotropy is larger than the coupling, (b) the sample has easy-plane anisotropy, and (c) the perpendicular anisotropy is smaller than the coupling. The arrows schematically indicate the orientations of the layers and the field is applied along the easy axis (perpendicular for (a, c) and longitudinal for (b)). Additionally in (a), the case for four identical layers is depicted. (*181*)

Fig. 1-3(b). In the absence of external fields, the magnetization of adjacent layers is aligned anti-parallel. In the presence of small in-plane fields, the layers are still aligned antiparallel to each other. As long as the field is small, the AIC contribution dominates and the adjacent layers point in almost opposite directions. With increasing field, the AIC is gradually overcome and the layers rotate into the field direction. At the saturation field H_S, all layers are aligned parallel to the field and the coupling constant results in (*181, 183*):

$$J_{IEC} = -\frac{\mu_0 t_{Co} M_S |H_S|}{4\left(1-\frac{1}{N}\right)}. \qquad \text{Eq. 1-25}$$

The denominator accounts for the ratio of outer single-coupled to inner and double-coupled layers. Eq. 1-25 is not exact for $N > 2$ and a closed formula cannot be derived (*184*). Examples of remagnetization curves for different sample systems including coercivity and a theoretical investigation can be found in (*162, 184*).

The last case describes multilayers consisting of two identical Co-layers with weak PMA ($K_{tot} < -J_{IEC}/t_{Co}$), which is shown in Fig. 1-3(c). Without an external field, the two layers of the sample are aligned antiparallel. For small out-of-plane fields, the magnetization of the two layers remain antiparallel due to the small PMA and the AIC.

At the spin-flop field H_F, the magnetization of the layer opposing the external field flips its magnetization direction. This is because the AIC is stronger than the PMA at H_F. Consequently, it is energetically favorable for both layers to cant the magnetization with respect to the easy axis in order to maximize the angle between both magnetization directions (see Fig. 1-3(c)).By further increasing the field, the angle reduces and finally vanishes at H_S. In this case, J_{IEC} can be extracted from both H_F and H_S (*181, 184, 185*) with

$$J_{IEC} = -\frac{t_{Co}}{2} \cdot (\mu_0 M_S |H_S| + 2K_{tot}), \qquad J_{IEC} = -K_{tot} t_{Co} \left(\left(\frac{\mu_0 M_S |H_F|}{2K_{tot}} \right)^2 - 1 \right). \qquad \text{Eq. 1-26}$$

Analogous to the second case ($K_{tot} \leq 0$), a closed formula cannot be derived for $N > 2$. For this case, numerical calculations are required as boundary effects for the canting angle varying across the stack have to be taken into account. The occurring error in the calculations, however, was found to be less than 10 % (*181*).

It should be noted that in literature Eq. 1-23– Eq. 1-26 are also found with an additional factor of 0.5 due to an additional factor of two in the coupling energy (Eq. 1-22). So care has to be taken when comparing with published data (*181*).

1.2 Domains and domain walls

Thus far, only homogenous magnetization distributions have been considered. In general, this is not the case in ferromagnets as a lower total energy (see Eq. 1-1) can be realized by inhomogeneities of the magnetization, i.e. domains and domain walls. This section addresses the non-homogenous magnetization distribution in thin films with PMA.

1.2.1 The origin of domains

First, let us consider a homogenously magnetized thin film with perpendicular easy-axis of magnetization in the absence of external magnetic fields and DMI. This kind of magnetization distribution is associated with a large amount of surface charges, leading to a large stray-field energy of $E_d = \mu_0/2\, M_S^2$. All the remaining energy terms in Eq. 1-1 are zero and the total energy is dominated by the stray-field energy term. The formation of a non-homogenous magnetization distribution, i.e. a magnetic domain pattern, leads to a significant reduction of E_d while increasing the anisotropy and exchange energy. Inside a domain, the magnetization is homogenous in order to minimize E_{ex} and E_{MC}. As no discontinuous transition between domains exists, the transition occurs via a gradual rotation over several spins. The gradual rotation is the so-called domain wall with the width δ_w and energy γ_w determined by E_{ex} and E_{MC}. The domain wall energy γ_w increases with the number of domain walls and the minimum of the total energy, consisting of the domain wall energy and magnetostatic energy determines the equilibrium size of the magnetic domains. The minimum of the total energy of γ_w and E_d determines the equilibrium size of the magnetic domains. Kaplan and Gehring (*186*) first calculated the equilibrium domain size for periodic stripe domains analytically, and were confirmed by Millev (*187*). In this case, they assumed single magnetic layers, large domains ($d \gg t_{FM}$), infinitesimal small domain walls, and no pinning. The result is given by:

$$d = t_{FM} \cdot \exp\left(\frac{\pi}{2} b + 1\right) \cdot \exp\left(\frac{\pi}{2} \cdot \frac{\gamma_w}{K_d \cdot t_{FM}}\right), \qquad \text{Eq. 1-27}$$

with the ferromagnetic film thickness t_{FM} and the domain pattern parameter b = -0.667 for stripe and b = 2.525 for checkerboard.

1.2.2 Domain walls

Within the transition region of two magnetic domains with PMA, the magnetization rotates by 180° over several atomic spins. In order to describe the type of domain wall it is useful to introduce a specific coordinate frame. The magnetization $\mathbf{M} = (M_x, M_y, M_z)$ of the domains is aligned along the z-axis, parallel to the sample normal. In the sample plane, M_z changes along the x-axis and is constant along the y-axis. There are two fundamental modes for the magnetization to rotate in a domain wall, known as Bloch and Néel wall. For Bloch walls, M_x is everywhere zero and $\mathbf{M}$ rotates around the x-axis. The components M_y, M_z, depend on the x coordinate and can be described in polar coordinates by

$$M_z(x) = \cos\vartheta(x)\,, \qquad M_y(x) = \sin\vartheta(x)\,, \tag{Eq. 1-28}$$

with the boundary conditions

$$\vartheta(-\infty) = 0, \qquad \vartheta(\infty) = \pi\,. \tag{Eq. 1-29}$$

For a given sense of rotations M_y, M_z are shown in Fig. 1-4. The domain wall profile $\vartheta(x)$ is obtained from energy minimization of the exchange and anisotropy energy. The exchange energy favors a very broad domain wall so that the angle between adjacent spins is as small as possible. A narrow domain wall is favored by the anisotropy energy, as it is increased with each spin having an angle with respect to the easy axis. This results in the domain wall energy γ_w:

$$\gamma_w = \int_{-\infty}^{\infty} \left(K_{1,\mathrm{eff}} \sin^2(\vartheta) + A_{\mathrm{Ex}} \left(\frac{d\vartheta}{dx}\right)^2 \right) dx. \tag{Eq. 1-30}$$

The minimization $\delta_{\gamma_w} = 0$ can be carried out analytically and yields:

$$\cos\vartheta = \tanh\left(\frac{x}{\sqrt{A_{\mathrm{ex}}/K_{1,\mathrm{eff}}}}\right). \tag{Eq. 1-31}$$

The magnetization profile of a Bloch wall is shown in Fig. 1-4. Following the definition by Lilley (*188*), δ_w is the distance between the points at which the tangent at $x = 0$ crosses $\vartheta(0)$ and $\vartheta(\pi)$. The distance δ_w and γ_w, the domain wall energy per unit area of a Bloch wall is given by

$$\delta_w = \pi\sqrt{\frac{A_{\mathrm{ex}}}{K_{1,\mathrm{eff}}}}, \qquad \gamma_w = 4\sqrt{A_{\mathrm{ex}} K_{1,\mathrm{eff}}}. \tag{Eq. 1-32}$$

Träuble et al. calculated both terms including the second order anisotropy contributions (*189*)

$$\delta_w = \pi\sqrt{\frac{A_{\mathrm{ex}}}{K_{1,\mathrm{eff}} + K_{2V}}} = \pi\sqrt{\frac{A_{\mathrm{ex}}}{K_{\mathrm{tot}}}}, \tag{Eq. 1-33}$$

$$\gamma_w = 2\sqrt{A_{\mathrm{ex}} K_{1,\mathrm{eff}}}\left(1 + \frac{K_{1,\mathrm{eff}} + K_{2V}}{K_{1,\mathrm{eff}} \cdot K_{2V}} \sin^{-1}\frac{K_{2V}}{K_{1,\mathrm{eff}} + K_{2V}}\right).$$

An important property of the Bloch wall is that the magnetization distribution is free of divergence and thus free of volume charges ρ_V = - div **M**. This is not the case for Néel walls, thus Bloch walls are lower in energy and occur as the natural ground state in films with PMA in the absence of DMI.

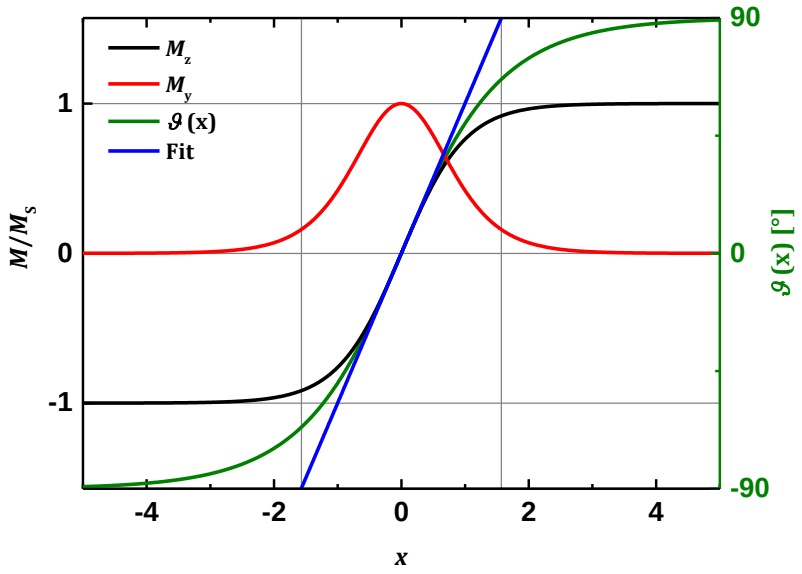

Figure 1-4: The width δ_w and the profile of the domain wall transition $\vartheta(x)$ result from a balance between the exchange energy A_{ex} and anisotropy energy K_{tot} (*121*).

The Néel wall rotates into the x-axis (in Fig. 1-4, M_y is replaced by M_x), which gives rise to volume charges. The width of a Néel wall is equal to the one of a Bloch wall, except for a difference of less than 1 % (*37*). For decreasing film thickness, the energy density difference between the two types decreases (*190*), as the volume charges reduces. In the presence of DMI, the domain wall energy is described by (*71, 190–192*):

$$\gamma_{w,Néel} = 4\sqrt{A_{ex}K_{1,eff}} - \pi|D_{DMI}| + t\frac{\ln 2}{\pi}\mu_0 M_S^2, \qquad \text{Eq. 1-34}$$

with the effective DMI constant D_{DMI}. This can be understood by assuming a domain wall that runs along that x-axis, with the magnetization **M** constant along the y-axis, and a DMI vector **D** is parallel to the y-axis. E_{DMI} is reduced, if the spins $\mathbf{S}_i$ rotate around the y-axis, thus just like the Néel wall. For all other directions of **D** or in case of a Bloch wall, E_{DMI} is unaffected.

For small values of D_{DMI}, neither pure Néel nor Bloch walls are present. Instead, the magnetization rotates as a mix of Bloch and Néel wall with a specific angle φ between M_x and M_y direction. Then, Eq. 1-34 follows to (*190–192*)

$$\gamma_{w,Néel} = 4\sqrt{A_{ex}K_{1,eff}} - \pi|D_{DMI}|\sin\varphi + t\frac{\ln 2}{\pi}\mu_0 M_S^2 \sin^2\varphi. \qquad \text{Eq. 1-35}$$

The angle φ follows from minimization of Eq. 1-35. For φ = 90° Eq. 1-35 turns back into Eq. 1-34 for Néel walls and for φ = 0° into Eq. 1-32 in case of a Bloch wall. The threshold DMI, D_{thr}, required to fully turn a Bloch into a Néel wall is expressed by (*37*)

$$D_{\mathrm{thr}} \approx \frac{2t\mu_0 M_S^2}{\pi^2}. \qquad \text{Eq. 1-36}$$

Besides the mentioned simplest types of domain walls, other more complex types exist. I.e. crosstie walls, asymmetric Bloch and Néel walls, and "hybrid" domain walls. The hybrid type frequently appears in multilayers and is a combination of Bloch and Néel walls. They are addressed later on in this thesis (see chapter 5.2).

1.3 Soft X-ray holographic microscopy and X-ray resonant magnetic scattering

This chapter introduces the basic principles of soft X-ray holographic microscopy (XHM) and X-ray resonant magnetic scattering. First, the X-ray magnetic circular dichroism (XMCD) is described (section 1.3.1). Subsequently, the basics of X-ray resonant magnetic scattering in the framework of the small-angle approximation and magnetic samples with out-of-plane easy-axis of magnetization are discussed (section 1.3.2). Finally, the image formation in XHM is described in detail (section 1.3.3).

1.3.1 X-ray magnetic circular dichroism

The X-ray magnetic circular dichroism measures the dependence of X-ray absorption on the helicity of X-rays passing through a magnetic material. It is an element-specific technique and is able to distinguish between the spin and orbital part of the magnetic moment.

The intensity of an X-ray beam with the energy $E = \hbar\omega$ traversing matter decreases exponentially due to X-ray absorption. Within the spectral range of soft X-ray light, the dominant absorption process is the photoelectric effect. The remaining intensity after traveling the distance t through a material is described by the Beer-Lambert law (*193*):

$$\frac{I(E,Z,t)}{I_0} = e^{-\mu(E,Z)t}. \qquad \text{Eq. 1-37}$$

The absorption coefficient μ is strongly dependent on the atomic number Z ($\sim Z^4$) and monotonically decreases with increasing E ($\sim E^{-3}$) (*194*). Within the X-ray spectrum, the progression of μ for a constant Z is interrupted by the so-called absorption edges, where the absorption is strongly

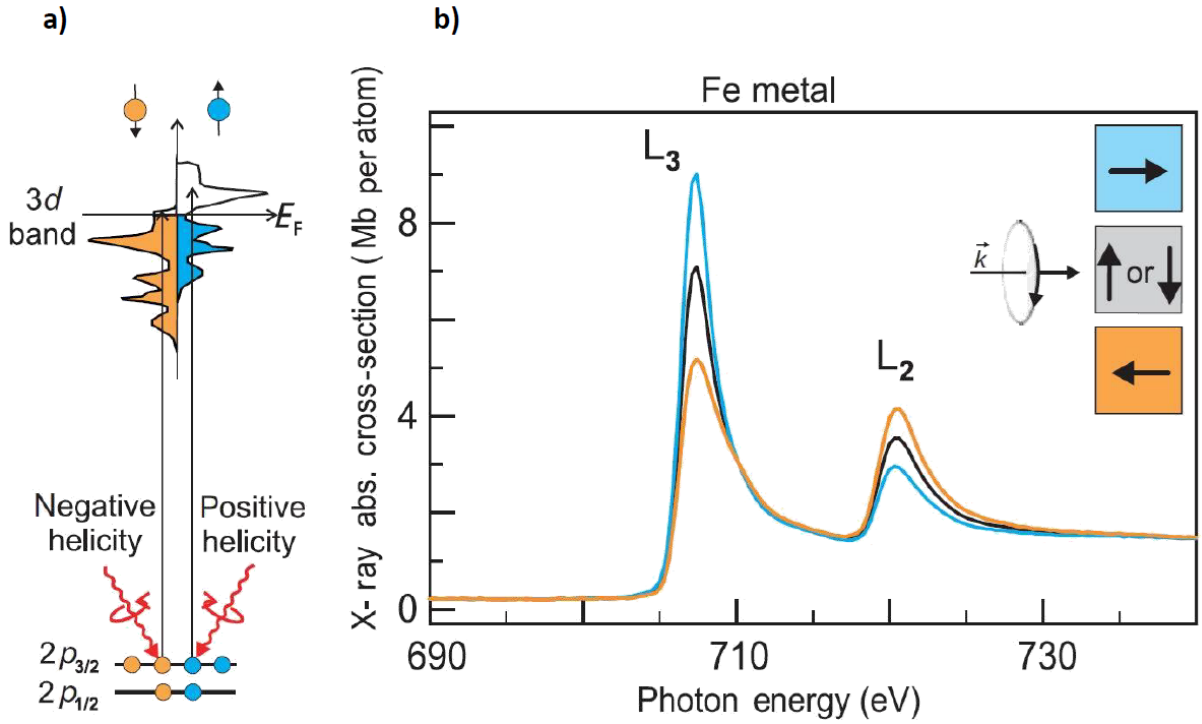

Figure 1-5: XMCD effect at the *L* edges of iron. a) Excitation of spin-polarized photoelectrons into the exchange-splitted *d*-bands of iron using X-rays with opposite helicity. b) X-ray absorption cross section of circularly polarized X-rays in the soft X-ray regime using a ferromagnetic iron sample with magnetization direction aligned with respect to the direction of the photon angular momentum (*193*).

increased. At these resonance energies, the photons excite core-level electrons onto unoccupied states above the Fermi energy.

In magnetic materials, the absorption further depends on the polarization of the photons relative to the magnetization direction **M**. For circular polarized light, this effect is called X-ray magnetic circular dichroism (XMCD) and appears when the photon-wave vector **k** and **M** are aligned (anti-)parallel. Dichroism refers to the instant that for **k** and **M** pointing into the same direction, the absorption of left (σ^-) and right (σ^+) circular polarized light differs strongly ($\mu^+ \neq \mu^-$) as shown in Fig. 1-5(b) for Fe. In the following the XMCD effect is described by a two-step model for the L_2 and L_3 absorption edges in 3*d* transition metals, e.g. Co and Fe (*193*):

In the first step, electrons of the core-level spin-orbit slit 2*p* states absorb circular polarized photons. Right (left) circular polarized photons have an angular momentum of $l^+ = +\hbar$ ($l^- = -\hbar$), aligned parallel (antiparallel) to the wave vector **k**, that points in propagation direction. Due to the spin-orbit coupling, the 2*p* states are split into two sublevels with an energy difference

$\Delta E \approx 15\,\text{eV}$, $2p_{3/2}$ ($j = l + s$, L_3–edge) and $2p_{1/2}$ ($j = l - s$, L_2–edge). For electrons in spin-split states, the absorbed angular momentum of the photon can be partially transferred to the spin by spin-orbit coupling leading to a spin polarization of the excited electrons. For left and right circular polarized photons, the spin polarization is opposite, as well as for the two edges with opposite spin-orbit coupling. The quantization axis of the excited electron is identical to the incident X-rays, i.e. parallel or antiparallel to the wave vector **k**. The selection rules for dipolar transitions $\Delta l = \pm 1$, $\Delta m = \pm 1$, and $\Delta s = \pm 1$ apply for this process, thus the spin s of the electrons is conserved. The probabilities of the possible transitions are described by the Clebsch-Gordan coefficients. They show a higher probability for a σ^+-photon to excite an electron of minority spin and vice versa (*193*).

$\Delta E \approx 15\,\text{eV}$, $2p_{3/2}$ ($j = l + s$, L_3–edge) and $2p_{1/2}$ ($j = l - s$, L_2–edge). For electrons in spin-split states, the absorbed angular momentum of the photon can be partially transferred to the spin by spin-orbit coupling leading to a spin polarization of the excited electrons. For left and right circular polarized photons, the spin polarization is opposite, as well as for the two edges with opposite spin-orbit coupling. The quantization axis of the excited electron is identical to the incident X-rays, i.e. parallel or antiparallel to the wave vector **k**. The selection rules for dipolar transitions $\Delta l = \pm 1$, $\Delta m = \pm 1$, and $\Delta s = \pm 1$ apply for this process, thus the spin s of the electrons is conserved. The probabilities of the possible transitions are described by the Clebsch-Gordan coefficients. They show a higher probability for a σ^+-photon to excite an electron of minority spin and vice versa (*193*).

In the second step, the electrons are excited into the exchange-split $3d$ valence bands (*193, 195*). Due to the exchange splitting, the $3d$ bands are shifted in energy for spin-up and spin-down electrons. This is depicted in Fig. 1-5(a). Compared to the minority spin, the valence band for the majority spin has a lower energy and is filled to a higher degree. Thus, the density of unoccupied states near the Fermi energy is imbalanced. As the absorption is directly proportional to the number of unoccupied states, the XMCD is directly proportional to this imbalance, and therefore the spin moment.

Fig. 1-5(b) depicts the L_3 and L_2 absorption edges for Fe at a photon energy of 707 and 720 eV (778 eV and 793 eV for Co and 853 eV and 870 eV in Ni). The XMCD has a maximum for parallel alignment of **k** and **M** and does not apply for an orthogonal alignment of the two vectors. In-between it follows a cosine behavior.

1.3.2 X-ray resonant magnetic scattering

X-ray resonant magnetic scattering is a technique, which combines X-ray magnetic circular dichroism with X-ray scattering. It is an exceptional element-specific probe to investigate magnetic textures on the nanoscale. It gives ensemble-averaged information about magnetic domain patterns, e.g., mean domain periodicity, pattern geometry, and spatial correlation lengths. X-ray resonant magnetic scattering has a close link to X-ray absorption as the excited core electron after X-ray absorption decays back into the core shell by emission of a photon with the same energy. This process is then called resonant elastic X-ray scattering. Coherent X-ray scattering data allows for probing spatial symmetries of the magnetic microstructure and performing time correlations to map out magnetization dynamics via X-ray photon correlation spectroscopy (XPCS).

Before X-ray resonant scattering at magnetic domains and the magnetic resonant scattering amplitude is discussed, the basic principles of X-ray scattering are addressed. X-rays illuminating an atom are scattered by the electron cloud of the atom. In this case, it is assumed that the total scattered amplitude is just the sum of the amplitudes of the individual electrons. The atomic form factor is a measure of the scattering amplitude of a wave by an atom and is given by (*196*):

$$f_0(\mathbf{q}) = -\frac{1}{e}\int \rho_e(\mathbf{r}) \cdot e^{i\mathbf{q}\mathbf{r}}\, d\mathbf{r}\,. \qquad \text{Eq. 1-38}$$

$\rho_e(\mathbf{r})$ is the spatial density distribution or charge density. Eq. 1-38 shows that the atomic form factor is the Fourier transform of the electron density and that the scattering process is angle dependent. The scattering vector or momentum transfer $\mathbf{q} = \mathbf{k} - \mathbf{k}'$ is expressed by:

$$q = |\mathbf{q}| = 2k \sin\theta = \frac{4\pi}{\lambda}\sin\theta\,, \qquad \text{Eq. 1-39}$$

where 2θ is the angle between the incoming $\mathbf{k}$ and outgoing wave $\mathbf{k}'$.

The non-resonant differential atomic scattering cross-section gives the angular distribution of the scattering by an atom:

$$\left(\frac{d\sigma}{d\Omega}\right)_{\text{atom}} = r_0^2 \cdot |\boldsymbol{\varepsilon} \cdot \boldsymbol{\varepsilon}'|^2 \cdot |f_0(\mathbf{q})|^2, \qquad \text{Eq. 1-40}$$

with the unit polarization vectors of the incident and scattered wave $\boldsymbol{\varepsilon}$ and $\boldsymbol{\varepsilon}'$, the Thomson scattering length (or classical electron radius) r_0 = 2.82 fm.

In the soft X-ray region, the wavelength λ of the incident light is large compared to the atomic size, thus the atomic form factor is approximately Z, the total number of electrons.

In case of resonant X-ray scattering, the resonant process can be treated semi-classically by a collection of harmonic oscillators, where each oscillator corresponds to a quantum mechanical resonant excitation process of a core shell. The resonant scattering factor or resonant scattering amplitude is expressed by

$$f(\mathbf{q}, \hbar\omega) = f_0(\mathbf{q}) + f'(\hbar\omega) + if''(\hbar\omega), \qquad \text{Eq. 1-41}$$

with the energy-dependent dispersive and absorptive contributions $f'(\hbar\omega)$ and $f''(\hbar\omega)$. Resonant X-ray scattering and absorption can be linked by means of the optical theorem which states that the imaginary part of $f(\mathbf{q}, \hbar\omega)$ is proportional to the absorption cross section (*193*):

$$\mathrm{Im}\big(f(\mathbf{q}, \hbar\omega)\big) = f''(\hbar\omega) = \frac{1}{2\lambda r_0}\sigma_{\mathrm{abs}}(\hbar\omega). \qquad \text{Eq. 1-42}$$

For X-ray resonant magnetic scattering, the energy of the photons matches the energy difference of two specific electronic levels and the scattering intensity is enhanced. This can be expressed as the resonant absorption and emission of a photon.

Within a quantum mechanical approach, this process can be treated by the time-dependent perturbation theory. An X-ray photon excites an electron in the initial state a into the intermediate state n, which then relaxes back to a via an emission of a photon. The differential elastic scattering cross section in the dipole approximation (*193*) follows to

$$\left(\frac{d\sigma}{d\Omega}\right)_{\mathrm{atom}} = |f(\hbar\omega)|^2 = \frac{\hbar^2\omega^4\alpha_{\mathrm{f}}^2}{c^2} \cdot \left|\sum_n \frac{\langle a|\mathbf{r}\cdot\boldsymbol{\varepsilon}'|n\rangle\langle a|\mathbf{r}\cdot\boldsymbol{\varepsilon}|n\rangle}{\hbar\omega - E_R(n) + i(\Delta_n/2)}\right|^2, \qquad \text{Eq. 1-43}$$

with the fine structure constant α_{f}, the resonant energies $E_{\mathrm{R}}(n) = E_{\mathrm{n}} - E_{\mathrm{a}}$ and the energy distribution Δ_{n}. For a detailed derivation and description, it is referred to (*193, 196*).

Magnetic multilayers with out-of-plane easy-axis of magnetization form magnetic domain patterns, which can exhibit various geometries, e.g., stripe, labyrinth-like or bubble (see chapter 1.2). These domain patterns can be described via a two-dimensional magnetization distribution $\mathbf{m}(\mathbf{r})$ where the magnetization direction is either parallel or antiparallel to the sample's normal. In this case, a homogeneous magnetization along the depth of the film is assumed. The elastic resonant magnetic scattering amplitude is given by (*197–199*):

$$f_0(\mathbf{r}) + (\boldsymbol{\varepsilon}'\cdot\boldsymbol{\varepsilon})f_c(\mathbf{r}) + i(\boldsymbol{\varepsilon}'\times\boldsymbol{\varepsilon})\mathbf{m}(\mathbf{r})f_{m1} + \big(\boldsymbol{\varepsilon}'\cdot\mathbf{m}(\mathbf{r})\big)\big(\boldsymbol{\varepsilon}\cdot\mathbf{m}(\mathbf{r})\big)f_{m2}\,. \qquad \text{Eq. 1-44}$$

The magnetization independent scattering amplitudes $f_0(\mathbf{r})$ (Thomson contribution) and $f_c(\mathbf{r})$ (anomalous charge scattering) are also described by two-dimensional distributions. f_{m1} and f_{m2}

are magnetization-sensitive scattering amplitudes. The first two charge scattering terms of Eq. 1-44 can be combined to $f_C(\mathbf{r})$ in the small-angle limit. The third term depends linearly on the magnetization and polarization and accounts for the XMCD (*198, 200–202*). The fourth and last term describes the X-ray liner magnetic dichroism (XMLD) (*203, 204*). For linearly polarized light, the magnetic scattering causes a rotation of the polarization plane. For perpendicularly magnetized samples $\mathbf{m}(\mathbf{r})\|\mathbf{k}$, the fourth term vanishes. However, non-zero contributions remain in case of canted states or a small tilt of the sample. But the XMLD effect is in general much smaller than the XMCD and can thus be neglected, especially due to the fact that it is quadratic in the magnetization (*193, 205, 206*). Thus, for incident circularly polarized X-rays, the elastic resonant magnetic scattering amplitude can be simplified to (*199*):

$$f(\mathbf{r}) = f_C(\mathbf{r}) + \mathbf{m}(\mathbf{r}) f_{m1}. \qquad \text{Eq. 1-45}$$

f_{m1} is drastically increased at the resonance of the magnetic material. If the charge and the magnetic scattering exhibit similar length scales and thus coincide in the reciprocal space, the resonant magnetic scattering can be distorted. For the samples used in this thesis, charge inhomogeneities on the length scale of the magnetic domains (approximately 100 nm) do not exist (10 nm grains) so that the charge contribution in Eq. 1-45 can be neglected in the following. The magnetic scattering intensity is expressed by

$$I(\mathbf{q}) \propto I_0 \left| \int f(\mathbf{r}) \exp(i\mathbf{q}\mathbf{r}_n) d^2\mathbf{r} \right|^2 = I_0 \left| \int \mathbf{m}(\mathbf{r}) f_{m1} \exp(i\mathbf{q}\mathbf{r}_n) d^2\mathbf{r} \right|^2, \qquad \text{Eq. 1-46}$$

where $\boldsymbol{I_0}$ is the incident photon flux. From Eq. 1-46 follows that the magnetic scattering intensity is proportional to the squared modulus of the two-dimensional Fourier transform of the magnetic domain pattern $\mathbf{m}(\mathbf{r})$. In case of highly ordered magnetic stripe domain patterns and bubble-like patterns, the magnetic scattering intensity can be described by (*207*):

$$I(\mathbf{q}) = F(\mathbf{q})^2 \cdot S(\mathbf{q}) \cdot I_0, \qquad \text{Eq. 1-47}$$

where $F(\mathbf{q})$ is the form factor and $S(\mathbf{q})$ the structure factor. The form factor is the Fourier transform of the shape of the object (magnetic unit cell) and the structure factor accounts for the arrangement of the scattering objects (basic lattice). So far, the influence of the domain wall on the magnetic scattering intensity has been neglected. In order to take the domain wall profile into account, $\mathbf{m}(\mathbf{r})$ in Eq. 1-46 and the magnetic unit cell prior to the FFT in Eq. 1-47 have to be convolved with an adequate convolution kernel. To obtain a hyperbolic-tangent domain wall (HTDW) profile with a Bloch wall width according to Lilley (see chapter 1.2.2), the magnetization distribution or magnetic

unit cell has to be convolved with the derivative of the HTDW (*208*). The domain-wall profile results in a domain wall factor in Fourier space. This factor can lead to a shift of the actual peak position of the scattering intensity profile, which is often used to obtain the mean domain size. For ordered stripe domain patterns and slightly disordered maze domain patterns, the effect of the domain wall on the scattering intensity is in first approximation negligible. This is the case for the magnetic samples investigated in this thesis. Other effects on the scattering profile, especially in case of highly disordered maze domain patterns, are discussed in detail elsewhere (*208, 209*).

1.3.3 Soft X-ray holographic microscopy

In far-field microscopy, the achievable resolution is limited by the Abbe diffraction limit to roughly $d_{\mathrm{res}} = \lambda/2$, with λ the wavelength of the illuminating wave (*89*). Using visible light, no features smaller than ~200 nm can be resolved. In order to resolve smaller features, than possible with the visible light, various approaches are possible. The easiest approach is reducing the wavelength of the illuminating wave, i.e. using X-rays or electrons. Other approaches in the visible light spectrum involve special techniques, called super-resolution microscopy techniques, i.e. near-field fluorescence microscopy, and photon tunneling microscopy. Using soft X-rays at absorption edges has the advantage, next to the short wavelength enabling nanometer resolution, of an element specific contrast mechanism. With the XMCD and XMLD, X-rays are also sensitive to the magnetization. The disadvantage is the requirement for special X-ray lenses, so-called zone plates, as the diffractive index of glass is negligible and the absorption too high.

Four imaging techniques have evolved utilizing circular polarized soft X-rays to image magnetic domain structures. They all share the transmission geometry and are thus sensitive to the M_{z}-component, with $\mathbf{z}\|\mathbf{k}$. Scanning transmission X-ray microscopy (STXM) is the analog to scanning electron microscopy. The beam scans over the sample and the transmitted intensity is recorded for each point or pixel, thus creating a 2D intensity map. The resolution is limited by the illuminated area, or spot size on the sample. By using zone plates, the X-ray beam can be focused down to around d_{res} = 7– 30 nm on the sample (*95, 210*). The big issue is the fabrication of high-quality zone plates, which requires high technical expertise. Crucial for the resolution is the thinnest and outermost zone of a lens, which at the same time has the highest circumference. The second technique is the full-field transmission X-ray microscope (TXM), which is the analog to a standard light microscope. While STXM requires only one zone-plate for the illumination (condenser), TXM requires a second projective lens. The highest resolution has been reported to d_{res} = 12– 20 nm (*93, 211*).

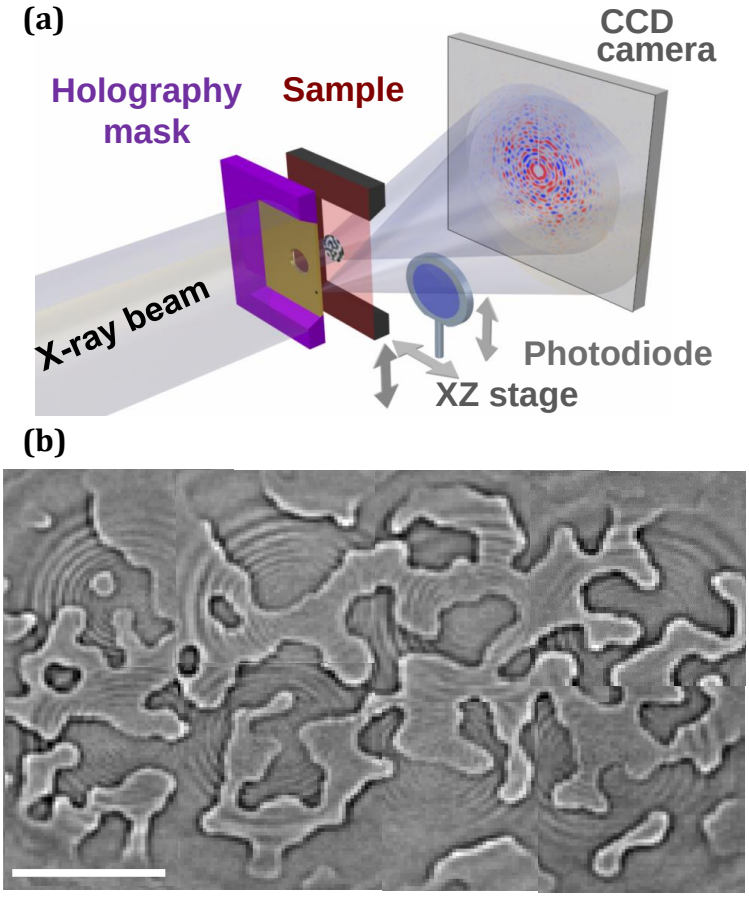

Figure 1-6: (a) Sketch of the X-ray holographic microscope. The key components are the holography mask, the sample in form of a second Si_3N_4 membrane, and a CCD camera. The holography masks, consisting of an object and reference hole, is rigidly located in the center of the X-ray beam. The second membrane, which carries the sample, can be moved freely with respect to the holography mask. Both membranes are in close contact (in the sketch, where they are separated by a small gap for better visualization). The waves emitted from object and reference hole interfere on the CCD camera, where the hologram is recorded. (b) Eight reconstructed images of the domain structure of a DyCo alloy sample at the Co L_3-edge are stitched together to increase the field of view. The scale bar indicates a distance of 1 μm.

The remaining two imaging techniques are lensless scattering and diffraction methods, where the real space information is reconstructed from the scattering intensity (see Eq. 1-47) and interference pattern, thus obtained indirectly. The theoretically achievable resolution is diffraction limited by the wavelength. With $\lambda = 1.6\,\text{nm}$ at the Co L_3-edge, d_{res} is one order of magnitude smaller compared to zone-plate techniques. Both techniques require a sufficient degree of coherent illumination (constant phase relation (*212*)). The obstacle, however, is the loss of phase information in the

recorded scattering intensity, required for the real space reconstruction. For coherent diffraction imaging (CDI), iterative phase retrieval algorithms accomplish this. Coherent X-rays illuminate a region of the sample and the scattering intensity pattern is recorded with a CCD. In order for the algorithms to work, several patterns are required with spatial overlap in the illuminated region. The highest achieved resolution for soft X-rays is d_{res} = 10 nm (*105, 106*), limited by the algorithms.

In holography, the scattered object wave (OW) is coherently superimposed on the detector with a reference wave (RW), where the two interfere. The phase information is encoded in the interference pattern and can be reconstructed. In the Fourier transform holography (FTH) geometry, the coherent illumination is split into an OW and a point-like RW, both originating in the same plane. A simple 2D Fourier transform reconstructs the real space information (image). The geometry was first proposed and realized with visible light in 1964 (*213–216*). The first realization with X-rays succeeded 30 later using a zone-plate to produce the RW (*217, 218*). In 2004, Eisebitt et al. (*219*) demonstrated magnetic imaging with a Pt\Co\Pt multilayer using a small pinhole to produce the RW and achieved a resolution of d_{res} = 50 nm. Their sample consisted of a Si_3N_4 membrane with 800 nm Au on one side and the magnetic multilayer on the other. A 2 µm diameter opening was structured into the Au and Si_3N_4, not penetrating the multilayer, emitting the OW. Close by, the pinhole (reference hole (RH)) penetrated the entire sample, forming the RW. The fabrication of these samples is much less complicated than the fabrication of a zone plate; however, the field of view (FOV) is limited to the predetermined area of the opening.

X-ray holographic microscopy (XHM) was realized in 2010 by our group (*220*). It is based on FTH and has the benefit of enabling a positioning of a sample with respect to an optics mask, extending the area that can be imaged on a sample. This is achieved by splitting the sample structure used by Eisebitt et al. up and placing them on two separate membranes in close proximity. The approach is shown in Fig. 1-6. The purple holography mask carries the 800 nm thick Au film with a 2 µm wide object hole (OH) and a small RH inside. The sample membrane (brown) carries the magnetic sample and can be moved freely in space. The OW and RW interfere on the CCD camera, where the hologram is recorded. One obstacle of this approach is the tiny gap (typically single digit µm-wide) separating the two membranes. The real space image is reconstructed by the Fourier transformation in the plane of the holographic mask. Due to the gap, the image features appear blurred and "out of focus". The issue was solved by wavefield back propagation, demonstrated in the same year (*221*).

In the following sections the image formation, reconstruction, and wavefield back propagation in XHM are discussed.

1.3.3.1 Image formation and reconstruction in Fourier transform holography

Under far-field conditions, the scattering intensity $I(k_x, k_y) = |O(k_x, k_y)|^2$ (see Eq. 1-47) of an object $o(x, y)$ corresponds to the squared Fourier transform of the objects exit wave (*222–224*). If both the amplitude and the phase of the diffracted wave field $O(k_x,k_y) = A \exp i\varphi$ could be measured, a simple inverse Fourier transform would reconstruct the real space image of the object:

$$o(x, y) = \mathcal{F}^{-1}O(k_x, k_y) \Leftrightarrow O(k_x, k_y) = \mathcal{F}o(x, y). \qquad \text{Eq. 1-48}$$

Small letters indicate the wave front in real space and big letters in reciprocal space. As the phase information is lost during detection and only the intensity of the light can be recorded in a diffraction pattern, the inverse Fourier transform of the diffraction pattern represents the spatial autocorrelation:

$$\mathcal{F}^{-1}|O(k_x, k_y)|^2 = o(x, y) \otimes o^*(-x, -y). \qquad \text{Eq. 1-49}$$

One can now introduce a reference source $r(x - x_0, y - y_0)$ which is placed close to the object with an offset (x_0, y_0). The resulting diffraction pattern or hologram $H(k_x,k_y)$ can be expressed as:

$$\begin{aligned} H(k_x, k_y) &= \mathcal{F}|o(x, y) + r(x - x_0, y - y_0)|^2, \\ H(k_x, k_y) &= \mathcal{F}(o(x, y) + r(x - x_0, y - y_0)) \cdot \mathcal{F}^*(o(x, y) + r(x - x_0, y - y_0)) \\ H(k_x, k_y) &= O(k_x, k_y) \cdot O^*(k_x, k_y) + R(k_x, k_y) \cdot R^*(k_x, k_y) \\ &\quad + O(k_x, k_y) \cdot R^*(k_x, k_y) \cdot \exp\left(i(k_x x_0 + k_y y_0)\right) \\ &\quad + O^*(k_x, k_y) \cdot R(k_x, k_y) \cdot \exp\left(-i(k_x x_0 + k_y y_0)\right). \end{aligned} \qquad \text{Eq. 1-50}$$

The reconstruction of the objects exit wave front in Eq. 1-50 can now be calculated using an inverse Fourier transform using the shift and convolution theorem of Fourier transform (*225*):

$$\begin{aligned} \mathcal{F}^{-1}\left(H(k_x, k_y)\right) &= o(x, y) \otimes o^*(-x, -y) + r(x, y) \otimes r^*(-x, -y) \\ &\quad + o(x + x_0, y + y_0) \otimes r^*(-x, -y) \\ &\quad + o^*(-x + x_0, -y + y_0) \otimes r(x, y). \end{aligned} \qquad \text{Eq. 1-51}$$

In an ideal case, the reference wave is a point-like Dirac δ-distribution, with the identity property $f(x + x_0, y + y_0) \otimes \delta(x) = f(x + x_0, y + y_0)$:

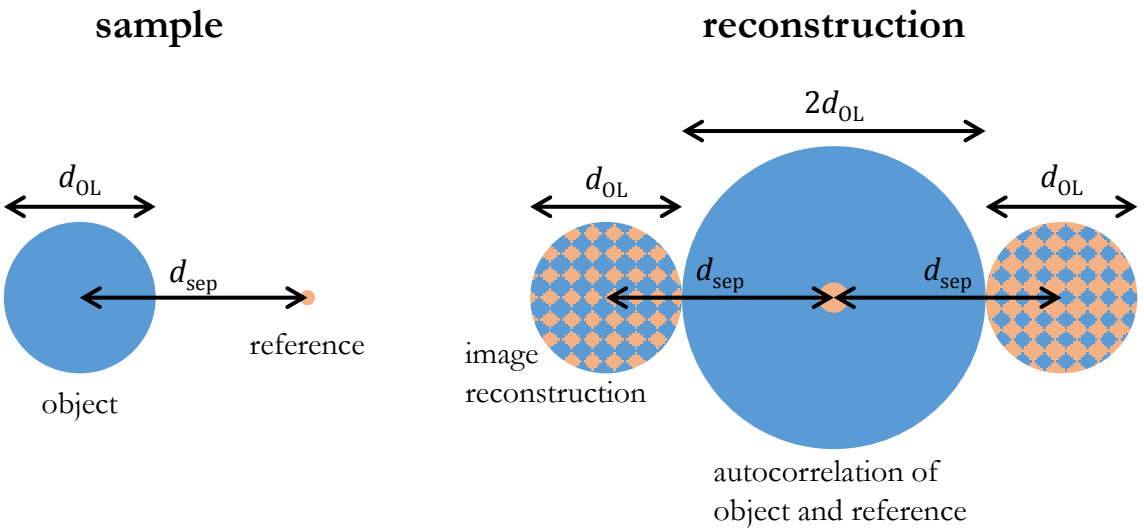

Figure 1-7: Sketch of the FTH geometry. On the sample, the object of size d_{OL} and the reference are separated by d_{sep}. In the reconstruction, both image reconstructions are spatially separated from the autocorrelation if d_{sep} is at least 1.5 times larger than d_{OL} (*224*).

$$\mathcal{F}^{-1}\left(H(k_x,k_y)\right) = o(x,y) \otimes o^*(-x,-y) + \delta(x,y) + o(x+x_0,y+y_0) + o^*(-x-x_0,-y-y_0). \quad \text{Eq. 1-52}$$

The first two terms are the autocorrelation of the object and reference wave, which appear in the center of the image reconstruction. The third term is the reconstruction of the object wave front displaced relative to the origin by (x_0, y_0), and the fourth its complex conjugated twin image at (-x_0, -y_0).

Shown in Fig. 1-7 is the layout of the FTH geometry. The object has a diameter of d_{OL} and is separated from the reference by d_{sep}. The autocorrelation of the object and reference wave in Eq. 1-52 have twice the size of the object and reference source with the reconstruction on one side and the complex conjugate twin image on the opposite. In order for the reconstructions of the object wave to be spatially separated from the autocorrelation, d_{sep} has to be at least 1.5 times the size of the object: $d_{sep} \geq 1.5\ d_{OL}$.

Furthermore, the FTH geometry is not limited to one object and one reference. Using multiple references is called multiplexing and adds two reconstructions for each reference. Additional cross correlation terms between references appear as well. The references have to be places accordingly that the individual reconstructions are separated from one another (*220, 226–228*). Multiplexing

opens the possibility to have references of different sizes and thus resolution and contrast C, with the two quantities being inversely proportional to one another: $C \propto 1/d_{\mathrm{res}}$. Alternatively, the individual reconstructions can be averaged to reduce the noise using identical-sized references. It should be noted, that if the largest separation of an object-reference ensemble or two references d_{max} is larger than the transversal coherence length, the individual holograms of the pairs are added incoherently (*229*). Further, multiple objects can be imaged simultaneously as well (*230, 231*).

Magnetic imaging

Typically, FTH is used to image magnetic multilayer samples with perpendicular magnetization and layers of other nonmagnetic materials, i.e. Si_3N_4, Pt, and Ir (see chapter 4.1). The scattering intensity, and therefore the hologram, of such a sample consists of polarization dependent (XMCD) and independent (charge) terms (see Eq. 1-44 and Eq. 1-45). Upon switching the polarization of the X-rays, the charge terms of the hologram remain unchanged; the XMCD terms change sign. By subtracting holograms of both polarizations, the so-called difference hologram, the charge terms cancel each other out while the XMCD terms add up which is called difference hologram. If holograms of both polarizations are added up, the so-called sum hologram, the XMCD terms cancel while the charge terms add up. The reconstruction of a difference hologram will thus only show magnetic information of the object, and only charge information for the sum hologram, respectively.

Resolution and contrast

Due to the interference between reference and object wave the relative phase information is encoded. This interference results in a modulation of the intensity pattern and is related to the distance between reference and object (*230, 231*). Its direction corresponds directly to the vector between reference and object and the modulation wavelength λ_{mod} can be described mathematically by

$$\lambda_{\mathrm{mod}} = \frac{\lambda z}{d_{\mathrm{sep}}}, \qquad \text{Eq. 1-53}$$

with the detector-sample distance z. According to the Shannon-Nyquist sampling theorem each continuous signal like a hologram modulation needs to be sampled at least twice per wavelength of the signal to record its information (*231, 232*). As the detectors (CCD camera) are divided into pixels with pixel size s_{px}, it is necessary that the modulation length corresponding to the largest distance within the complete holographic mask, $d_{\mathrm{sep}} = d_{\mathrm{max}}$, is larger than two pixels to get an image reconstruction:

$$d_{\max} \leq \frac{\lambda z}{2 s_{\mathrm{px}}}. \qquad \text{Eq. 1-54}$$

Thus, limiting $d_{\max}$ for a given z and λ. Together with the separation condition, $d_{\mathrm{sep}} \geq 1.5\, d_{0\mathrm{L}}$, the sampling of the detector limits the maximum size of the object that can be imaged. Using the parameters of the experiments later shown of λ = 1.6 nm, z = 0.2 m, and s_{px} = 15 µm, results in $d_{\max}$ = 10.6 µm.

The smallest sample feature that can be resolved is related to the diffraction-limited resolution $d_{\mathrm{res,diff}}$. With a detector of $n \times n$ pixels and q = 0 in the center, $d_{\mathrm{res,diff}}$ corresponds to (*233*):

$$d_{\mathrm{res,diff}} = \frac{\lambda}{2\mathrm{NA}} = \frac{\lambda}{2m \sin 2\theta} = \frac{\lambda z}{2 n s_{\mathrm{px}}}. \qquad \text{Eq. 1-55}$$

The numerical aperture NA in microscopy is given by the product of the refractive index m (= 1 for vacuum) and the sine of half the acceptance angle 2θ. Using the experimental parameters from above and n = 4096, this results in $d_{\mathrm{res,diff}}$ = 2.6 nm. A second limitation to the achievable resolution is the finite size of the reference. The reconstructed image is the convolution between object and reference and be pictured as scanning the object with the reference. Using the 10–90 % criterion, the size of the reference limits the resolution to (*224*):

$$d_{\mathrm{res,ref}} = 0.7 d_{\mathrm{ref}}. \qquad \text{Eq. 1-56}$$

With RH diameters of around $d_{\mathrm{res}} \approx$ 20 nm (see chapter 3.2.3), a resolution of $d_{\mathrm{res,ref}} \approx$ 14 nm is achievable. With the given experimental parameters, the resolution is limited by the size of the reference. The resolution can be further increased by employing additional phase retrieval with the reconstruction as initial guess, (*234, 235*). It should be noted, the previous discussion assumed unlimited photon flux. For limited flux, the numerical aperture might not be defined by the detector size further limiting the resolution.

The image contrast is directly connected to the contrast of the intensity modulations, thus the interference between object and reference waves. By decreasing the size of the reference, less photons pass through the aperture and partake in the interference, thus reducing the intensity of the reference wave. The contrast of the modulation can be expressed in terms of fringe visibility Υ (*236*):

$$C = \Upsilon = 2 \frac{\sqrt{I_{OW} \cdot I_{RW}}}{I_{OW} + I_{RW}}. \qquad \text{Eq. 1-57}$$

The scattering intensity of the object and reference in the detector plane is approximately proportional to the total X-ray intensity transmitted through the OH and RH. The transmitted intensity in turn is proportional to the area, and thus the diameter of the OH and RH (it is assumed that the transmission rate is proportional to the square of the radii):

$$C = \frac{d_{\mathrm{RH}} \cdot d_{\mathrm{OH}} \cdot \sqrt{t}}{d_{\mathrm{RH}}^2 + t d_{\mathrm{OH}}^2}. \qquad \text{Eq. 1-58}$$

With the relative transmission for the object t and for the reference set to unity. It should be noted that Eq. 1-58 describes the mean contrast and assumes full coherence, thus is an upper limit estimation. Small features can have a lower scattering intensity and thus exhibit lower contrast. A more rigorous description would have to include the momentum transfer dependence to describe the fringe visibility in different parts of the hologram.

1.3.3.2 X-ray holographic microscopy and wavefield back propagation

In FTH, the object wave is reconstructed in the plane of the reference source. A conventional sample for this technique is prepared on transparent Si_3N_4 membranes with an opaque Au film on one side and the magnetic sample on the other. A circular opening is generated in the Au with the magnetic sample remaining as the object. Close to the object, a small pinhole milled through the Au and sample to generate the reference. Due to the direct connection of the holographic optics mask, the Au film with OH and RH, and the magnetic sample, the plane of the reference source and sample are identical.

In XHM on the other hand, holographic mask and magnetic sample are prepared on two different Si_3N_4 membranes to enable free movement of sample. The geometry is shown in Fig. 1-8. The incident X-rays illuminate the holography mask with the opaque Au film containing the OH and RH, generating the object wave and reference wave. The second membrane holding the sample is separated from the first by a gap of width Δ, typically in the range of Δ = 5– 35 µm. It is usually caused by dirt particles or a slight tilt of the sample with respect to the holographic mask. Thus, the OW propagates through vacuum the gap distance before interacting with the sample. A reconstruction of the object wave in the plane of the holographic mask yields a blurred or "out of focus" image for Δ < 10 µm. For wider gaps, the object is not discernible at all. In or-der to obtain a focused image despite the separating gap, the reconstructed object wave need to be propagated into the sample plane (*221*). This issue is known in Fourier optics and can be solved by free space propagation using the Helmholtz propagator (*222, 223*).

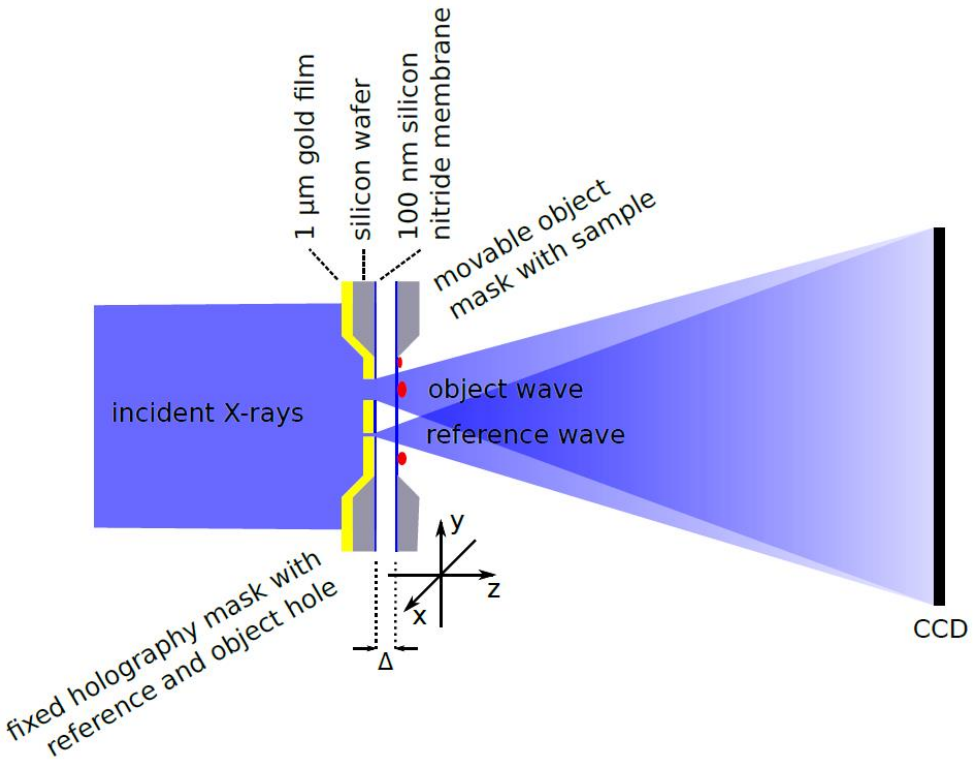

Figure 1-8: In the XHM geometry, the separation of the holography mask from the object allows to move the sample with respect to the holography mask, extending the accessible area for imaging (*224*).

Considering the complex wave field $\psi(x,y,z = 0)$ in the plane $z = 0$. The plane propagates along the optical axis into the plane $z = \Delta$ without absorption, becoming $\psi(x,y,z = \Delta)$. This can be solved using the time-independent Helmholtz equation:

$$(\nabla^2 + \mathbf{k}^2)\psi(x,y,z) = 0. \qquad \text{Eq. 1-59}$$

with the wave vector $\mathbf{k} = (k_x, k_y, k_z)$. One solution to this equation is the plane wave

$$\psi_p(x,y,z) = \exp\left(i\left(k_x x + k_y y + k_z z\right)\right), \qquad \text{Eq. 1-60}$$

with $\mathbf{k} = \left(k_x^2 + k_y^2 + k_z^2\right)$. With $|\mathbf{k}| = k$, k_z can be expressed as $k_z = \sqrt{k^2 - k_x^2 - k_y^2}$ and it follows:

$$\psi_p(x,y,z) = \exp\left(i\left(k_x x + k_y y\right)\right) \cdot \exp\left(iz\sqrt{k^2 - k_x^2 - k_y^2}\right). \qquad \text{Eq. 1-61}$$

Eq. 1-61 describes the propagation of a plane wave (first term) through space with the second term being the free space propagator. In general $\psi(x,y,z=0)$ is, no plane wave, but a complicated composition of a spatial wave spectrum. However, any wave can be written as a Fourier integral, decomposing it into its plane wave components:

$$\psi(x,y,z=0) = \iint \mathcal{F}\left(\psi\left(k_x,k_y,k_z=0\right)\right)\cdot\exp\left(i\left(k_x x + k_y y\right)\right)dk_x dk_y. \qquad \text{Eq. 1-62}$$

After propagating each plane wave component by multiplying the free space propagator, the complete propagated wave is obtained by taking the inverse Fourier transform:

$$\begin{aligned}\psi(x,y,z=\Delta) &= \iint \mathcal{F}\left(\psi\left(k_x,k_y,k_z=0\right)\right)\cdot\exp\left(i\left(k_x x + k_y y\right)\right)\\ &\quad\cdot\exp\left(i\Delta\sqrt{k^2-k_x^2-k_y^2}\right)dk_x dk_y,\\ \psi(x,y,z=\Delta) &= \mathcal{F}^{-1}\exp\left(i\Delta\sqrt{k^2-k_x^2-k_y^2}\right)\mathcal{F}\cdot\psi(x,y,z=0)\\ \psi(x,y,z=\Delta) &= P_\Delta\cdot\psi(x,y,z=0).\end{aligned} \qquad \text{Eq. 1-63}$$

Using the Helmholtz propagator P_Δ any wave can be propagated forward and backward along z. Back to XHM, we can now reconstruct the object wave in the sample plane instead of the plane of the reference source. We substitute in Eq. 1-63 $\mathcal{F}\,\psi(x,y,z=0)$ by $H(k_x,k_y)$, which is the Fourier transform of the object wave:

$$\begin{aligned}\psi(x,y,z=\Delta) &= \mathcal{F}^{-1}\exp\left(i\Delta\sqrt{k^2-k_x^2-k_y^2}\right)\cdot H\left(k_x,k_y,k_z=0\right)\\ \psi(x,y,z=\Delta) &= P_\Delta^H H\left(k_x,k_y,k_z=0\right)\\ P_\Delta^H &= \mathcal{F}^{-1}\exp\left(i\Delta\sqrt{k^2-k_x^2-k_y^2}\right).\end{aligned} \qquad \text{Eq. 1-64}$$

Before the image reconstruction, a plane wave has to be multiplied to the hologram to propagate it into the sample plane. By putting Eq. 1-52 into Eq. 1-64, the object wave can be reconstructed in the sample plane. By reducing Eq. 1-52 to its third and fourth cross correlation term it follows:

$$\begin{aligned}\psi(x,y,z=\Delta) &= \mathcal{F}^{-1}\exp\left(i\Delta\sqrt{k^2-k_x^2-k_y^2}\right)\mathcal{F}\\ &\quad\cdot\left(o(x+x_0,y+y_0,z=0)+o^*(-x-x_0,-y-y_0z=0)\right)\\ \psi(x,y,z=\Delta) &= o(x+x_0,y+y_0,z=\Delta)+o^*(-x-x_0,-y-y_0z=-\Delta).\end{aligned} \qquad \text{Eq. 1-65}$$

The first term is reconstructed as expected in the sample plane. The second term, however, is propagated in the opposite direction, further away from the sample plane. Thus, only one of the twin images is focused, while for the second the features are blurred even stronger. It is worth

mentioning that due to the propagation, the autocorrelation terms become laterally more extended and the reconstruction might no longer be spatially separated from the autocorrelation for $d_{\mathrm{sep}} = 1.5\ d_{\mathrm{OL}}$. To ensure the separation also for larger gaps, typically is chosen to $d_{\mathrm{sep}} = 2.5\ d_{\mathrm{OL}}$.

2 Sample fabrication and experimental techniques

This chapter deals with the experimental techniques that are used to fabricate, characterize and image the sample systems investigated in this thesis. First, the sputter chamber (section 2.1) is described that is used for the sample fabrication. This is followed by a brief introduction to the magneto-optical Kerr effect (MOKE) setup (section 2.2). Subsequently, a combined focused ion beam/scanning electron microscope (FIB/SEM) (section 2.3) setup is presented that is used for the preparation of the holography masks. Finally, the X-ray holographic microscope (section 2.4) is introduced, with which the scattering and imaging experiments were conducted.

2.1 Sputter chamber

All samples investigated in this thesis were prepared at room temperature in the UHV sputter chamber with a base pressure of $< 10^{-8}$ mbar that is depicted in Fig. 2-1. In this chamber, electron–cyclotron resonance (ECR) (*237*) and direct-current-magnetron (DC) (*238*) sputtering techniques are available for the deposition of in total nine materials. Following the findings described in (*129, 239*), both techniques are made use of for their respective advantages to maximize the perpendicular magnetic anisotropy (PMA) in the magnetic thin films.

For ECR sputtering, an Ar pressure of 3.2×10^{-4} mbar and an extraction voltage, and therefore Ar^+ ion energy, of 1.2 keV is used. The Pt target is a quadratic plate of 5×5 cm², ensuring the whole Ar^+ ion beam hitting the plate under an angle of 45°. Using these parameters and an ion current of 40 mA, Pt is deposited with a rate of 0.33 nm/s on the 10 cm distant sample.

DC sputtering requires a higher Ar pressure[6] of $3.4 \cdot 10^{-3}$ mbar in the chamber to start and operate the magnetrons. Nine materials are available. All investigated samples consist of Co, Ir, and Pt. The other six materials are Au, Cu, Fe, Ni, Pd, and Ta. Co is sputtered from a 2" magnetron (*A 320-XP, Aja International Inc.*) with an Ar^+ energy of (290– 310) eV at a constant ion current of 50 mA. These parameters result in a rate of 0.025 nm/s. Pt and Ir, on the other hand, are sputtered from 1" targets (*A 310-XP, Aja International Inc.*) with ion energies of 420– 550 eV at a constant current of 30 mA and 20 mA, respectively. The deposition rates are 0.05 nm/s for Pt and 0.025 nm/s for Ir. The error of the sputter rates is estimated to be smaller than 5 %.

The key difference between ECR and DC sputtering are the resulting energies of the atoms leaving the target (*127*). For ECR, the atoms have an average energy of 30 eV, resulting in a mean free path

[6] The pressure gauge (*CVG101 and VGC301, InstruTech Inc.*) used for this measurement is calibrated for N_2. The true pressure for Ar is approximately 80 % of the one indicated, and therefore $2.7 \cdot 10^{-3}$ mbar.

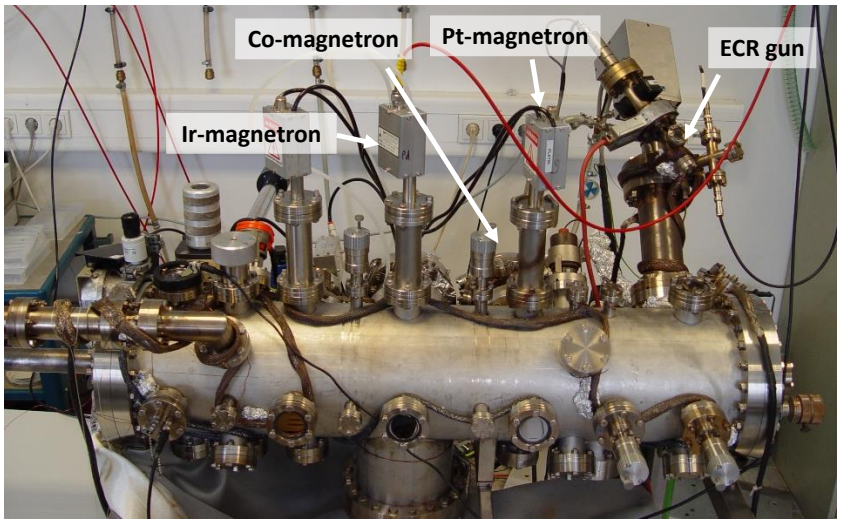

Figure 2-1: Photograph of the UHV sputter chamber with the ECR gun for the deposition of Pt seed layer and several magnetrons for the depositions of among other materials Co, Pt, and Ir.

of 40 cm at the prevailing pressure. With 5 cm distance from target to substrate, the atoms reach the substrate mostly without losing energy. DC sputtering results in the atoms having about 20 eV energy and, due to the higher pressure, a mean free path of only 2 cm (*15*). The distance between target and substrate is 10 cm. Therefore, the atoms loose a high proportion of their energy on their way to the substrate. The higher energy and mobility of the ECR-sputtered atoms induces a pronounced (111) texture in the polycrystalline deposited layer with random in-plane orientation and a grain size of 11 nm for layers of 4 nm (*128–130*). With its lower energy, DC sputtered layers exhibit less interdiffusion and consequently sharper interfaces. Subsequently, the combination of the pronounced texture of an ECR sputtered seed layer with the sharp interfaces of DC-sputtered layer stack, retaining the properties of the seed, enhances the overall PMA (*239*). A detailed analysis of the structural properties is given in (*129*).

Deposition of Wedge-Shaped Layers

Wedge shaped layers are used to study the thickness-driven evolution of magnetic properties. The penumbra of a shadow mask is used for the deposition of such layers. The sample holder containing the shadow mask is shown in Fig. 2-2. It consists of a sample holder made of Al and a Cu flap. The flap is opened and closed by gravitation via a rotation of the whole sample holder along its transfer axis. With 10 cm distance between sample and 2" DC sputter target and 2 mm between sample and flap, the resulting wedges show a length of ~2.5 mm. An infinitely thin flap would create a wedge with the profile of an error function. With its thickness of 1 mm however, the flap

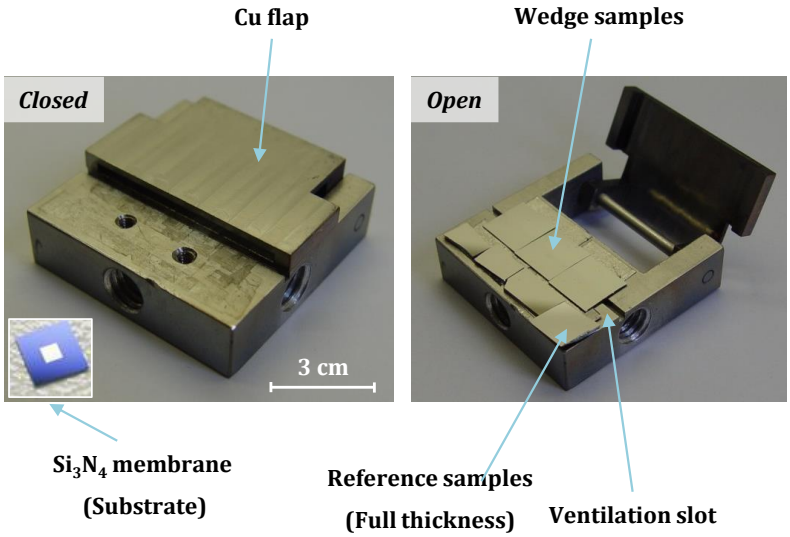

Figure 2-2: Photograph of the shadow mask used for the fabrication of wedge-shaped layers. It consists of an Al sample holder and a Cu flap. The flap can be opened and closed to deposit plane or wedge-shaped films, respectively. The samples are positioned on a ventilation slot that prevents distortions of the thin membrane (substrate) due to rapid pressure changes during transfer into and out of the vacuum chamber.

creates wedge profiles, which are a superposition of the profiles caused by the lower and upper edges of the flap. The same geometry with a 1 ” target results in a wedge of around 500 µm length.

2.2 Magneto-optical Kerr effect setup

The setup for magneto-optical Kerr effect (MOKE) allows the measurement of the magnetic anisotropies and the remagnetization of samples. The effect occurs when light is reflected on a ferromagnetic sample, changing the polarization of the light. The spin-orbit coupling causes a dependence of the dielectricity tensor on the orientation of the magnetization. In first-order approximation, the rotation Θ and ellipticity ε of the reflect light depend linearly on the magnetization, thus enabling field-dependent measurements of the magnetization. Due to the penetration depth of optical light in metals of about 10 nm, MOKE is ideally suited for the investigation of thin films. For further information about MOKE, the interested reader is referred to (*86*).

The setup consists mainly of a conventional electromagnet using two water-cooled coils to magnetize the CoFe pole pieces, a sample holder, an ultra-low noise laser diode (λ = 635 nm, P = 5 mW), a polarizer , an analyzer, and a photodiode. The sample holder is positioned in the

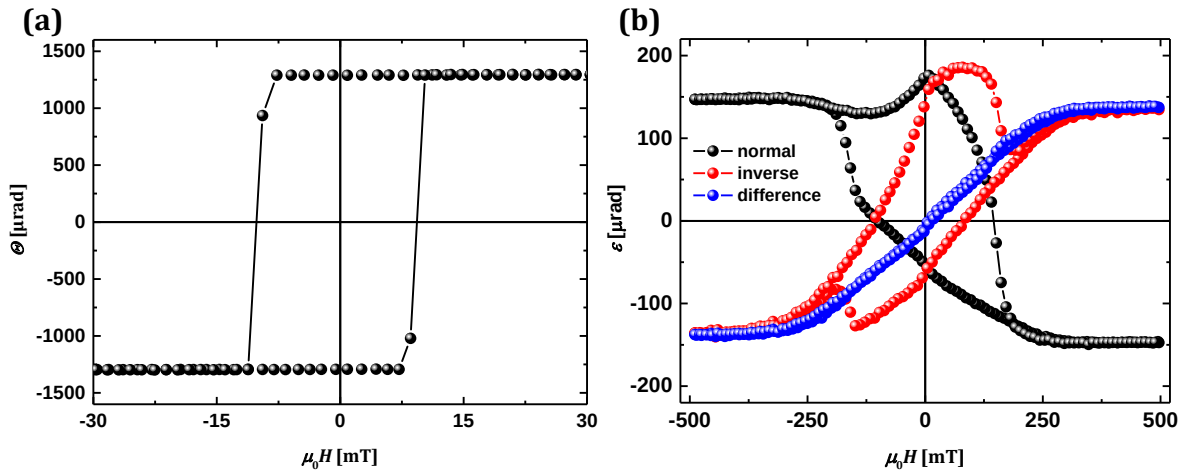

Figure 2-3: $M(H)$ curves are shown measured by MOKE in a Pt\Co$_{1.1\,nm}$\Pt sample. In (a) the polar rotation Θ is measured in dependence of $\mu_0 H$, revealing the polar remagnetization curve. In (b), two measured curves with inversed beam path (black and red dots) for the longitudinal ellipticity ε are shown that include parasitic contributions of the polar ellipticity. Due to the inversed beam path, the longitudinal ε changes sign while the polar ε remains unchanged. The blue curve, free of the parasitic signal, is obtained by subtracting the black and red curve and dividing by two.

center of the two pole pieces, which can be rotated freely around it. Within this thesis, they are arranged to generate magnetic fields either along the surface normal (polar geometry) or within the sample plane (longitudinal geometry). The pole pieces are usually separated by a 3-cm-wide air gap, yielding a maximum field at the sample position of ± 0.95 T measured by a Hall probe. By narrowing the gap to 2 cm, fields up to ± 1.35 T are feasible. This, however, is only necessary for samples with high anisotropies ($K_{tot} \geq 500\,kJ/m^3$) and makes the alignment of the setup more difficult. After passing the polarizer the laser light is linearly polarized, and impinges on the sample at an angle of 45°. With the analyzer and the photodiode , the rotation Θ of the reflected light can be measured. By placing an additional $\lambda/4$-plate in front of the photo diode, the ellipticity ε of the laser light becomes accessible as well.

As the polar Kerr effect is ~10 times stronger than the longitudinal, parasitic signals of the polar effect are inevitably measured superimposed to the longitudinal one. Thus, a method to separate the longitudinal and polar Kerr effect contributions from each other is briefly introduced (*240*). The separation is required for samples with perpendicular easy axis of magnetization when applying in-plane fields (along the hard plane). In Fig. 2-3, $M(H)$ curves are shown for a Pt\Co$_{1.1\,nm}$\Pt sample. A polar remagnetization curve is shown in (a), where the rotation Θ is measured and no

parasitic contribution is present. The two measured curves, shown in (b) as black and red dots, for the longitudinal ellipticity ε vs field include parasitic polar ellipticity contributions. In-between measuring the two curves, the beam path was inverted. This causes the longitudinal ellipticity to change its sign while the parasitic signal remains unchanged. Thus, the polar components can be eliminated by subtracting the red and black curves and a subsequent division by two. This yields the blue remagnetization curve, exhibiting the hard axis behavior for the in-plane loop.

2.3 Dual beam setup with focused ion beam and scanning electron microscope

The holographic masks required for XHM are structured in a FIB/SEM dual-beam setup. Fig. 2-4 shows the setup, which is described in detail in (*241*). The advantage of a dual-beam setup is the possibility to image and position the specimen without damage using the SEM before and after structuring with the FIB. The underlying principles of both techniques are not described here and the interested reader may refer to (*242–244*).

Unlike most commercially available setups, where the emphasis is set on the resolution and stability of the SEM column, this setup focusses on the performance of the FIB. The FIB column (*Canion*

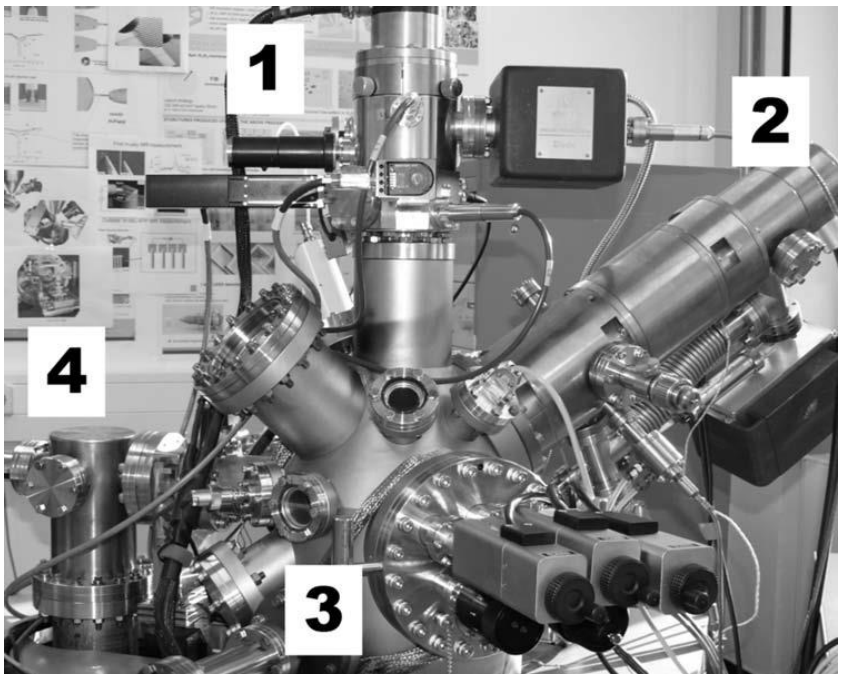

Figure 2-4: Photograph of the FIB/SEM dual-beam setup with the vertically mounted FIB column (1), the SEM column (2), which is tilted by 58° with respect to the FIB column, the motorized five-axis samples stage and the transfer chamber (4).

31-Plus, *Orsay Physics)* is therefore mounted vertically, while the SEM column (*JAMP-30*, *JEOL Ltd.*) is tilted by an angle of 58° with respect to the FIB. Typical operating conditions for the FIB setup are a base pressure $< 5 \times 10^{-9}$ mbar, Ga^+ ion energies of 30 keV, a probe current of 15– 35 pA using a 50 µm aperture or 2– 10 pA with a 20 µm aperture, respectively. The ion beam scans the specimen with a step size of 5 nm. Under these conditions, the ion beam is focused to about 10 nm (full width at half maximum). To ensure a homogenous sputtering of the specimen, areal structures are milled over several cycles, each applying an area dose of 360 µC/cm². The number of cycles depends on the depth of the milling and the milled material. 500 cycles are typically used to remove 1.4 µm AuPd (60:40) alloy. Point doses, used to sputter point-like structures, are applied in a single cycle. The point dose depends again on the depth of the milling and the milled material. For a through hole in the prior mentioned AuPd alloy with 1.4 µm thickness, around 2.5 nC are typically needed.

The setup is equipped with a 5-axes stage (*AP-81030*, *JEOL Ltd.*) for sample alignment. The 5 degrees of freedom are the lateral x-, y- and z-direction, as well as a rotation around the y- and z-axis. The lateral degrees of freedom can be controlled either manually with an accuracy of few tens of microns or using a motor-control unit for single micron accuracy. The rotational degrees are controlled manually with an accuracy of 0.1 °. Around the z-axis, unlimited rotation is possible, while for the y-axis a rotation of approximately -10– 45° is feasible. In addition, two micromanipulators (*MM3A-EM UHV*, *Kleindiek Nanotechnik*) are mounted on the stage. The tips of these micromanipulators are electrically insulated from the sample stage and can be used for contacting individual parts of the sample to measure the local specimen current.

2.4 X-ray holographic microscope

The X-ray holographic microscope is an endstation for X-ray resonant magnetic scattering (XRMS) and X-ray holographic microscopy (XHM, (*219, 220*) specifically designed for the use at the P04 beamline (*245*) at the PETRA III storage ring of DESY.

The XHM endstation is shown in Fig. 2-5(a) and consists of three chambers, each capable of introducing different optical components into the photon beam. The chambers are individually pumped and connected only via 2 mm wide apertures. Thus, they serve as a differential pumping stage, allowing for short downtimes (20 min) during sample exchange. The first chamber is equipped with a motorized stage carrying a sequence of circular apertures (pinholes) with diameters of 20, 30, 40, and 100 µm, and 1 mm. The pinholes are used to cut the beam size to a dimension similar to its transverse coherence length and to define the illuminated area on the sample (*246, 247*). In the second chamber, an electromagnetically driven fast shutter (*XRS6 Uni-stable X-ray*

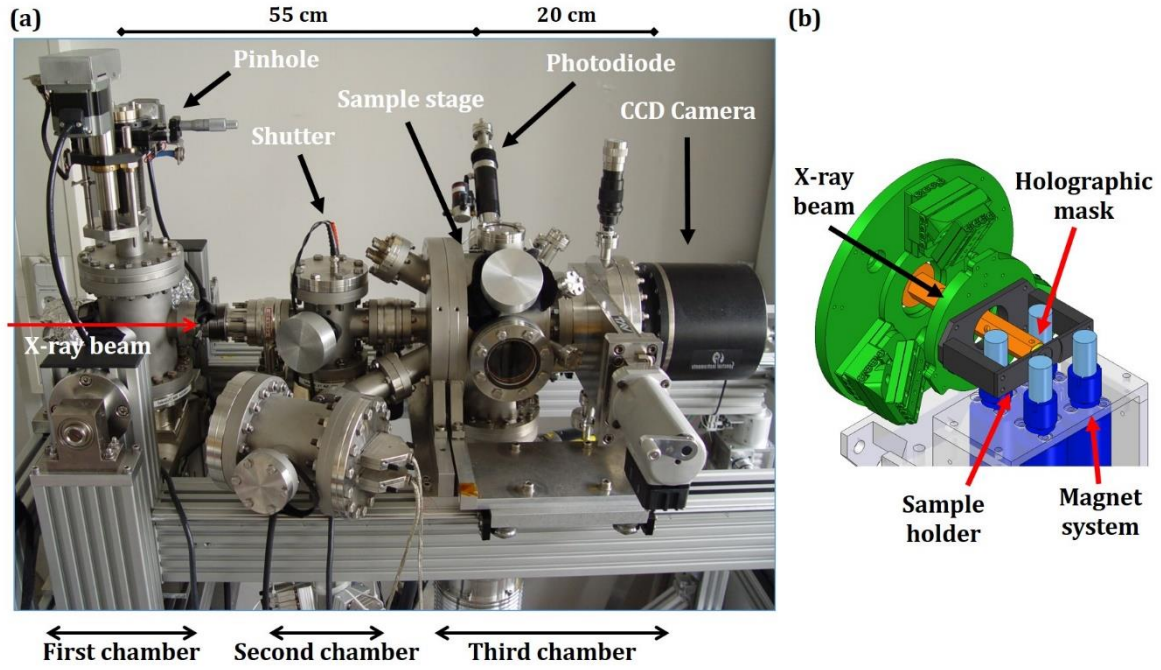

Figure 2-5: (a) Photograph of the X-ray holographic microscope designed for the P04 beamline at Petra III (DESY) in Hamburg. The endstation consists of three chambers that are connected via 2 mm wide apertures, serving as differential pumping stations. The X-ray beam enters the XHM from the left and passes in the first chamber through a pinhole that selects the center part of the beam to ensure a high coherent volume. Pinholes with variable diameters are available. In the second chamber, a fast shutter is used to set the exposure time for the experiments. 55 cm downstream of the pinhole, in the third chamber, is the sample stage located. The scattered light can be recorded either spatially resolved by a CCD camera (with sample-detector distance of 20 cm) or intensity-integrated using a photodiode. (b) Sketch of the sample stage in the third chamber. The X-ray beam passes through the hollow orange rod, at the end of which either a holographic mask or pinhole is fixated. The green 6-axis sample positioning systems enables lateral movement and rotation of the sample with sub-nm accuracy. The grey sample holder is attached to this positioning system and located in the center of the blue magnet system consisting of 4 diametrically magnetized and rotatable permanent magnets. Fields of up to 145 mT can be generated in in-plane or out-of-plane direction or 70 mT with arbitrary angle in the XZ-plane.

Shutter, Vincent Associates) defines the exposure time for the experiments. Minimum exposure times of ~ 4 ms with a repetition rate of up to 2 Hz are feasible.

Inside the third chamber, shown in Fig. 2-5(b), a piezoelectric 6-axis sample positioning system (*Smarpod 110.45, SmarAct GmbH*) enables lateral travel ranges of the sample of ± 4.5 mm in X, Y, and Z directions with sub-nanometer accuracy, as well as rotation around the X- and Y-axes of

± 20° and around the Z-axis of ± 35° (green). The sample is mounted on an Al sample holder, which is attached to the positioning system (grey). The sample is located in the center of a magnet system (blue). It consists of four rotatable, diametrically magnetized NeFeB permanent magnets, arranged in a quadrupole configuration (*210, 248*). Magnetic fields of up to ± 145 mT can be applied in either in-plane or out-of-plane directions. Alternatively, a field of ± 70 mT can be applied at arbitrary angles within the XZ-plane. Depending on whether the endstation is used for holographic imaging or scattering experiments, a holographic mask or an additional pinhole is mounted and placed in front of the sample (tip of the hollow orange rod). Holographic masks and their fabrication are discussed in chapter 3. The pinhole that is used for scattering experiments has a diameter of 100 µm. It is used to suppress the high intensity signal of the projection of the membrane windows and scattering off the edges of samples, thus decreasing the background intensity.

Two detectors located in the third chamber are used to detect the X-rays transmitted through the sample. First, a photodiode (*AXUV100Al*, *Opto Diode*) can be positioned behind the sample to measure the transmitted intensity. The diode is coated with 200 nm Al to block visible and the IR light that is emitted from the position encoders of the sample stage. The second detector is a Peltier-cooled 16 Mpx CCD camera (*1100S*, *Spectral Instruments Inc.*) that is used to record the small-angle scattering intensities and the holograms. Each pixel has a size of 15 × 15 µm, resulting in a total detector size of 61 × 61 mm². The CCD-sensor chip consists of four quadrants, each with a read-out port providing a read-out speed of up to 2 MHz. This results in a total read-out time of down to two seconds. To protect the camera from the high intensity of the direct beam a beam stop, a small sphere of steel with a diameter of 500 µm or 1.5 mm glued to a 50-µm-diameter tungsten wire, can be centered by a motorized stage in the beam.

Like any microscope, the optical axis of the XHM endstation (setup axis) has to be aligned with the photon beam axis (beam path) provided by the beamline. The design of the endstation enables a manual pre-alignment, largely independent of the incidence angle of the beam path entering the endstation. Therefore, the first chamber is connected to the beamline by a bellows. It is then positioned such that the beam passes through a 2 mm aperture and another bellows into the second chamber. The aperture has a conical bore with a setting angle of 30°, suppressing reflections in direction of the setup axis. Further, it is coated with fluorescent Yttrium Aluminate nanopowder ($Y_3Al_5O_{12}$:Ce), rendering the X-ray beam visible in case of misalignment. The flexible bellows between the first and second chamber enable a motorized alignment of second chamber with respect to the first. Chambers two and three are rigidly connected and pre-aligned to form an optical

bench. They can be moved on a spherical surface with micrometer accuracy around the center of chamber one (pivot point), where the pinholes can be placed into the beam path.

2.4.1 P04 beamline at DESY

The P04 beamline (*245*) at the PETRA III storage ring of DESY provides soft x-rays within the photon energy range of 250– 3000 eV, an integral photon flux > 10^{15} photons/s and a resolving power of $\lambda/\Delta\lambda = 10^4$. In the current state, only circularly polarized light is available, while linear might become available in the future. The beam is monochromatized using a varied–line-space grating (VLS) together with an exit-slit aperture (monochromator). By decreasing the width of the exit slit, the resolving power can be increased, and hence the longitudinal coherence length of the beam. The latter is accompanied by a loss in intensity. Additionally, the vertical focal-spot size at the sample position is predominantly determined by the width of the exit slit (≈ 33 % of the exit-slit opening). In the focal point of a horizontal and a vertical refocusing Kirkpatrick-Baez (KB) mirror unit (plane-elliptical mirrors), a spot size of $10 \times 10\,\mu m^2$ (FWHM) can be achieved. The transverse coherence length has been determined as $5.8 \times 6.5\,\mu m^2$ (rms, horizontal × vertical) for 778 eV photons in the focus (*208, 249*).

3 Fabrication of the holography masks for ultra-high-resolution imaging

The holographic mask is the main optical component of the X-ray holographic microscope and has a strong impact on the quality of the real-space image reconstructions. As already discussed in chapter 1.3 and analyzed in detail in (*229, 236, 250*), the holographic mask is the limiting factor for the obtainable spatial resolution, and contrast. For most of the holographic imaging experiments so far (*219, 221, 251–253*), a spatial resolution down to 50 nm has been sufficient. However, magnetic imaging of domain walls, nanometer-sized nanostructures and topological spin textures becomes increasingly important, especially due to their potential applications in future data storage devices. Imaging of these structures requires a spatial resolution down to 10 nm, which sets a high demand on the fabrication of the holography mask. The following chapter deals with the fabrication of high-quality holography masks and the resulting experimental resolution. First, the key features and related problems of a holography mask are introduced. Subsequently the fabrication procedure for high-quality masks is described and the chapter is concluded by the determination of the experimentally achieved resolution.

3.1 Standard holography mask

A holography mask consists of two main features (see chapter 1.3). First, a central object hole aperture (OH) defining the field of view (FOV) on the sample. Secondly, a point-like reference hole aperture (RH) providing the reference wave required for the reconstruction of a real-space image. The diameter of the RH predefines both the obtainable spatial resolution (~ 70 % of the diameter) and the contrast[7] of the final image. A small RH diameter will improve the resolution but decrease the contrast. A large diameter acts in the opposite way. As a limiting condition, the distance between the center of the OH and the RH has to be 1.5 times the diameter of the OH or larger. Otherwise, the reconstructed real-space image is not spatially separated from the autocorrelation of the OH. Typical used parameters are an OH diameter of 2 µm and five RHs evenly spread out on a circle with 5 µm radius around the OH. They have a diameter of 30– 90 nm, resulting in spatial resolutions of 21– 63 nm. Such a holography mask is shown in Fig. 3-1 and its fabrication described in detail in (*109*). In the following, selected key features and related problems are introduced.

Using a FIB (see chapter 2.3), the mask is milled into an Au or Au\Pd multilayer film deposited on a 100 nm SiN membrane (*Silson Ltd.* or *Norcada Inc.)*. The membrane is located on a 200 µm

[7] The contrast is proportional to the intensity of the reference wave emitted from the RH and therefore its area.

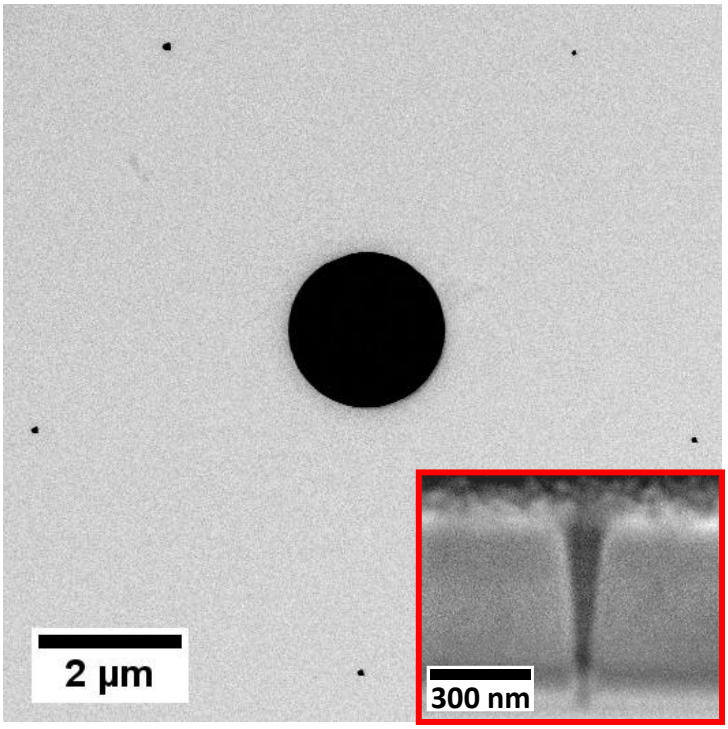

Figure 3-1: An SEM image of a holography mask milled into an 800 nm thick Au film. In the center, the 2 µm OH determines the field of view. Five RHs with diameters of 30– 90 nm are evenly distributed on a circle with 5 µm radius around the OH. In the inset, a cross section of a RH is shown. The RH is structured from above and has a diameter of 50 nm. Due to the Gaussian intensity distribution of the FIB beam, material is also removed in the tail regions on the incidence site. This results in walls tilted by 6° with respect to the surface normal (*109*).

thick Si frame and sized 250 × 250 µm². The Au and Au\Pd multilayer film is deposited by DC magnetron sputtering (*K575XD*, *Gaia Instrumente GmbH*). The Au films are 800 nm thick in order to be opaque for 778 eV photons (transmission < 0.005 %). Such Au films exhibit grain sizes of ~ 100 nm (*254*), giving rise to pinholes for the X-ray radiation as well as to locally varying milling rates due to channeling effects (*255–258*). This local variation leads to an unwanted variation in RH diameter, making the fabrication of smaller RHs very difficult. Among other reasons not applying here (see (*109*) for details), $Au_{100\,nm}\backslash(Pd_{100\,nm}\backslash Au_{220\,nm})_4$ multilayers (total thickness of 1380 nm) are used to decrease the influence of the channeling effect due to smaller grain sizes (~ 50 nm) (*254*) and therefore obtain locally more homogeneous milling rates. Yet, RHs with diameter below 30 nm could still not be achieved previously.

As shown in the inset of Fig. 3-1, the RHs are of a conical shape with an opening angle of approximately 6° with respect to the surface normal (*109*). This angle defines the maximal angle, which

the RH path can be tilted with respect to the beam path of the photons in the XHM endstation while still providing a reference wave. In prior beamtimes, the reconstruction of real space images was impossible for most holography masks, while magnetic information was evident within the autocorrelation. Therefore, the problem was the absence of a reference wave. Two possible sources for errors can act additively. First, due to an imperfect alignment of the sample in the FIB, the RHs are not milled along the mask normal, but at some angle. Second, the mounting of the mask in the XHM endstation could be tilted with respect to the incoming X-ray beam. The latter cause for error is excluded as great care was taken while designing and producing the rigid and self-aligning mounting in the microscope, leaving the non-parallel milling as sole cause.

An important feature for the achievable contrast of a holography mask is the longest distance in-between two structures on a mask. When multiplexing, meaning using a mask with several RHs, the hologram recorded on the detector is a superposition of the individual holograms formed by each RH with the OH, and the holograms formed between the RHs (*229*). Two cases have to be considered. In the coherent case, meaning all RHs fit within the transversal coherence area of the illumination, the individual holograms are coherently superimposed, and full contrast is achieved. In the incoherent case, not all RHs fit within the transversal coherence area and the holograms are incoherently superimposed. This causes a reduced contrast for the reconstructed real-space images. For the mask shown in Fig. 3-1, the longest distance between one RH to the one after next is $x_{max} = 9.51\,\mu m$, while the transverse coherence area is $\sim 5.8 \times 6.5\,\mu m^2$ at the P04 for typically used conditions[8] (*208, 249*). Thus, the incoherent case applies and the contrast is reduced. Thus, longer acquisition times are necessary for images of identical quality compared to a holography mask with shorter x_{max}.

3.2 Fabrication of high quality masks

In the previous chapter, three key features of holographic masks and their related problems are described. This chapter introduces solutions to the problems limiting the general usability (non-parallel milling), the contrast (longest distance in the mask structure), and the resolution (RH diameter) in order to fabricate holographic masks capable of 10 nm resolution.

[8] Typical conditions are a photon energy of 778 eV, a 50 µm exit slit and a 100 µm pinhole inserted into the beam 0.55 m upstream, blocking incoherent tails.

3.2.1 Alignment of the sample stage

Non-parallel milling of RHs with respect to the surface normal of the mask has been identified as an issue limiting the usability of the XHM endstation. This alignment error can stem from several sources, e.g. crooked sample holder or sample stage. However, great care was taken when manufacturing the sample holder and the sample stage is designed rigidly; making the most probable cause an offset in the one rotational degree of freedom of the sample stage capable of causing this. The sample stage has been enhanced with micromanipulators and its mechanics of the rotational axis were repaired, giving ample possibilities for an offset. Here an alignment procedure is described.

Images acquired with a FIB, like for any 2D-microscopy technique, show projections of the sample on an image plane. Fig. 3-2(a) shows the cross-section sketch of a sample consisting of two bars indicated by black rectangles. The bars are separated by the distance Δx along the x-axis, while the y-axis points into the plane. When imaged from above, the full distance Δx is projected onto the image plane, indicated by the black arrow. If the sample is rotated around the y-axis by an angle of χ, the distance projected into the image plane is $\Delta x \cdot \cos\chi$, shown by the blue rectangles and arrow. In order to align the sample stage, the distance projected into the image plane between two edges is measured for different values of χ. This distance is maximal for a parallel alignment of sample and image plane, therefore sample normal and incident FIB.

Fig. 3-2(b) shows a FIB-image of two bars milled into AuPd alloy deposited on Si_3N_4. The bars are 4 µm wide in x- and 50 µm long in y-direction. The inner edges of the bars are separated by $\Delta x = 42\,\mu m$. The darker areal regions in the image are damaged by repeated scanning with the FIB. For several values of χ, the distance between the two inner edges of the bars is measured. The degradation of the edges by repeated scanning with the FIB limits the amount of measurement points and makes averaging measurements along the whole y-length of the bars necessary to ensure sufficient accuracy. Further, the large extent of the structures minimizes the error, as the effect of edge degradation and the resolution is negligible compared to Δx. In Fig. 3-2(c) measured distances are plotted over the angle χ together with a cosine fit. The maximum of the fitted distance, and therefore the angle for parallel alignment, is $\chi = 9.57°$ with an error of $\sigma\chi = 0.18°$. This error is sufficiently small compared to the measured opening angle of the RHs 6 ° (*109*) and the accuracy with which the angle can be set of $\Delta\chi = 0.1°$.

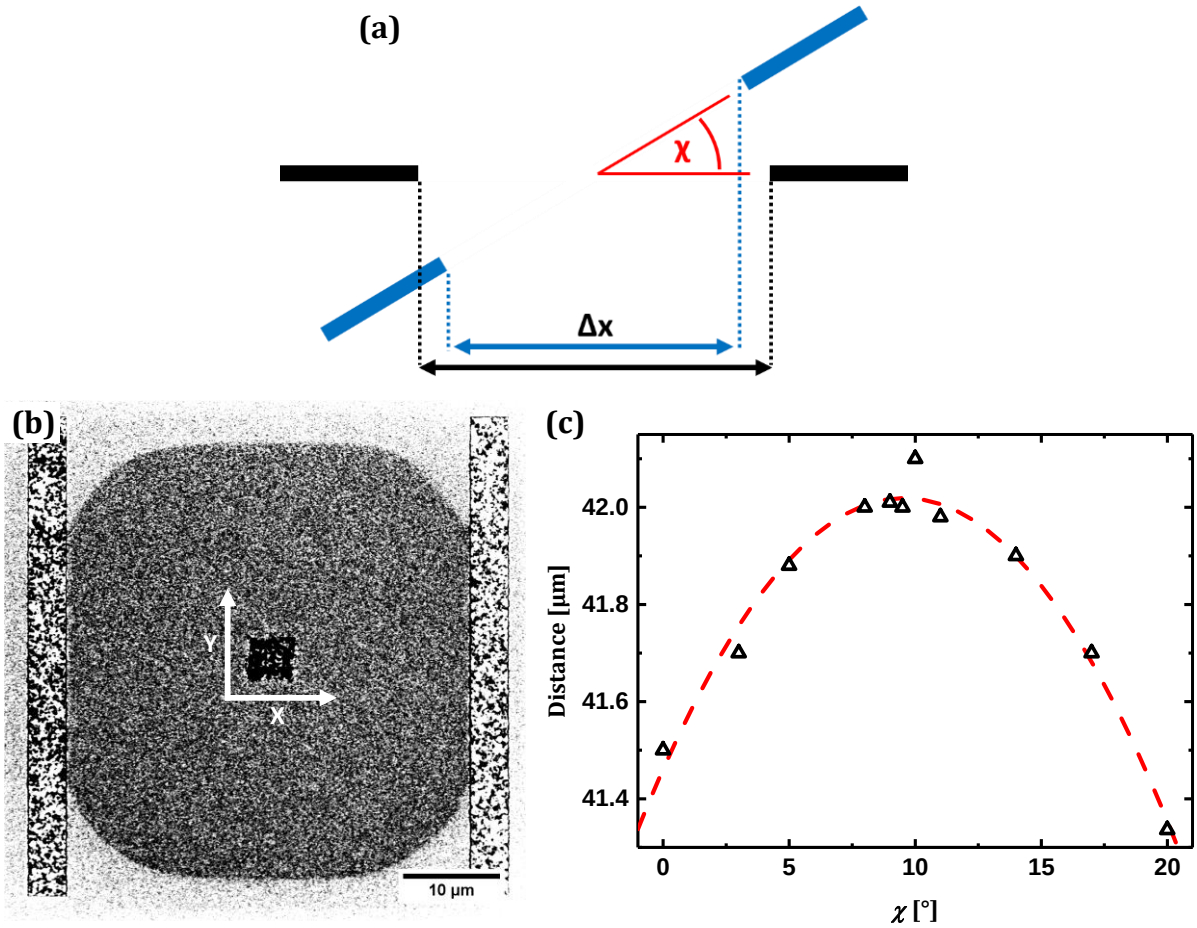

Figure 3-2: (a) Cross-sectional sketch of the measuring principle for the stage alignment. The black and blue bars both have the same width and distance in-between their inner edges. The blue bars are rotated by an angle of χ with respect to the black bars. When imaged, this distance is projected into the image plane, indicated by the arrows, and follows a cos χ behavior with the maximum when the bars and the image plane are aligned in parallel. (b) FIB image of two bars milled into an AuPd alloy film. The dark regions are damaged by repeated imaging with the FIB. Within the bars, the dark and bright spots are the consequence of locally varying milling rates due to the grains and the channeling effect. (c) Projected distances are plotted over the angle χ. The measured points are indicated by black triangles and the cosine fit by the red dashed line. The fit has a maximum at $\chi = (9.56 \pm 0.18)$ nm, which is the angle for parallel alignment of the sample stage to the image plane.

3.2.2 Matching holography mask design and coherence length

The contrast is one of the key quality parameters of an image. It is proportional to the intensity of the wave emitted by the RH, thus its area or its squared radius. Shrinking the RH by a factor of two reduces the contrast by a factor of four. Therefore, increasingly long acquisition times are necessary to gain a sufficient signal to noise ratio. While aiming to minimize the RH size, loss of

contrast from other sources should be minimized. As discussed in chapters 1.3.3 and 3.1, the mismatch of the longest distance in the mask structure (x_{max} = 9.51 µm) and the coherence area of the beam (5.8 × 6.5 µm² (*208, 249*)) reduces the contrast due to only partially coherent superposition of several holograms on the detector (*229*).

One possible solution is shrinking the radius of the RH circle and with it the OH diameter. With a 3 µm radius of the RH circle, the OH has to be as small as 1.2 µm (see 1.3.3). The accompanying reduction of the FoV is, however, highly undesirable for any imaging technique.

Another solution is omitting three of five RHs, with the remaining two located next to one another, as shown in Fig. 3-3(c). With this layout, the longest distance is x_{max} = 6 µm, from the far edge of the OH to a RH, matching the coherence area. Thus, less contrast is lost as the remaining individual holograms are to a higher degree coherently superimposed.

3.2.3 Reducing the reference hole diameter

RHs are structured by applying a predetermined point dose of Ga ions to the mask without moving the beam (*109*). In order to achieve a small diameter of the RH, the dose is chosen close to the value where the mask is typically penetrated by the ions. However, RHs structured in this way vary greatly in size, for some the mask surface is not penetrated at all. This is caused by inhomogeneities in the mask, e.g. grains with different orientations. Due to the channeling effect (*256–259*), milling rates differ depending on the orientation of the grains (see Fig. 3-2(c)). The grain size in a 800 nm thick Au film is around 100 nm (*254*) and eight grains are stacked on average. Because a uniform distribution of the orientations is unlikely for only 8 grains, the dose required to breach the mask varies locally as well. For 1.38 µm thick Au\Pd multilayer films, the grain size is around 50 nm and 28 grains are stacked on average, decreasing the local variation of milling rate. Yet, the targeted 20 nm diameter RHs was still not achieved. Two improvements are introduced in the following. First, AuPd alloy is introduced instead of multilayers to further decrease the grain size. Second, a method to monitor the penetration of Ga ions through the RH is implemented.

AuPd alloys are materials widely used for catalysts and coating SEM specimen. According to literature, grains in the size of 5– 30 nm are formed for a wide range of stoichiometry (*260, 261*). However, no values for DC sputtered films above 10 nm thickness are available. A comparable grain size for pure Au films would require 10– 50 nm thin films, requiring a high amount of Au\Pd repetitions. Measurements on a 1.4 µm thick DC sputtered AuPd (60:40) alloy film using an SEM

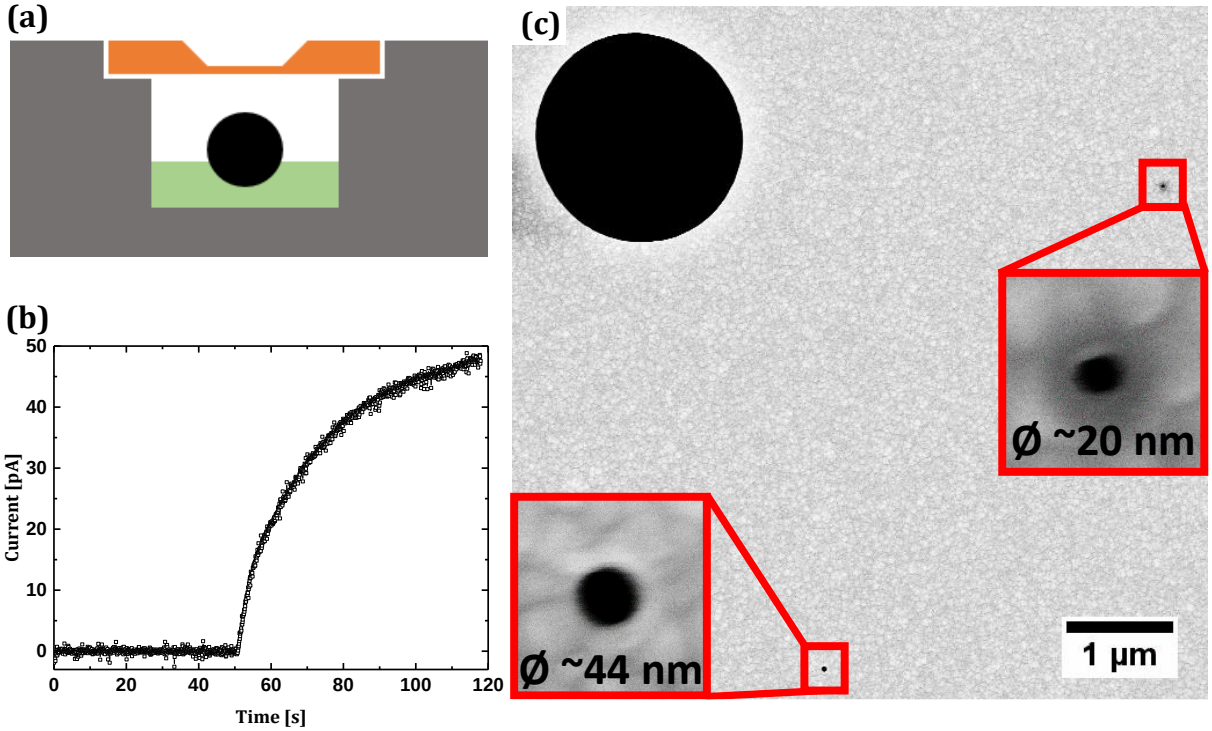

Figure 3-3: (a) Cross-section sketch of the FIB sample holder. The holder is made of aluminum (grey) and has two grooves. In the first and more shallow one, the mask is placed and electrically entangled with the holder to prevent charging effects. In the second and deeper groove, a wire (black) is fixated with non-conductive glue to isolate it electrically from the sample holder. Once the FIB breaches the mask, ions reach the wire and a current is measured. (b) A typical current graph measured during the milling of a RH. The FIB mills the mask material for ~50 s and no current is measured. Once the mask is breached, the current increases rapidly. To achieve small RH diameter of around 20 nm, the milling process is stopped immediately, once the rise is identified (typically ~3 pA). (c) A high quality holography mask. The 2 µm OH is accompanied by two RHs, located on the same side of the OH. The longest distance is x_{max} = 6 µm, from one RH to the far end of the OH. The smaller RH has a diameter of ~ 21 nm.

(*Sigma*, *Carl Zeiss Microscopy GmbH*), revealed an average grain size of 35 nm. In a 1.4 µm thick film, 40 grains are stacked on average, which further homogenizes the milling rate.

A downside of the material is increased stress acting on the membrane. It has turned out, that even for an AuPd alloy film of 50 nm thickness, a 100 nm membrane is deformed by stress, corrugating the surface and rendering the mask unusable. A 500 nm thick membrane, on the other hand, is not affected by the AuPd alloy film, even for thicknesses above 2 µm. In the following, holographic masks are structured into 1.4 µm thick AuPd alloy films deposited onto 500 nm thick Si_3N_4 membranes.

Estimating the required dose to stop the milling precisely when the mask surface is penetrated is a tedious process. Several RHs with varying doses have to be structured into a sample and their sizes analyzed by high-resolution SEM afterwards. After penetrating the mask surface, the RHs grow rapidly in size, and many iterations are needed to identify the perfect dose. Once found, even the smallest variation in milling rate or film thickness will cause a considerable amount of rejects. To resolve this issue, a method to identify the moment of ion penetration is implemented. The sample holder of the FIB setup has a groove over which the mask membrane is located. In this groove, a wire is fixed with electrically non-conductive epoxy glue (*H55, Epoxy Technology Inc.*), and therefore electrically isolated from the sample stage. Fig. 3-3(a) shows a cross-sectional sketch of the sample holder. The non-conductive epoxy glue is shown in green, the isolated wire in black, and the mask in orange. The current on the wire is picked up using one of the micromanipulators present in the setup and measured with a picoampere meter (*6485, Keithley Instruments*). Fig. 3-3(b) shows a typical current measurement during the milling of a RH. While the FIB is milling the mask material, no ions reach the wire underneath the mask and no current is measured. A steep rise in the current indicates the breaching of the surface, as ions now reach the wire. To achieve the smallest possible diameter of the RHs, the FIB is blanked as soon as the rising edge is identified by the operator. The limiting factors are the beam size, the time needed for the identification, and the reaction time of the operator. A diameter of 20 to 25 nm is achieved by stopping the process at around 3 pA, which is around the noise level. A stop at around 5 pA results in a diameter of 40 to 45 nm.

Fig. 3-3(c) shows an SEM image of a high-quality mask. The OH is accompanied by two RHs, making the longest distance of the structure $x_{max} = 6\,\mu m$ from the far end of the OH to a RH. The two RHs are of different sizes in order to obtain one real-space image with high contrast, and one with a resolution of down to 10 nm.

3.3 Determining the experimental resolution

In this chapter, the experimental resolution of the XHM endstation, equipped with a high-quality holography mask, is determined. The experiment was performed at the P04 beamline (*245*) at Petra III, using a photon energy of 778 eV (Co L_3 absorption edge) and a 50 µm wide exit slit. A 100-µm-sized pinhole was inserted in the beam 0.55 m upstream of the sample. The pinhole cuts the horizontally extended component of the beam down to 15 µm at the sample position, matching its vertical size. In this configuration, the beam has a lateral coherence length of $5.8 \times 6.5\,\mu m^2$ (*208, 249*). The resolution was determined by imaging an ASI (artificial spin ice) nanodot sample prepared by S. Freercks. The inset of Fig. 3-4 shows an XHM image of the sample. For this image, 20

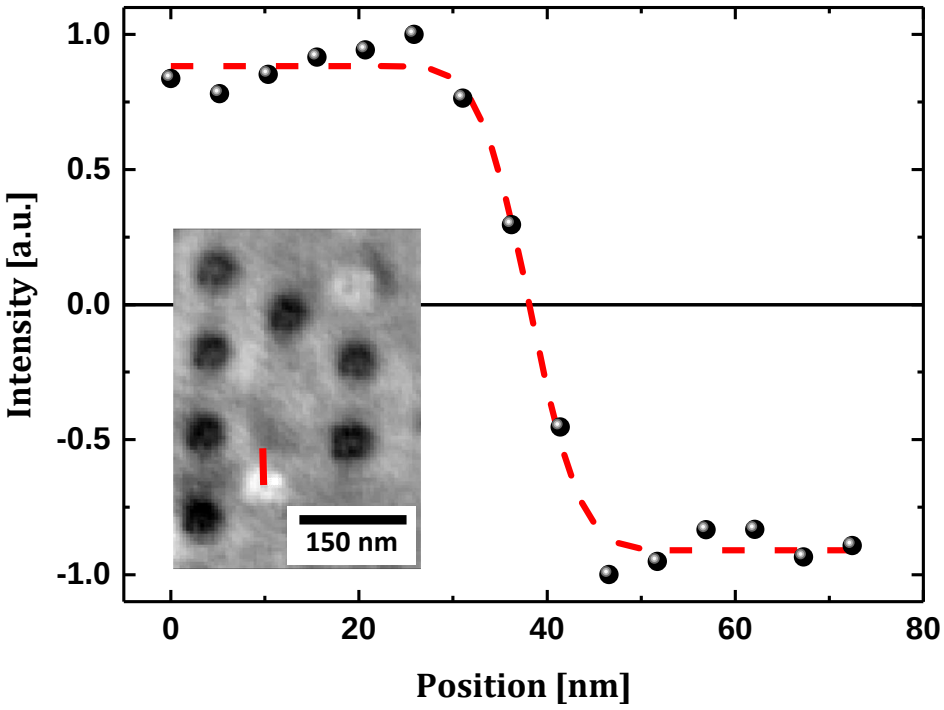

Figure 3-4: Determining a lateral resolution of 12 nm. The graph shows a line profile along the red line indicated in the inset. The black squares are the experimental values for the dichroic contrast in the reconstruction; the dashed red line is the fit of a Gaussian error function. Shown in the inset is an XHM image of a perpendicularly magnetized nanodot sample, structured out of a Pt\(Co1.1 nm\Pt1 nm)10 film. The dots have a magnetic diameter of ~80 nm and are arranged in a kagome lattice with center-to-center distance of 130 nm. The line profile shows the intensity across an edge of a nanodot. The fit of a Gaussian error function yields an edge width of $2\sigma = (8.27 \pm 1.53)$ nm. This is the equivalent of a determination using the 15/85 criterion at an edge.

individual acquisitions were summed for each photon helicity with an illumination time of one second per acquisition.

The dots were fabricated (*262*) out of a Pt\(Co1.1 nm\Pt1 nm)10 film[9] and exhibit perpendicular magnetization, causing the bright and dark contrast in the image. Between the dots, no magnetic material is present. The average diameter is 80 nm with a center-to-center distance of 130 nm and the dots are arranged in a kagome lattice[10]. Fig. 3-4 shows the line profile, indicated by the red line,

[9] The film is grown on a Si_3N_4 membrane with a 4 nm Pt_{ECR} and 6 nm Pt_{DC} seed layer. The uppermost Pt_{DC} layer is 3 instead of 1 nm thick to prevent oxidization.

[10] The kagome lattice is an example for magnetic frustration with respect to minimization of the stray field energy (*263–266*). Three dots form a triplet with a degenerate ground state, where two dots are magnetized in one direction and the third in the opposite one. Three of the four triplets, shown in the image, follow this so-called spin-ice rule, while one violates it.

across the edge of the bright dot. One pixel has a size of 5.2 nm. Fitting a Gaussian error function to the edge profile yields a resolution of $2\sigma = (8.27 \pm 1.53)$ nm, the equivalent of the 15/85 criterion. A statistical evaluation of several edge profiles in the image yields a resolution of $2\sigma = (12 \pm 3)$ nm. Individual profiles exhibit a resolution down to 6 nm. Not considered have been the width of the ferromagnetic transition on the edge of the nanodots (the width of which is unknown) as well as possible magnetic flowering effects. The real optical resolution of the X-ray holographic microscope would emerge out of the root of the difference of the squared individual contributions, firmly establishing a resolution of at least 10 nm.

4 Basic properties of ultrathin Co layers

The total energy of layered magnetic structures is composed of six basic properties, the vector field $\mathbf{M}(x,y,z)$ and the external field (c.f. Eq. 1-1). These six basic properties are the exchange stiffness constant A_{ex}, the magnetocrystalline and surface anisotropy constants K_V and K_S, the saturation magnetization M_S, the interlayer exchange coupling constant J_{IEC}, and the Dzyaloshinskii-Moriya interaction constant D_{DMI}. Thorough knowledge of them is required in order to describe static and dynamic behavior, e.g. the domain structure or domain wall movement, and obtain accurate results from micromagnetic simulations. The most basic property is M_S as it can be measured directly and without additional knowledge of the others. The remaining five, A_{ex}, K_V, K_S, J_{IEC}, and D_{DMI}, are only accessible via indirect means that rely on knowledge of M_S. All of them, however, are known to vary strongly in ultrathin magnetic films depending on its thickness. This regime is currently in the focus of intense research efforts.

This chapter addresses a systematic investigation of the five properties in four sample systems, disregarding the D_{DMI}. In section 4.1, the different systems and a corresponding nomenclature for the stacking order is introduced. Section 4.2 addresses the saturation magnetization M_S in samples with moderate ($t_{Co} \geq 2\,\mathrm{nm}$) and ultrathin ($t_{Co} < 2\,\mathrm{nm}$) magnetic layers. In section 4.3, the total anisotropy K_{tot} of the samples is investigated from which the two constants K_V and K_S are disentangled. In section 4.4, the exchange stiffness constant is measured and a model proposed to describe its thickness-dependence in the ultrathin regime. Finally, the interlayer exchange coupling is investigated in section 4.5, which exhibits peculiar features within the antisymmetric systems.

4.1 Sample systems

In this chapter, four sample systems are introduced that consist of multilayers of Co, Ir, and Pt in different sequences. In two, the Co layers are symmetrically sandwiched by either Pt or Ir (section 4.1.2), and two antisymmetrical ones with Co sandwiched by Pt and Ir (section 4.1.3). In order to study each of these systems systematically, numerous samples were fabricated and investigated using a variety of methods. To ease the following discussion of the properties, a nomenclature is introduced to identify the key features. Beforehand, the sample substrate is discussed briefly in section 4.1.1.

4.1.1 Sample substrate and seed layer

The choice of substrate has a major influence on sample properties, such as texture and internal film stress. Frequently used substrates include GaAs, Si_3N_4, and SiO_2, both with native oxide (SiO_{2N}) and thermally (SiO_{2T}) oxidized. To minimize the influence of substrates, seed layers are grown before growing the sample itself. While this minimizes the influence of the substrate, it does not vanish entirely. In (*127, 129*) Pt\Co\Pt sandwiches are prepared simultaneously on SiO_{2N}, SiO_{2T}, and Si_3N_4 with a 4 nm Pt_{ECR} seed layer. In the following investigation of the effective anisotropy $K_{1,eff}$ in dependence on the cobalt thickness, $K_{1,eff}$ was found to differ systematically depending on the substrate. Thus, great care should be taken even when comparing values of properties for samples grown simultaneously on different substrates or seed layers.

All samples in the following are prepared on amorphous Si_3N_4 substrate with an in-situ deposited 4 nm Pt_{ECR} seed-layer (*239*). The ECR-grown Pt seed-layer is polycrystalline with random in-plane orientation but has a pronounced (111) texture with grains of roughly (11 ± 2) nm size (*128, 129*). The orientation of the grains with respect to the film normal resembles a normal distribution with a FWHM of $(14 \pm 1)°$.Thin film samples grown on top retain both texture and grain size. Si_3N_4 is chosen as substrate as it results in a stronger texture compared to $SiO_{2T,N}$ (FWHM: $(23 \pm 2)°$ (*127–129*)). Further, it is commercially available both as continuous film on Si wafer, and as X-ray transparent membranes[11] (*Silson Ltd.* or *Norcada Inc.)*. The X-ray transparency is a prerequisite for X-ray transmission experiments at synchrotron light sources. The thickness of the Si_3N_4[12] has no further influence on the samples properties, except for the stability and transparency of the membrane. Thus, the thickness of the Si_3N_4-membranes is neglected in the following.

Samples were prepared with either homogeneous or wedge shaped Co layers. Samples with homogeneous Co are deposited on Si_3N_4-wafer. Samples with wedge-shaped Co layers are deposited on Si_3N_4-membranes with $2 \times 2\,mm^2$ windows for synchrotron experiments.

4.1.2 Symmetric systems – Pt\Co\Pt and Ir\Co\Ir

Since the work of P.F. Carcia in 1988 (*136*), ultrathin cobalt layers sandwiched between two adjacent layers of platinum are known to exhibit perpendicular magnetic anisotropy (PMA), meaning

[11] Membranes exhibit a significant variation of surface roughness, resulting in a variation of sample properties. A 5 min exposure to O_2 plasma reduces the variation and consistent properties are achieved

[12] The Si_3N_4 supported by Si has a thickness of 200 nm. For X-ray transmission experiments, samples were grown on both 200 and 500 nm Si_3N_4 membranes. No difference in sample properties was observed, except for transparency and mechanical stability.

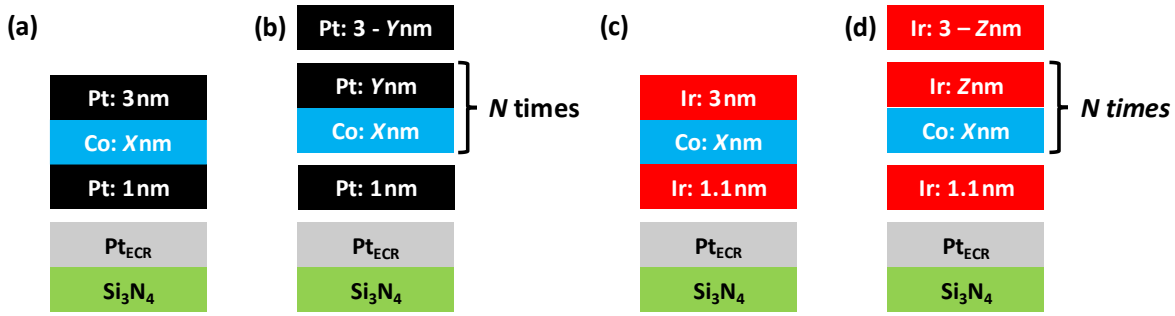

Figure 4-1: Sketch of the sample build-up for symmetric Pt\Co\Pt (a, b) and Ir\Co\Ir (c, d) samples. All samples are deposited by DC magnetron sputtering on top of Si_3N_4 with a 4 nm Pt_{ECR} seed layer and capped by a 3 nm layer of the corresponding material to prevent oxidation. (a, c) A single cobalt layer of thickness X is sandwiched between two layers of Pt (a) and Ir (c). (b, d) On top of a 1 nm Pt (b) or 1.1 nm Ir (d) layers, N Co layers of thickness X are separated by (N-1) spacer layers of Y nm Pt (b) or Z nm Ir (d). The N^{th} spacer layer is 3 nm thick to prevent oxidation.

an easy axis of magnetization parallel to the film normal. Since then, Pt\Co\Pt became a model system for studies related to the PMA and its resulting domain formation. Over the past years, this working group has acquired expertise in the fabrication of single and multilayers of Pt\Co\Pt with sputter-techniques (*128, 129, 147, 148, 239, 267, 268*).

The Pt\Co\Pt system is deposited by DC magnetron sputtering on top of a Si_3N_4 substrate with Pt_{ECR} seed layer. DC sputtering results in the atoms being deposited with lower kinetic energy (see chapter 2.1), causing less interdiffusion, and thus interfaces of higher quality compared to ECR-sputtered films. Fig. 4-1 shows two sketches of Pt\Co\Pt stacks, a single layer in (a) and a multilayer in (b). For a single layer, first a 1 nm Pt layer is deposited, followed by a Co layer of thickness X (t_{Co}). The single layer is then capped by a 3 nm Pt layer for a second Co\Pt interface and to prevent oxidation of the Co layer. Such a sample is indicated in the following by $Pt\backslash Co_{X\,nm}\backslash Pt$.

A Pt\Co\Pt multilayer consists of N Co layers, separated by (N-1) Pt spacer layers of thickness Y, capped with 3 nm Pt. Like a single layer, the stack starts with a 1 nm Pt layer. Subsequently, Co layers of thickness X and a Pt spacers of thickness Y are repeated N times. The N^{th} and final Pt layer is 3 nm thick instead of Y to prevent oxidation, analogous to the single layer. Latest experiments have shown that 1 nm layers are sufficient to prevent oxidation (*269*). In the following, such a multilayer sample is indicated by $Pt\backslash(Co_{X\,nm}\backslash Pt_{Y\,nm})_N$. Additionally, multilayer samples with wedge-shaped Co layers were grown for X-ray transmission experiments using a shadow mask

(Fig. 2-2). The resulting wedge has a length of 2.5 mm with a negligible slope on the lengthscale of the performed experiments. Wedged samples are indicated by Pt\(Co0-Xnm\Pt$Y$nm)N with the maximum t_{Co} of the plateau stated explicitly.

Three years after its publication for Pt\Co\Pt, in 1991 PMA was also reported for Ir\Co\Ir layers (*137*). In the same year, oscillatory interlayer exchange coupling (see chapters 1.1.5 and 4.5) was found for in-plane magnetized Ir\Co\Ir multilayers (*162*). In 1999, both properties combined were first reported for epitaxially grown Ir\Co\Ir (001) on MgO(001) substrate (*270*). However, the observed aperiodicity of the oscillations was later attributed to biquadratic coupling (*271*) (see chapter 1.1.5). The first realization of periodic oscillatory interlayer exchange coupling combined with PMA was reported in 2003 by H. Itoh (*185*).

The Ir\Co\Ir system is deposited analogous to Pt\Co\Pt and sketched in Fig. 4-1 (c-d). The one exception is the first Ir layer with a thickness of 1.1 nm[13]. An Ir\Co\Ir single layer sample is in the following indicated by Ir\Co$X$nm\Ir, a multilayer by Ir\(CoXnm\Ir$Z$nm)N, and wedged samples by (Co0-Xnm\Ir$Z$nm)N.

4.1.3 Antisymmetric systems – Pt\Co\Ir and Ir\Co\Pt

Antisymmetrically sandwiched ultrathin magnetic films have moved into focus of research quite recently. This is due to their potential to host strong interfacial Dzyaloshinskii-Moriya interactions (iDMI) (*40, 41*) and room-temperature (RT) skyrmions (*70, 192*). In symmetrical systems (like Pt\Co\Pt and Ir\Co\Ir), the net iDMI contribution from both surfaces is zero, due to their identical sign and mirror symmetry (under the assumption of identical interface qualities). In antisymmetrical systems, on the other hand, the contributions from both surfaces can have an opposite signs and therefore add up. This was reported for the Co\Pt and Co\Ir interface (*191*). Furthermore, 2016 the first skyrmions in multilayers at RT were reported in Ir\Co\Pt (*70*).

Fig. 4-2 depicts the Pt\Co\Ir (a, b) and Ir\Co\Pt (c, d) systems. They are prepared analogous to the symmetric systems in the prior chapter (4.1.2). For a single layer Pt\Co\Ir, first a 1 nm Pt layer is deposited, followed by Xnm Co, and capped by 3 nm Ir. It is indicated in the following by Pt\Co$X$nm\Ir. A multilayer consists of N times Ynm Pt, Xnm Co, and Znm Ir, where the first Pt layer is always 1 nm and the N^{th} Ir layer always 3 nm. A multilayer is indicated by (PtYnm\Co$X$nm\Ir$Z$nm)N, one with wedge-shaped Co layers by (PtYnm\Co0-Xnm\Ir$Z$nm)N.

[13] The sputter rate had increased by 10% due to morphological changes of the Ir target since the last calibration.

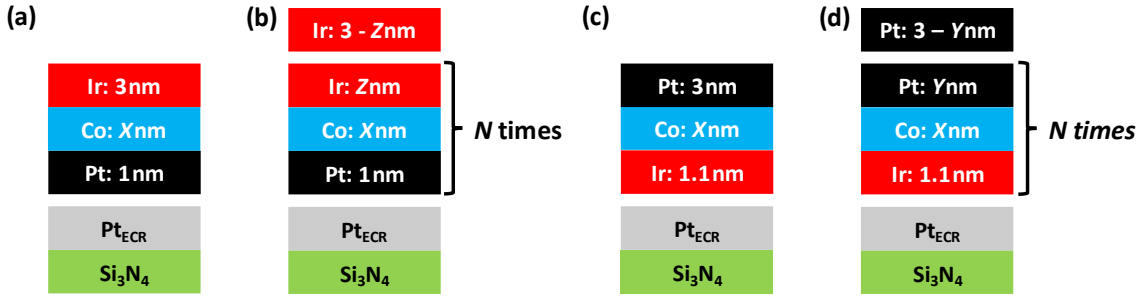

Figure 4-2: Sketch of the sample build-up for antisymmetric Pt\Co\Ir (a, b) and Ir\Co\Pt (c, d) samples. All samples are deposited by DC magnetron sputtering on top of Si_3N_4 with a 4 nm Pt_{ECR} seed layer and capped by a 3 nm layer of the topmost material to prevent oxidation. (a, c) A single cobalt layer of thickness X is deposited on top of a 1 nm Pt (1.1 nm Ir) layer and capped by 3 nm Ir (Pt). (b, d) The sample consists Y nm Pt (Z nm Ir), X nm Co, and Z nm Ir (Y nm Pt) repeated N times. The N^{th} Ir (Pt) layer is 3 nm thick to prevent oxidation.

For a single layer Ir\Co\Pt, first a 1.1 nm Ir layer is deposited, followed by X nm Co, and capped with 3 nm Pt. Such a sample is indicated in the following by $Ir\backslash Co_{X\,nm}\backslash Pt$. A multilayer consists of N times Z nm Ir, X nm Co, and Y nm Pt, where the first Ir layer is always 1.1 nm and the N^{th} Pt layer always 3 nm. A multilayer is indicated by $(Ir_{Z\,nm}\backslash Co_{X\,nm}\backslash Pt_{Y\,nm})_N$ and wedge-shaped one by $(Ir_{Z\,nm}\backslash Co_{0-X\,nm}\backslash Pt_{Y\,nm})_N$.

4.2 Saturation magnetization

M_S is one of the key parameters characterizing magnetic samples. Thorough knowledge of it is required as it also determines other parameters, like the uniaxial anisotropy constant K_{tot} and exchange stiffness A_{ex}, which in turn have to be known e.g. to perform micromagnetic simulations or to calculate the equilibrium domain size using domain spacing models. In this chapter, M_S is determined for all four systems in multilayers with $N = 8$ (and $N = 6$ in Pt\Co\Ir) using ferromagnetic resonance spectroscopy (FMR) at RT for $t_{Co} \geq 2$ nm (section 4.2.1). Further, M_S is extrapolated for thinner films with the help of the t_{Co} dependence of the saturation polarization Θ_{Sat} obtained from polar MOKE measurements (see chapter 2.2) for samples with N =1 and 8 (section 4.2.2).

4.2.1 Saturation magnetization of Co layers of 2 and 4 nm determined by FMR

FMR is the resonant absorption of microwaves by precessional motion of the magnetic moments connected with the excitation of spin waves in ferromagnets (*272–275*). In order to couple the microwaves into the sample, it was placed upside down on a coplanar waveguide. The microwave frequency ν is swept from 10 MHz to 10 GHz and the transmission through the waveguide measured by a vector network analyzer. Sample and waveguide are located in the center of an array of four pole pieces of a vector-field electromagnet setup capable of up to ± 95 mT parallel to the waveguide, and ± 140 mT at an angle of 45 ° to it. Before every sweep, the sample's magnetization is aligned in-plane perpendicular to the waveguide; during the sweep, the field is applied alongside it. The microwaves then excite a precession of the magnetization around the field direction. Further information on the setup is given in (*276, 277*).

In previous experiments, A. Philippi-Kobs measured M_S at RT for Pt\Co\Pt single layers with $t_{Co} \geq 4$ nm, that were fabricated in the same sputter chamber (*127*). The bulk value for Co of $M_S = 1.44$ MA/m (*125*) was found for all samples within the margins of error. For thinner layers the SNR was insufficient to determine M_S. Here, M_S is measured for multilayers of all four systems: $Pt\backslash(Co_{4\,nm}\backslash Pt_{2\,nm})_8$, $Ir\backslash(Co_{2\,nm}\backslash Ir_{1.75\,nm})_8$, $(Pt_{1\,nm}\backslash Co_{2\,nm}\backslash Ir_{1.1\,nm})_6$, $(Pt_{1\,nm}\backslash Co_{2\,nm}\backslash Ir_{1.1\,nm})_8$, $(Pt_{1\,nm}\backslash Co_{4\,nm}\backslash Ir_{1.1\,nm})_8$, and $(Ir_{1.1\,nm}\backslash Co_{2\,nm}\backslash Pt_{1\,nm})_8$. For $Pt\backslash(Co_{2\,nm}\backslash Pt_{2\,nm})_8$, the single domain state is present only for $|\mu_0 H| \geq 150$ mT, exceeding the field achievable with the setup. The latter is a consequence of the formation of a three-dimensional magnetic microstructure, which is discussed in chapter 5.2. Therefore, for Pt\Co\Pt a sample with $t_{Co} = 4$ nm is used for the determination of M_S. Concerning the determination of M_S from the data, a multilayer with N identical magnetic layers of thickness t_{Co} can be treated as a single layer of thickness t_{Co}, if the magnetization is aligned parallel in all the layers (*278*). The experiments are conducted analogous to (*127*).

For a single-domain state, the precession of the magnetization around the effective field H_{eff} is described by the Landau-Lifschitz-Gilbert equation (*193*)

$$\frac{\mathrm{d}\mathbf{M}}{\mathrm{d}t} = \gamma\,\mathbf{M}\times\mathbf{H}_{\mathrm{eff}} + \frac{\alpha}{M_S}\times\frac{\mathrm{d}\mathbf{M}}{\mathrm{d}t} = \frac{\gamma}{1+\alpha^2}\mathbf{M}\times\left(\mathbf{H}_{\mathrm{eff}} + \frac{\alpha}{M_S}\mathbf{M}\times\mathbf{H}_{\mathrm{eff}}\right), \qquad \text{Eq. 4-1}$$

where α is the damping parameter, $\gamma = g\cdot\mu_B/\hbar = g\ 88.5$ GHz/T the gyromagnetic ratio, $\hbar$ the reduced Planck constant, and g the Landé-factor of the electron, which is $g = 2.14$ for bulk fcc Co (*279*). The resonance condition then follows to (*275, 280, 281*):

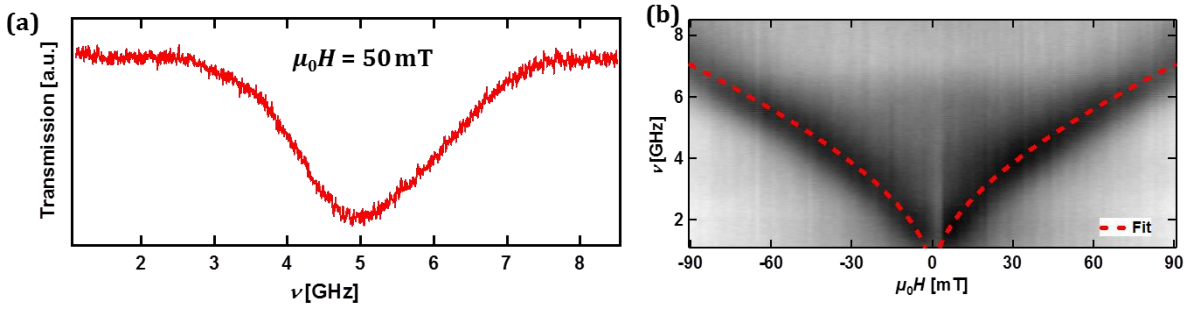

Figure 4-3: (a) FMR frequency sweep at $\mu_0 H$ = 50 mT for Ir\(Co$_{2\,nm}$\Ir$_{1.75\,nm}$)$_8$. The transmission exhibits a broad minimum, revealing the resonance frequency ν_r(50 mT) = 5.07 GHz. (b) FMR spectrum of the same sample, consisting of 120 frequency sweeps. Light gray indicates transmission through the coplanar waveguide, while dark indicates absorption by the sample. The dark trace shows the square-root-like dependence of ν_r on $|\mu_0 H|$. Indicated by the red dashed line is a fit of Eq. 4-2 to $\nu_r(\mu_0 H)$, yielding M_{eff} = 0.417 MA/m.

$$\nu_r(H) = \frac{\omega_r(H)}{2\pi} = \frac{\gamma \mu_0}{2\pi} \sqrt{H\,(H + M_{eff})}. \qquad \text{Eq. 4-2}$$

M_{eff} is the effective magnetization, which includes next to M_S also the surface K_S and magnetocrystalline K_V anisotropy constants in first order approximation:

$$M_{eff} = \frac{1}{\mu_0 M_S}\left(\mu_0 M_S^2 - 2K_V - \frac{4K_S}{t_{Co}}\right). \qquad \text{Eq. 4-3}$$

Fig. 4-3(a) shows a frequency sweep for Pt\(Co$_{2\,nm}$\Ir$_{1.75\,nm}$)$_8$ with $\mu_0 H$ = 50 mT. The transmission has a broad dip, revealing the resonance frequency ν_r(50 mT) = 5.07 GHz. In (b) 120 sweeps for different fields are combined to one FMR spectrum. The transmission is encoded in grayscale with dark contrast indicating low transmission, thus the resonance frequency $\nu_r(\mu_0 H)$. From the spectrum, M_S is obtained in three steps. First, $\nu_r(\mu_0 H)$ is determined for each frequency sweep by fitting a Lorentzian to the dip. Subsequently, M_{eff} = (0.417 ± 0.002) MA/m is extracted by fitting Eq. 4-2 to $\nu_r(\mu_0 H)$ for $|\mu_0 H| \geq 10$ mT where a single-domain state is present. Finally, using Eq. 4-3 and the anisotropy constants given in chapter 4.3.3, results in M_S = (1.40 ± 0.05) MA/m. This closely resembles the value for bulk fcc Co, M_S = 1.44 MA/m (*125*).

The obtained values for M_{eff} and M_S for all systems are listed in Tab. 4.1. All systems exhibit M_S values that are close to the bulk value of Co.

Table 4.1 Effective magnetization M_{eff} and saturation magnetization M_S determined from FMR spectra for the four sample systems. M_S was calculated from M_{eff} using Eq. 4-3 and anisotropy constants $2K_S$ and K_V (see chapter 4.3.3)

Sample	M_{eff} [MA/m]	M_S [MA/m]	$2K_S$ [mJ/m²]	K_V [MJ/m³]
$Pt\backslash(Co_{4\,nm}\backslash Pt_{2\,nm})_8$	0.701 ± 0.003	1.37 ± 0.04	1.43 ± 0.04	0.22 ± 0.03
$Ir\backslash(Co_{2\,nm}\backslash Ir_{1.75\,nm})_8$	0.417 ± 0.002	1.40 ± 0.05	1.68 ± 0.04	0.025 ± 0.007
$(Pt_{1\,nm}\backslash Co_{2\,nm}\backslash Ir_{1.1\,nm})_6$	0.285 ± 0.002	1.41 ± 0.04	1.55 ± 0.03	0.23 ± 0.02
$(Pt_{1\,nm}\backslash Co_{2\,nm}\backslash Ir_{1.1\,nm})_8$	0.250 ± 0.005	1.40 ± 0.05	1.55 ± 0.03	0.23 ± 0.02
$(Pt_{1\,nm}\backslash Co_{4\,nm}\backslash Ir_{1.1\,nm})_8$	0.736 ± 0.002	1.44 ± 0.04	1.55 ± 0.03	0.23 ± 0.02
$(Ir_{1.1\,nm}\backslash Co_{2\,nm}\backslash Pt_{1\,nm})_8$	0.402 ± 0.004	1.37 ± 0.05	1.35 ± 0.04	0.16 ± 0.02

Fig. 4-4(a) shows the FMR spectrum for $(Ir_{1.1\,nm}\backslash Co_{2\,nm}\backslash Pt_{1\,nm})_8$. The sample has antiferromagnetic interlayer exchange coupling. This results in an antiparallel alignment of adjacent Co layers at low fields (see chapter 4.5). The microwaves thus excite a precession of opposite rotational sense in adjacent coupled layers, inhibiting a precession and the resonant absorption. For fields exceeding 60 mT, the interlayer exchange coupling is overcome and the magnetization in the Co layers aligned parallel. Thus, the resonant absorption reemerges.

4.2.2 Saturation magnetization for Co layers below 2 nm

Usually, M_S is measured either using FMR, like shown in the previous chapter, or SQUID-VSM[14]. In SQUID-VSM, the paramagnetic background of all non-magnetic layers and the substrate is measured in addition to the weak signal of ultrathin magnetic films. The low signal-to-background ratio and SNR makes the investigation of ultrathin samples increasingly difficult. On the other hand, the used FMR setup can only apply in-plane fields and requires a homogenously magnetization of the sample. Thus, samples with strong PMA, e.g. thin Co layers, are inaccessible with the available setup.

In the limit of low film thicknesses, $t_{Co} < 10$ nm (*86, 282, 283*) , the saturation Kerr rotation Θ_{sat}, obtained from MOKE measurements in polar geometry, depends linearly on $M_S \cdot t_{Co}$ (*86, 284, 285*). Thus, a linear behavior of Θ_{sat} with respect to t_{Co} implies a constant M_S. However, deducing

[14] SQUID-VSM is the abbreviation for superconducting quantum interference device vibrating-sample magnetometry.

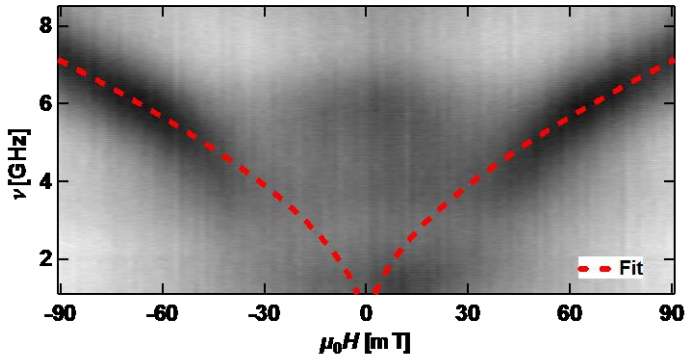

Figure 4-4: (a) FMR spectrum for $(Ir_{1.1\,nm}\backslash Co_{2\,nm}\backslash Pt_{1\,nm})_8$ with AFM interlayer coupling. For $|\mu_0 H| < 50,\mathrm{mT}$ adjacent Co layers are antiparallel aligned, resulting in zero absorption. For $|\mu_0 H| > 50\,\mathrm{mT}$, the interlayer exchange is overcome and the Co layers aligned parallel.

absolute values of M_S from individual measurements of Θ_{sat} is highly speculative due to the complicated magneto-optics involved in a multiple-reflection interference description (*86, 285*), e.g. dependencies on the interface structure, thickness of seed and cap layer, and angle of incidence. However, the regime of constant M_S in ultrathin Co layers might be estimated from the measurement of M_S for a thickness accessible with FMR and a linear dependency of Θ_{sat} on t_{Co}.

Fig. 4-5 shows Θ_{sat} plotted over t_{Co} for the four sample systems with $N = 1$. A linear behavior is apparent for all systems, except for the thinnest samples that show $\Theta_{sat} \approx 0$. These samples exhibit paramagnetic behavior due to T_C falling below RT (Fig. 4-22(b) shows T_C in dependence of t_{Co}). The transition to $\Theta_{sat} \approx 0$ is observed for all systems but Pt\Co\Pt. The thickness of the thinnest sample with $T_C >$ RT is denoted with t_{on}. For Ir\Co\Pt $t_{on} = 0.4\,\mathrm{nm}$, in Pt\Co\Ir $t_{on} = 0.58\,\mathrm{nm}$ and Ir\Co\Ir $t_{on} = 0.6\,\mathrm{nm}$. In Pt\Co\Pt all samples were ferromagnetic, thus $t_{on} = 0.3\,\mathrm{nm}$. This is in line with an earlier study within our group on samples with t_{Co} down to $t_{Co} = 0.35\,\mathrm{nm}$ retaining ferromagnetism (*285*). The dashed lines represent linear least square fits to the region $t_{Co} \geq t_{on}$. Even without the fits, the relative shift of the systems along the vertical direction is obvious. These offsets are frequently found for magneto-optic studies of layered Pt\Co\Pt and Pd\Co\Pd samples and usually attributed to magneto-optical effect (*285*) and/or polarization of the Pt atoms near the interfaces (*285, 286*). The polarization of Pt by adjacent Co atoms at Pt\Co\Pt interfaces and in alloys, and subsequently an effective enhancement of M_S, is reported in literature for low temperatures (*287–292*) and RT (*70, 290, 293, 294*). No such polarization is reported for Ir\Co\Ir layers or alloys. With Pt\Co\Pt exhibiting the largest offset of $\Theta_{sat}(t_{Co} = 0\,\mathrm{nm}) = (665 \pm 66)\,\mu\mathrm{rad}$ and Ir\Co\Ir showing none within the margins of error, the polarization of Pt could account nicely for the offset. However, FMR revealed an identical M_S in all systems for $t_{Co} = 2\,\mathrm{nm}$ or $4\,\mathrm{nm}$, yet they still differ significantly in $\Theta_{sat}(t_{Co} = 2\,\mathrm{nm})$. Thus, Θ_{sat}

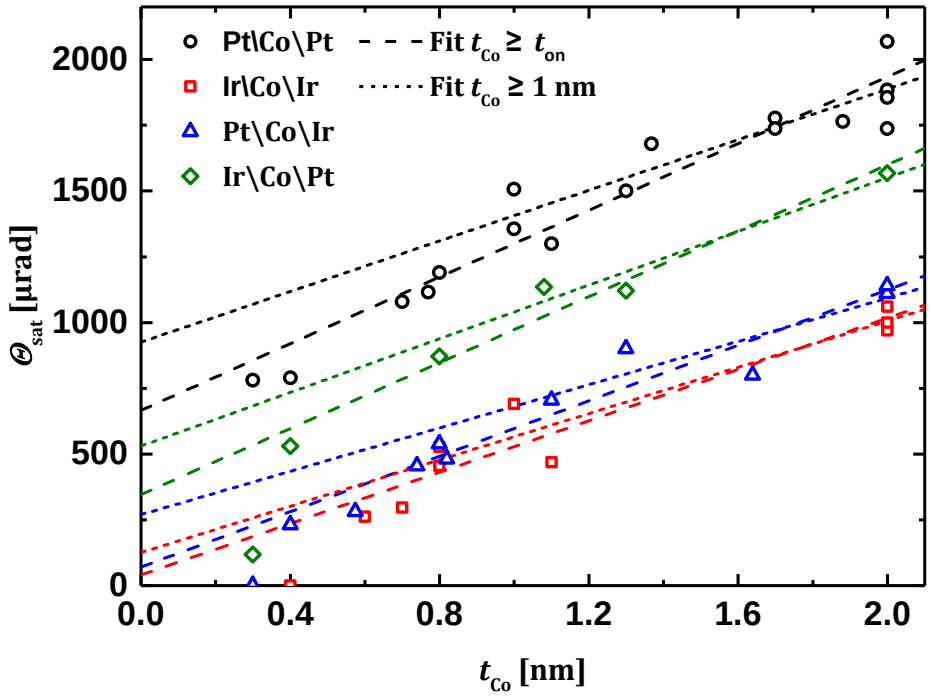

Figure 4-5: Saturation Kerr rotation Θ_{sat} plotted over t_{Co} for the four systems obtained by MOKE. Samples below a system-dependent, specific thickness t_{on} are paramagnetic. In Ir\Co\Pt t_{on} = 0.4 nm, Pt\Co\Ir t_{on} = 0.58 nm, and Ir\Co\Ir t_{on} = 0.6 nm; for Pt\Co\Pt all samples are ferromagnetic. The dashed lines are fits to the thickness regime $t_{Co} \geq t_{on}$, the dotted lines for $t_{Co} \geq 1$ nm. The fit parameters are summarized in Tab. 4.2.

does not solely depend on $M_S \cdot t_{Co}$, and magneto-optical effect are most likely the cause for the offsets.

Further, the slopes differ between the systems. Pt\Co\Pt and Pt\Co\Ir have identical slopes with m = (634 ± 47) µrad/nm and (627 ± 69) µrad/nm, respectively. For Ir\Co\Ir a slope of m = (488 ± 57) µrad/nm is obtained and m = (527 ± 57) µrad/nm for Pt\Co\Ir; within the margin of errors the two values can be treated as equal. The slope apparently depends on whether Pt or Ir is used for the capping layer. In general, non-magnetic layers are assumed to contribute a constant offset, if both, the thicknesses and interface morphologies of these layers, remain unchanged. The changing thickness of t_{Co} would thus cause an identical slope in all systems, if M_S behaves identical. A different slope indicates a different M_S present for t_{Co} < 2 nm, or again the influence of magneto-optical effects. As has been pointed out above, for the thinnest samples T_C falls below RT. This occurs at different thicknesses dependent on the system. For decreasing T_C, M_S at RT should also decrease, thus a constant M_S down to the thinnest ferromagnetic samples as might be concluded

Table 4.2 Parameters obtained for the fits to Θ_{sat} over t_{Co} for the four systems in two thickness regimes. The data and fits are shown in Fig. 4-5

	Fit $t_{Co} \geq t_{on}$		Fit $t_{Co} > 1$ nm	
Sample	m [µrad/nm]	$\Theta_{sat,0}$ [µrad]	m [µrad/nm]	$\Theta_{sat,0}$ [µrad]
Pt\Co\Pt	634 ± 47	665 ± 66	481 ± 76	925 ± 122
Ir\Co\Ir	488 ± 57	40 ± 76	440 ± 110	125 ± 186
Pt\Co\Ir	527 ± 57	69 ± 75	412 ± 129	269 ± 212
Ir\Co\Pt	627 ± 69	345 ± 85	510 ± 135	529 ± 204

from the linear behavior displayed in Fig. 4-5 would be surprising. In the following, the present literature dealing with M_S for the four systems is briefly discussed to answer the question whether M_S might vary from system to system for the thin Co-layer regime.

Kisielewski et al. investigated Pt\Co\Pt by MOKE and concluded a constant M_S for $t_{Co} \geq 1$ nm. For thinner t_{Co}, a transition occurs from linear behavior of Θ_{sat} over t_{Co} to an exponential decrease crease (*131*). They attributed this instance to an interdiffusion zone of $\sigma = 0.41$ nm per interface. The structural (grain size, strong texture, roughness, and interdiffusion) and magnetic properties (anisotropies) of their samples closely matches the ones examined in this thesis. Other studies report M_S values for Pt\Co\Pt measured by SQUID-VSM or neutron scattering at RT[15] (*70, 287, 290, 291, 293–299*). The reported values are summarized in Fig. 4-6(a). E-beam evaporated samples are indicated by half-filled symbols while open ones are DC-sputtered. The investigations were performed on both single and multilayers. With the exception of Heap et al. (brown triangles), fcc bulk values are reported for M_S for $t_{Co} \geq 0.9$ nm. For thinner Co layers, reduced, increased, and constant values for M_S are found. If addressed, the increased values are attributed to polarization of adjacent Pt layers at the interfaces, and the decreased ones to alloying at the interfaces and a reduction of T_C (see Fig. 4-21(b) and 4-22(b)). It should be noted that Shan et al. (red triangles) found strongly increased M_S at low temperatures.

For Ir\Co\Ir, only few studies from the 1990s are available, which were also not focused on a systematic investigation of M_S. Fig. 4-6(b) summarizes the reported M_S values for Ir\Co\Ir (*137, 144, 185, 300, 301*). E-beam evaporated and MBE-grown samples are indicated by half-filled sym-

[15] The values taken from van Kesteren et al. (blue circles) (*291*) might also be for 77 K.

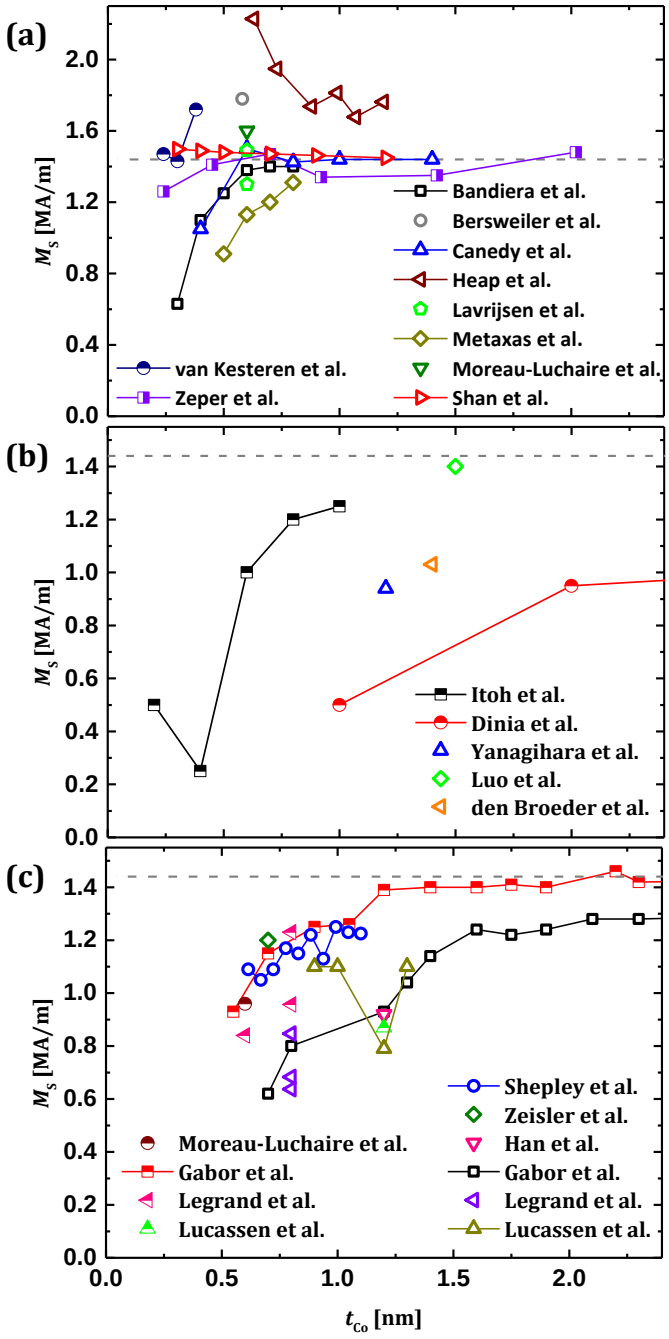

Figure 4-6: Summaries of values found in literature for M_S at RT for ultrathin Co-layers in single and multilayer samples for the four systems. The values were acquired using (SQUID-)VSM and neutron scattering. (a) Pt\Co\Pt: half-filled symbols indicate samples grown by e-beam evaporation; open symbols are DC-sputtered. Values taken from van Kesteren et al. (blue circles) (*291*) might also be for 77 K. (*70, 287, 290, 291, 293–299*), (b) Ir\Co\Ir: half-filled symbols indicate MBE-grown samples; open symbol are DC-sputtered (*137, 144, 185, 300, 301*), and (c) Pt\Co\Ir is indicated by open symbols; Ir\Co\Pt by half-filled ones. All samples are DC-sputtered (*69, 70, 182, 302–305*). The grey dashed line represents M_S for fcc bulk Co (*125, 292*) and the lines are guides to the eye.

bols, while open ones are DC-sputtered. Dinia et al. (red circles) report strongly reduced values for M_S even up to t_{Co} = 3 nm for e-beam evaporated samples and conclude the formation of a magnetic dead layer (MDL) with a thickness of 0.4 nm per interface. On the other hand, Luo et al. (black boxes) observed even for a single monolayer of Co grown by MBE significant M_S, and lightly reduced values compared to bulk M_S for $t_{Co} = 1$ nm. Another study by Luo et al (green diamond) reported bulk M_S for $t_{Co} = 1.5$ nm in DC-sputtered samples. The two remaining studies report values in-between the outcome of Dinia's study, and the ones by Itoh and Luo, and concluded MDLs or suspected considerable interdiffusion at the interfaces.

Analogous, Fig. 4-6(c) summarizes values reported for M_S in Pt\Co\Ir (*69, 182, 302–305*) and Ir\Co\Pt (*70, 182, 302, 305*). Here, the half-filled symbols indicate Ir\Co\Pt while the open ones are Pt\Co\Ir. All samples are prepared by DC-sputtering and both single and multilayers are investigated using SQUID-VSM. For Ir\Co\Pt, three studies are in reasonable agreement, while Lucassen's result deviates to lower M_S (green triangle). Gabor (red squares) found M_S equal to bulk fcc Co for $t_{Co} \geq 1.1$ nm, and reduced values for thinner samples. They attribute the reduced M_S either to a reduction of T_C, which in turn might be a consequence of intermixing or strain. The remaining two studies contribute individual values matching to the ones reported by Gabor.

For Pt\Co\Ir the variation in reported values is more pronounced. Gabor et al. (black squares) report a smaller M_S even for samples with t_{Co} = 6 nm of $M_S \approx 1.3$ MA/m (not shown). This value is retained down until it drops for $t_{Co} \leq 1.4$ nm. From the reduction for thick samples, they conclude a magnetic dead layer (MDL) formation with a thickness of 0.18 nm on the Co\Ir interface, and M_S matching to the inversely stacked system (Pt\Co\Ir) after correction for the MDL (bulk M_S for $t_{Co} \geq 1.2$ nm). The difference to the inverse system is attributed to the known formation of a wider interdiffusion zone at the upper compared to the lower interface. The M_S values found by Legrand and Han match well to the outcome of Gabor's study. On the other hand, Shepley and Zeissler (both used the same sputtering facility) report higher values for M_S that mimic the behavior of Ir\Co\Pt reported by Gabor (red squares). The presence of a MDL is not addressed. The study by Lucassen (golden triangles) reports values that match to both Shepley and Gabor.

Apparently, literature is not very consistent regarding M_S in ultrathin Co layers and great variations are reported. This is not surprising, as the influence of structural properties and interface morphology is especially strong for ultrathin layers, and systematic errors, i.e. from erroneous Co volumes, might occur. Despite the variation, it seems reasonable to assume M_S equal to its bulk value for

$t_{Co} \geq 0.9\,nm$ in Pt\Co\Pt and $t_{Co} \geq 1.1\,nm$ in Ir\Co\Pt. For Pt\Co\Ir, the FMR measurements do not support the existence of a MDL, as bulk M_S is obtained for $t_{Co} = 2\,nm$. Thus, it seems reasonable to adopt Gabor's MDL-corrected regime of $t_{Co} \geq 1.2\,nm$ for constant M_S. Both interfaces of Co to Ir, Ir\Co and Co\Ir, apparently shift the onset of constant M_S to larger values of t_{Co}. For Ir\Co\Ir, the FMR measurements also do not indicate the presence of a MDL as bulk-like M_S was found for $t_{Co} = 2\,nm$. Thus, the onset of constant M_S for Ir\Co\Ir is between the one for Pt\Co\Ir ($t_{Co} = 1.2\,nm$) and $t_{Co} = 2\,nm$. With the value reported in Luo's study for bulk M_S for $t_{Co} = 1.5\,nm$, once may assume constant M_S for $t_{Co} \gtrsim 1.3\,nm$.

With the onsets for constant M_S from literature, the experimental values for Θ_{sat} are reevaluated. The dotted lines in Fig. 4-5 represent linear least square fits to the data for the region $t_{Co} \geq 1\,nm$. Within this region, the fits yield comparable slopes for all systems within the margins of error, indicating similar M_S. For $t_{Co} < 1\,nm$, the measured Θ_{sat} is lower than the fits, qualitatively matching the decrease of M_S found in literature for this thickness regime. The fit parameters for the fits to the data in the regions $t_{Co} \geq t_{on}$ and $t_{Co} \geq 1\,nm$ are summarized in Tab. 4.2.

Apparently, the large scattering of values obtained for Θ_{sat} at any given t_{Co} prohibits a clear identification of a deviation from the linear behavior. Such a scattering can be caused by minor variations of the interface morphology or non-magnetic layer thickness (*285*). Furthermore, the investigated thickness regime was insufficient, i.e. additional values for Θ_{sat} at $t_{Co} = 3$ and $4\,nm$ could help to decide whether Θ_{sat} follows the dotted or dashed fit. Samples of these thicknesses, however, cannot be saturated by the used experimental setup. In a previous diploma thesis within our group by G. Winkler (*283*), two differing dependencies of Θ_{sat} on t_{Co} has been identified for Pt\Co\Pt grown on Si with the transition at $t_{Co} = 1\,nm$. The presence of the two regimes was attributed to the limited penetration depth of light in metals and a reduction of M_S not considered.

We now shortly address the outcome for samples with $N > 1$. If the light interacts with two identical magnetic layers, twice the rotation of a single layer is expected within the description of ultrathin films. With an increasing number of repetitions, less light reaches the lower layers to interact, thus leading to a diminished experimental sensitivity of the lower layers. In Fig. 4-7 Θ_{sat} is plotted over t_{Co} for samples with $N = 1$, 2, 4, 6 and 8 in $(Pt_{1\,nm}\backslash Co_t\backslash Ir_{1.1\,nm})_N$. For a given t_{Co}, Θ_{sat} does not increase beyond $N = 2$. Thus, only the upper two layers contribute significantly to the measured rotation A linear fit to the samples with $N > 1$ yields a slope of $632\,\mu rad/nm$, thus 17– 53 % larger than for samples with $N = 1$ (c.f. Tab. 4.2), which is smaller than the expected increase of 100 %

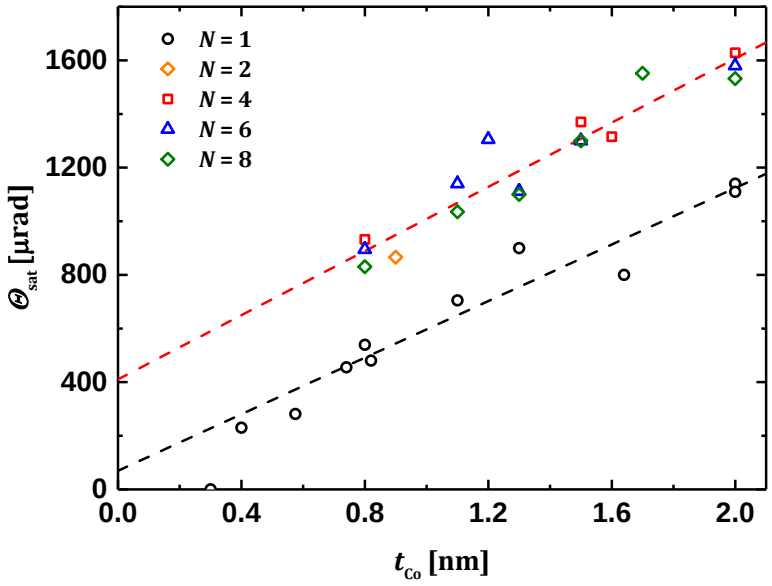

Figure 4-7: Saturation Kerr rotation Θ_{sat} plotted over t_{Co} for $(Pt_{1\,nm}\backslash Co_t\backslash Ir_{1.1\,nm})_N$ for N = 1– 8 with linear fits to N = 1 (black dashed line) and N > 1 (red dashed line). The values for Θ_{sat} with N = 1 exhibit a linear dependency on t_{Co}, and from the fit a slope of m = 527 µrad/nm is obtained. For N > 1, Θ_{sat} is shifted along the Θ_{sat}-axis and do not depend on N. The linear fit to the data with N > 1 has a slope of m = 632 µrad/nm.

for N = 2. Thus, multilayer cannot be described within the formalism of ultrathin films, making a magneto-optical investigation of such samples highly complicated. This is probably caused by the limited penetration depth of light (~10 nm in metals (*86, 282, 283*)) and/or interference of the multiple-reflections from the interfaces (*86, 285*).

In conclusion, the saturation magnetization of multilayer samples of all four systems was investigated. Using FMR, M_S values that closely resemble the bulk value for fcc Co of M_S = 1.44 MA/m(*125*) were obtained for Co-layer thicknesses of t_{Co} = 2 and 4 nm in all systems. Furthermore, no indication for the formation of a MDL at the Co\Ir interface was found. Using MOKE, the saturation Kerr rotation in polar geometry Θ_{sat} of samples with $t_{Co} \leq$ 2 nm and N = 1 was investigated. The insufficient investigated thickness regime and the scatter of data points inhibited a clear identification of the regime in which Θ_{sat} depends linearly on t_{Co} that would indicate a constant M_S. By reviewing the literature addressing M_S in the four systems and comparing the reported values to the FMR measurements, onsets for the regimes of constant M_S are estimated to $t_{Co} \geq$ 0.9 nm in Pt\Co\Pt, $t_{Co} \geq$ 1.3 nm in Ir\Co\Ir, $t_{Co} \geq$ 1.2 nm in Pt\Co\Ir, and $t_{Co} \geq$ 1.1 nm in Ir\Co\Pt. Further measurements of Θ_{sat} for samples with thicker t_{Co} could help to identify if

two regimes of differing dependency of Θ_{sat} on t_{Co} exist and whether the transition occurs at different thicknesses in the systems. Furthermore, VSM or polarized neutron reflectivity measurements could verify the estimated behavior of M_S in the systems. A corresponding proposal for polarized neutron reflectivity measurements has been submitted.

4.3 Uniaxial magnetic anisotropy

In this chapter, the uniaxial magnetic anisotropy constant K_{tot} is investigated by means of MOKE and supplementary using the anomalous Hall Effect (AHE). Section 4.3.1 shows typical remagnetization curves for samples with $N = 1$ to illustrate standard cases. Subsequently, selected curves for $N = 8$ are shown that represent special deviating cases. Section 4.3.2 deals with two experimental methods to extract the uniaxial anisotropy from the curves, and the results are compared for the cases of $N = 1$ and 8. In section 4.3.3, the obtained anisotropy constants for the systems with various N are presented and discussed. Furthermore, a dependency of K_{tot} on the spacer layer thickness t_{NM} is shown for $t_{NM} < 1.75$ nm.

4.3.1 Remagnetization curves obtained via MOKE and AHE

In this chapter, polar and longitudinal MOKE is employed to study the magnetization reversal for the four sample systems. The MOKE setup (see chapter 2.2) provides magnetic fields of up to 0.95 T in polar geometry, which is insufficient to align the magnetization perpendicular to the sample plane for $t_{Co} > 2.5$ nm. To determine K_{tot} in this regime, remagnetization curves were acquired from magnetoresistance (MR) measurements making use of the anomalous Hall Effect (AHE) (*306*). The measurements were done by S. Ziesmann as part of a MSc thesis (*307*). The AHE occurs in ferromagnetic materials and is only sensitive to the magnetization component perpendicular to the sample plane (for current-in-plane geometry). The experimental MR setup provides magnetic fields up to 11 T, sufficient to align the magnetization of all samples along arbitrary directions. Further information about the AHE can be found in (*127, 308, 309*) and on the data acquisition and evaluation in (*127*).

Typical remagnetization curves for samples with $N = 1$ are shown in Fig. 4-8. The curves for Ir\Co\Pt ($t_{Co} = 0.8$ nm) sample shown in (a) and (b) reveals an easy-axis perpendicular to the film normal (PMA). The perpendicular remagnetization curve (a) is almost rectangular and fully remanent. The sample switches its magnetization direction abruptly at its coercive field of about ± 7 mT. The in-plane MOKE curve in (b) displays a reversible behavior revealing a coherent rotation of

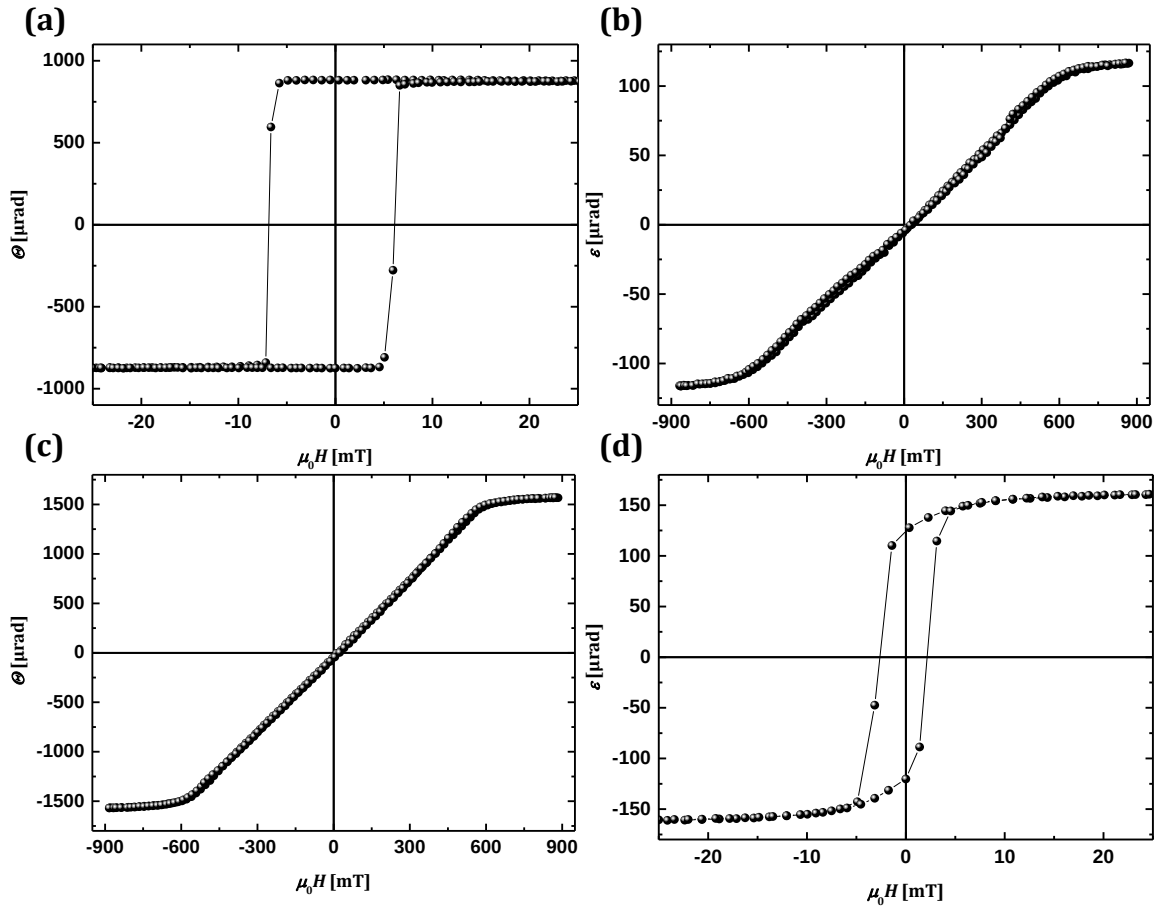

Figure 4-8: Exemplary remagnetization curves obtained by MOKE for Ir\Co\Pt samples with $N = 1$ and Co-layer thickness of (a, b) $t_{Co} = 0.8\,\text{nm}$, (c, d) $t_{Co} = 2\,\text{nm}$. The polar remagnetization is shown in (a, c) and the longitudinal in (b, d).

the magnetization with the field. For a sample with an easy plane (Ir\Co\Pt with $t_{Co} = 2\,\text{nm}$, cf. Fig. 4-8(c) and (d)), the perpendicular curve displays a reversible behavior of coherent rotation, while the in-plane curve is almost fully remanent with close-to rectangular shape.

The remagnetization curves for samples with $N > 1$ partially exhibit a different behavior. Fig. 4-9 shows selected examples deviating from the previously shown fundamental behavior. The sample shown in (a) and (b), Pt\(Co1 nm\Pt2 nm)8, exhibits PMA. In contrast to the case of $N = 1$, the sample is no longer fully remanent for its easy-axis behavior but a decay into a multi-domain state occurs at around 25 mT. This state is stable over a wide range up to about 100 mT as the domain walls do not rush through the sample, but are pinned during the movement. Consequently, the domains grow on the expanse of others aligned antiparallel to the field. The slanted form of the

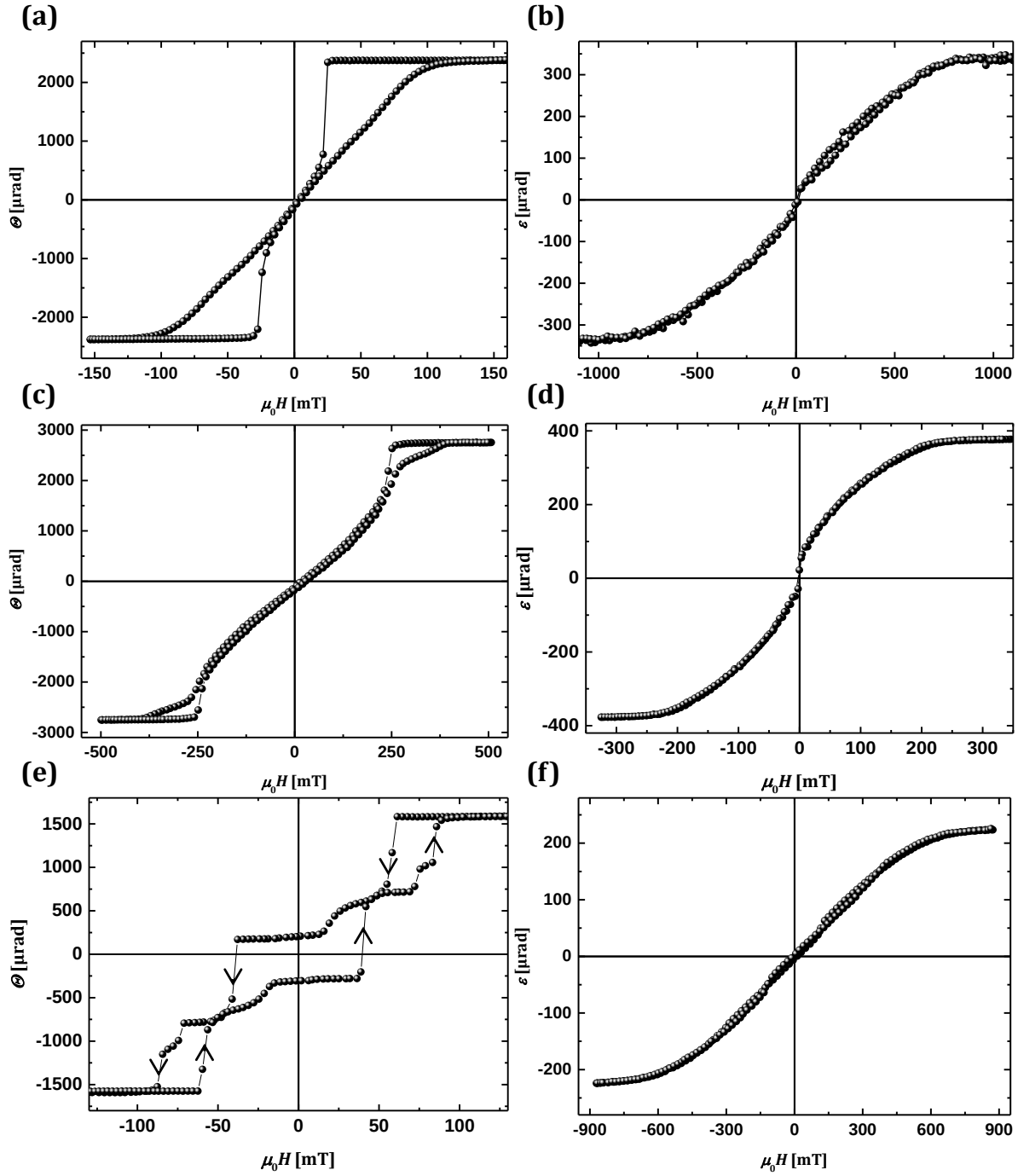

Figure 4-9: Remagnetization curves obtained by MOKE for multilayers with $N = 8$. The polar curves are shown in (a, c, e), longitudinal curves in (b, d, f). In (a, b) curves for $Pt\backslash(Co_{1\,nm}\backslash Pt_{2\,nm})_8$ are shown that exhibit a switching of magnetization via domain decay. (c, d) shows $Pt\backslash(Co_{1.7\,nm}\backslash Pt_{2\,nm})_8$ where a three-dimensional magnetic microstructure is present. Both curves exhibit typical features of easy axis behavior. (e, f) shows $(Ir_{1.1\,nm}\backslash Co_{1\,nm}\backslash Pt_{1\,nm})_8$ where the Co-layers are coupled antiferromagnetically via IEC. At zero fields, the magnetization in adjacent layers is aligned antiparallel. With applied fields, the outer most layers switch first as they are only coupled to one neighboring Co-layer. The inner layers are coupled to

two adjacent layers, thus experience twice the coupling and a second transition occurs at twice the field of the first. Three layers switch at the second step in this sample, the splitting of the second transition is probably caused by small variations of the IEC or other magnetic properties.

remagnetization curve is typical for this behavior. The hard axis curve of the same sample exhibits again a fully reversible behavior due to coherent rotation.

For a similar sample with slightly thicker t_{Co} (Pt\(Co1.7 nm\Pt2 nm)8), from the shape of the hysteresis curves it is quite impossible to determine which is the easy and hard axis of magnetization. The curve for perpendicular fields shown in (c) exhibits similar features like the sample with PMA shown in (a), i.e., it displays the slanted remagnetization curve, namely showing a non-reversible behavior that saturates at around 375 mT. On the other hand, the curve for in-plane fields shown in (d) displays a reversible behavior but saturates at a lower field of around 250 mT. The sample exhibits a three-dimensional magnetic microstructure around zero magnetic fields with perpendicular domains but easy plane. The ground state is further discussed in chapter 5.2.

The perpendicular magnetization curve shown in (e) ((Ir1.1 nm\Co1 nm\Pt1 nm)8) reveals that the sample exhibits PMA and antiferromagnetic interlayer exchange coupling (AIC). The sample is not remanent, as it is energetically favorable for the magnetization of the Co layers to be aligned antiparallel with respect to the one of the adjacent layers. Outermost layers are coupled to one adjacent layer, while the central ones are coupled to two, thus switch at a field twice as strong. This phenomenon is discussed in more detail in the chapters 1.1.5 and 4.5. The in-plane remagnetization curve of this sample shown in (f) depicts a reversible behavior with coherent rotation.

Two methods are introduced in the following to determine the anisotropy constants K_{tot} from the remagnetization curves. The first one is based on the coherent rotation of magnetization occurring during hard axis magnetization reversal while for the second method the differences of energy densities are extracted to achieve saturation along the easy and hard axes of magnetization.

4.3.2 Determination of anisotropy constants

This chapter introduces two methods to determine the anisotropy constants from the remagnetization curves. First, the constants are extracted from hard-axis remagnetization curves (loops) in chapter 4.3.2.1. Subsequently, an alternative method is introduced in chapter 4.3.2.2 that deter

mines K_{tot} from the difference of energy densities required to achieve saturation in easy and hard axes loops. Finally, both methods are compared with each other in chapter 4.3.2.3.

4.3.2.1 Determination of K_{tot} from hard axis curves

In physics, a system is in equilibrium when (E/V) is minimized with respect to internal and external energy contributions e.g. connected with temperature and applied field. So, if a magnetic field is applied, the Zeeman energy $E_Z = -\mu_0 M_S H \cos \Phi$, with Φ the angle between magnetization and applied field, has to be considered as well in the free energy. The dependence of the free energy on the direction of magnetization is composed of the terms for the uniaxial magnetic anisotropy (up to second order)[16] and the Zeeman energy:

$$\frac{E}{V} = K_{1,\mathrm{eff}} \cdot \sin^2(\Theta) + K_{2V} \cdot \sin^4(\Theta) - \mu_0 M_S H \cdot \cos \Phi, \qquad \text{Eq. 4-4}$$

where Θ is the angle between the easy axis and the magnetization. Two cases are now considered: First, the easy axis is perpendicular to the sample and the field applied in any in-plane direction (hard axis), thus $\Theta + \Phi = 90°$. The energy density is minimized when the condition $\partial(E/V)/\partial\theta = 0$ is met:

$$\begin{aligned} 2K_{1,\mathrm{eff}} \cdot \sin(\Theta) + 4K_{2V} \cdot \sin^3(\Theta) &= \mu_0 M_S H, \\ \frac{2K_{1,\mathrm{eff}}}{M_S} m_\parallel + \frac{4K_{2V}}{M_S} m_\parallel^3 &= \mu_0 H(m_\parallel), \end{aligned} \qquad \text{Eq. 4-5}$$

with $m_\parallel = M_\parallel / M_S = \sin \Theta$, the in-plane (field aligned) component of the magnetization. Thus, by fitting Eq. 4-5 to the $\mu_0 H(m_\parallel)$ curve of a perpendicular sample, the anisotropy constants $K_{1,\mathrm{eff}}$ and K_{2V} can be obtained.

The second case is the determination of anisotropy constants $K_{1,\mathrm{eff}}$ and K_{2V} for samples with easy plane behavior. Here the field has to be applied perpendicular to the sample plane (hard axis), thus $\Theta = \Phi$. Then $\partial(E/V)/\partial\theta = 0$ yields

$$\begin{aligned} 2K_{1,\mathrm{eff}} \cdot \cos(\Theta) + 4K_{2V} \cdot \cos(\Theta)\sin^2(\Theta) &= -\mu_0 M_S H, \\ -\left(\frac{2K_{1,\mathrm{eff}} + 4K_{2V}}{M_S}\right) m_\perp + \frac{4K_{2V}}{M_S} m_\perp^3 &= \mu_0 H(m_\perp), \end{aligned} \qquad \text{Eq. 4-6}$$

with $m_\perp = M_\perp / M_S = \cos \Theta$, the perpendicular component of the magnetization (parallel to field).

[16] Phenomenological, the free energy can be expanded into a power series with respect to Φ and terms of orders higher than 4 are neglected

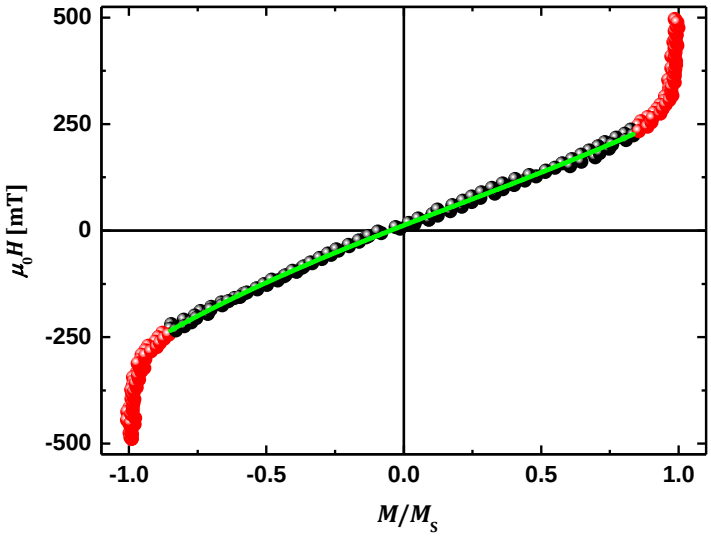

Figure 4-10: Polar remagnetization curve of Pt\Co1.1 nm\Pt with the field plotted over the normalized magnetization. The curve exhibits typical hard-axis behavior with a coherent rotation of the magnetization. The green dashed line represents a fit of Eq. 4-5 to the data. Only the black data points with $M/M_S < 0.85$ were considered for the fit, as the model is only applicable for fields sufficiently smaller than the field saturating the sample. The data shown in red is disregarded.

Fig. 4-10 shows the hard axis behavior of the Pt\Co1.1 nm\Pt sample that exhibits PMA (i.e., blue curve from Fig. 2-3. When using M_S = 1.4 MA/m (taken from chapter 4.2) the fit (shown as green dashed line) provides the parameters $K_{1,eff}$ = (173 ± 2) kJ/m³, K_{2V} = (12 ± 3) kJ/m³, resulting in K_{tot} = (185 ± 4) kJ/m. K_{2V} is much smaller in this sample than reported for Pt\Co\Pt (*127, 129, 131*). It manifests as a curvature superimposed on the linear slope, which is $K_{1,eff}$. For large values of $K_{1,eff}$, this curvature is negligible and thus hard to extract. Therefore, a reliable measurement of K_{2V} is only possible for $K_{1,eff} \approx 0$.

The described method, henceforth called "K_1, K_2-fitting-method", for determining the anisotropy constants only considers a coherent rotation of the magnetization from the easy axis following the field direction. In addition to that, the magnetization can follow the field by domain nucleation and domain wall movement. In general, ultrathin samples meet this requirement, where nucleation and movement processes are not (significantly) contributing to the hard-axis remagnetization curves. The projection of the magnetization along the field direction is the same in each domain for arbitrary field strengths (*127*). However, within domain walls, this condition is violated. For samples with small domains, thus a high filling of domain walls, the fitting returns false values. A further prerequisite for multilayer samples is that all magnetic layers are strongly coupled and act as a single

macro-spin. For the multilayer samples with $N \geq 4$ investigated in this thesis, this prerequisite is not met for small and negative K_{tot}, inhibiting the use of this method. The resulting three-dimensional magnetic microstructures, which are discussed in chapter 5.2, require an alternative approach for the extraction of K_{tot} that is introduced in the following section.

4.3.2.2 Determination of K_{tot} using the area method

The method introduced in the previous chapter fails for multilayer samples with low interlayer exchange coupling, where three-dimensional magnetic microstructures are prevalent. For instance, the sample shown in Fig. 4-9(c) and (d) shows domains in its hard-axis remagnetization curve, thus violating the prerequisites for the applicability of the model presented in section 4.3.2.1. The determination of K_{tot} from the so-called "area-method" (*126*), is free of any presumptions and constraints, like the (multilayer) sample acting as a single macro-spin, coherent rotation of the magnetization being the dominant process or even knowing which of the curves the hard axis is.

The energy density to saturate a sample in a random direction is given by (*126*):

$$\frac{E}{V} = \mu_0 \int_0^{M_S} H(M)\, dM. \qquad \text{Eq. 4-7}$$

Subtracting the energy densities required to saturate a sample along the hard and the easy axes, reveals the total anisotropy energy K_{tot} (*126, 310*). In the present case of fcc Co (111), this are the magnetic working functions required to saturate a sample in-plane and perpendicular to the sample plane, thus the perpendicular and in-plane remagnetization curve. With the convention of subtracting the obtained values for the perpendicular from the in-plane curve, the correct sign of K_{tot} is obtained (see Eq. 4-4).

Fig. 4-11 shows the remagnetization curves for the Pt\(Co1.7 nm\Pt2 nm)8 sample from Fig. 4-9(c) and (d), with the x- and y-axis switched[17]. The perpendicular curve is shown in (a), and in (b) the in-plane one. The grey areas represent the integral in Eq. 4-7. If the integration is carried out across $\pm M_S$, a division by a factor of 2 is required but systematic errors due to offsets and open loops[18] are avoided. In order to obtain (E/V), the integrated areas are multiplied by M_S = 1.4 MA/m (see chapter 4.2), resulting in (E/V) = 254.5 kJ/m³ for (a) and 112.3 kJ/m³for (b). Subtracting (a) from (b) yields K_{tot} = -142.2 kJ/m³.

[17] In order to obtain M/M_S, the measured rotation Θ (ellipticity ε) is normalized to its respective value in saturation.
[18] In the presence of an open hysteresis, the M/M_S values of both sweep directions have to be averaged (*126*).

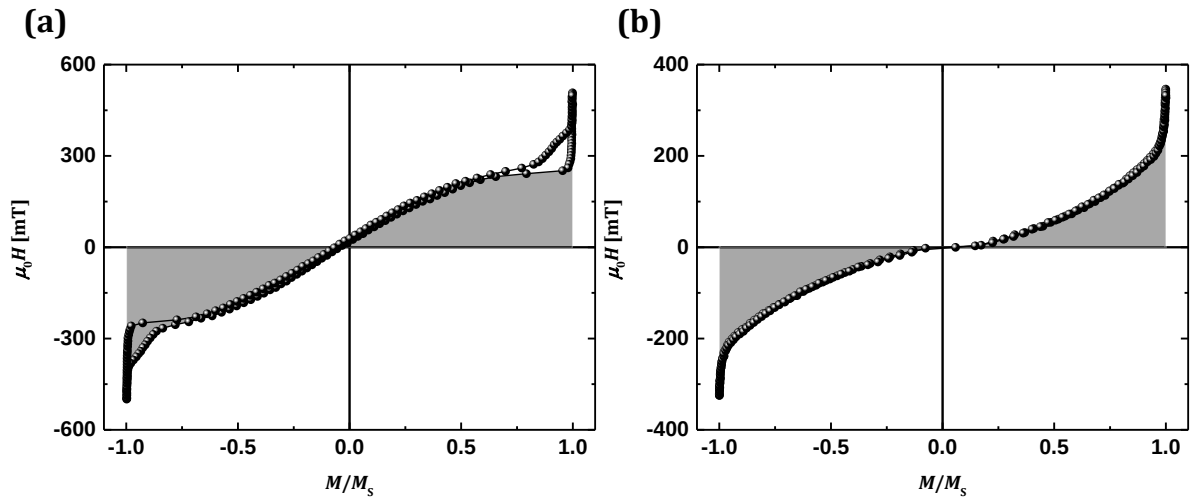

Figure 4-11: Remagnetization curve of Pt\(Co$_{1.7\,nm}$\Pt$_{2\,nm}$)$_8$ with the field plotted over the normalized magnetization. (a) shows the polar remagnetization and (b) the longitudinal. The grey areas represent the integrated area in Eq. 4-7 for the bounds of integration $\pm M_S$, thus requiring no further treatment than division by a factor of 2.

The disadvantage of this method is not being able to discern between first and second order anisotropy constants.

4.3.2.3 Comparison of the two experimental methods

In this section, the anisotropy constants obtained for both methods are compared. For the case $N = 1$ the boundary condition of the K_1, K_2-fitting-method are met, thus a consistency check of the area-method is possible. K_{tot} was extracted for all Pt\Co\Ir samples with $N = 1$ using both methods. Fig. 4-12(a) shows the obtained values plotted as suggested in Eq. 1-17, $K_{tot} \cdot t_{Co}$ over t_{Co}. The obtained values for both methods are in very good agreement with only small differences never exceeding $\pm$ 8 % and both signs equally represented.

Fig. 4-12(b) illustrates the outcome for $N = 8$ in (Pt$_{1\,nm}$\Co$_t$\Ir$_{1.1\,nm}$)$_8$. For samples with strong PMA, both methods still yield identical results. With increasing t_{Co} (= 1.3– 1.5 nm), however, differing K_{tot} values are extracted. The ones obtained by the K_1, K_2-fitting-method, for which the boundary conditions are not met, exceed the ones from the area-method. This is either caused by the high domain-wall area filling (the average domain size is $d_{avg} \approx 120$ nm for these samples (see chapter 5.1), the formation of the three-dimensional magnetic microstructure (see chapter 5.2), or a combination of both. Finally, in the range of t_{Co} = 1.7– 2 nm, both remagnetization curves exhibit

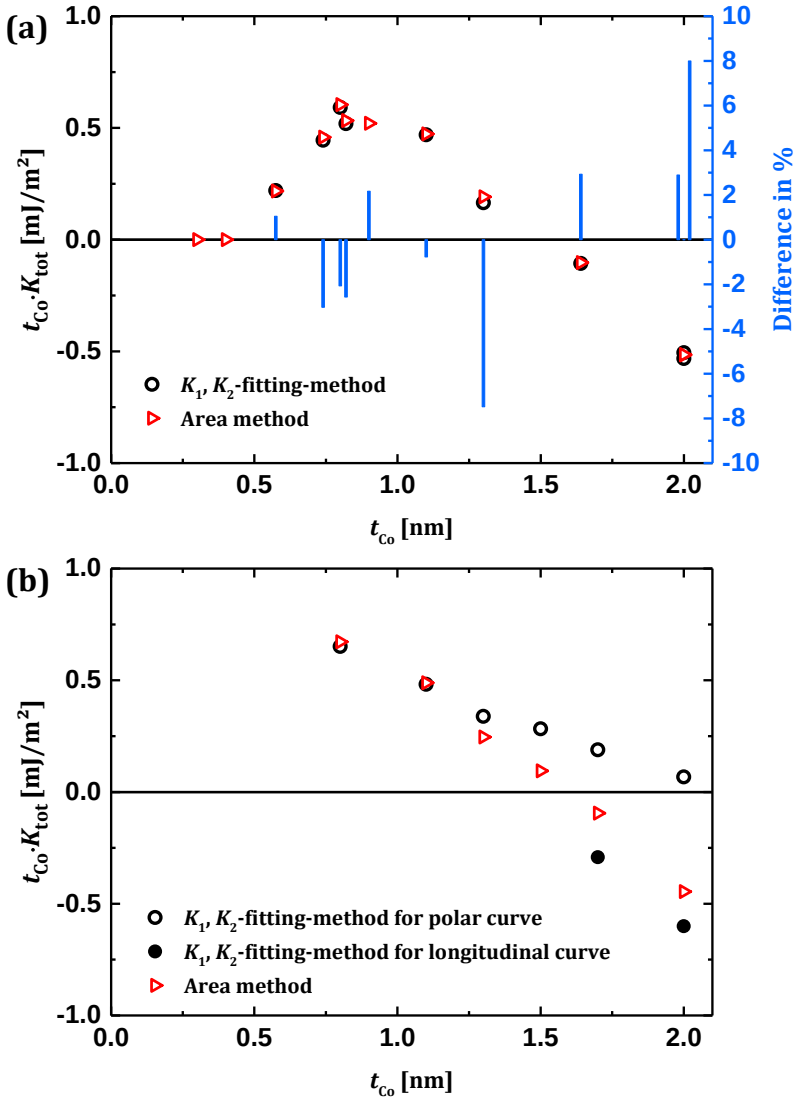

Figure 4-12: Comparison of the two methods for the determination of K_{tot} for $(Pt_{1\,nm}\backslash Co_t\backslash Ir_{1.1\,nm})_N$ samples with N = 1 in (a) and N = 8 in (b). The black circles are obtained from fitting to the hard axis loops (K_1,K_2–fitting-method), while the red triangles stem from the differences of magnetic working function along the easy and hard axis (area method). In (a), the blue bars indicate the differences of area method to K_1,K_2–fitting-method for each sample, which are below ± 8 % and evenly distributed with respect to the sign. In (b), the hard axis could not be determined unambiguously from the remagnetization curves, thus the K_1,K_2–fitting-method was employed to both curves. Filled circles represent fits to the longitudinal curve, while open circles are fits to the polar curve.

typical hard axis features, thus two different K_{tot} values can be obtained for each sample. The perpendicular curve shows an open hysteresis while the in-plane curve saturates at lower fields. The fit to neither curve yields a comparable result to the one of the area method. Further, the fits

with $K_{tot} < 0$ yield high negative K_{2V} values ($\approx$ -100 kJ/m³), while for thinner samples only positive values are obtained. This unphysical discontinuity of K_{2V} is a consequence of the violated boundary conditions.

In conclusion, both methods yield identical results in the case of $N = 1$, particularly revealing the applicability of the area method. However, for multilayers with $N \geq 4$, the boundary conditions are not met for using the K_1, K_2-fitting-method, as the samples exhibit a high domain-wall area filling and/or three-dimensional magnetic microstructures. Using the method anyway, leads to unphysical discontinuities in both K_{2V} and K_{tot}. Thus, the method is not suited for the extraction of the anisotropy constants in the multilayer samples investigated in this thesis.

4.3.3 Anisotropy constants in X/Co/Y with X, Y = (Pt, Ir)

In this chapter, the experimentally obtained anisotropy constants K_{tot} are presented for the four systems in dependence of t_{Co} and t_{NM}. Section 4.3.3.1 addresses the dependency of K_{tot} on t_{Co} for the case of $t_{NM} \geq 1.75$ nm, where no dependency on t_{NM} exists. The results for all four systems are presented and discussed. Subsequently in section 4.3.3.2, the dependency of K_{tot} on t_{NM} for $t_{NM} < 1.75$ nm is briefly described. Throughout this chapter $M_S = 1.4$ MA/m is used[19].

4.3.3.1 K_{tot} in the sample systems with $t_{NM} \geq 1.75$ nm

This chapter addresses the dependency of the anisotropy constant K_{tot} on t_{Co} in the four investigated systems. To this end, single and multilayer samples within the Co-thickness range of $t_{Co} = 0.3 - 20$ nm were prepared for single layers ($N = 1$) and $t_{Co} = 0.8 - 4$ nm for multilayers ($N = 4$, 6, and 8). In the case of multilayers, the spacer layer thickness has a considerable influence on the anisotropy of the sample as will be shown in section 4.3.3.2. The samples presented here have spacer layer thicknesses of $t_{NM} = t_{Pt} = 2$ nm in the case of Pt\(Co\Pt)$_N$, $t_{NM} = t_{Ir} = 1.75$ nm for Ir\(Co\Ir)$_N$, $t_{NM} = t_{Pt} + t_{Ir} = (1 + 1.1)$ nm = 2.1 nm for (Pt\Co\Ir)$_N$ and (Ir\Co\Pt)$_N$. For the chosen spacer layer thicknesses, the anisotropy is found to be independent of the number of repetitions N. The results for K_{tot} in each system are plotted in Fig. 4-13 as

[19] For ultrathin samples a reduction of M_S is expected (c.f. discussion in chapter 4.2.2). Furthermore, the thickness, above which to obtain a constant bulk-like M_S is expected to vary from system to system. The absolute value of M_S for any given sample with $t_{Co} \lesssim 1$ nm is unknown, thus is also the progression of the reduction. An overestimation of M_S leads to an overestimation of the magnitude of K_{tot}, thus the presented values are upper limits of K_{tot} for the thinnest samples.

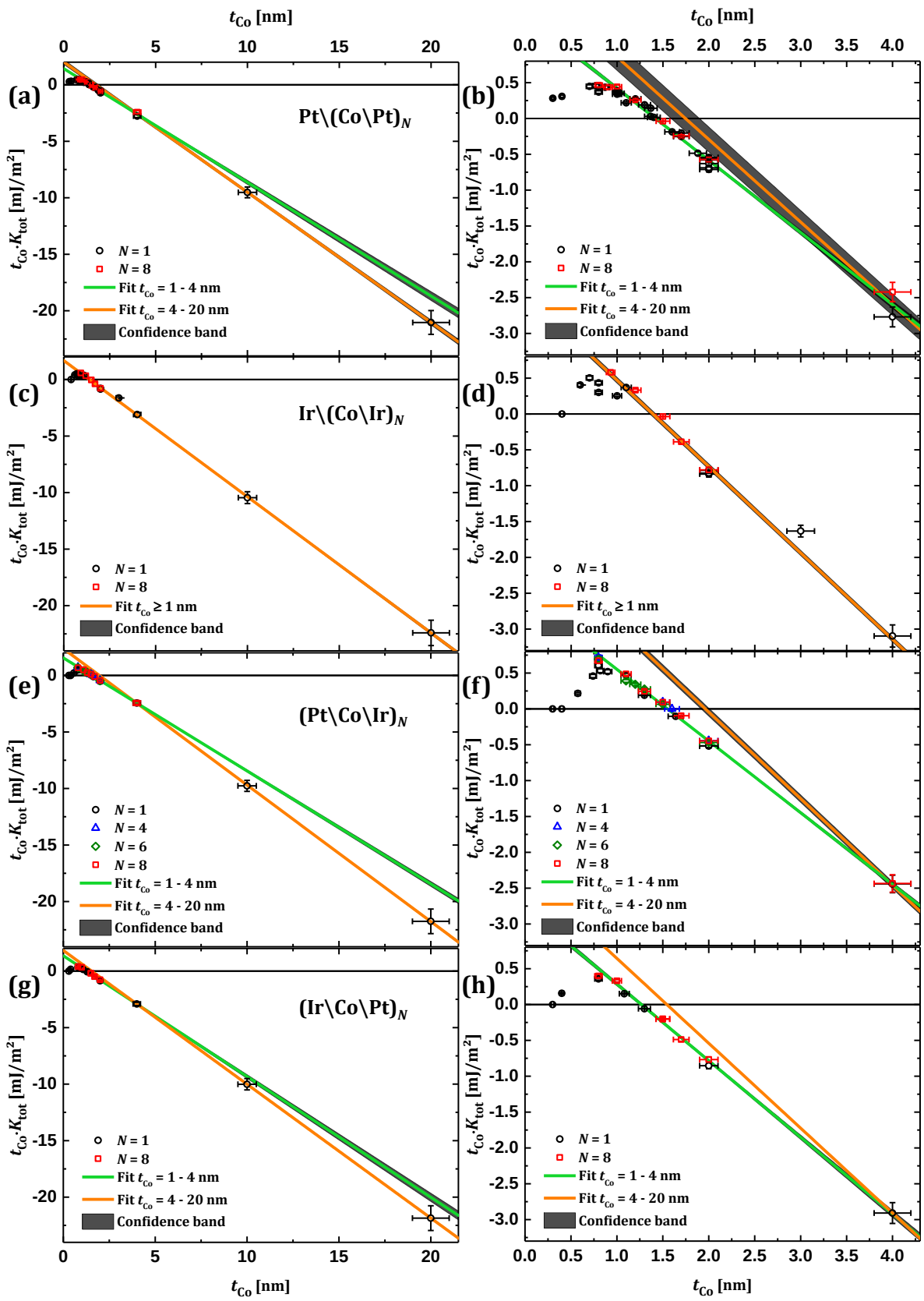
(a)
Pt\(Co\Pt)$_N$
(b)
(c)
Ir\(Co\Ir)$_N$
(d)
(e)
(Pt\Co\Ir)$_N$
(f)
(g)
(Ir\Co\Pt)$_N$
(h)
t_{Co} [nm]
$t_{Co}\cdot K_{tot}$ [mJ/m^2]
N = 1
N = 4
N = 6
N = 8
Fit t_{Co} = 1 - 4 nm
Fit t_{Co} = 4 - 20 nm
Fit t_{Co} ≥ 1 nm
Confidence band

Figure 4-13: Co thickness dependence of the anisotropy K_{tot} in the four systems Pt\(Co\Pt)$_N$ in (a, b), Ir\(Co\Ir)$_N$ in (c, d), (Pt\Co\Ir)$_N$ in (e, f), and (Ir\Co\Pt)$_N$ in (g, h) for N = 1– 8. The left column (a, c, e, g) shows the entire range of t_{Co} of 0.3– 20 nm while in the right one (b, d, f, h) a more detailed view of the range of t_{Co} = 0.3– 4 nm is given. The lines are linear fits to the respective regions; the 1σ-wide confidence bands (grey) represent the error of the fit at any given t_{Co}. The fit parameters and errors are summarized in Tab. 4.3.

$K_{tot} \cdot t_{Co}$ over t_{Co} (Eq. 1-18). The observed behavior is first qualitatively described and subsequently the features qualitatively discussed. A quantitative analysis is beyond the scope of this thesis.

First, the dependence of $K_{tot} \cdot t_{Co}$ on t_{Co} is described for the Pt\(Co\Pt)$_N$ system. Fig. 4-13(a) shows the entire range of t_{Co}. On this scale, the data points follow the expected linear behavior with a negative slope, except for the thinnest samples. The orange line is a linear fit to the data points in the range of t_{Co} = 4– 20 nm yielding the fit constants of $2K_{1S}$ = (1.84 ± 0.09) mJ/m² and $K_{V,eff}$ = -(1.14 ± 0.010) MJ/m³. The grey, 1σ-wide[20]confidence bands represent the uncertainty of the fit at any given t_{Co}. From the fit parameters follows with K_d = 1.23 MJ/m³ and Eq. 1-18, K_V = (0.09 ± 0.010) MJ/m³. Subtracting K_{2V} = (0.07 ± 0.03) MJ/m³, the second order anisotropy constant, leads to K_{1V} = 0 within the margins of error. In the more detailed view on low thicknesses shown in (b), the data deviate from the orange fit for t_{Co} = 4– 20 nm, while still exhibiting a linear behavior with a smaller slope down to t_{Co} = 1 nm. The green line is a linear fit to the data in this second regime of t_{Co} = 1– 4 nm that yields $2K_{1S}$ = (1.48 ± 0.05) mJ/m² and $K_{V,eff}$ = -(1.05 ± 0.03) MJ/m³, thus K_V = (0.18 ± 0.03) MJ/m³. Subtracting K_{2V} reveals K_{1V} = (0.11 ± 0.06) MJ/m³. For even thinner samples t_{Co} < 1 nm, the data deviate from a linear behavior and their graph bends toward the abscissa. The differing dependencies of $K_{tot} \cdot t_{Co}$ on t_{Co} reveal significant changes in the three thickness regimes of t_{Co} = 4– 20 nm, t_{Co} = 1– 4 nm, and t_{Co} < 1 nm. Possible reasons for the three regimes will be discussed later on.

Next, the behavior of Ir\(Co\Ir)$_N$ is addressed. The results for the entire t_{Co}-range are shown in Fig. 4-13(c), exhibiting the expected linear behavior. Contrary to Pt\(Co\Pt)$_N$, no deviation from the linear behavior is apparent down to t_{Co} = 1 nm in the detailed view in (b). Thus, one fit is sufficient to describe the data in the range of t_{Co} = 1– 20 nm, yielding $2K_{1S}$ = (1.68 ± 0.04) mJ/m²

[20] This is the equivalent to σ in a Gaussian distribution representing 68.3 % of the data.

and $K_{V,eff}$ = -(1.205 ± 0.007) MJ/m³, or K_V = (0.025 ± 0.007) MJ/m³. For even thinner samples with t_{Co} < 1 nm, the data deviate from a linear behavior with their graph bending to the abscissa. Samples with $t_{Co} \leq t_p$ = 0.4 nm are no longer ferro- but paramagnetic.

The results for the two antisymmetric systems, (Pt\Co\Ir)$_N$ and (Ir\Co\Pt)$_N$, are shown in Fig. 4-13(e, f) and (g, h), respectively. Both systems qualitatively resemble the behavior found for Pt\(Co\Pt)$_N$ with two linear regimes of differing linear dependency of $K_{tot} \cdot t_{Co}$ on t_{Co} for t_{Co} = 4– 20 nm and t_{Co} = 1– 4 nm. This is followed by a bending of the data curve towards the abscissa for t_{Co} < 1 nm. Furthermore, the thinnest samples exhibit paramagnetic behavior, like in Ir\(Co\Ir)$_N$.

The values obtained from the fits for the surface and volume anisotropies are summarized in Tab. 4.3 in combination with t_{on} for each system. It is worth pointing out that for Pt\Co\Pt in the regime of t_{Co} = 4– 20 nm K_V apparently only consists of the second-order volume anisotropy constant K_{2V} = (0.07 ± 0.03) MJ/m³ (*127, 129, 131*). It may be speculated that the observed values of K_V for the other investigated systems in this thickness regime also consist only of the second-order volume anisotropy constant and $K_V = K_{2V}$ thus varies slightly from system to system. This is however highly speculative and a dedicated investigation with appropriate samples is required to answer this question.

In the following, the obtained values are compared to literature. For Pt\Co\Pt, the values for K_{1S} and K_V in the two linear regimes are within the span of values found in literature[21], $2K_{1S}$ = 0.54– 2.58 mJ/m² and K_V = 0– 0.95 MJ/m³ (*126, 127, 131, 137, 286, 287, 296, 299, 311–313*). Considering the huge spread of values this is not surprising. The deviations are generally attributed to varying preparation methods, residual strain or mixtures of hcp and fcc phases (*126, 314*). Considering only studies that clearly indicate an fcc structure in samples prepared by sputtering techniques follows $2K_{1S}$ = 0.96– 2 mJ/m² and K_V = 0– 0.76 MJ/m³ (*127, 137, 287, 296, 311*), while for hcp volume anisotropies of $K_{V,hcp}$ = 0.41– 0.95 MJ/m³ are reported (*131, 299, 315*). The spans are still considerable and clearly illustrate the important role of strain on the anisotropy. The obtained values for both thickness regimes still agree with the ones found in literature, although the value for $2K_{1S}$ in the regime t_{Co} > 4 nm exceeds the reported ones slightly. The thickness regime of t_{Co} > 4 nm was not investigated in any of the mentioned studies except for one by Philippi-Kobs

[21] In some studies only $K_{V,eff}$ is reported. If M_S was not stated K_V was obtained by adding K_d = 1.23 MJ/m³.

Table 4.3: Anisotropy constants of the four samples systems obtained from fits to the respective thickness regimes. For Ir\Co\Ir, only one fit was sufficient, thus, both regimes have the same values. The thickness for the thinnest sample with ferromagnetic behavior is indicated by t_{on}

System	$2K_{1S}$ [mJ/m²]	K_V [MJ/m³]	$2K_{1S}$ [mJ/m²]	K_V [MJ/m³]	t_{on} [nm]
	t_{Co} = 1– 4 nm		t_{Co} = 4– 20 nm		
Pt\Co\Pt	1.43 ± 0.04	0.22 ± 0.03	2.01 ± 0.16	0.09 ± 0.02	0.3
Ir\Co\Ir	1.68 ± 0.04	0.025 ± 0.007	1.68 ± 0.04	0.025 ± 0.007	0.6
Pt\Co\Ir	1.55 ± 0.03	0.23 ± 0.02	2.37 ± 0.05	0.023 ± 0.005	0.58
Ir\Co\Pt	1.35 ± 0.04	0.16 ± 0.02	1.828 ± 0.0010	0.046 ± 0.0010	0.4

who reported $2K_{1S}$ = 2 mJ/m² (*127*). Consequently, a transition for $t_{Co} \approx 4$ nm between two linear regimes was not observed by any study except for the previous mentioned one by Philippi-Kobs. The bending-regime for $t_{Co} < 1$ nm is frequently reported for both, hcp and fcc structure, and samples prepared by sputtering and MBE (*131, 137, 287, 296, 299, 311, 312*) and commonly attributed to strain, intermixing, pinholes or a reduction of T_C.

For the remaining systems, only one study is found for each that investigates the anisotropy systematically. The one study for Ir\Co\Ir by den Broeder et al. reported $2K_{1S}$ = 1.6 mJ/m² and K_V = 0.03 MJ/m³ for DC-sputtered samples (*137*). These values are almost exactly reproduced within this thesis. Considering the huge span reported for Pt\Co\Pt, this agreement is quite surprising. However, the findings in the study differ for t_{Co} = 1– 1.5 nm as they observed a bending for $t_{Co} < 1.5$ nm[22], so for samples with 0.5 nm thicker Co layers than in this thesis. Thus, the similar values for the surface and volume anisotropy indicate similar structural properties; the different onset for the bending-regime indicates at least small differences. It should be noted that the small value of K_V = 0.025 MJ/m³ ≈ 0 strongly indicates fcc structure of the Co-layers ($K_{V,\,hcp}$ = 0.56 MJ/m³ and $K_{V,\,fcc} \approx 0$ for bulk Co (*125, 126*)).

Both, Pt\Co\Ir and Ir\Co\Pt, were investigated within the same study by Gabor et al for DC-sputtered samples with $t_{Co} < 2.5$ nm (*182*). For Ir\Co\Pt, they observed a bending for $t_{Co} < 1.1$ nm and reported $2K_{1S}$ = 1.5 mJ/m² in combination with K_V = 0 within the margins of error. The values obtained for the same thickness regime (t_{Co} = 1– 4 nm) vary from the ones in Gabor's study. The K_V observed in this thesis is a little larger (0.16 MJ/m³) and instead $2K_{1S}$ a little

[22] The bending-regime was accompanied by a reduction of M_S; within the linear regime, bulk-like M_S was measured.

smaller (0.15 mJ/m²). For Pt\Co\Ir, Gabor's observed a magnetic dead layer (MDL) of t_{mdl} = 0.18 nm. After correcting for the MDL, they observed a bending for t_{Co} < 1.2 nm, $2K_{1S}$ = 1.76 mJ/m² and, within the margins of error, K_V = 0. A similar MDL is not observed for the samples in this thesis (c.f. discussion in section 4.2.2) and, like for the inversely stacked system, K_V in this thesis is slightly larger (0.23 MJ/m³) and instead $2K_{1S}$ a little smaller (0.26 mJ/m²). The variation in both systems is most likely caused by structural differences, but considering the huge span found in Pt\Co\Pt seems small. The thickness regime of t_{Co} > 4 nm was not investigated in Gabor's study.

In the following, possible reasons for the origin of the three thickness regimes are qualitatively discussed. First, the bending to the abscissa or collapse of the anisotropy for $t_{Co} \lesssim 1$ nm is addressed that is observed in all four systems. This kind of collapse of K_{tot} is frequently found for Co-based layered systems in this thickness regime (*126, 127, 129, 131, 137, 182, 286, 287, 296, 299, 311, 312*) and commonly attributed to strain, intermixing causing a reduction of T_C, or a transition between fcc and hcp structure of the Co. A transition from fcc to hcp structure was observed for $t_{Co} = 1.5$ nm (*312*). The hcp phase of Co is energetically more favorable at RT, so that once an hcp structure is initiated it will be retained. However, structural investigations of the Pt\Co\Pt samples have shown that the Co layers exhibit fcc structure (*129*). Furthermore, the low values of K_V found for all systems especially within the region of t_{Co} = 4– 20 nm (K_V = 0.023– 0.09) MJ/m³ are very close to the values expected for fcc bulk Co of K_V = 0.03– 0.09 MJ/m³ (*124, 125, 311, 312*) and strongly deviate from hcp Co of K_V = 0.56 MJ/m³ (*125*). Thus, a transition between fcc and hcp is unlikely.

The second frequently proposed explanation for the collapse concerns the relaxation of the residual strain within the Co material with increasing Co thickness (see section 1.1.3). Considering elastic and dislocation energies (*145*), a bend in the otherwise linear $K_{tot} \cdot t_{Co}$ over t_{Co} behavior is expected when a transition from pseudomorphic to partially coherent, i.e. incoherent, stacking occurs (*126*). For the incoherent stacking, the strain is assumed to be partially accommodated via dislocations suchlike that the strain is inversely proportional to the magnetic layer thickness. Structural investigations have shown that for Pt\Co\Pt, due to the large lattice mismatch of 11 % with respect to the lattice parameter of Co no pseudomorphic growth proceeds (*127*). However, it was found that the prevalent strong tensile strain for t_{Co} = 0.8 nm is partially relaxed somewhere within the range up to t_{Co} = 12 nm, which could accommodate for the bending for t_{Co} < 1 nm and is the most probable cause for the transition occurring for $t_{Co} \approx 4$ nm (*127*). A striking feature concerning the

latter transition for $t_{Co} \approx 4\,nm$ is that, within this thesis, it is observed in all systems containing Pt but not in Ir\Co\Ir. With 8 % (*144*), the lattice mismatch of Ir with Co is only slightly smaller than for Pt. However, the 3 % difference is seemingly sufficient to initiate the second transition. Structural investigations are required to link the observed magnetic properties firmly with structural ones and a corresponding proposal has been submitted for an X-ray diffraction (XRD) investigation.

The third frequently found explanation for the collapse is t_{Co} falling below the width of the interdiffusion zones of both interfaces making a separation into surface and volume contributions questionable. The sample contains then only a magnetic layer resembling an alloy of Co with both interface materials and a heterogeneous depth profile, while the composition depends on t_{Co}. For Pt\(Co\Pt)$_N$ samples prepared within our group, an interdiffusion zone with a width of $\sigma = (0.5 \pm 0.1)\,nm$ per interface was measured (*127–129*), which coincides perfectly with the region of collapse of $t_{Co} < 1\,nm$. Furthermore, it was found that the collapse is suppressed in Pt\Co\Cu\Pt until smaller t_{Co} as Co and Cu are immiscible and thus no alloy forms at the Co\Cu interface (*295, 296*). In alloys of Co with Pt and Ir, T_C is reduced causing a reduction of M_S (c.f. Fig. 4-21(b)) (*125, 289, 316, 317*). M_S is estimated to decrease for $t_{Co} \leq (1-1.3)\,nm$ depending on the system (see chapter 4.2.2), which closely resembles the regime of the bending. Furthermore, the reduction of T_C in CoIr alloys is much more pronounced than in CoPt (c.f. Fig. 4-21 (b)). Thus, T_C is expected to drop below RT for thicker t_{Co} in samples containing CoIr than for CoPt, consequently rendering them paramagnetic. This is in accordance with the values observed for t_{on} for Pt\Co\Pt and Ir\Co\Ir. Finally, the interdiffusion zone width is known to be wider for the upper than the lower interface in Pt\Co\Pt (*127, 129, 296*) and it may therefore be assumed that less alloying with Ir occurs at the lower interface compared to the upper. Thus, t_{on} is expected for a lower t_{Co} in Ir\Co\Pt than for Pt\Co\Ir, which is in line with the experimental observations (see also discussion in chapter 5.1). Consequently, the interdiffusion at the interfaces is the most likely cause for the collapse of the anisotropies for $t_{Co} < 1\,nm$.

4.3.3.2 The dependence of K_{tot} on t_{NM} in multilayer samples

This section briefly addresses the dependence of K_{tot} on the thickness of the non-magnetic spacer layer t_{NM}. It is shown exemplary for Pt\(Co\Pt)$_N$ samples with $N = 8$, $t_{Co} = 0.8–2\,nm$, and $t_{NM} = 1–2\,nm$.

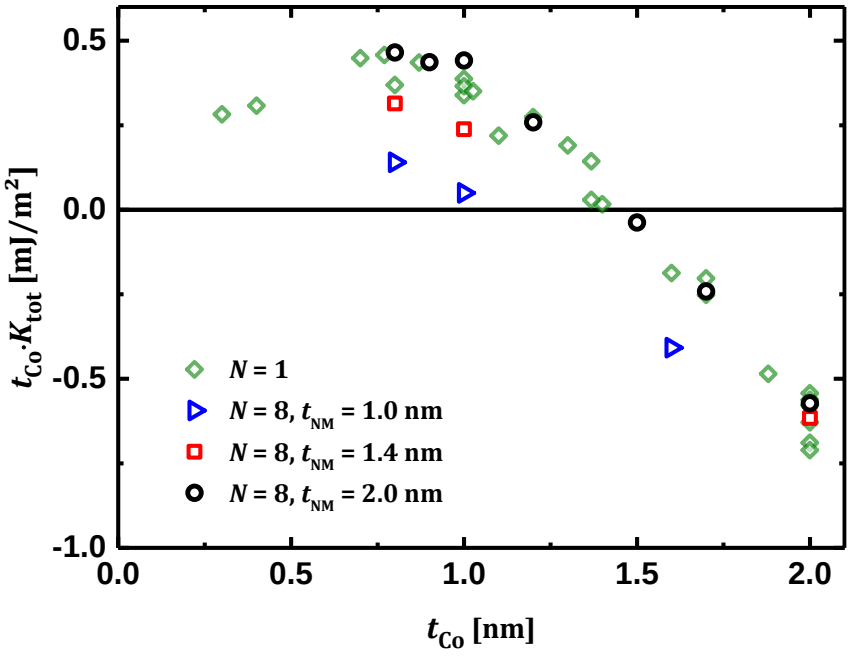

Figure 4-14: Co thickness dependence of K_{tot} for Pt\(Co\Pt)$_8$ with varying spacer layer thicknesses of t_{NM} = 1– 2 nm. Additionally, Pt\Co\Pt single layers are plotted to illustrate that for t_{NM} = 2 nm comparable K_{tot} in single and multilayers is obtained.

Fig. 4-14 shows $K_{tot} \cdot t_{Co}$ plotted over t_{Co} for samples[23] with t_{NM} = 1 nm (blue rectangles), 1.4 nm (red squares), and 2 nm (black circles). For comparison, the data for Pt\Co\Pt with N = 1 is shown as green diamonds. Despite the few available data points, a clear trend for the dependence of K_{tot} on t_{NM} is visible, especially in the bending region of t_{Co} = 0.8– 1 nm. At fixed t_{Co} the anisotropy constant K_{tot} is smallest for t_{NM} = 1 nm, largest for t_{NM} = 2 nm, with t_{NM} = 1.4 nm residing in-between. Due to the lack of data points available, a quantitative evaluation of K_{1S} and $K_{V,eff}$ in dependence of t_{NM} is not possible. However, from the shift of $K_{tot} \cdot t_{Co}$ to lower values along the ordinate for thinner t_{NM}, a reduction of the interface anisotropy $2K_{1S}$ can be deduced. This is in agreement with an earlier study in our group (*127, 147*) and literature (*137, 149, 313, 318*). The dependency on t_{NM} is commonly attributed to strain, roughness, and interdiffusion, namely the formation of a closed Pt layer with increasing t_{NM}.

For t_{NM} = 2 nm, the obtained values for K_{tot} coincide perfectly with the values obtained for N = 1. Thus, for $t_{NM} \geq$ 2 nm K_{tot} is independent of N. The earlier study in our group found an

[23] The samples for t_{NM} = 1 nm and 1.4 nm with t_{Co} = 0.8 – 1 nm were prepared and measured by A. Philippi-Kobs from the Coherent X-ray Scattering group at DESY.

equal K_{tot} for samples with t_{Co} = 0.8 nm and N = 1 and 4 for spacer layers of $t_{NM} \geq 3$ nm (*127*). The origin of the change to multilayers with smaller t_{NM} hosting comparable K_{tot} is unclear and beyond the scope of this thesis.

In the remaining sample systems, the dependence of K_{tot} on t_{NM} has not been investigated systematically. However, from Fig. 4-13 it is evident that K_{tot} is independent of t_{NM} in Ir\(Co\Ir)$_N$ for t_{Ir} = 1.75 nm. A similar conclusion can be drawn for (Pt\Co\Ir)$_N$ and (Ir\Co\Pt)$_N$ for $t_{NM} = t_{Pt} + t_{Ir}$ = (1 + 1.1) nm = 2.1 nm. Furthermore, two individual measurements in (Ir\Co\Pt)$_N$ with $t_{Pt} + t_{Ir}$ = (0.85 + 0.9) nm = 1.75 nm revealed anisotropies comparable to the respective single layer samples.

In conclusion, the remagnetization behavior of all four systems was in investigated for single- and multilayer samples and a rich variety of remagnetization curves was observed. Two methods were applied to extract the anisotropy constant K_{tot} from the remagnetization curves. The first method extracts K_{tot} by fitting a model to hard-axis remagnetization curves. Two prerequisites of the model are not met in the multilayer samples investigated in this thesis. First, all magnetic layer have to act as one single macro-spin, and second, coherent rotation being the dominant process. The second method is free of constraints and extracts K_{tot} from the difference of energy densities required to achieve saturation in easy and hard-axis remagnetization curves. It is shown that both methods yield comparable results for single layer samples but deviate for multilayers with $N \gtrsim 4$. Furthermore, the dependence of K_{tot} on t_{Co} was investigated in all four systems for single and multilayers. For multilayers, spacer layer thicknesses were chosen in the regime where comparable K_{tot} are obtained independent of N. In the three systems containing Pt (Pt\Co\Pt, Pt\Co\Ir and Ir\Co\Pt), three distinct thickness regimes with differing dependence of $K_{tot} \cdot t_{Co}$ on t_{Co} were observed with transition occurring around $t_{Co} \approx 1$ nm and 4 nm. For $t_{Co} \geq 4$ nm a linear dependency is found with very small $K_V \leq 0.09$ MJ/m³. Within the region of $t_{Co} = 1-4$ nm, a second linear regime is observed with a smaller slope indicating values of $K_V = 0.16-0.23$ MJ/m³. For $t_{Co} < 1$ nm a bending towards the abscissa is found, which is probably caused by interdiffusion at the interfaces. The relaxation of residual stress, which affects the anisotropy via magneto-elastic coupling, is probably the origin of the second transition around $t_{Co} \approx 4$ nm, and cannot be ruled out completely as the cause for the bending. For the system not containing Pt, (Ir\Co\Ir) only one linear regime for $t_{Co} > 1$ nm with $K_V \approx 0$ was found and a bending of $K_{tot} \cdot t_{Co}$ toward the abscissa for $t_{Co} < 1$ nm. The single transition here is also expected to originate from the interdiffusion at the

interfaces. The absence of the second linear regime in the absence of Pt is surprising, together with the fact that a single interface with Pt is sufficient to cause it. Structural investigations are required to link the transitions between regimes of differing dependence of the anisotropy on t_{Co} to structural changes. A corresponding propoasal for XRD measurements in ultrathin samples has been submitted to PETRA III.

4.4 The influence of interdiffusion on the exchange stiffness in ultrathin ferromagnetic layers

In this chapter, the thickness-dependent exchange stiffness parameter A_{ex} for ultrathin Co layers is extracted from domain-wall profiles. Subsequently, a model is introduced to describe the value of A_{ex} in dependence of the cobalt-layer thickness t_{Co} and the amount of interdiffusion at the interfaces.

A_{ex} is a phenomenological parameter in continuum micromagnetic theory, that reflects how rigidly two neighboring spins are coupled due to the exchange interaction. It can be related to microscopic parameters of the system, like the exchange integral in the Heisenberg model of ferromagnetism (see chapter 1.1.1). For unstrained cubic systems, e.g. fcc Co, A_{ex} is a scalar quantity (while it is a tensor in other systems, e.g. hcp Co) (*112, 319*). Understanding this parameter is crucial for the investigation of non-uniform spin alignments, like magnetic domains, domain walls, and skyrmions, as it relates to the energy cost involved in non-collinear orientations of neighboring spins.

A_{ex} has been investigated theoretically and experimentally for various systems, yet literature still reports a wide range of values, even for a simple and widely used material like bulk Co. Theoretical values reported for Co both, fcc and hcp lattices range from 14.5– 46 pJ/m (*320, 321*). The large variation is usually attributed to the complexity of ab initio calculations of excited states and the required approximative schemes involved (*292*). Experimentally the parameter is very difficult to access and can only be measured indirectly. Measurement schemes are based on one of three general approaches (*319*): first, relating the exchange energy to thermal excitation destroying the magnetic order; second, measurements of the spin-wave stiffness or related properties; and third, measurements of non-collinear spin states, e.g. the domain wall energy or width. For bulk Co, the reported values depend on the crystal structure[24]. The values for hcp Co range from 24.8– 33.1 pJ/m (*292, 315, 322–331*), with two studies reporting deviating values of 15.5 pJ/m (*332*) and 18.9 mJ/m²

[24] Most of the cited studies report the spin wave stiffness D_{Spin} instead of A_{ex}. One parameter can be converted into the other using Eq. 1-4, with $M_S(T = 300\,K) = 1.44\,MA/m$ (*125*), $g_{hcp} = 2.18$ (*125*) and $g_{fcc} = 2.14$ (*279*).

(*333*). For fcc bulk Co, A_{ex} is reported to 19.8– 23.3 pJ/m (*125, 292, 325, 327*), with one study reporting 27.1 pJ/m (*320*). To date, values measured by neutron scattering are considered to give the best estimate available (*292, 334*). Therefore, in the following the bulk values for $A_{ex,\,hcp}$ = 28 pJ/m and $A_{ex,\,fcc}$ = 23.3 pJ/m (*327*) from neutron scattering data will be used.

Only a very limited number of studies on A_{ex} in Co thin films below 10 nm are reported in literature (*298, 303, 304, 335–337*) using spin-polarized electron energy loss spectroscopy (SP-EELS) or Bloch's $T^{3/2}$ law at low temperatures. Neutron scattering experiments are not yet feasible due to the weak interaction and thus long penetration depths of neutrons in matter. This very important thickness regime is addressed in the following.

4.4.1 Exchanges stiffness constant in thin films

In this chapter, A_{ex} is determined from the domain wall width δ_w measured by XHM in a $(Pt_{1\,nm}\backslash Co_{0\text{-}2\,nm}\backslash Ir_{1.1\,nm})_6$ wedge sample.

The width of a Bloch[25] wall δ_w depends on two parameters, the exchange stiffness constant A_{ex} and the total uniaxial anisotropy K_{tot} (*188, 189*) (see Eq. 1-33). Domain walls in Co are typically some few nm wide, depending on the strength of K_{tot} and A_{ex} in the sample. For A_{ex} = 10 pJ/m and K_{tot} = 500 kJ/m³, values frequently used for the simulation of skyrmions in micromagnetics, the domain wall width is 14 nm. Using the bulk value for the exchange in fcc Co, 23.3 pJ/m (*325*), and an anisotropy in the vicinity of the SRT of 100 kJ/m³, one obtains δ_w = 47 nm. Therefore, a high spatial resolution is necessary to image the domain wall with sufficient accuracy. As shown in chapter 3.3, XHM provides sufficient resolution (12 nm) to resolve domain walls for significant parts of the parameter space.

In the experiment[26], a $(Pt_{1\,nm}\backslash Co_{0\text{-}2\,nm}\backslash Ir_{1.1\,nm})_6$ sample with wedge-shaped Co layers is used in order to access a wide range of K_{tot}. Prior to the measurement, the sample was demagnetized by an exponentially damped oscillating out-of-plane magnetic field starting from ± 1 T, transferring

[25] With sufficient iDMI present, which is likely the case in the discussed sample, the Bloch wall turns into a Néel wall. The difference in widths between both, however, is less than 1 % and therefore neglected (*37*).

[26] The experiment was performed at the P04 beamline (*245*) at Petra III, using a photon energy of 778 eV (cobalt L_3 absorption edge) and a 50 µm wide exit slit. A 100 µm-sized pinhole was inserted 0.55 m upstream of the sample, in the converging beam after the refocusing mirror. The pinhole shapes the horizontally extended component of the beam down to 15 µm at the sample position, matching its vertical size. In this configuration, the beam has a lateral coherence length of 5.8 × 6.5 µm² (*208, 249*).

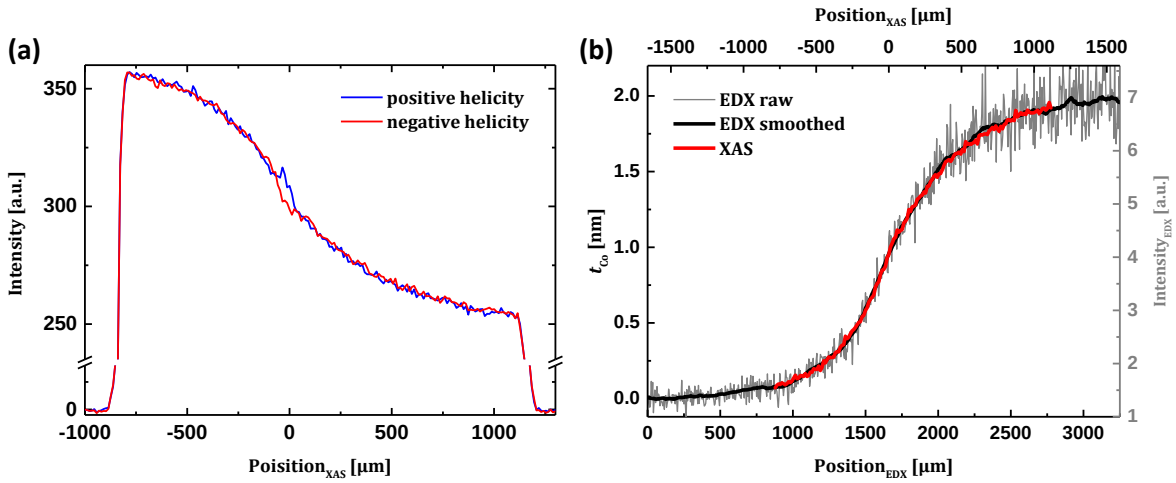

Figure 4-15: (a) X-ray transmission profiles along the $(Pt_{1\,nm}\backslash Co_{0\text{-}2\,nm}\backslash Ir_{1.1\,nm})_6$ with positive (blue) and negative (red) helicity taken at a photon energy of 778 eV. The transmission profiles are taken by scanning the sample with respect to the beam and measuring the transmitted intensity with a photodiode. The resolution is limited by the beam size in the sample plane to ~15 µm. The opening between the scans around -50 µm indicates the presence of perpendicular domains larger than 15 µm, e.g. the resolution of the experiment. (b) EDX (Co L_3 peak) intensity profile of the same sample with a primary electron energy of 8 keV (grey). The smoothed profile (black) and normalized to the known final thickness of 2 nm. The X-ray transmission profiles, shown in (a), are transformed by taking the logarithm and averaging into a dichroism-free X-ray absorption profile (red). Subsequently, the X-ray absorption profile is aligned to the smoothed and normalized EDX profile, revealing the cobalt thickness t_{Co} in dependence of the position on the wedge.

the sample as close as possible into the magnetic ground state. Furthermore, the permanent magnets of the microscope setup were removed, ensuring the absence of external fields.

The cobalt thickness t_{Co} as function of the position on the wedge , and subsequently the effective anisotropy K_{tot}, are calibrated similar to (*208*). A 100 µm pinhole is mounted just in front of the sample, to block off-axis light. The spatial resolution is limited by the beam size on the sample to ~15 µm. Fig. 4-15 (a) shows the transmitted X-ray intensity for positive and negative helicities measured along the wedge using a photo diode behind the sample. Following the Beer-Lambert law (see Eq. 1-37), taking the logarithm of the transmission profiles converts them into X-ray absorption profiles (XAS). Averaging of both helicities eliminates any dichroic contribution pre- sent due to domains, e.g. visible around -50 µm. As the total width of the wedge of 2.5 mm is larger than the 2 mm wide membrane window, the plateaus corresponding to t_{Co} = 0 and 2 nm are not fully

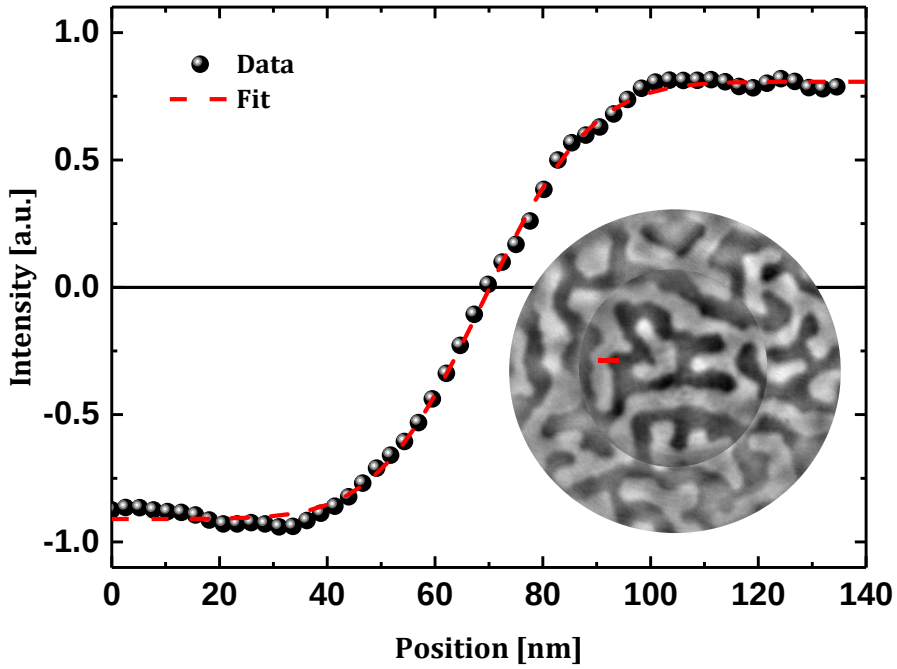

Figure 4-16: Determination of a domain wall width of 35 nm in the $(Pt_{1\,nm}\backslash Co_{0\text{-}2\,nm}\backslash Ir_{1.1\,nm})_6$ sample at t_{Co} = 1.41 nm. The graph shows a line profile along the red line indicated in the inset. The black dots are the experimental values; the dashed red line is the fit of a Gaussian error function. Shown in the inset is an XHM image of the perpendicularly magnetized sample exhibiting a maze domain pattern with an average domain size of d_{avg} = 104 nm. The fit of a Gaussian error function to the domain wall profile yields $\sigma_{w,exp}$ = (15.8 ± 0.3) nm. After deconvolution with the experimental resolution, a domain wall width of δ_w = (35 ± 2) nm is obtained.

accessible. Thus, a reference profile is needed for the final thickness calibration. This reference profile is acquired by energy dispersive X-ray spectroscopy (EDX) (*338*) in a SEM. Fig. 4-15(b) shows the raw EDX profile of the Co L_3 peak in grey. The smoothed curve in black is normalized to the known thickness of the wedge, t_{Co} = 0– 2 nm. Subsequently, the XAS profile (red) is aligned to the EDX profile, revealing the local t_{Co} in dependence of the position on the wedge during the imaging experiment.

Along the wedge, images of the equilibrium domain configuration were acquired by XHM using the same holographic mask as for the measurement of the experimental resolution (chapter 3.3). For each image, 100 individual acquisitions were summed per photon helicity with an illumination time of 1 s per acquisition. The inset of Fig. 4-16 shows the XHM image for t_{Co} = 1.41 nm. The image has a diameter of about 2 µm with a pixel size of 5.2 × 5.2 nm². At this thickness, the sample exhibits a maze domain pattern with an average domain size of d_{avg} = 104 nm. Fig. 4-16 shows a

line profile across a domain wall, as indicated by the red line in the inset. Fitting a Gaussian error function to the profile yields $\sigma_{w,exp}$ = (15.8 ± 0.3) nm. This value, however, is the convolution of the domain wall with the experimental resolution $2\sigma_{res}$ = (12 ± 3) nm:

$$\sigma_w = \sqrt{{\sigma_{w,\,exp}}^2 - {\sigma_{res}}^2}. \qquad \text{Eq. 4-8}$$

After correcting for the resolution, a domain wall width of $\delta_w = 2.4 \cdot \sigma_w$ = (33 ± 2) nm is obtained. By statistically evaluating several domain wall profiles across the image, an average domain wall width of $\delta_{w,avg}$ = (33 ± 6) nm is found for t_{Co} = 1.41 nm. From this value the exchange is calculated using Eq. 4-8 and K_{tot} = (100 ± 23) kJ/m³ (see chapter 4.3.3), yielding A_{ex} = (11 ± 4) pJ/m. Analogous evaluation for t_{Co} = 1.28 nm results in $\delta_{w,avg}$ = (25 ± 5) nm and A_{ex} = (13 ± 6) pJ/m, with K_{tot} = (212 ± 24) kJ/m³. The relatively large uncertainties stem mainly from the uncertainty of the domain-wall-width.

The general reduction of A_{ex} compared to the bulk fcc value A_{ex} = 23.3 pJ/m is in accordance to other studies concerning DC-sputtered thin film samples with t_{Co} < 2 nm (*298, 303, 304*). The reported values are shown in Fig. 4-17. Legrand et al. found values of $A_{ex} \approx$ 10 pJ/m for t_{Co} = 0.8– 1 nm (golden triangles) in Pt\Co\Ir and Ir\Co\Pt, determined from the measurement of T_C (*302*). Metaxas et al. (*298*) reported a gradual reduction of A_{ex} in Pt\Co\Pt sandwiches from 22 to 14 pJ/m (orange diamonds) upon reducing t_{Co} from 0.8 to 0.5 nm, also deduced from T_C. Shepley et al. (*303*) also reported a reduction of A_{ex} from 28 to 12 pJ/m (blue squares) for t_{Co} = 1.1 to 0.56 nm in Pt\Co\Ir sandwiches, using Bloch's $T^{3/2}$ law (measuring the variation of M_S at low T). Zeissler et al. (*304*) deduced A_{ex} = 12– 15 pJ/m, by the same method for $(Pt_{2.3\,nm}\backslash Co_{0.7\,nm}\backslash Ir_{0.5\,nm})_N$ samples with N = 1– 10 (green triangle). The microscopic origin of the reduced exchange stiffness with decreasing t_{Co} is not addressed in any of the publications.

The exchange-stiffness values extracted from domain wall widths in this work are comparable to the ones found in Legrand's study, but lower compared to the remaining studies for DC-sputtered samples. A difference in structural properties between the samples investigated in each study could cause deviations of the material parameters. I.e. properties like the crystal structure, lattice strain or interface quality are not addressed in either study. For instance, the value reported by Shepley et al. of A_{ex} = 28 pJ/m for t_{Co} = 1.1 nm exceeds the value for bulk fcc Co by 20 %, but would fit to bulk hcp Co. Further, Metaxas et al. compare the deduced values of A_{ex} to bulk hcp Co. Both crystalline structures can be stabilized in layered systems at RT (*126*), with an expected transition from fcc to

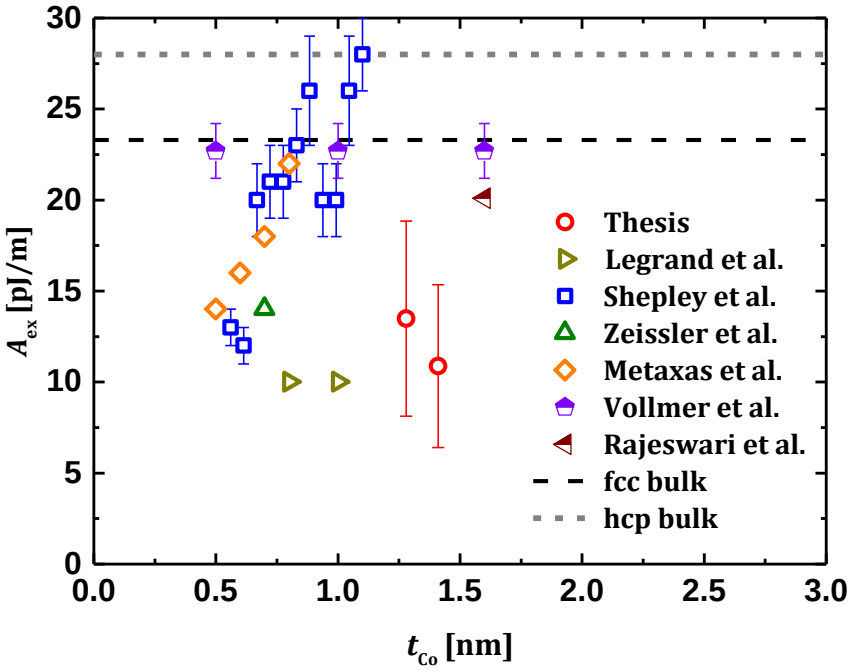

Figure 4-17: Summary of experimental values for A_{ex} at RT in ultrathin Co-layers for single and multilayer samples obtained in this thesis (red circles) and found in literature. Half-filled symbol indicate samples prepared by MBE or e-beam evaporation (*335, 336*), while open symbols are DC-sputtered (*298, 302–304*). All DC-sputtered samples are (Pt\Co\Ir), except for Metaxas's, which are for Pt\Co\Pt. Legrand's study also includes Ir\Co\Pt. The dotted grey line represents the bulk value for hcp Co and the dashed black line for fcc Co, both obtained from neutron scattering (*327*).

hcp structure for $t_{Co} > 1.6$ nm (*339, 340*). However, the investigated thicknesses are below this threshold, making an fcc structure very likely. Further, XRD investigations within this working group indicate an fcc structure without a transition to hcp up to $t_{Co} = 50$ nm (*129, 130*). The non-occurrence of the transition could be caused by the pronounced (111) texture induced by the ECR-grown buffer layer. Finally, the investigations of M_S (chapter 4.2) and K_{tot} (chapter 4.3.3) reveal similar values and behavior for the samples in this thesis and the studies, hinting at comparable properties of the samples.

On the other hand, the models used to derive A_{ex} can be the origin of the discrepancy (the interested reader is referred to (*292*) for a more detailed analysis). The two models are briefly discussed in the following:

Metaxas et al. used a mean-field model for two-dimensional (monoatomic) layers including anisotropy to estimate the exchange integral J from T_C (*341*):

$$T_C = \frac{4\pi\,(S+1)}{3}\frac{2\,J\,S}{\ln(8\pi\,J\,S/\Delta')}, \qquad \text{Eq. 4-9}$$

with the atomic spin S, the Bohr magneton μ_B, and the gap opened in the spin-wave spectrum by the anisotropy Δ'. In turn, J is put into Eq. 1-4 to obtain A_{ex} for T = 0 K. The investigated samples, however, consist of 2.5– 4 ML, thus are three-dimensional. The applicability of the model is therefore questionable. Furthermore, within a single ML, every atom has six instead of 12 next-neighbors, thus requiring alterations of the model. Within mean-field theory, a relation between A_{ex} and T_C can also be derived for three-dimensional samples (compare Eq. 1-4) (*118*):

$$A_{ex}(T=0) = \frac{a^2 k_B}{8 g \mu_B}\frac{T_C}{(S+1)} M_S(T=0), \qquad \text{Eq. 4-10}$$

with the lattice spacing parameter a, the Landé-Factor g, and the Boltzmann constant k_B. Stoner excitations are assumed as the sole cause for the loss of magnetic order. The impact of spin waves with short-wavelength is disregarded. Second, ultrathin Co films experience strain (see discussion in chapter 4.3.3) resulting in a change of the lattice spacing parameter a from bulk values (*127*). With the proportionality of A_{ex} to the square of a in Eq. 4-10, strain could cause considerable deviations. Third, an enhancement of the orbital moment in ultrathin films induced by the symmetry breaking at interfaces may lead to a sizeable increase of the Landé-factor g, which is also used in Eq. 4-10, resulting in a reduction of A_{ex} (*292*). Increased values of up to g = 2.46 are reported for ultrathin Pt\Co\Pt and Pt\Co\Au samples (*342*).

In the second approach, D_{Spin} is derived using Bloch's $T^{3/2}$ law from measurements of the variation of M_S at low temperatures T (*118, 292, 343*):

$$\frac{M_S(T)}{M_S(T=0)} = 1 - \frac{g\mu_B\eta}{M_S(T=0)}\left(\frac{k_B T}{D_{Spin}(T=0)}\right)^{\frac{3}{2}}. \qquad \text{Eq. 4-11}$$

By inserting D_{Spin} into Eq. 1-4, A_{ex} for T = 0 K is obtained. However, the method is less simple than this expression suggests. The necessary magnetic field opens an energy gap in the spin wave dispersion that needs to be taken into account and leads to a more complicated version of Eq. 4-11 (*344*). Estimates from the simple $T^{3/2}$ expression are generally in poor agreement with neutron data (*292*). Further, M_S depends on other terms than spin waves such as defects, magnetic susceptibility, anisotropy distribution in polycrystalline samples and inclusions. In addition, the previously made point on the Landé-factor is applicable here as well, however with opposite effect as it would further increase A_{ex}. Finally, Nembach et al. (*343*) pointed out that the prefactor η

depends on the magnon density, and thus the thickness of the sample. Short spin waves with energies higher than $k_B T$ are populated following a Boltzmann-like factor $\exp(-D_{Spin}\mathbf{k}/k_B T)$. Reducing the samples dimension along a quantization axis freezes all spin-wave modes along that direction, except for the lowest order excitation that remains highly populated, the FMR mode. This results in an enhancement of η. For $t_{Co} < 10$ nm η increases considerably from the value for bulk material. I.e. for $t_{Co} = 1$ nm, η increases by a factor of ~5, thus A_{ex} by ~3.3. Whether the thickness dependence has been considered in the studies of Shepley et al. (*303*) and Zeissler et al. (*304*) is unclear[27], but the papers suggest the use of the bulk value. However, a correction for the thickness would only further increase the values of A_{ex}, thus exceeding the bulk value for fcc Co even further. A rescaling of A_{ex} to RT is not addressed either (*120*).

In contrast, a decrease of A_{ex} for ultrathin t_{Co} has not been observed for epitaxial grown samples. Vollmer et al. (*335, 336*) measured in molecular beam epitaxy (MBE)-grown fcc Co films with t_{Co} = 1.6, 1 and 0.5 nm on Cu(001), $A_{ex} = (22.7 \pm 1.5)$ pJ/m (purple pentagons in Fig. 4-17) employing spin-polarized electron energy loss spectroscopy (SP-EELS). These values are in very good agreement with the bulk value. Considering the linear relation between and A_{ex} and the coordination number Z (= 12 for fcc lattices), which is the number of next neighbors in the lattice, (see Eq. 1-4) (*81*), the resemblance is surprising. By rescaling the exchange stiffness according to the reduced Z at the interfaces ($Z = 9$, see chapter 4.4.2), A_{ex} =18.5, 21, and 21.8 pJ/m is expected for t_{Co} = 0.5, 1, and 1.6 nm respectively. However, considering the spread of reported bulk values, this discrepancy seems negligible. Rajeswari et al. (*345*) also reported SP-EELS investigations on epitaxial 1.6 nm fcc Co on Cu(001), finding A_{ex} = 20.1 pJ/m (brown triangle in Fig. 4-17). This value is in reasonable agreement with fcc bulk Co.

The different behavior for ultrathin films prepared by the different preparation methods most likely stems from structural differences caused by just these (*126*). MBE-grown samples are single crystalline; sputtered samples are polycrystalline. However, for hcp Co comparable values where measured by neutron scattering for single crystalline samples (*325–327*) as well as polycrystalline ones (*323, 324*), excluding the crystallinity as the cause. Another important difference is the sharpness of the interfaces. Preparation by MBE results in atomically flat interfaces with little interdiffusion; sputtering causes interdiffusion zones of several monolayers due to the higher kinetic energy of the atoms (*128, 129*). Such interdiffusion zones cause a reduction of the average coordination number

[27] Both authors were contacted, but did not reply.

and thus of A_{ex} (compare Eq. 1-4). This effect will be predominant in thin samples where the interdiffusion zones make up most of or the entire sample. Interdiffusion seems the ideal explanation for the reported behavior. In the following chapter, a model relating interdiffusion and A_{ex} is derived.

4.4.2 Modeling the exchange stiffness in the presence of interdiffusion

In the prior chapter, interdiffusion zones at interfaces have been identified as the most probable cause for the different reported values of A_{ex} for ultrathin samples grown by MBE and sputtering. In this chapter, a model is developed to estimate a scaling of the exchange stiffness with the width of interdiffusion zones. It is almost identical to one developed by Devolder et al. (*346, 347*) for estimating the number of next-neighbors. The model is tested by comparing its predictions to published values for CoPt alloys with varied compositions and ultrathin Co layers found in literature.

The exchange stiffness is linearly proportional to the number of next-neighbor Co atoms Z (*81, 118, 292*) (see Eq. 1-4). In hcp and fcc lattices $Z_{bulk} = 12$. Fig. 4-18(a) shows an fcc lattice with each colored plane being a (111) plane in the closed-packed stacking order **ABC**. The lattice plane spacing for bulk Co is $d_{Co} = 0.2035\,\text{nm}$ (*129, 144*) at RT and the distance between two atoms $a/\sqrt{2}$ with $a = 0.354\,\text{nm}$ (*292*). The black sphere represents a Co atom with its total 12 next neighbors in the crystal. The six red spheres are the next neighbors in the same lattice plane; the three blue and green spheres represent the next-neighbors in the adjacent planes.

In a prefect bulk crystal, all 12 colored spheres are Co atoms, resulting in bulk fcc $A_{ex,\,bulk} = 23.3\,\text{pJ/m}$ acting on the black Co atom. If it is located on a perfect interface to a non-
In a prefect bulk crystal, all 12 colored spheres are Co atoms, resulting in bulk fcc $A_{ex,\,bulk} = 23.3\,\text{pJ/m}$ acting on the black Co atom. If it is located on a perfect interface to a non-magnetic material, the green or blue spheres are non-magnetic atoms reducing Z to 9. Using Eq. 1-4, the exchange stiffness for Co atoms at interfaces is reduced to $A_{ex,\,int} = 9/12\ A_{ex,\,bulk}$. A similar effect occurs when interdiffusion is considered. Within the width of the interdiffusion zone (σ) around the interface, the non-magnetic material statistically replaces Co atoms. If κ Co atoms are replaced, the exchange acting on the considered Co atom is $A_{ex,\,diff} = A_{ex,\,bulk} \cdot (12 - \kappa)/12$. The effective exchange stiffness $A_{ex,\,eff}$ of a sample is obtained by averaging over all Co. For ultrathin samples and broad interdiffusion zones, a considerable reduction of $A_{ex,\,eff}$ is expected.

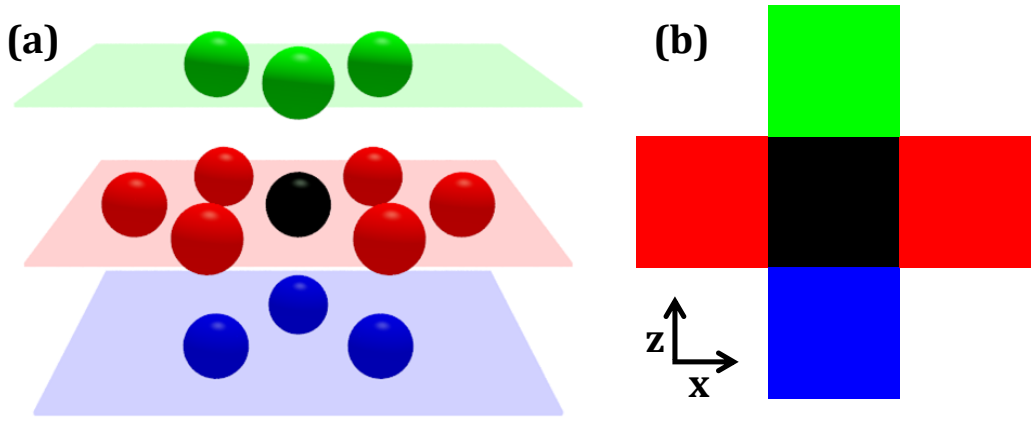

Figure 4-18: (a) Visualization of an fcc lattice with closed packed stacking with each color being a (111) lattice plane. The black sphere represents one atom with its 12 next-neighbors; six within the same lattice plane (red spheres) and three in adjacent planes (blue and green spheres). (b) Projection of the three-dimensional lattice onto a two-dimensional square model. The 12 next-neighbor atoms are split into four groups of three each with respect to the black atom in the center. The first (second) group consists of the three blue (green) spheres in the plane below (above) the black one. The third (fourth) is made up of the three red spheres left (right) of the black one.

In order to model the influence of an interdiffusion zone on the number of next-neighbors (*346*), first the sole influence of perfect interfaces ($\sigma = 0\,\mathrm{nm}$) in a layered structure is considered. A layered sample, consisting of z lattice planes with the spacing $d = 0.2\,\mathrm{nm}$, can be described by a one-dimensional array $X[z](\sigma)$[28] with z entries. Thus, a layer of $t = 1.4\,\mathrm{nm}$ consists of seven lattice planes. The value for each entry represents the probability of a Co atom occupying the lattice positions within the plane. For perfect interfaces, the probability is one within a Co layer and zero outside of it. The average coordination number in each lattice plane $Z_{\mathrm{avg}}[z](\sigma)$ is now obtained by the probability of the central atom itself being a Co atom, times the sum of the probabilities to have a Co atom occupy one of the twelve next-neighbor positions in Fig. 4-18(a) (*346*):

$$Z_{\mathrm{avg}}[z](\sigma) = X[z](\sigma) \cdot \left(3X[z-1](\sigma) + 6X[z](\sigma) + 3X[z+1](\sigma) \right). \qquad \text{Eq. 4-12}$$

$Z_{\mathrm{avg}}[z](\sigma = 0\,\mathrm{nm})$ is 9 for the interface and 12 for the "bulk" lattice planes, otherwise 0. The average coordination number per Co atom $Z_{\mathrm{avg}}(\sigma)$ is obtained by summing $Z_{\mathrm{avg}}[z](\sigma)$ over z and normalizing to the total amount of Co in the sample:

[28] In this chapter, square brackets are used for the coordinates in arrays while round brackets imply dependencies.

$$Z_{\mathrm{avg}}(\sigma) = \frac{\sum_z Z_{\mathrm{avg}}[z](\sigma)}{\sum_z X[z](\sigma)}\,. \qquad \text{Eq. 4-13}$$

The sample investigated in the previous chapter consists of $N = 6$ Co layers with $t_{\mathrm{Co}} = 1.4\,\mathrm{nm}$ each, corresponding to seven lattice planes, separated by five layers of a non-magnetic material of $t_{\mathrm{NM}} = 2\,\mathrm{nm}$ (it actually has $t_{\mathrm{NM}} = 2.1\,\mathrm{nm}$, but the model is limited to integer multiples of d) or 10 lattice planes. Underneath the first Co layer is a 5 nm-thick layer of non-magnetic material and on top of the sixth is a non-magnetic layer of 3 nm. The array $X[z](\sigma = 0\,\mathrm{nm})$ representing this sample is shown in Fig. 4-19(b) as black line. Evaluating Eq. 4-13 yields $Z_{\mathrm{avg}}(\sigma = 0\,\mathrm{nm}) = 11.14$. Subsequently, the effective exchange stiffness is $A_{\mathrm{ex}}(\sigma = 0\,\mathrm{nm}) = 21.64\,\mathrm{pJ/m}$, using:

$$A_{\mathrm{ex}}(\sigma) = \frac{Z_{\mathrm{avg}}(\sigma)}{Z_{\mathrm{bulk}}} A_{\mathrm{ex,bulk}}. \qquad \text{Eq. 4-14}$$

This value is 93 % of the bulk value, implying only a small influence of the interface for layers of $t_{\mathrm{Co}} = 1.4\,\mathrm{nm}$. When interdiffusion is considered, the sharp transitions from the Co layer to the adjacent non-magnetic layer is smeared out over the width of the interdiffusion zone σ. Co is statistically intermixed with the second material, resulting in a gradual change of the probability for Co to occupy a lattice position across the interface (*346*). A Gaussian error function can describe this gradual transition. Thus the product of two, one for each interface, describes the probability distribution across one Co layer including interdiffusion zones(*346, 347*):

$$X_N[z](\sigma, z_N, t_{\mathrm{Co}}) = \frac{1}{4}\left(1 + \mathrm{erf}\left(\frac{z - z_N}{\sqrt{2}\cdot\sigma}\right)\right)\cdot\left(1 - \mathrm{erf}\left(\frac{z - z_N + t_{\mathrm{Co}}}{\sqrt{2}\cdot\sigma}\right)\right), \qquad \text{Eq. 4-15}$$

with z_N, the position of the lower interface of the Nth Co layer.

For very thin layers and broad interdiffusion zones, the two error functions overlap significantly and X_N reaches no plateau. The amount of Co represented by X_N is then less than t_{Co}, making a normalization neccessary:

$$X_{N,\mathrm{norm}}[z](\sigma, z_N, t_{\mathrm{Co}}) = \frac{t_{\mathrm{Co}}}{\sum_z X_N[z](\sigma, z_N, t_{\mathrm{Co}})}\cdot X_N[z](\sigma, z_N, t_{\mathrm{Co}}). \qquad \text{Eq. 4-16}$$

A sample of N layers then follows to:

$$X[z](\sigma, z_N, t_{\mathrm{Co}}) = \sum_N X_{N,\mathrm{norm}}[z](\sigma, z_N, t_{\mathrm{Co}})\,. \qquad \text{Eq. 4-17}$$

Fig. 4-19(b) shows $X[z](\sigma)$ for the previously described sample for perfect interfaces in black, and with interdiffusion in red ($\sigma = 0.5\,\mathrm{nm}$) and blue ($\sigma = 1\,\mathrm{nm}$). Compared to the distribution for

perfect interfaces, the layers are broadened and non-cohesive without a plateau of 100 % Co. For the blue line, indicating σ = 1 nm, the distinction between magnetic and non-magnetic layer ceases to be valid, the distribution rather resembles an alloy. Yet the total amount of Co is identical in all cases.

For σ = 0.5 nm, the average coordination number is reduced down to Z_{avg} = 7.62, resulting in A_{ex} = 13.99 pJ/m. X-ray diffraction (XRD) measurements revealed such an interdiffusion zone width for Pt\(Co\Pt)$_N$ samples prepared within our group (*128, 129*)[29]. This value is in reasonable agreement with A_{ex} = (11 ± 4) pJ/m that was measured in the previous chapter.

Fig. 4-19(a) is visualizing the impact of σ on ultrathin layers. The three-dimensional lattice is projected onto a two-dimensional square model, representing only one in-plane direction and the surface normal. For this, the 12 next-neighbors are split into four groups with respect to the black Co atom in the center of Fig. 4-18(a). The first (second) group consists of the three blue (green) spheres in the plane below (above) the black one. The third (fourth) is made up of the three red spheres left (right) of the black one. Fig. 4-18(b) illustrates the resulting 2D lattice. The 2D-array is filled by generating a random number $\in$ (0, 1) for each lattice position. If the random number is smaller than $X[z](\sigma)$, the entry is set to one (Co) and otherwise zero (no Co). The reducing effect of interdiffusion on the coordination is obvious. Next neighbors are missing more and more throughout the whole layer as σ increases and Co is appearing within the non-magnetic layer. At even higher sigma, the initially layered structure rather resembles an alloy.

Within this model, the exchange stiffness can be evaluated for various t_{Co} and σ (also t_{NM} and N[30]). Fig. 4-20 shows A_{ex} plotted over t_{Co} for σ = 0, 0.2, 0.5 and 1 nm. The dots represent the data points for evaluated thicknesses with the lines being linear interpolations in-between. For all σ, A_{ex} vanishes for t_{Co} = 0 nm and asymptotically reaches the bulk value for thick Co layers. In the intermediate region of t_{Co} = 0– 5 nm, A_{ex} is highly susceptible to σ. For σ = 0 nm (black), A_{ex} is almost constant down to t_{Co} = 0.8 nm (~85% of bulk value), where it starts to rapidly decline. For σ > 0 nm, the constant regions end at higher t_{Co}, smearing out the decrease down to zero.

[29] XRR measurements showed that the upper Co\Pt interface is wider than the lower Pt\Co. XRD, however, only reveals the average of both interfaces. Further, no experimental data involving Ir is available thus far. The presence of CoIr alloy at the interfaces in Ir\Co\Ir samples was shown by negative AMR ratios for thin samples (*307*), which is solely reported for alloys of Ir with 3d transition metals, i.e. Co (*348*).

[30] For σ < 0.7 nm and t_{NM} > 1.4 nm, the obtained values for A_{ex} in single and multilayers differ less than 2 %.

In chapter 4.2.2, it is shown that the sample systems become paramagnetic below a respective thickness t_{on}, where the Curie temperature drops below RT. Within the model, this influence is so far neglected. For alloys, the dependency of the Curie temperature on the Co content is well known and shown in Fig. 4-21(b) for CoIr and CoPt alloys. T_C drops below RT at $X_{cut} \approx 0.15$ for CoPt (*125, 289*) and 0.6 for CoIr (*316, 317*). The influence of T_C on the exchange stiffness can be estimated by excluding entries of $X[z](\sigma)$ that represent alloys with lower concentration than X_{cut}:

$$X[z](\sigma) = 0 \text{ for } \frac{X[z-1] + 2X[z] + X[z+1]}{4} < X_{cut}\,. \qquad \text{Eq. 4-18}$$

Thus, for large X_{cut} and thin Co layers, $X[z](\sigma)$ does not exceed X_{cut} at all, creating an offset along the t_{Co}-axis. The effect is shown in Fig. 4-20 for three different values of X_{cut}. The data shown in

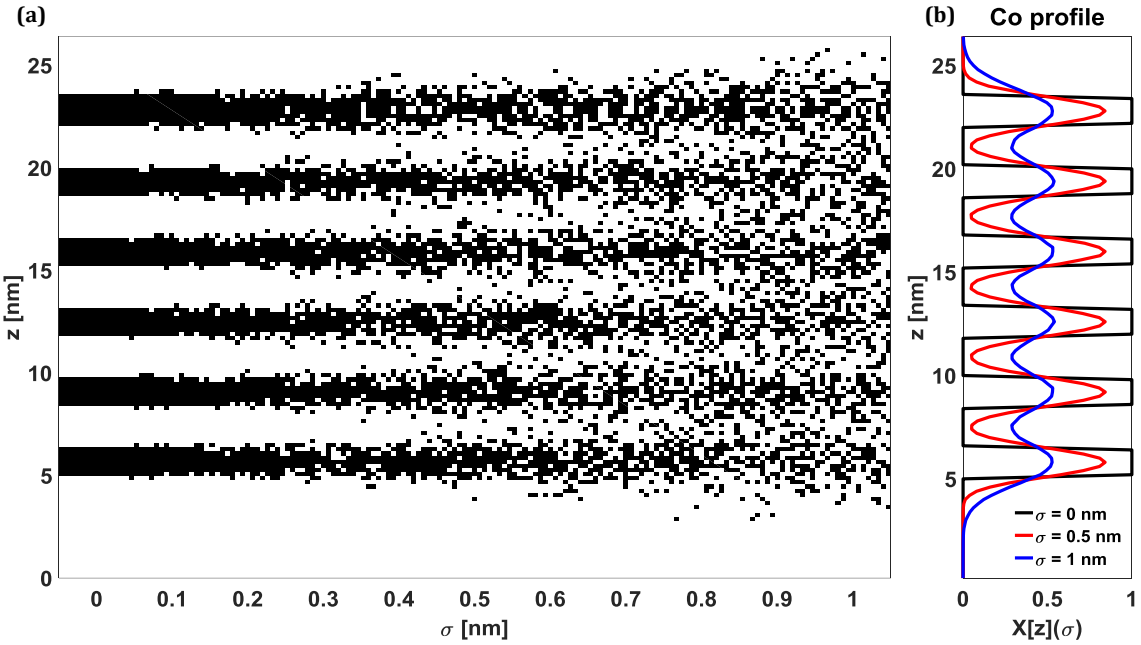

Figure 4-19: (a) Visualization of the impact of interdiffusion widths σ on a sample with $N = 6$ Co-layers ($t_{Co} = 1.4$ nm) sandwiched between non-magnetic spacer layers ($t_{NM} = 2$ nm). The projection (c.f Fig. 4-18(b)) is calculated from $X[z](\sigma)$, the probability of a Co atom occupying a lattice position in the lattice plane z. A Co atom occupying a lattice position is indicated in black; white indicates the non-magnetic material. σ is varied in discrete steps of 0.1 nm. With increasing σ, the disorder of the lattice increases and the resemblance to an alloy increases. (b) z is plotted over $X[z](\sigma)$ for $\sigma = 0$, 0.5, and 1 nm (black, red and blue line). For $\sigma = 0$ nm, a sample with sharp interfaces, the probability distribution resembles a rectangular function with probabilities of either 0 or 1. For $\sigma = 0.5$ and 1 nm, the sharp transitions from a Co to a non-magnetic layer are smeared out and no plateaus with a probability of 0 or 1 are present.

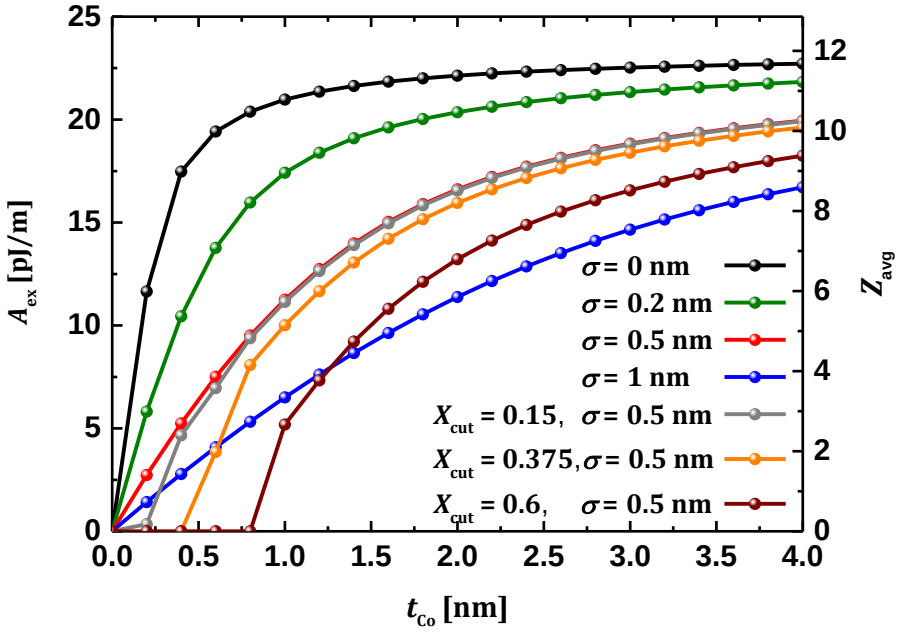

Figure 4-20: Co-thickness dependence of the exchange stiffness constant A_{ex} obtained from the model for various interdiffusion zone widths σ and values for X_{cut}. The dots represent calculated values; the lines are guides to the eye. The right ordinate indicates the average coordination number Z_{avg}.

grey (brown) represent X_{cut} = 0.15 (X_{cut} = 0.6) for CoPt alloy (CoIr alloy) in combination with σ = 0.5 nm, the data shown in orange is for X_{cut} = 0.375, which is the average between CoPt and CoIr. X_{cut} = 0.15 yields a small value of A_{ex} = 0.33 pJ/m for t_{Co} = 0.2 nm, thus an offset of 0.2 nm; X_{cut} = 0.375 (X_{cut} = 0.6) yields zero exchange in-between t_{Co} = 0.4– 0.6 nm (t_{Co} = 0.8– 1 nm). A comparison to experimentally obtained offsets follows later in this chapter.

By using this model, the exchange stiffness can be easily calculated from the sample geometry, one directly measureable parameter σ quantifying the width of the interdiffusion zone, and the bulk value for the exchange stiffness. However, in order to test the validity of the model, the predicted A_{ex} has to be compared to values found in literature for alloys and thin films.

Alloys are inherently disordered systems. In layered structures, on the other hand, disorder is usually an unwanted byproduct with the extent of it not sufficiently accessible. For models addressing disorder, alloys present the perfect test case. In Co1-*x*Pt*x* alloys, $X[z]$ is constant throughout the sample and independent of σ, thus Eq. 4-13 is simplified to $Z_{avg} = 12 \cdot (1-X)$. Harzer et al. (*315*) reported a Brillouin light scattering (BLS) study on polycrystalline fcc (111) Co1-*x*Pt*x* alloys with 43, 60, 74, and 75 at.% Pt content. The samples was grown by physical vapor deposition (PVD) on

a 4 nm Pt buffer layer on top of etched Si_3N_4 by co-evaporating both materials. The sample with 75 at.% deviates in the preparation from the others, as it was grown by subatomic layering and no buffer layer deposited prior to the alloy. The obtained values for A_{ex} are plotted as red circles in Fig. 4-21(a) over the Pt content of the alloy[31]. Further, the values predicted by the model are shown as a black line. The model reproduces the experimental values quite well. However, the samples with 74 and 75 at.% deviate a little from the predicted values. If the deviation lies within the margins of the experimental error is unclear as no error bars are available. Further, if A_{ex} is averaged for the two samples, the resulting value fits perfectly well. Whether the averaging is justified or the sample with 75 at.% Pt should be omitted entirely due to the different preparation is debatable. If it is omitted, the experimentally measured exchange stiffness is a bit higher than predicted by the model. This could be caused by the negligence of contributions from next-next-neighbor interactions and of the polarization of Pt atoms in the model (*125, 289, 292*). Especially the latter would have an increasing impact for more dilute alloys, with the moment per Co atom increasing by up to a factor of two. An additional data point from Murayama et al. (*349*) for hcp $Co_{0.86}Pt_{0.14}$ is shown. The 25 nm thick sample was prepared by RF-sputtering of a Co target with Pt pellets on top. No buffer layer was deposited prior to the alloy. The discrepancy was acknowledged already in Harzer's study; however, no explanation for the lower value was given.

It should be noted that with decreasing Co content T_C is reduced in alloys. Consequently, M_S decreases when T approaches T_C. With A_{ex} being linked via M_S to T_C (see Eq. 1-4 and Eq. 4-10) (*119, 120*), a further reduction of A_{ex} is expected when T is close to T_C, i.e. for more dilute alloys. Fig. 4-21(b) shows the dependency of T_C for CoPt (*125, 289*) and CoIr (*316, 317*) alloys. T_C is equal to RT in CoPt for ~0.15 Co content, while in CoIr this happens at a much higher concentration ~0.6. These Co contents set the lower limits for the applicability of the model. Further, due to the negligence of the T_C-influence, a deviation for low Co content is expected. In conclusion, the model describes the experimentally obtained values for A_{ex} in alloys with good accuracy.

With the model successfully reproducing A_{ex} in alloys, next it is applied to ultrathin-layered samples, which are the focus of this thesis. Fig. 4-22(a) shows A_{ex} over t_{Co} for single and multilayer samples (t_{NM} > 1.4 nm) obtained from the model with σ = 0.5 nm as black line, in combination with X_{cut} = 0.375 as black dashed line and experimental values obtained from domain-wall widths in this work as red circles. The experimentally obtained values in this thesis and the ones predicted

[31] The paper included an additional theoretical value for the exchange stiffness in hcp bulk Co. This value is not included here due to the different crystalline structure and theoretical nature.

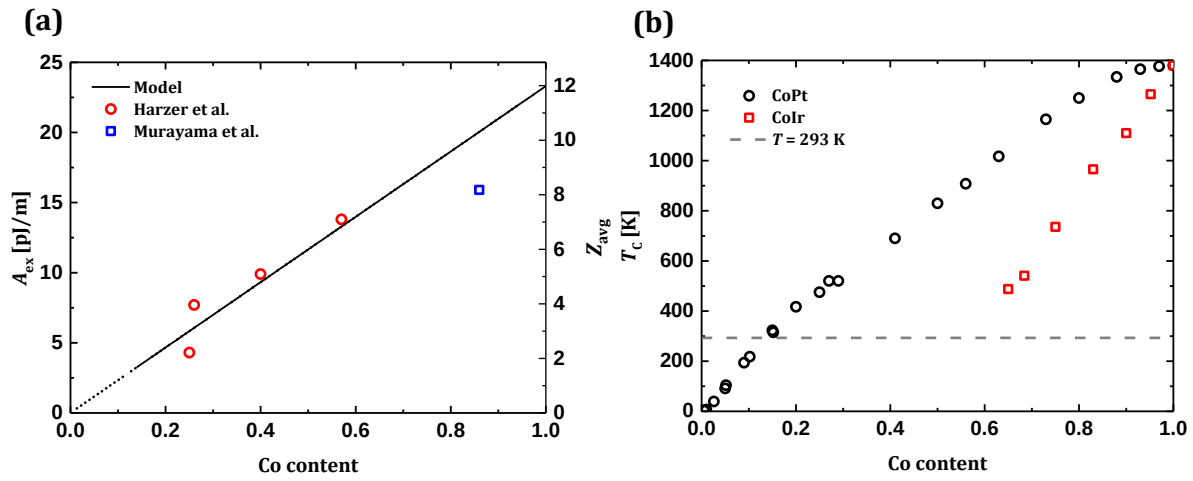

Figure 4-21: (a) Comparison of A_{ex} values for alloys predicted using the model to values found in literature for fcc CoPt alloy (*315*) and hcp CoPt alloy (*349*). For a Co content of less than 0.15, T_C of such alloys is below RT, thus the values predicted by the model are dashed in the region of Co content < 0.15. (b) Experimental values for T_C found for fcc CoPt and both, fcc and hcp, CoIr alloy (*125, 289, 316, 317*). For CoIr, the three values with highest Co content are fcc, the remaining are hcp. The dashed line indicates RT.

by the model are in reasonable agreement. When X_{cut} is considered as well, the agreement is further improved.

X_{cut} mimics the influence of T_C on A_{ex}. Analogous to the alloys, M_S and subsequently A_{ex} is reduced when T_C approaches RT. Fig. 4-22(b) shows experimental values for T_C obtained in this thesis and found in literature for MBE-grown and e-beam evaporated (half-filled symbols) (*291, 350*) and DC-sputtered (open symbols) (*295, 298, 351*) samples. For Pt\Co\Pt single layers, MOKE measurements suggest T_C > 300 K for t_{Co} = 0.3 nm (see Tab. 4.3 and chapter 4.2.2); XAS and SAXS measurements for multilayers with N = 8 indicate $t_{Co}(T_C = 300\,K) \approx 0.2$ nm (black circles) (see chapter 5.1). This is in line with the offset obtained from X_{cut} = 0.15 of ≈ 0.2 nm, shown in Fig. 4-20.

In Pt\Co\Ir, MOKE measurements indicate T_C reaching RT for $t_{Co} \approx 0.5$ nm in single layers (see Tab. 4.3 and chapter 4.2.2), while XAS and SAXS measurements for multilayers indicate the same for $t_{Co} \approx 0.5$ nm with N = 6, and $t_{Co} \approx 0.45$ nm with N = 8 (red circles) (see chapter 5.1). This is again close to the offset range of (0.4– 0.6) nm obtained using X_{cut} = 0.375 within the model.

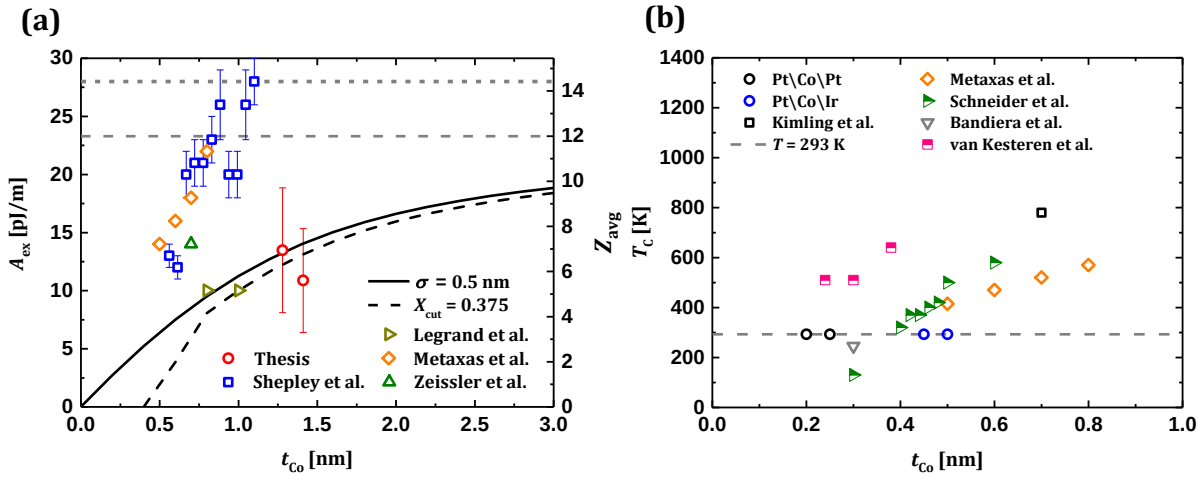

Figure 4-22: (a) Comparison of the Co thickness of A_{ex} for ultrathin samples predicted by the model with the experimentally obtained values within this thesis and others found in literature(*298, 302–304*). The grey dashed line represents the bulk value for fcc Co A_{ex} = 23.3 pJ/m (*327*) and the dotted line hcp Co with A_{ex} = 28 pJ/m (*327*). The right ordinate indicates the corresponding average coordination number Z_{avg}. (b) Co-thickness dependence of the Curie temperature T_C for ultrathin layers. The open circles, values obtained within this thesis, are from X-ray absorption spectroscopy measurements indicating the onset of dichroic signal (see chapter 5.1) or MOKE measurements, which indicate the thinnest sample with T_C > RT. Additional values found in literature are plotted (*291, 295, 298, 350, 351*).

Next to the values obtained within this thesis, Fig. 4-22(a) also reproduces values found in literature. It should be noted that no structural information is found in those studies; therefore, it is assumed that comparable interface morphologies are present. The values reported for A_{ex} by Legrand et al. (golden triangles) from measurements of T_C in (Pt\Co\Ir)$_N$ and (Ir\Co\Pt)$_N$ are well reproduced by the model (*302*). Contrary, values reported for (Pt\Co\Ir)$_N$ using a $T^{3/2}$ model by Shepley et al. (*303*) (blue squares) and Zeissler et al. (*304*) (green triangle) deviate from the model and cannot be reproduced by any choice of σ, including zero. This is evident, as they surpass the value for bulk fcc Co considerably, which is used as reference. The choice of a different reference, e.g. hcp Co, does not change this outcome (within physically reasonable values; only for A_{ex} = 40 pJ/m, σ = 0.2 nm, and X_{cut} = 0.375 reasonable agreement is achieved). This discrepancy is puzzling as the samples exhibit similar values for the anisotropy compared to the samples in this thesis. In addition, values for Pt\Co\Pt sandwiches are shown, deduced using a T_C model for two-dimensional films (*341*) by Metaxas et al. (golden diamonds) (*298*). Again, the discrepancy is obvious and cannot be resolved by any choice of σ or reference. On the other hand, these samples

exhibit lower anisotropies, thus structural differences seem likely. Further, the reported values of M_S, A_{ex}, and T_C do not show the expected correlation between the parameters (*119, 120*). I.e., for their thickest sample, T_C is strongly reduced while the other two parameters exhibit almost bulk values. Possible reasons for the discrepancies are discussed in the previous chapter.

In conclusion, the exchange stiffness in ultrathin Co layers was extracted from domain wall profiles imaged with XHM. For $t_{Co} = 1.28\,\text{nm}$ (1.41 nm) a value of $A_{ex} = (13 \pm 6)\,\text{pJ/m}$ ($(11 \pm 4)\,\text{pJ/m}$) was found. The obtained values are strongly reduced compared to the bulk value for fcc Co of $A_{ex} = 23.3\,\text{pJ/m}$. Qualitative similar reductions of A_{ex} in ultrathin films are found in literature for DC-sputtered samples, but not epitaxially prepared ones. For epitaxial samples bulk-like values are obtained down to $t_{Co} = 0.8\,\text{nm}$. As the difference is only found in ultrathin samples, it originates most likely from structural differences at the interfaces, namely interdiffusion. Consequently, a model was developed, which estimates the reduction of A_{ex} in dependence of the interdiffusion zone width σ. Furthermore, the influence of T_C was incorporated by comparing the local Co content to alloys and excluding the regions for which alloys are paramagnetic. This gives rise to a different onset of ferromagnetic order depending on the interface materials. The model successfully reproduced the experimentally obtained values of A_{ex} and the ones found in literature for CoPt alloys. Furthermore, the predicted offsets along t_{Co} are in line with measurements of the onset of dichroic signals found in X-ray absorption measurements in respective samples. A_{ex} values reported in literature for ultrathin Co films are partially reproduced; others show quantitative deviations from the model, the reported reduction in dependence of t_{Co} can be explained qualitatively.Furhter measurements of domain patterns in various systems should be conducted to extract the domain wall profiles and A_{ex} to verify the predictions of the model.

4.5 Interlayer exchange coupling

This chapter addresses the interlayer exchange coupling (IEC) between two or more magnetic layers separated by non-magnetic spacer layers. In the first section 4.5.1, the IEC is discussed exemplarily in the well-studied symmetric systems with opposite coupling behavior, Co\Pt\Co and Co\Ir\Co. Subsequently, the results of the investigation of the antisymmetric systems, Co\Pt\Ir\Co and Co\Ir\Pt\Co, are shown in section 4.5.2.

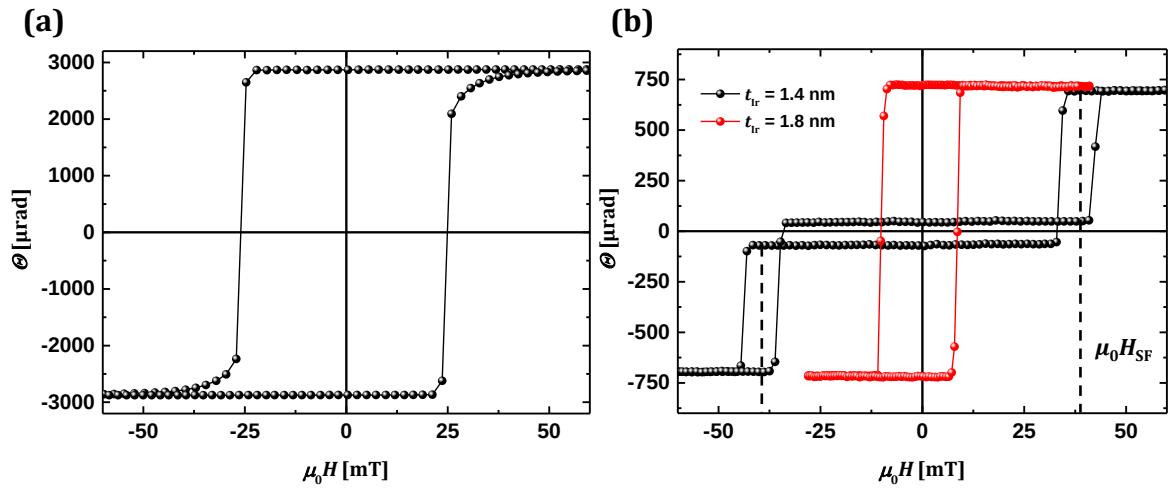

Figure 4-23: (a) Perpendicular MOKE remagnetization curve for $Co_{0.8\,nm}\backslash Pt_{1.4\,nm}\backslash Co_{0.8\,nm}$. Both Co layers switch the magnetization direction simultaneously, exhibiting the for Pt spacer-layer typical FIC. (b) Perpendicular MOKE remagnetization curves for two $Co_{1\,nm}\backslash Ir_t\backslash Co_{1\,nm}$ samples. For the same spacer layer thickness as in (a), t_{Ir} = 1.4 nm (black), both Co layers are coupled antiferromagnetically and align antiparallel at zero fields. For $\mu_0 H_{SF} = \pm$ 38.5 mT, the AIC is compensated by the applied field and the layer aligned antiparallel to the field switches its direction. For t_{Ir} = 1.8 nm (red), both Co layer couple ferromagnetically.

4.5.1 Interlayer exchange coupling in symmetric Co\Pt\Co and Co\Ir\Co

In this chapter, the interlayer exchange coupling in Co\Pt\Co with ferromagnetic interlayer coupling (FIC), and Co\Ir\Co with AIC is addressed. The Co layers in each stack are of identical thickness.

First, the IEC in Co\Pt\Co across Pt-spacer layers is addressed, which is the case in $Pt\backslash(Co\backslash Pt)_N$ samples. In Co\Pt\Co, the Co layers couple ferromagnetically through the Pt spacer layers, making a parallel alignment of the magnetization in all layers energetically favorable. Therefore, in an easy-axis remagnetization curve, the magnetization of the all layers switches simultaneously. In Fig. 4-23(a), such a remagnetization curve is shown for $Co_{0.8\,nm}\backslash Pt_{1.4\,nm}\backslash Co_{0.8\,nm}$[32]. During the easy-axis remagnetization curve, the sample remains fully remanent in the single-domain state until the coercive field is applied against the magnetization direction, initiating a simultaneous switching of both Co layers. For a Pt-spacer-layer thickness of t_{Pt} = 1.4 nm, coupling constants in the range

[32] The sample was prepared and measured by M. Riepp from the Coherent X-ray Scattering group at DESY.

of J_{IEC} = (1.5– 3.4) mJ/m² were measured using BLS. This is three to seven times stronger than the largest value for $K_{tot} \cdot t_{Co}$ found in Pt\(Co\Pt)$_N$ (see chapter 4.3.3). J_{IEC} is approximately[33] proportional to $1/t_{NM}^2$ (*162, 181*), with J_{IEC} = (0.45– 0.8) mJ/m² for t_{Pt} = 2 nm, and vanishing around t_{Pt} = (3– 4) nm. For extended multilayers with Pt spacers only FIC is reported, although an oscillating strength of J_{IEC} with t_{NM} was observed (*175, 176*). The oscillation periods is expected to be determined by critical spanning vectors of the spacer material (*172*) (see chapter 1.1.5). Contrary to the often-reported exclusive FIC, AIC has been reported for multilayers with PMA in a spin-valve geometry, if the Pt layers exceed a thickness of 2.4 nm (*177–179*). The coupling is two orders of magnitude smaller than found for commonly considered AIC coupling materials, i.e. Ir and Ru, and it is usually attributed to the so-called orange-peel or antiferromagnetic magnetostatic interlayer coupling (*172, 352*). The Pt\(Co\Pt)$_N$ samples investigated in this thesis are limited to $t_{Pt} \leq 2$ nm and do not have spin-valve geometry. Consequently, only FIC is observed.

Next, we turn to the IEC across Ir-spacer layers in Co\Ir\Co structures prevalent in Ir\(Co\Ir)$_N$ samples. In Co\Ir\Co, the coupling constant oscillates periodically with t_{Ir} between FIC and AIC. The sign of J_{IEC} switches every 0.9 nm with the peak value decreasing $\propto 1/t_{Ir}^2$. This was first observed for Co\Ir\Co with in-plane anisotropy in 1990 by Parkin et al (*162*), and for PMA in 2003 by Itoh et al (*185*). Fig. 4-23(b) shows the remagnetization curves for two Co$_{1\,nm}$\Ir$_t$\Co$_{1\,nm}$ samples with t_{Ir} = 1.4 (black) and 1.8 nm (red). Both samples exhibit strong PMA. The sample with t_{Ir} = 1.4 nm has the same spacer layer thickness as the sample in Fig. 4-23(a), but exhibits AIC. Increasing the spacer layer by 0.4 nm to t_{Ir} = 1.8 nm (red dots), changes the sign of J_{IEC}, thus favoring parallel alignment. Averaging H_{SF} obtained from the forward and backward sweeps yields $\mu_0 H_{SF} = \pm$ 38.5 mT and subsequently J_{IEC} = -0.054 mJ/m² with Eq. 1-23.

In Fig. 4-24, J_{IEC} is plotted over t_{Ir} for Co\Ir\Co with two discontinuities, showing the values extracted in this thesis (red circles) compared to values reported in literature (*162, 182, 185, 270, 271, 300, 353, 354*)[34]. Data points appear in lumps every 0.9 nm, the oscillation period for the Ir spacer layer (*162*). In-between, FIC is observed (only shown for samples from this thesis as zeros). In addition, the peak values are strongly reduced after every period. The investigated samples in this thesis cover the range t_{Ir} = 1.1– 2.2 nm and include the second and third oscillation maxima

[33] The dependence is strongly influenced by the morphology of the interface and a faster decay of J_{IEC} is frequently observed (*162, 172, 181*).

[34] Knowledge of M_S is required to extract J_{IEC}. Some values for M_S taken from the cited studies are summarized in Fig. 4-6 (*144, 185, 300, 301*), for the remaining studies it is unclear which value for M_S was used. If reduced values of M_S were present and bulk-like was used for the extraction of J_{IEC}, its value is overestimated.

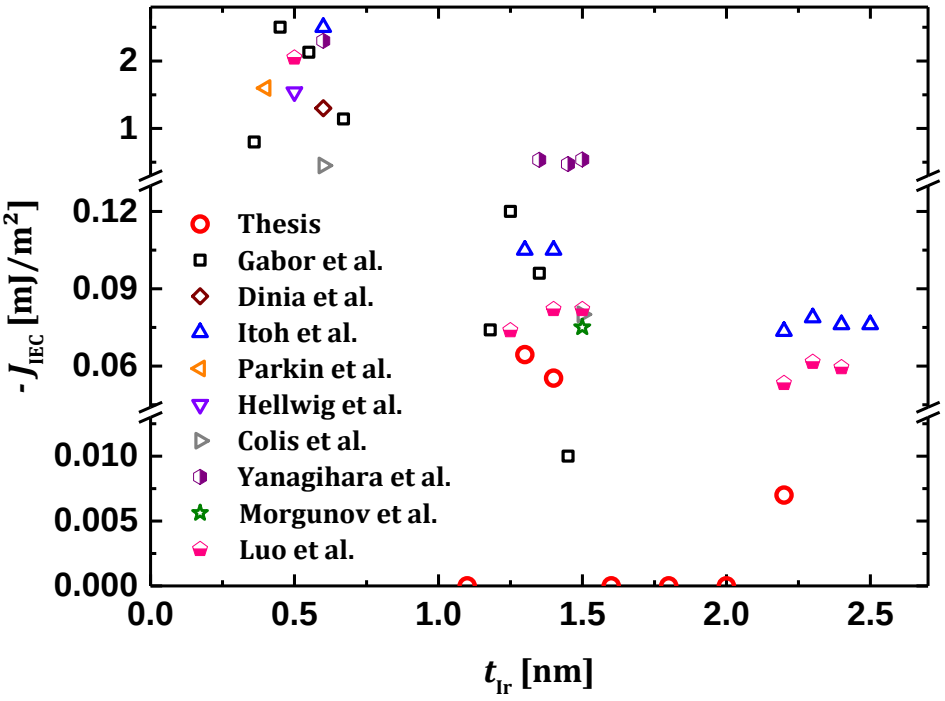

Figure 4-24: Summary of experimental values for J_{IEC} at RT in Co\Ir\Co samples obtained in this thesis (red circles) and found in literature (*144, 162, 182, 185, 270, 271, 300, 353, 354*). MBE-grown samples are indicated by half-filled symbols, open symbols are sputtered. The ordinate has two discontinuities to account for the great span of values. Data appear in lumps every 0.9 nm, the oscillation period for the Ir spacer layer. The peak values are strongly reduced after each period and in-between FIC is observed. Samples exhibiting FIC are indicated by $J_{IEC} = 0$ and only shown for samples investigated in this thesis.

of the AIC. The second maximum was found at $t_{Ir} = 1.3$ nm, the third at $t_{Ir} = 2.2$ nm. This qualitatively reproduces the AIC behavior from literature However, the obtained values for J_{IEC} at the second AIC peak are a little smaller compared to literature; the third peak is only one tenth of the values reported in (*144, 185*). In Fig. 4-25(b), a model is fitted to the data (*355*):

$$J_{IEC}(t_{Ir}) \propto \frac{\sin\left(\phi + 2\pi \frac{t_{Ir}}{\lambda}\right)}{t_{Ir}^{p}}, \qquad \text{Eq. 4-19}$$

with an arbitrary phase ϕ, the oscillation period λ, and the damping parameter p. The model yields[35] $\lambda = (0.98 \pm 0.05)$ nm and a damping parameter of $p = (4 \pm 1)$. The oscillation period is in good agreement with $\lambda = 0.9$ nm found in literature (*162*). The values obtained from the fitting of the model should not be overestimated; only three real data points are available with the FIC data

[35] The data point for $t_{Ir} = 1.8$ nm is not used for the fitting.

points actually exhibiting $J_{IEC} < 0$. The interface morphology, i.e. roughness, interdiffusion, and pinholes, strongly affects the damping of J_{IEC} and values larger than the theoretically expected exponent of 2 are frequently found in experiments (*172*). Further, J_{IEC} is also affected by seed and capping layers (*356–358*). The ECR-grown Pt layer with its strong texture is unique to the samples investigated in this thesis; its influence on the coupling is unknown.

4.5.2 Interlayer exchange coupling in antisymmetric Co\Pt\Ir\Co and Co\Ir\Pt\Co

In this chapter, the peculiar IEC across layered spacer-layers is presented in the antisymmetric cases of Co\Ir\Pt\Co and Co\Pt\Ir\Co.

Interlayer exchange coupling in Co\Pt\Ir\Co

First, IEC in Co\Pt\Ir\Co is addressed, which is the stacking order in (Ir\Co\Pt)$_N$. Fig. 4-25(a) shows three remagnetization curves. Co\Pt$_{0.85\,nm}$\Ir$_{0.9\,nm}$\Co, shown in red, exhibits FIC and the magnetization switches its direction via domain decay. The combined spacer-layer thickness is $t_{NM} = t_{Pt} + t_{Ir} = 1.75\,nm$, thus is close to the Co\Ir\Co sample with FIC shown in Fig. 4-23(b) in red. The blue curve in Fig. 4-25(a), Co\Pt$_{1\,nm}$\Ir$_{1.1\,nm}$\Co, exhibits AIC with the switching fields $\mu_0 H_{SF} = \pm 27\,mT$. The total spacer-layer thickness here is $t_{NM} = t_{Pt} + t_{Ir} = 2.1\,nm$. By only considering these two spacer-layer thicknesses, one might conclude that the IEC shows in Co\Pt\Ir\Co an analogous thickness-dependence with respect to t_{NM} as in Co\Ir\Co with respect to t_{Ir}.

In contrast, the remagnetization curve shown in black in Fig. 4-25(a) is obtained from Co\Pt$_{0.6\,nm}$\Ir$_{1.1\,nm}$\Co, thus $t_{NM} = t_{Pt} + t_{Ir} = 1.7\,nm$, exhibits AIC with $\mu_0 H_{SF} = \pm 35\,mT$. Both samples, shown as black and red, have almost the same spacer-layer thickness, yet opposite signs of J_{IEC}. On the other hand, both samples with AIC, shown as black and blue, have different total spacer-layer thicknesses, yet the same t_{Ir}. Furthermore, the values obtained for J_{IEC} in both samples are quite similar: $J_{IEC} = -0.049\,mJ/m^2$ for Co\Pt$_{0.6\,nm}$\Ir$_{1.1\,nm}$\Co and $J_{IEC} = -0.042\,mJ/m^2$ for Co\Pt$_{1\,nm}$\Ir$_{1.1\,nm}$\Co. Apparently, in the case of Co\Pt\Ir\Co, the IEC depends not only on the thickness of the spacer-layer but also its composition. So the question arises: How does the Pt-layer influence the IEC in Co\Pt\Ir\Co?

In order to answer this question, Co$_{1\,nm}$\Pt$_t$\Ir$_{1.1\,nm}$\Co$_{1\,nm}$ samples were prepared in which the Pt-layer thickness was systematically varied within the range of $t_{Pt} = 0–1.6\,nm$. Before turning to the results, the remagnetization curve of Co\Pt$_{1.3\,nm}$\Ir$_{1.1\,nm}$\Co is discussed, shown in Fig. 4-25(d). It represents a special case of weak AIC. Two separate switching fields are observed,

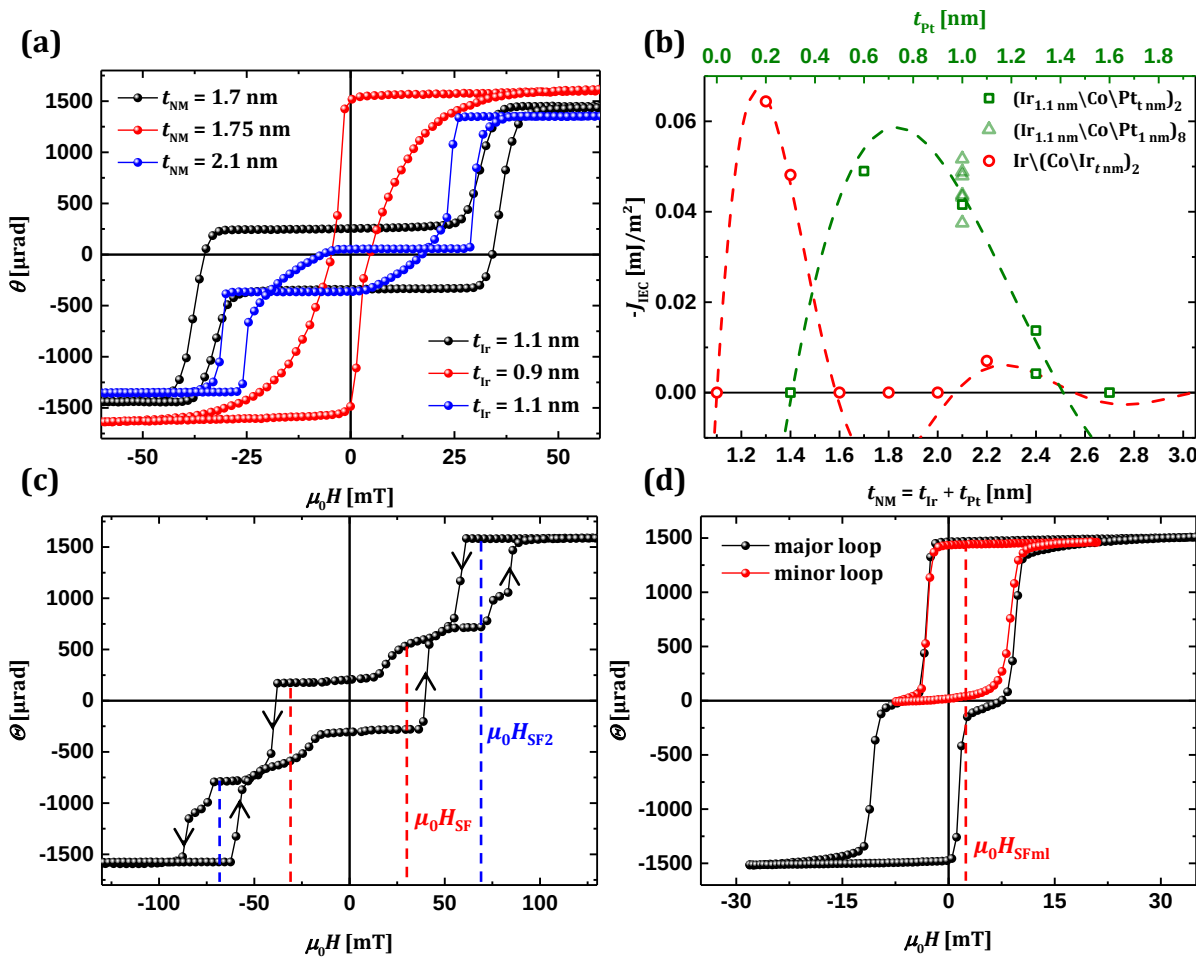

Figure 4-25: (a) Polar MOKE remagnetization curves for Co\Pt\Ir\Co with varying spacer layer composition. Two samples with almost identical $t_{NM} = t_{Pt} + t_{Ir} = 1.7$ (black) and 1.75 nm (red), but varying composition exhibit opposite signs of J_{IEC}. Two samples with identical $t_{Ir} = 1.1$ nm, but varying t_{NM}, host AIC with similar switching fields. (b) J_{IEC} in dependence of t_{NM} for $Co_{1\,nm}\backslash Pt_t\backslash Ir_{1.1\,nm}\backslash Co_{1\,nm}$ samples (or $(Ir_{1.1\,nm}\backslash Co_{1\,nm}\backslash Pt_t)_2$) with varying t_{Pt} shown as green squares. The upper abscissa indicates t_{Pt}. Additional data points for $(Ir_{1.1\,nm}\backslash Co_t\backslash Pt_{1\,nm})_8$ are added as green triangles. In the range of $t_{NM} = 1.7$– 2.4 nm (or $t_{Pt} = 0.6$– 1.3 nm) AIC is found and FIC for the remaining samples. The dashed line is a fit of Eq. 4-19 to the data yielding $\lambda = (2.2 \pm 0.10)$ nm. The red circles indicate $Co_{1\,nm}\backslash Ir_t\backslash Co_{1\,nm}$ samples (the upper abscissa does not apply). The red dashed line is a fit to all data points, except $t_{Ir} = 1.8$ nm, yielding $\lambda = (0.98 \pm 0.05)$ nm. (c) Perpendicular MOKE remagnetization curve for $(Ir_{1.1\,nm}\backslash Co_{1\,nm}\backslash Pt_{1\,nm})_8$ with two switching fields for the single coupled outer Co-layers at $\mu_0 H_{SF} = \pm 31.2$ mT and approximately twice the field with $\mu_0 H_{SF2} = \pm 68.5$ mT for the double-coupled inner layers (c.f. description for Fig. 4-9(e, f)). (d) Perpendicular MOKE remagnetization curve for $Co_{1\,nm}\backslash Pt_{1.3\,nm}\backslash Ir_{1.1\,nm}\backslash Co_{1\,nm}$ with weak AIC. The major loop remains fully remanent at zero fields, but exhibits two separated switching fields. The minor loop is shifted along the abscissa to positive field by $\mu_0 H_{SFml} = 3$ mT.

but the sample remains fully remanent at zero fields. Rectangular remagnetization curves indicate magnetization reversal via the nucleation of reversed domains, followed by domain walls rushing through the sample. The field required for the nucleation of the domains, the nucleation field H_N, corresponds to the coercive field and is larger than the propagation field of the walls (*359*). The observed change of magnetization direction takes place at[36] $\mu_0(H_{SF} - H_N)$ (*360*). In the case of weak AIC, the switching field H_{SF} is very small and can be smaller than the nucleation field H_N of the individual layer. Thus, $\mu_0(H_{SF} - H_N)$ can be negative in the presence of weak AIC and the fully remanent state is stabilized at zero fields by the nucleation field. The nucleation field can be determined from a minor loop, i.e. a remagnetization curve of only one layer, which is shown in red in Fig. 4-25(d). The switching in the minor loop occurs at $H_{SFml} \pm H_N$. Thus, averaging the switching fields in the minor loop eliminates the contribution of H_N. In the case $H_{SFml} > 0$, weak AIC is prevalent and J_{IEC} follows to (*360*):

$$J_{IEC} = -\mu_0 t_{Co} M_S H_{SFml} . \qquad \text{Eq. 4-20}$$

$\mu_0 H_{Fml} = 3\,\text{mT}$ yields $J_{IEC} = -0.0042\,\text{mJ/m}^2$. For $H_{SFml} < 0$, on the other hand, weak or zero FIC is prevalent (compare Fig. 4-26(b)) (*176, 352, 360*).

We now turn to the results for J_{IEC} in Co\Pt$_t$\Ir$_{1.1\,nm}$\Co with $t_{Pt} = 0-1.6\,\text{nm}$. In Fig. 4-25(b), the obtained values for J_{IEC} are plotted as green squares over t_{NM} (bottom axis) and t_{Pt} (upper axis); zeros imply FIC. Additionally, values obtained for samples with $N = 8$ are plotted for $t_{Pt} = 1\,\text{nm}$ with varying Co layer thickness. Fig. 4-25(c) shows exemplarily the remagnetization curve for (Ir$_{1.1\,nm}$\Co$_{1\,nm}$\Pt$_{1\,nm}$)$_8$. Furthermore, the results for Co\Ir\Co are shown as red circles in Fig. 4-25(b) as well (the top axis does not apply here obviously). It is apparent that the two systems behave very differently. For $t_{NM} = 1.4\,\text{nm}$ Ir\Co$_t$\Ir hosts AIC while Ir\Co\Pt exhibits FIC. In the range $t_{NM} = 1.6-2\,\text{nm}$ it is the other way around. The period length for Ir\Co\Pt is estimated to $\lambda = (2.2 \pm 0.10)\,\text{nm}$ with a peak at $t_{NM} \approx 1.9\,\text{nm}$ and J_{IEC} of comparable magnitude to Ir\Co\Ir at the second peak. The damping is inaccessible with the data points only including one oscillation.

Literature has little to offer regarding experimental studies on layered spacer layers, but theoretical works by Bruno et al. (*361*) and Kudrnovský et al. (*362*) (both authors were in the same group) studied the influence of (dis-)ordered spacer alloys in Co(001)\Cu$_{1-z}X_z$\Co using first-principles calculations at $T = 0\,\text{K}$. They considered X = Au, Ni, and Zn, i.e. a material isoelectronic to Cu

[36] This assumes a field sweep starting at positive field values.

(Au), a material with one valence electron less than Cu, thereby decreasing the surface of the Fermi surface (Ni), and one with an additional electron (Zn), thereby increasing the surface of the Fermi surface. They considered only alloys up to 25 at.% for Ni, as beyond the alloy turns ferromagnetic. For the disordered case, they find a reduction of J_{IEC} for all materials compared to pure Cu, while the period is not affected by an isoelectric material, shortened by one with fewer electrons, and elongated by the opposite (25 at.% Zn leads to an elongation of the coupling period of 60 %). The unchanged period in Co\CuAu\Co has been experimentally verified in (*363, 364*).

For the ordered case only the isoelectric case is discussed, i.e. Co\(Cu\Au)$_N$\Co with alternating mono-atomic layers of Cu and Au. They find a 14 % elongation of the coupling period, and an additional superimposed coupling period originating from the superlattice spacer period with a period length of approximately six times the superlattice period ($\approx 6(t_A + t_B)$), with t_X the thickness of spacer layer X (*365*). An experimental study by Parkin et al. (*363*), found an elongated period for a CuNi alloy spacer, no change for a CuAu alloy, and a phase shift and elongation for CuFe (three electrons less than Cu). Furthermore, they successfully modeled their findings for CuNi. The calculations were reproduced by Lathiotakis et al. (*366*), pointing out the strong influence of the alloy composition on the resulting Fermi surface, thus on the oscillation period (see chapter 1.1.5). The results from Parkin's study regarding CuNi and CuFe are contrary to the predictions by Bruno and Kudrnovský; the discrepancy is in neither study addressed.

In the following, the experimentally observed coupling period is compared with the studies found in literature. Pt has one additional valence electron with respect to Ir, thus it is equivalent to the case of Zn and Cu in literature. Therefore, the theoretical studies predict an elongation of the period. The observed period in Co\Pt\Ir\Co is about 130 % (2.3 times) longer than the one found for pure Ir. Thus, the theoretical prediction is generally met.

The case of an ordered alloy spacer with superlattice structure of alternating monolayers of isoelectric material is hardly applicable to the samples investigated in the thesis. First, Pt and Ir are not isoelectric, and second only one layer of each material is present which is thicker than one monolayer. Furthermore, the calculated elongation of 14 % is insufficient to account for the experimental observation. The additional period length of $\lambda \approx 6(t_{Pt} + t_{Ir})$ due to the "superlattice" structure would be $\approx$ 13 nm, several times larger than the spacer-layer thickness (in multilayer samples this might cause a variation of the coupling along the stacking direction as the total thickness of a sample can reach tens of nm).

In the case of a disordered alloy, the case of CuZn applies. The elongation of the oscillation period depends approximately linearly on the solvent content. For the largest considered content of 25 at.% Zn, an elongation of 60 % was calculated. Extrapolation to a content of 50 at.%, yields an elongation of 120 % or a period 2.2 times longer than for the pure spacer material. This fits surprisingly well to the observed period length. However, several things should be stressed. First, the extrapolation of data to values so far off is at best sketchy. Second, by varying the Pt-layer thickness in the samples, the "alloy composition" varies from sample to sample as well. Thus, there is not only one single value for the "alloy composition". Third, the extent of interdiffusion of Pt nd Ir is unknown but they most likely do not form a homogenously disordered alloy. Apparently, this is not required to cause the elongation of the oscillation period.

The IEC in Co\Pt\Ir\Co exhibits a peculiar dependence on both the Pt and Ir layer thickness. While varying the Pt-layer thickness while keeping the Ir-layer constant, a wider maximum is observed of comparable strength to pure Ir spacer layers. With respect to applications, broader maxima are desirable as they increase the acceptable margin of error. However, a broader spectrum of the parameter space needs to be investigated before reliable conclusions are drawn.

Interlayer exchange coupling in Co\Ir\Pt\Co

Next, the IEC in Co\Ir\Pt\Co is addressed, which is the stacking order in (Pt\Co\Ir)$_N$. In a naïve picture, the stacking order in-between Co layers should not affect the IEC, as the stacking appears to be mirror symmetric. Thus, the same coupling behavior is expected for Co\Ir\Pt\Co and Co\Pt\Ir\Co, if the Pt and It thicknesses are identical. Fig. 4-26(a) shows the polar remagnetization curve for a sample with t_{Pt} = 1 nm and t_{Ir} = 1.1 nm in black that exhibits FIC. The inversely stacked system with the same layer thicknesses exhibits AIC (c.f. Fig. 4-25(a) blue curve and (b)). Thus, an inversion of the stacking order does not result in mirror symmetric samples and the naïve picture does not hold (similarly the anisotropy in the corresponding systems depends on the stacking order, c.f. section 4.3.3). The breaking of the mirror symmetry could stem from varying interfaces in-between the Co-layers in dependence of the stacking order or influences of the capping and seed layer (*356–358, 367*).

First, the interfaces in-between Co-layers are addressed. For Pt\Co\Pt it is known, that the upper Co\Pt interface has a wider interface compared to the lower Pt\Co (*127, 129, 130, 295*). Similar observations have been made for Pt\Co\Ir and Ir\Co\Pt where a wider Co\Ir interface compared to the lower Ir\Co was concluded from the formation of a magnetic dead layer in Pt\Co\Ir (c.f. discussion in section 4.2.2) (*182*). Accordingly, in the case of Co\Pt\Ir\Co with AIC, a wider

Co\Pt interface and a narrower Co\Ir interface might be expected. Contrary, in Co\Ir\Pt\Co with FIC, a wider Co\Ir interface and a narrower Pt\Co interface would follow. Thus, the variation of interface widths could account for the opposite coupling in samples with inverse stacking order but identical spacer layer composition.

In order to investigate if in Co\Ir\Pt\Co AIC can be found for another composition of the spacer layer, Co\Ir$t$\Pt1 nm\Co samples were prepared with varying Ir-layer thickness in the region of t_{I} = 1.1– 1.5 nm. The resulting remagnetization curves are shown in Fig. 4-26(a). For t_{NM} = 2.1, 2.4, and 2.5 nm (black, blue and green), the curves reveal strong FIC coupling with both layers switching simultaneously. Please note that the sample with t_{NM} = 2.1 nm (black) the Co-layers are slightly thinner with t_{Co} = 0.9 nm instead of 1 nm (for the remaining samples), thus causing the larger coercive field and lower saturation rotation. The samples with t_{NM} = 2.4 and 2.5 nm have identical coercive fields. For the spacer layer thickness in-between, t_{NM} = 2.3 nm, a different remagnetization behavior is observed. The sample shown in blue, (t_{NM} = 2.3 nm) remains fully remanent at zero fields and the magnetization changes its direction in a two-step process. The first step occurs at the coercive field of the samples with t_{NM} = 2.4 and 2.5 nm, while the second occurs at twice the field. From the minor loop, shown in Fig. 4-26(b), follows H_{SFml} = -2 mT. This type of remagnetization curve is frequently observed in studies addressing magnetostatic interlayer coupling and usually associated with weak FIC for follows $H_{\mathrm{SFml}} < 0$ (*175, 176, 352, 360, 368*). Accordingly, within the investigated region of t_{Ir} = 1.1– 1.5 nm, the samples change from strong to weak FIC and back again.

Apparently, the IEC oscillates in Co\Ir\Pt\Co in dependence of t_{Ir} with a short oscillation period of $\lambda \approx$ (0.3– 0.6) nm, but J_{IEC} does not change its sign within the small part of the parameter space that has been investigated. A similar behavior is reported for Co\Pt\Co samples (*175, 176*) with an oscillation period of $\lambda \approx$ 1 nm for $t_{\mathrm{Pt}} >$ 3 nm and was attributed to magnetostatic interlayer coupling (*176*). The different coupling behavior caused by the inversion of stacking order remains puzzling.

Next, the influence of the capping and seed layer on the IEC is addressed. Besides the material and thickness of the spacer layer, the IEC is also affected by the thicknesses of the ferromagnetic (*174, 369, 370*) and the capping layers (*356, 358, 367*) and oscillates with respect to the thicknesses of both. Thus, the coupling originates from the interference of electrons within the whole sample (*367*). However, the oscillation amplitudes originating from the ferromagnetic and the capping layers are much weaker compared to one corresponding to the spacer thickness. Furthermore, it

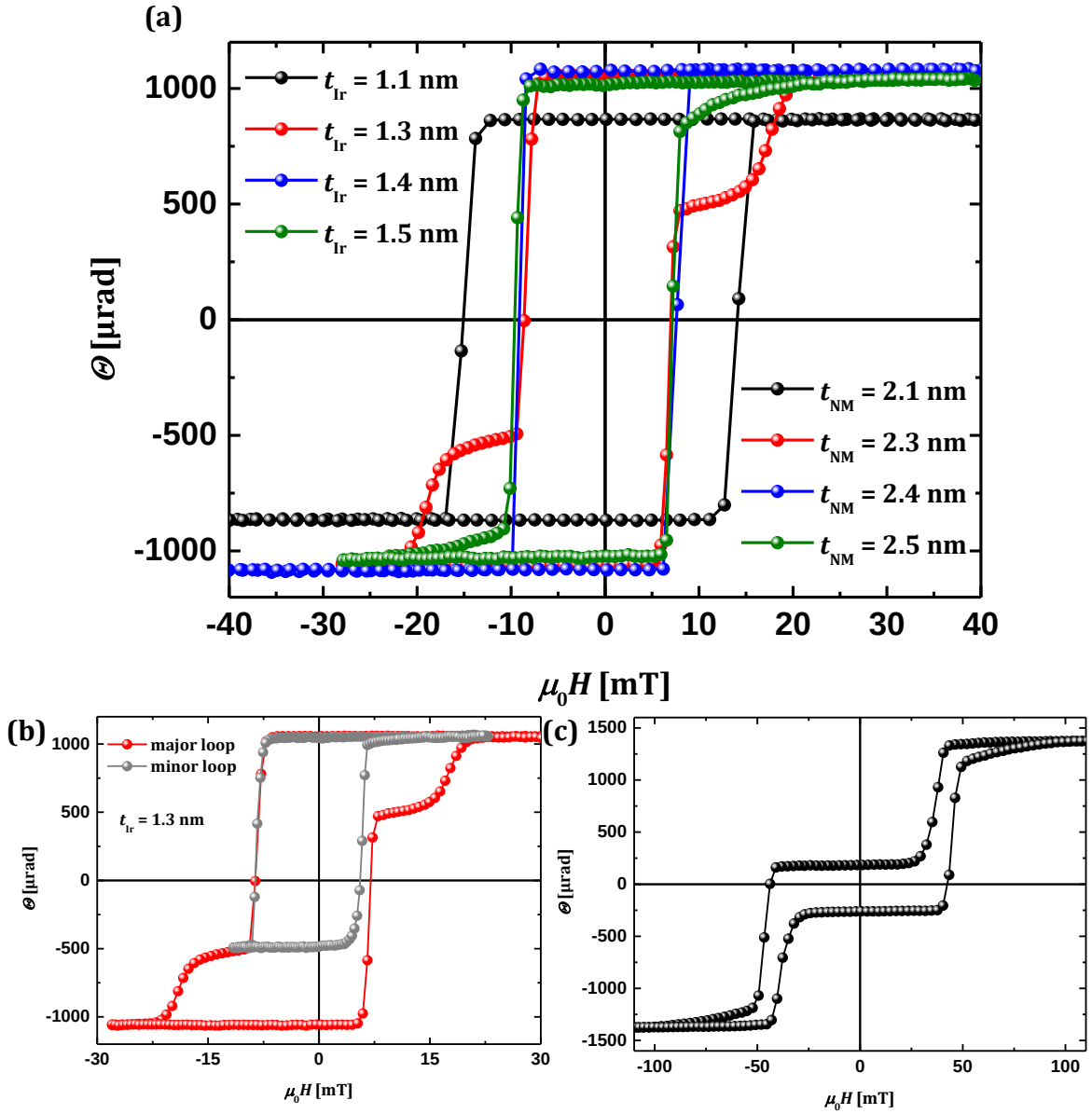

Figure 4-26: (a) Four perpendicular MOKE remagnetization curves for Co\Ir\Pt\Co samples (stacking order in (Pt\Co\Ir)$_2$) with constant t_{Pt} =1 nm and varying t_{Ir}. All samples have t_{Co} =1 nm, except for the one shown in black with t_{Co} =0.9 nm, causing the larger coercive field. The curves shown in black blue and green exhibit FIC and both layer switch simultaneously. The curve for the sample shown in red, exhibits a two-step process with a second step around twice the field of the first step. (b) Major and minor loop of the sample shown in (a) with a two-step remagnetization process. The minor loop of the remagnetization of only one layer is slightly shifted to negative fields by $\mu_0 H_{SFml}$ = -2mT, indicating weak FIC. (c) Perpendicular remagnetization curve for Pt\Co\Ir\Co\Pt with t_{Ir} =1.3 nm and t_{Co} =1 nm exhibiting with AIC with switching fields of $\mu_0 H_{SF}$ = ± 40.5 mT. The presence of AIC indicates that no considerable influence of the seed and capping layer is present that hinders AIC.

was found that the choice of seed layer affects the coupling strengths and oscillation periods (*357, 371*). Surprisingly, it was found that the strength of the coupling increases with the roughness of the seed layer (*357*).

An influence of the ferromagnetic layer thicknesses on the opposite coupling behavior in Co\Pt\Ir\Co and Co\Ir\Pt\Co can be excluded as (almost) all investigated samples have the same Co-layer thicknesses of t_{Co} = 1 nm. The layers enclosing the Co-layers, on the other hand, might influence the observed coupling. A Pt$_{1\,nm}$\Co$_{1\,nm}$\Ir$_{1.3\,nm}$\Co$_{1\,nm}$\Pt$_{3\,nm}$ sample was prepared to test the influence of the bottom and capping layers. The corresponding remagnetization curve is shown in Fig. 4-26(c), exhibiting AIC with a switching field of $\mu_0 H_{SF}$ = 40.5 mT. This results in a coupling strength of J_{IEC} = -0.057 mJ/m², which is 12 % weaker than for a corresponding sample with Ir bottom and capping layers (Ir\(Co$_{1\,nm}$\Ir$_{1.3\,nm}$)$_2$), hosting J_{IEC} = -0.064 mJ/m² (c.f. Fig. 4-25(b)). Considering the experimental constraints, both values can be assumed as being equal and no considerable influences of bottom and capping layers are present.

In conclusion, the interlayer exchange coupling has been investigated in all four sample systems. For both symmetric systems, Pt\Co\Pt and Ir\Co\Ir, the behavior found in literature is well reproduced. Co layers couple ferromagnetically through Pt spacer layers. Via Ir, J_{IEC} oscillates with the spacer layer thickness and changes its sign periodically. The peak values are strongly damped with increasing spacer thickness and an oscillation period of $\lambda \approx 0.9$ nm is found. In the antisymmetric systems, the interlayer exchange coupling is dependent on the stacking order and composition of the interlayer. AIC originates from the electronic band structure of the spacer and both Co layers, thus it should be unaffected by inverse stacking. Varying widths of the interdiffusion zones at the top and bottom interfaces of the Co layers could break the inversion symmetry. The coupling in Co\Pt\Ir\Co is qualitatively similar to the one found in Co\Ir\Co, but depends on the spacer thickness and composition. For a constant Ir-layer thickness of t_{Ir} = 1.1 nm, an oscillation period with respect to t_{Pt} is observed with an oscillation period of $\lambda \approx 2.2$ nm. Ab initio calculations suggest that a similar increase of the period can be caused by alloying in the spacer layer. In the inversely stacked Pt\Co\Ir system, the Co layers couple ferromagnetically. An oscillation of the coupling strength with a short period of $\lambda \approx (0.3–0.6)$ nm is observed, but no sign change of J_{IEC}. A similar behavior was reported for Pt\Co\Pt. For a better understanding of this phenomenon, the parameter space for both systems should be explored in more detail, over a wider range of both, thickness and composition of the spacer layers. Furthermore, structural investigations of the interfaces are required to investigate the widths of the interdiffusion zones at the interfaces and to

which extent Pt and Ir form alloys. Such a dependence of the IEC on the stacking order has not been reported in literature so far.

5 Magnetic domains in multilayers

This chapter addresses the formation and measurement of magnetic domains in multilayer samples. Section 5.1 introduces the data acquisition and analysis for magnetic small-angle X-ray scattering and subsequently presents the obtained results. In section 5.2, the presence of domains in the regions for easy-plane magnetization is discussed and corresponding states calculated by micromagnetic simulations. Subsequently in section 5.3, domain spacing models are employed to describe the observed dependency of the domain size on the Co-layer thickness and extract the iDMI present in the systems.

5.1 Average domain sizes measured by X-ray resonant magnetic scattering

The average domain size in dependence on t_{Co} is studied in all four systems by X-ray resonant magnetic scattering (XRMS) in transmission geometry. The technique is only sensitive to the magnetization component (anti-)parallel to the propagation vector of the X-ray photons and its spatial resolution limited by the maximum detectable scattering vector $\mathbf{q}$ and the wavelength $\lambda = 1.59\,\mathrm{nm}$ (photon energy of 778 eV, Co L_3 edge). A further limitation is the signal-to-noise ratio (SNR), as the intensity drops strongly towards higher $\mathbf{q}$ values ($I \propto |\mathbf{q}^{2-4}|$) (*372*) and the limited dynamic range of the CCD detector. However, the recorded scattering patterns exhibit a very high SNR, thus it is not limiting in the following experiments.

The experiment was performed at the P04 beamline (*245*) at Petra III, using a photon energy of 778 eV (cobalt L_3 absorption edge) and a 50 µm wide exit slit. A 100-µm-sized pinhole is inserted in the beam 0.55 m upstream of the sample. The pinhole cuts the horizontally extended component of the beam down to 15 µm at the sample position, matching its vertical size. A second 100-µm-sized pinhole is placed in front of the sample to prevent off-axis light from scattering off the edges of the sample. The distance between sample and detector is 0.9 m. The wedge-shaped samples are scanned in 15– 25 µm steps and 3– 5 scattering patterns recorded per step. The exposure time is chosen so that the detector does not reach saturation, typical values are in the range of (0.1– 0.7) s. For each step, the scattering patterns were summed, dark-image corrected, and normalized to the equivalent of 1 s illumination. Furthermore, beam stops with different diameters were used during the experiments (compare Fig. 5-1 (c) and (d)).

The wedge-shaped samples host nm-sized magnetic domains with either maze or stripe domain patterns. Maze domains are present if the sample is demagnetized by an exponentially damped oscillating out-of-plane magnetic field starting from ± 1 T, which transfers the sample as close as

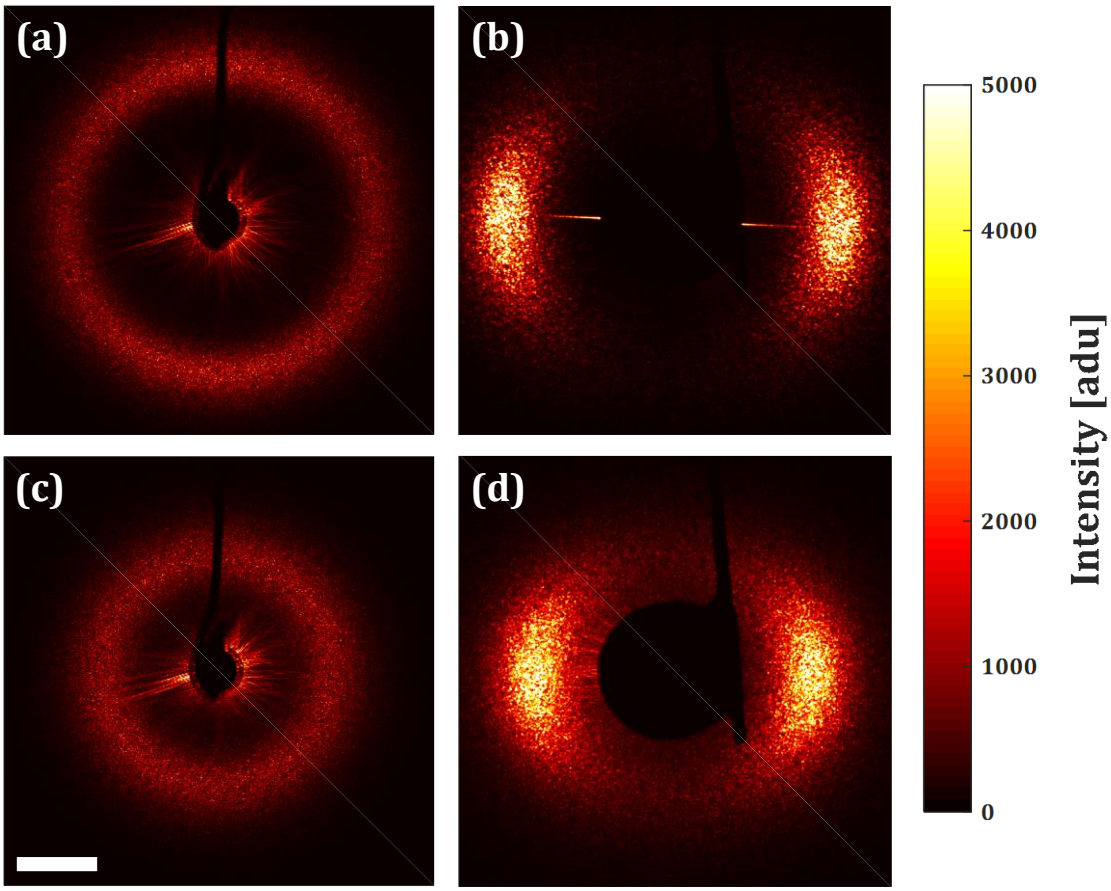

Figure 5-1: Scattering patterns obtained from $(Pt_{1\,nm}\backslash Co_t\backslash Ir_{1.1\,nm})_6$ with varying t_{Co} (a, c) maze domain patterns at t_{Co} = 1.82 nm and 1.42 nm (b, d) stripe domain patterns for $(Ir_{1.1\,nm}\backslash Co_t\backslash Pt_{1\,nm})_8$ at t_{Co} = 1.37 nm and 1.08 nm. For (a, c), five scattering patterns were averaged with an illumination time of 0.15 s each; for (b, d) five patterns with 0.3 s were averaged. All patterns are dark field corrected and normalized to an illumination time of 1 s. The scale bar indicates q = 0.2 nm^{-1}.

possible into the magnetic ground state. Stripe domains result from the same procedure but using an in-plane field, resulting in a higher-energy state than the maze pattern. Fig. 5-1 shows four magnetic diffraction patterns, two for maze domains in $(Pt_{1\,nm}\backslash Co_{0\text{-}2\,nm}\backslash Ir_{1.1\,nm})_6$ with (a) t_{Co} = 1.82 nm and (c) t_{Co} = 1.45 nm, and two for stripe domains $(Ir_{1.1\,nm}\backslash Co_{0\text{-}1.5\,nm}\backslash Pt_{1\,nm})_8$ with (b) t_{Co} = 1.37 nm and (d) t_{Co} = 1.08 nm.

Maze domains result in an isotropic donut-shaped diffraction pattern, from which an azimuthal averaging around the center yields the radial scattering intensity profile $I(q)$, with $q = |\mathbf{q}|$. The resulting profile from Fig. 5-1 (a) is shown as black line in Fig. 5-2. $I(q)$ contains both magnetic and background scattering contributions. The background scattering $B(q)$, shown in blue, acts as a

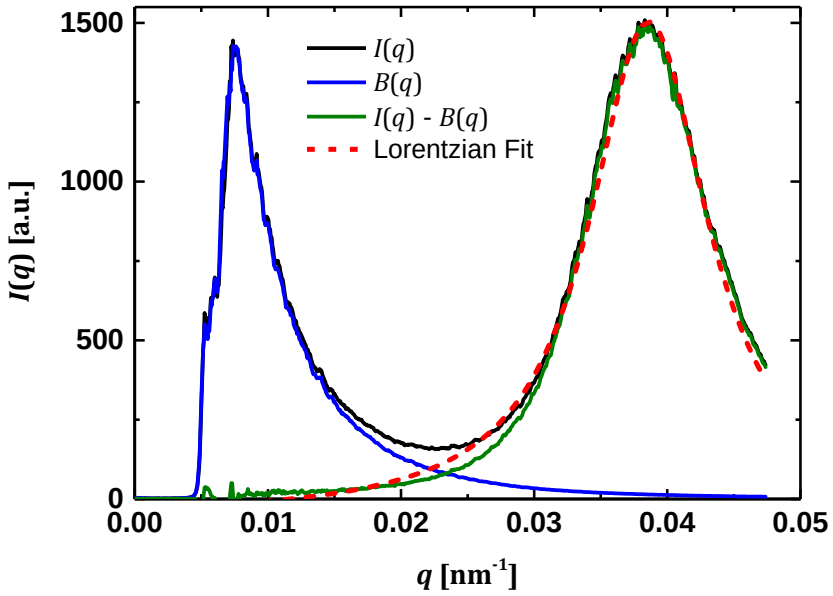

Figure 5-2: (a) Azimuthally integrated scattering pattern $I(q)$ (black) obtained from $(Pt_{1\,nm}\backslash Co_t\backslash Ir_{1.1\,nm})_6$ with t_{Co} = 1.82 nm. Background scattering $B(q)$ (blue) obtained from a scattering pattern with t_{Co} = 0.5 nm and normalized to $I(q)$ at q = 0.0075 nm^{-1}. (c) Magnetic scattering profile (green) from the difference $I(q)$ – $B(q)$. Fitting a Lorentzian (dashed red line) to the magnetic scattering reveals q_{max} = 0.039 nm^{-1}.

q-dependent background and can be obtained either from a scattering pattern of the saturated sample or from regions not exhibiting nm-sized domains. The general shape of $B(q)$ remains constant along the wedge, only its amplitude changes with the thickness of the sample. Thus, if $B(q)$ is obtained from a different sample position it can be normalized to match $I(q)$ in the region just outside the beam stop ($q \approx 0.0075$ nm^{-1} in Fig. 5-2). After subtracting the background scattering, a Lorentzian (red dashed line) is fitted to the magnetic scattering profile shown in green. It reveals the position q_{max} of the maximum scattering intensity, from which the ensemble-averaged domain size d_{avg} is obtained by:

$$d_{avg} = \frac{\pi}{q_{max}} . \qquad \text{Eq. 5-1}$$

This equation is only valid in the case of symmetric domain distributions, i.e. highly ordered domain patterns. For asymmetric distributions, a correction is required as the average domain size is smaller than obtained from q_{max} (*209*). The correction for the background scattering is especially important if q_{max} lies within the region of considerable background scattering, thus small q. Without the

subtraction, the large gradient of $B(q)$ deforms the magnetic scattering profile, resulting in an apparent peak shift.

Stripe domains do not result in an isotropic, but strongly anisotropic scattering pattern with two pronounced lobes of Gaussian-shape located on diametrically opposed sides of the scattering center (Fig. 5-1(b, d)). Thus, the azimuthal integration is not carried out over the entire angular range of 2π, but only in the range corresponding to the FWHM of the lobes. The angular width of the lobes corresponds to the quality of the stripe domain pattern. The wider the lobes, the more disturbed is the stripe pattern. The rest of the data analysis procedure is identical to the case of maze domains.

Fig. 5-3(a– f) shows magnetic scattering patterns of a wedge-shaped $(Pt_{1\,nm}\backslash Co_{0\text{-}2\,nm}\backslash Ir_{1.1\,nm})_6$ sample with maze domains for increasing t_{Co}. The wedge increases along the x-direction of the images. In (a), some anisotropic scattering is present with two lobes left and right of the beam stop region indicating stripe domains. With increasing t_{Co} in (b), the lobes shift towards the scattering center indicating an increase of d_{avg}. In (c), the scattering is isotropic, indicating a transition to maze domains, however q_{max} cannot be extracted as the scattering is inseparable from the beam stop region. With further increase of t_{Co}, the scattering is recorded further away from the center, thus d_{avg} decreases in (d) and (e). In (f), the scattering pattern exhibits again a little anisotropy with an increased intensity above and below the beam stop, thus the domain pattern starts to align in stripes parallel to the direction of the wedge.

In order to visualize the behavior derived from the scattering patterns, (g) shows a stitched image of the magnetic domain structure observed in a wedge-shaped $(Pt_{1\,nm}\backslash Co_{0\text{-}1.5\,nm}\backslash Ir_{1.1\,nm})_2$ sample. The domain size strongly depends on N, thus much larger domains are present for a sample with $N = 2$ (g) compared to $N = 6$ (a– f). The images have been obtained using differential full-field Kerr microscopy. For more information on the technique, the interested reader is referred to (*82, 87, 88*). Please note, that in (a– f) domains on the nanometer scale are probed while the scale bar in (g) represents 50 µm. The thickness of the Co-layers increases from left to right. Despite the different length scales, an analogous behavior is observed. Far to the left in (g), stripe-like domains appear and grow in size (a, b). This is followed by a region with very large domains (c), which then decrease in size (d, e). Only the counterpart to (f) is not observable in (g). The last feature only emerges in the case of $N \geq 4$ and is discussed in chapter 5.2.

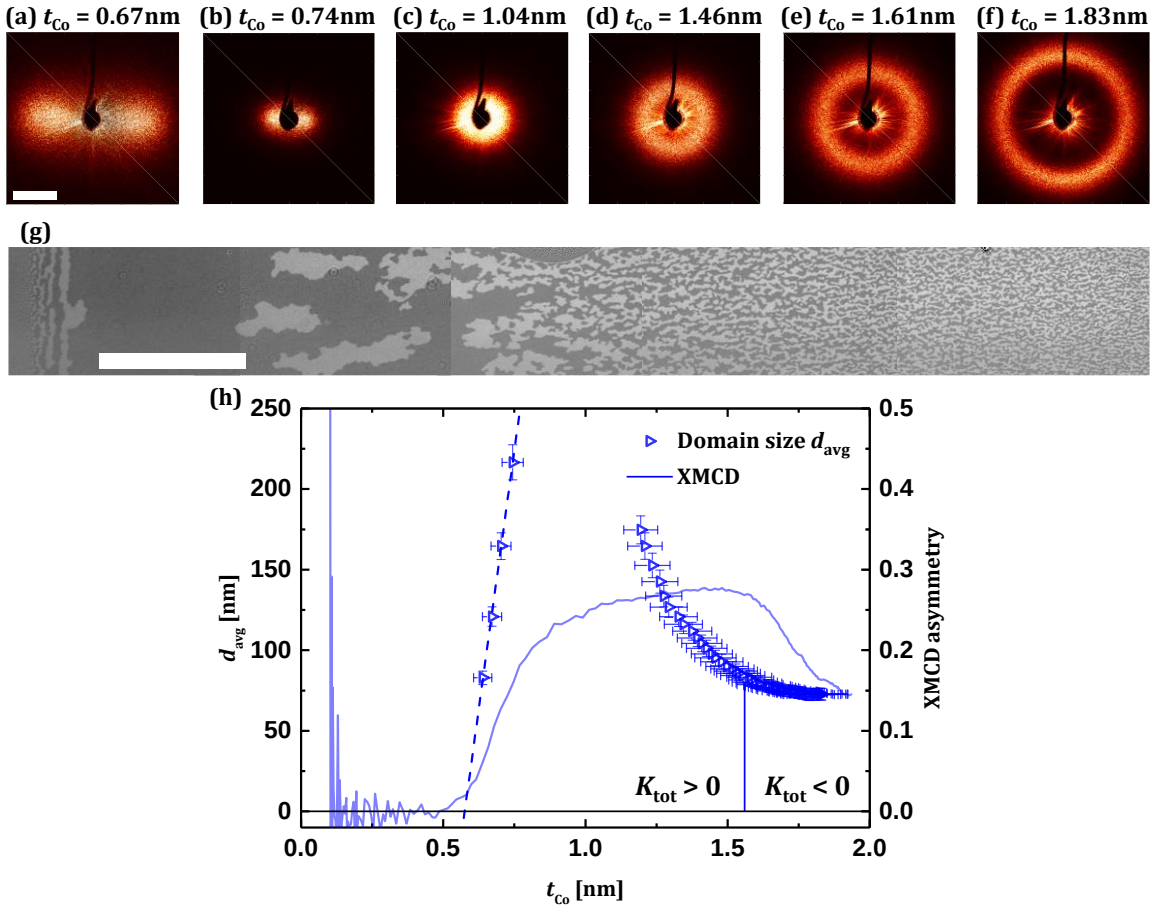

Figure 5-3: (a-f) Exemplary scattering patterns with maze domains in $(Pt_{1\,nm}\backslash Co_t\backslash Ir_{1.1\,nm})_6$ with varying t_{Co}. The scale bar indicates 0.3 nm^{-1}. (a, b) are corrected for background scattering to make the magnetic scattering. Furthermore the intensity in (a) is multiplied by a factor of 20. (g) Full-field Kerr microscopy of $(Pt_{1\,nm}\backslash Co_t\backslash Ir_{1.1\,nm})_2$ with t_{Co} = 0– 1.5 nm. The sample is almost identical to the one used in (a-f) but with N = 2, thus hosting larger domains. The scale bar indicates 50 µm. (h) Average maze domain sizes in $(Pt_{1\,nm}\backslash Co_t\backslash Ir_{1.1\,nm})_6$ extracted from scattering patterns along the wedge-shaped sample.

In Fig. 5-3(h), d_{avg} is plotted over t_{Co} for $(Pt_{1\,nm}\backslash Co_{0\text{-}2\,nm}\backslash Ir_{1.1\,nm})_6$ in maze geometry. The local t_{Co} in dependence of the position along the wedge is calibrated by aligning XAS and EDX spectra, as discussed in chapter 4.4.1 and shown in Fig. 4-15 (*208*). The different regions found in (a– f) are also apparent in the graph. The initial increase in domain size is followed by domains too large to be measured, and subsequently a gradual decrease of d_{avg} is seen. This dependence of d_{avg} on t_{Co} in the third region is frequently reported in literature (*373–377*) and discussed in accordance to domain spacing models (*71, 186, 378, 379*). The behavior at thinner t_{Co} is rarely investigated. However, for an annealed Au\Co\Au film an initial increase with a following decrease is reported (*375*),

albeit less pronounced. The initial increase can be correlated to the observed change in anisotropy, and thus to structural properties, as the increase of domain size and anisotropy starts from a similar t_{Co} (see Fig. 4-13 and chapter 4.3.3). d_{avg} increases linearly in this regime and a linear extrapolation of the data intercepts the abscissa at $t_{Co} = 0.53\,\text{nm}$. Interestingly, this value is close to the onset of the dichroic signal for $t_{on} = 0.5\,\text{nm}$, extracted from the magnetic XMCD asymmetry for the saturated sample, plotted in the same graph. For the measurement, a perpendicular field of $\approx 150\,\text{mT}$ was applied, sufficient to align the magnetization of the sample up to $t_{Co} \approx 1.5\,\text{nm}$. Under the given experimental constraints, it can be assumed that at this thickness ferromagnetism occurs (*208*), thus $T_C(t_{on}) = \text{RT}$. Furthermore, the first initial increase for $t_{Co} \approx 0.5-0.6\,\text{nm}$ might be the alignment of a superparamagnetic regime in the external field. The XMCD asymmetry is defined to (*196, 380*):

$$M_{asym} = \frac{\mu^+ - \mu^-}{\mu^+ + \mu^-}\,. \qquad \text{Eq. 5-2}$$

Moreover, the sample exhibits negative anisotropy for $t_{Co} > 1.56\,\text{nm}$, indicated by the vertical blue line, thus easy-plane magnetization might be expected, to which XRMS is not sensitive. Yet, scattering patterns are observed up to the largest t_{Co} accessible on the sample. This behavior is in contradiction to the previously mentioned domain spacing models, which expect a reorientation transition. However, such a behavior has already been described in literature for higher numbers of N and is attributed to the formation of a three-dimensional magnetic microstructure containing in-plane vortices(*373, 381*). A more detailed discussion follows in chapter 5.2.

Fig. 5-4(a) shows d_{avg} over t_{Co} for five samples with $N = 8$. Four of the five, namely Pt\(Co$_{0-1.5\,nm}$\Pt$_{2\,nm}$)$_8$ (black circles), Ir\(Co$_{0-1.5\,nm}$\Ir$_{1.75\,nm}$)$_8$ (red squares), (Pt$_{1\,nm}$\Co$_{0-1.5\,nm}$\Ir$_{1.1\,nm}$)$_8$ (blue triangles), and (Ir$_{0.9\,nm}$\Co$_{0-1.5\,nm}$\Pt$_{0.85\,nm}$)$_8$ (purple diamonds), display qualitatively the same behavior as the six-fold sample in Fig. 5-3(h), albeit being shifted along t_{Co} with respect to one another. Starting from small t_{Co}, the domains appear at a specific thickness and increase rapidly and almost linearly in size. For all but Ir\(Co$_{0-1.5\,nm}$\Ir$_{1.75\,nm}$)$_8$, the domains grow too large to be recorded. Upon further thickness increase, d_{avg} decreases. For all samples, out-of-plane domains are present up to the highest accessible Co-layer thickness. Pt\(Co$_{0-1.5\,nm}$\Pt$_{2\,nm}$)$_8$ and (Pt$_{1\,nm}$\Co$_{0-1.5\,nm}$\Ir$_{1.1\,nm}$)$_8$ retain $K_{tot} > 0$ along the wedge; in Ir\(Co$_{0-1.5\,nm}$\Ir$_{1.75\,nm}$)$_8$ and (Ir$_{0.9\,nm}$\Co$_{0-1.5\,nm}$\Pt$_{0.85\,nm}$)$_8$, however, K_{tot} falls below zero at $t_{Co} = 1.4\,\text{nm}$ (red vertical line) and $1.25\,\text{nm}$ (green vertical line), respectively. Analogous to the

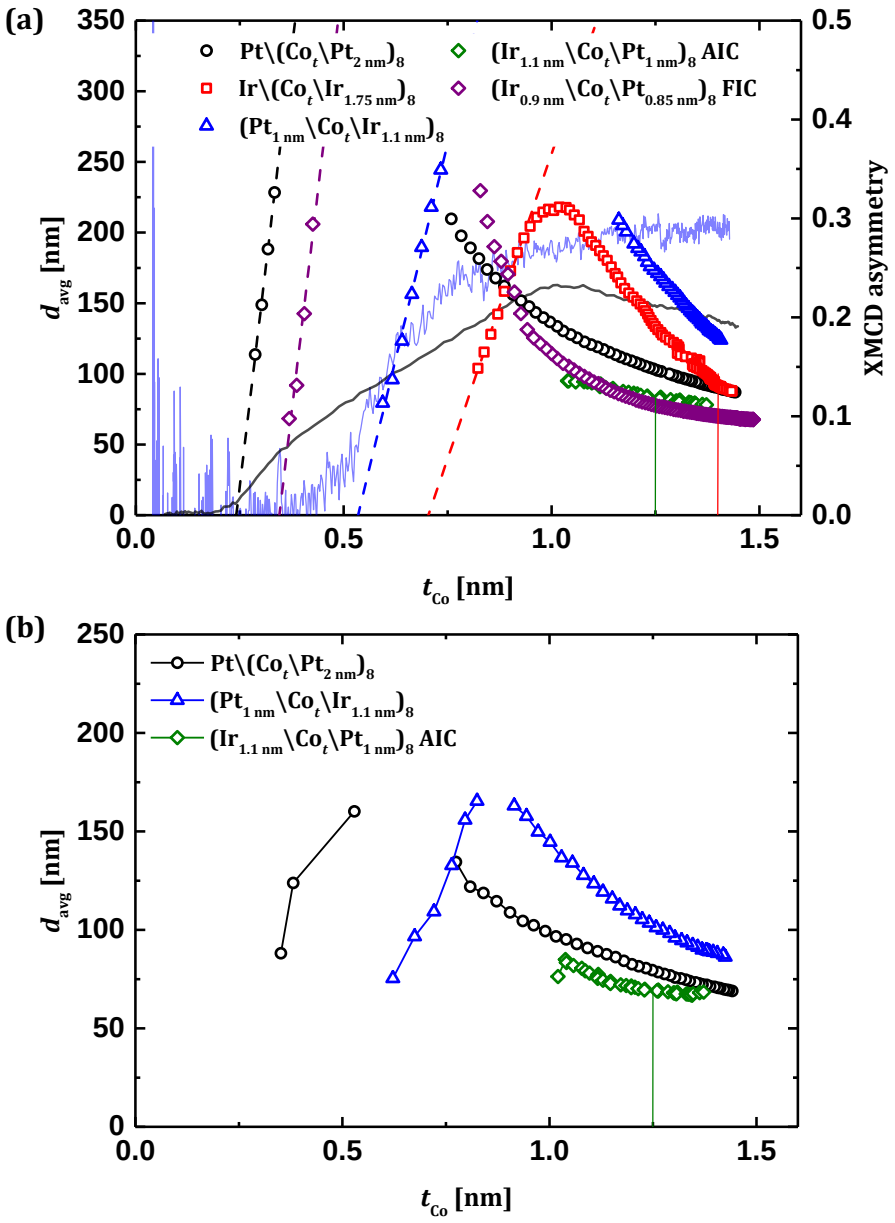

Figure 5-4: (a) Average maze domain sizes in various wedge-shaped samples with $N = 8$ extracted from corresponding scattering patterns. For Ir\Co\Pt, two samples were investigated with opposite IEC: one with antiferromagnetic interlayer exchange coupling (AIC) (green diamonds), and one with ferromagnetic interlayer exchange coupling (FIC) (purple diamonds). For Ir\Co\Ir and Ir\Co\Pt, the anisotropy favors easy-plane magnetization with $K_{tot} < 0$ for $t_{Co} = 1.4\,nm$ (Ir\Co\Ir, red vertical line) and $1.25\,nm$ (Ir\Co\Pt, green vertical line). The dashed lines represent linear fits to the data in the initial increase of the domain size. For Pt\Co\Pt and Pt\Co\Ir, the intercepts with the abscissa closely match the onset of dichroic signal, plotted as rad and black line with respect to the right ordinate. (b) Average stripe domain sizes in systems with $N = 8$. The same samples as in (a) were used with a different magnetic history. The lines are guides to the eye.

sample with $N = 6$, domains remain present, again caused by three-dimensional magnetic microstructures.

The dashed lines indicate linear extrapolations of the data from the first initial increase to the abscissa. For Pt\Co\Pt and Pt\Co\Ir, the interceptions with the abscissa at $t_{Co} = 0.24\,\text{nm}$ and $t_{Co} = 0.54\,\text{nm}$, respectively, are again close to the onsets for the dichroic signal obtained from XAS measurements of $t_{on} = 0.2\,\text{nm}$ and. $t_{on} = 0.45\,\text{nm}$. For the remaining samples no XAS data was acquired; nevertheless, they intercept the abscissa at $t_{Co} = 0.35\,\text{nm}$ (Ir\Co\Pt) and $t_{Co} = 0.7\,\text{nm}$ (Ir\Co\Ir). The values for t_{on} and the thicknesses for the intercepts with the abscissa are very close to the thicknesses of the thinnest ferromagnetic samples summarized in Tab. 4.3. The different thicknesses for the emergence of the magnetic signals in the systems might be explained as follows, assuming the interdiffusion zone widths are comparable for Pt and Ir: For ultrathin t_{Co}, the magnetic layers resemble alloys consisting of Co and both interface materials, with the composition depending on t_{Co}. T_C is reduced more strongly in alloys of Co with Ir than with Pt (c.f. Fig. 4-21(b)), requiring a Co-richer composition of the alloyed layer in Ir\Co\Ir than for Pt\Co\Pt in order for T_C to increase above RT. Thus, t_{Co} at the intercept with the abscissa is larger for Ir\Co\Ir than for Pt\Co\Pt. The interdiffusion width is known to be wider for the upper than the lower interface in Pt\Co\Pt (*127, 129, 296*) and it may therefore be assumed that less alloying with Ir occurs at the lower than the upper interface. Consequently, Ir as bottom interface material reduces T_C less than as upper interface and a Co-richer composition of the alloyed layer is required in Pt\Co\Ir than for Ir\Co\Pt. However, structural investigations are required to verify the extent of the interdiffusion zones and alloying in corresponding samples. A respective proposal has been submitted.

The fifth sample in Fig. 5-4(a), $(\text{Ir}_{1.1\,\text{nm}}\backslash\text{Co}_{0\text{–}1.5\,\text{nm}}\backslash\text{Pt}_{1\,\text{nm}})_8$ (green diamonds), deviates from the behavior of the remaining ones. The domains set in at $t_{Co} \approx 1.04\,\text{nm}$, but instead of rapidly increasing in size thereafter, they exhibit already their maximal size. Subsequently, they decrease in size until the edge of the membrane is reached. The difference in behavior is easily attributed to the antiferromagnetic interlayer coupling (AIC) (see chapter 4.5) present in the sample. In a simple picture, domains in presence of AIC should be unexpected. Domains form because they reduce the total energy of the system by reducing the stray field energy. In a multilayer sample with AIC, the stray fields of adjacent layers are expected to cancel each other, thus making the formation of domains obsolete. However, similar observations regarding the presence of domains in AIC multilayers are reported in literature (*353, 382–384*). Rößler et al. (*385*) proposed the presence of an

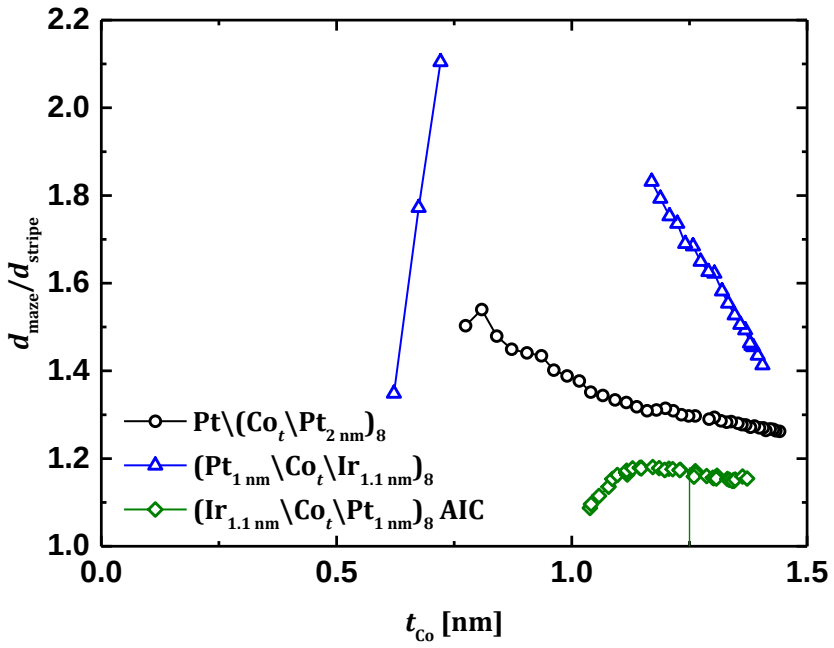

Figure 5-5: Ratio of domain sizes between maze and stripe patterns in Pt\Co\Pt, Pt\Co\Ir, and Ir\Co\Pt. In order to calculate the ratio, average maze domain sizes were linearly interpolated to t_{Co}-values for which domain sizes in stripe geometry were measured.

antiferromagnetic multi-domain ground state in multilayers with AIC for samples with weak anisotropy K_{tot}. In the presence of strong anisotropy, this state is suppressed. Consequently, $t_{Co} \approx 1.04\,nm$ does not mark the onset of ferromagnetism of the individual layers (which is at $t_{Co} \leq 0.4\,nm$; see chapters 4.2.2 and 4.3.3), but the transition from the "single-domain" state for strong anisotropy, where domains are suppressed, to the multi-domain ground state for weak anisotropy. For more information on this state, the interested reader is referred to (*353, 384, 385*).

Further, K_{tot} decreases below zero at $t_{Co} \approx 1.25\,nm$, yet domains are still present in the sample. This feature is not part of the domain formation process described for AIC multilayers in the listed publications, but again probably caused by the formation of a three-dimensional magnetization distribution. This region of the parameter space ($K_{tot} \lesssim 0$, $J_{IEC} < 0$, and $N \gg 1$) was not subject of any study in literature so far.

Fig. 5-4(b) shows the average domain sizes for stripe domains. The investigated samples are Pt\(Co$_{0\text{-}1.5\,nm}$\Pt$_{2\,nm}$)$_8$ (black circles), (Pt$_{1\,nm}$\Co$_{0\text{-}1.5\,nm}$\Ir$_{1.1\,nm}$)$_8$ (blue triangles), and (Ir$_{1.1\,nm}$\Co$_{0\text{-}1.5\,nm}$\Pt$_{1\,nm}$)$_8$ (green diamonds). A larger beam stop was used during these experiments, thus the scattering patterns of domain sizes larger than $\approx 180\,nm$ were inseparable from

the beam stop. For all three samples, in general, a similar behavior is observed to the one described for maze domains, albeit with smaller values for the domain sizes. In literature, either a ratio of 1.44 between the size of maze and stripe domains is frequently assumed (*267, 386, 387*), while domain spacing models give a ratio of 2.644 between checkerboard and maze domains (*186*) or claim that stripe and maze domains are equal in size (*71*). The ratio found in the scattering experiments is plotted in Fig. 5-5. It is evident that a constant ratio between both domain geometries does not exist; instead, the ratio differs from system to system and shows a strong dependency on t_{Co}. As both patterns were investigated on the same samples, only with a different magnetic history, varying structural properties can be excluded as the origin, leaving geometrical ones, and/or a different susceptibility to pinning. This seriously hampers the applicability of domain spacing models to predict average domains sizes in maze geometry, as the models are derived for stripe domains and the predicted sizes corrected by the falsely assumed fixed ratio.

5.2 Hybrid domain walls and 3D magnetic microstructures

This chapter addresses the formation of out-of-plane domains in multilayers for Co-layer thicknesses in which the anisotropy favors easy-plane magnetization. Experimental evidence of the microstructure is presented, which is then supplemented by micromagnetic simulations in section 5.2.1.

Fig. 5-3(f) shows a scattering pattern associated with the presence of perpendicular domains. It is recorded for a $(Pt_{1\,nm}\backslash Co_{0\text{–}2\,nm}\backslash Ir_{1.1\,nm})_6$ sample with $t_{Co} \approx 1.83$ nm, where the sample exhibits K_{tot} = -152 kJ/m³. Usually, domains are expected in the region of PMA and in the cone-state ($K_{2V} > 0$, $-2K_{2V} < K_{1,eff} < 0$) (*147, 148*). However, the region of the cone-state is in general not extended beyond a Co thickness wider than 0.1 nm (*139*) and should end in Pt\Co\Ir at $t_{Co} \approx 1.65$ nm, where $K_{1,eff}$ equals $-2K_{2V}$. This assumes K_{2V} to be of equal magnitude than in Pt\Co\Pt with K_{2V} = 70 kJ/m³ (*127–129*). Thus, K_{tot} clearly favors easy-plane magnetization for $t_{Co} > 1.65$ nm and no domains are expected beyond this thickness. The corresponding XHM image[37] with $t_{Co} = 1.82$ nm is shown in Fig. 5-6(a). It has a diameter of 2 µm and exhibits worm-like out-of-plane domains with d_{avg} = 72.6 nm. A line profile along the red dashed line, shown in (b),

[37] The experiment was performed at the P04 beamline (*245*) at Petra III, using a photon energy of 778 eV (cobalt L_3 absorption edge) and a 50 µm wide exit slit. A 100 µm sized pinhole was inserted 0.55 m upstream of the sample, in the converging beam after the refocusing mirror. The pinhole shapes the horizontally extended component of the beam down to 15 µm at the sample position, matching its vertical size. In this configuration, the beam has a lateral coherence length of 5.8 × 6.5 µm² (*208, 249*). 100 images per helicity were acquired with an illumination time of 0.7 s each.

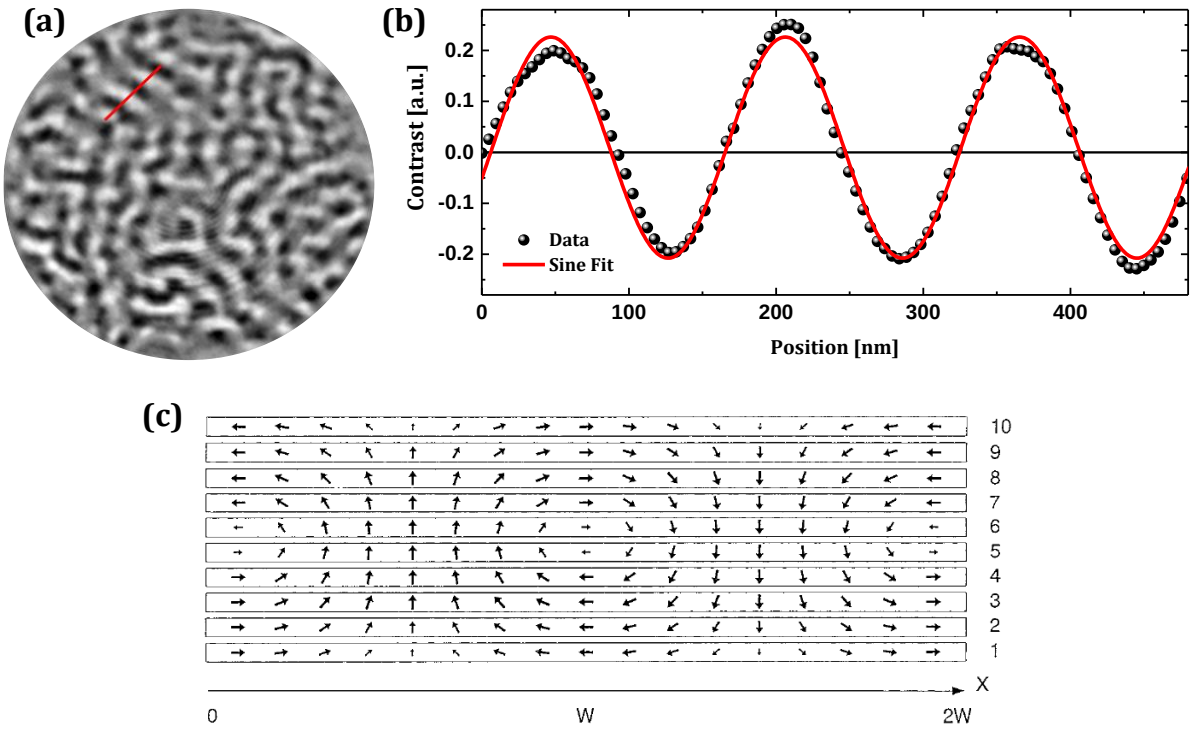

Figure 5-6: (a) Reconstructed XHM image for $(Pt_{1\,nm}\backslash Co_{0\text{–}2\,nm}\backslash Ir_{1.1\,nm})_6$ with $t_{Co} = 1.82\,nm$ and $d_{avg} = 72.6\,nm$; the diameter of the image is 2 µm and the Fresnel fringes from the propagation of the RH are visible due to the weak magnetic contrast. The resolution is limited to ~20 nm due to the use of a CCD camera with fewer pixels. (b) Perpendicular magnetization profile over three domain periods along the red line indicated in (a). The profile exhibits no plateaus, but a sinusoidal shape consisting only of domain walls, which is further indicated by a sinusoidal fit to the data shown in red. (c) Reproduction of the results of numerical simulations in Ref. (*388*) for a $X\backslash(Co_{2.4\,nm}\backslash X_{2.1\,nm})_{10}$ stack with non-magnetic spacer layers *X*. The length of an arrow represents the strength of the magnetization component in the xz-plane. The stack hosts a three-dimensional magnetic microstructure, called vortex state. Regions of perpendicular magnetization are separated by vortex-like hybrid domain walls. In the outer layers, Néel-character is prevalent, while the inner layers are Bloch like.

reveals the out-of-plane magnetization profile. The domains exhibit no region of constant magnetization; they rather have a sine-like profile and consist only of domain walls. A sine function, shown as red line, is fitted to the profile to illustrate the resemblance further. From Fig. 5-3(h) it is evident that a domain pattern exists over the entire accessible thickness range of the sample. Similar observations of perpendicular domains beyond the SRT region were made in $Ir\backslash(Co_{0\text{–}1.5\,nm}\backslash Ir_{1.75\,nm})_8$ and $(Ir_{0.9\,nm}\backslash Co_{0\text{–}1.5\,nm}\backslash Pt_{0.85\,nm})_8$, displayed in Fig. 5-4(a, b), albeit with the accessible thickness range being much smaller.

In the following, literature is reviewed addressing this kind of domain state. The existence of out-of-plane domains in regions with easy-plane favoring anisotropy was first observed in 1997 in$\mathrm{Pt\backslash(Co_{1.9\,nm}\backslash Pt}_t)_{10}$ multilayers with $t_{\mathrm{Pt}} = 1.3 - 4.3\,\mathrm{nm}$ by Belliard et al. (*373*). They attributed their observations to the appearance of vortex-like magnetic microstructures, so-called "vortex-states" that reduce the total energy of the system considerably. Two years later, numerical simulations of said samples found a three-dimensional vortex-like ground state (*388*). Their obtained results are reproduced in Fig. 5-6(c) for a $X\backslash(\mathrm{Co_{2.4\,nm}}\backslash X_{2.1\,\mathrm{nm}})_{10}$ stack with a non-magnetic spacer X (K_{tot} = -417 kJ/m³). Domain walls of both, Bloch and Néel character separate regions with perpendicular magnetization. A Néel character is prevalent for the outer layers of the stack, while the inner ones are Bloch like. This is called a hybrid domain wall and its energy is lower than for either pure Bloch or Néel wall. Within each layer, the magnetization rotates coherently, thus the domain period $2d_{\mathrm{vort}}$ is equal to two domain wall widths. The formation of this state reduces the anisotropy energy more than it increases the stray-field and exchange energies combined. For stronger easy-plane anisotropy of K_{tot} = -517 kJ/m³, they found a uniform easy-plane state while for values of $K_{\mathrm{tot}} > 0$ normal out-of-plane domains form, which are separated by hybrid DWs. The interlayer exchange coupling (IEC) was not considered in the simulations.

Similar experimental and numerical results were also reported for $\mathrm{Au\backslash(Co}_t\backslash\mathrm{Au_{3\,nm}})_N$ by Tekielak et al., where due to the large spacer-layer thickness no significant interlayer exchange was present (*381, 389*). They found that the vortex-like state has an onset in the region $N = 6 - 12$ and observed an accompanying slanting of the longitudinal MOKE remagnetization curves. They correlated the slanting with the vortex-state and the additional energy required to saturate the state. Furthermore, they observed an increase of the domain size with N.

Numerical studies by Kamberský et al (*390, 391*) investigated the influence of ferromagnetic IEC (FIC) on domain walls in multilayers with PMA. They found hybrid domain walls between domains in the absence of FIC and up to the highest investigated coupling constant J_{IEC} = 1.5 mJ/m². Furthermore, for samples with low in-plane anisotropy of $Q \lesssim 0.8$, they determined negative DW energies, making the implementation of DWs energetically favorable. Q is the so-called quality factor defined by (*391*):

$$Q = \frac{2\,K_{\mathrm{tot}}}{\mu_0 M_{\mathrm{S}}^2} + 1\,. \qquad \text{Eq. 5-3}$$

The presence of the predicted hybrid domain walls in multilayers was recently experimentally verified by Chauleau et al. (*392*) and Legrand et al. (*302*), where the chirality of the domain walls in

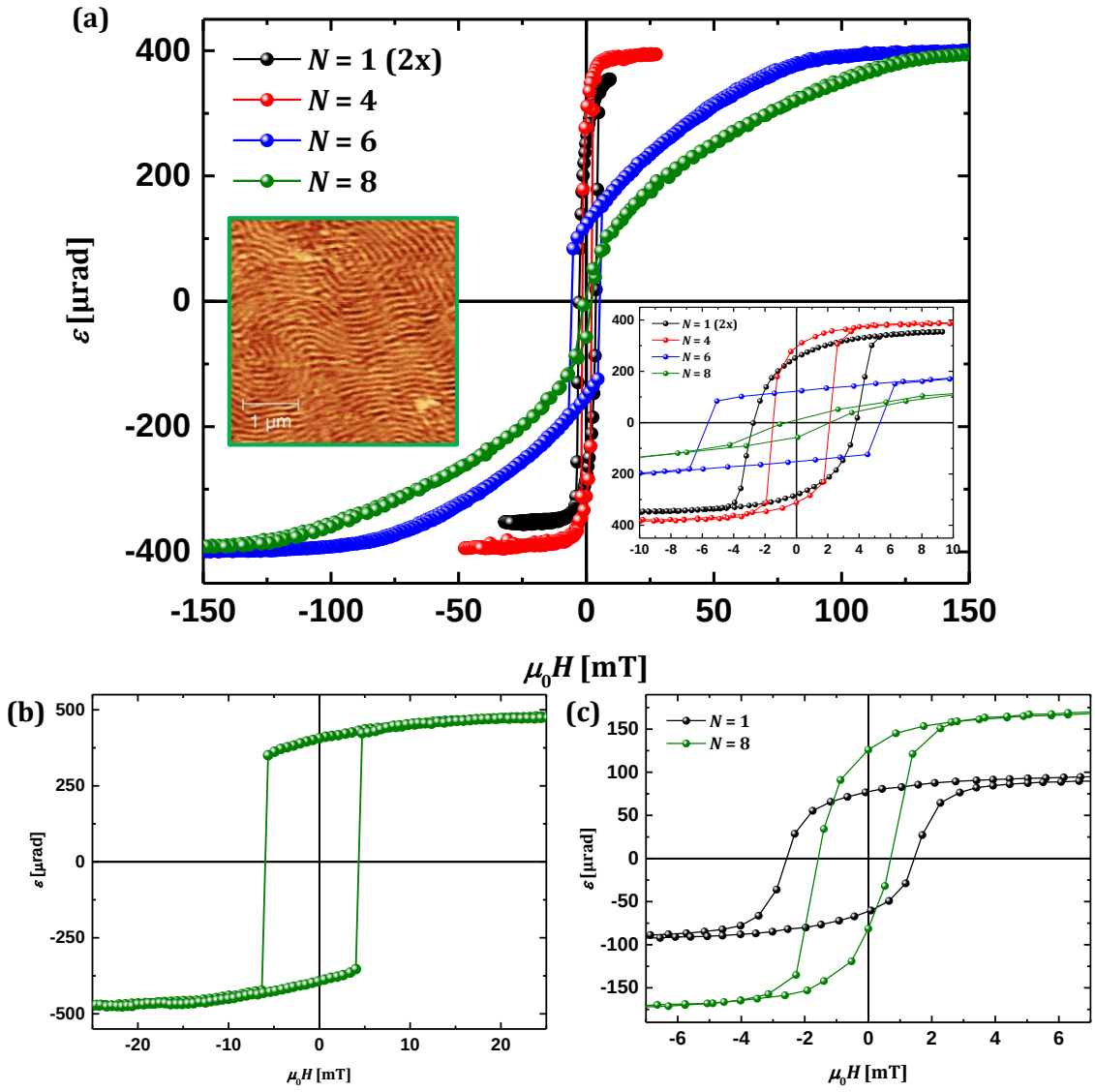

Figure 5-7: (a) Longitudinal remagnetization curves for Pt\(Co$_{2\,nm}$\Pt$_{2\,nm}$)$_N$ (K_{tot} ≈ -285 kJ/m³) for various number of repetitions obtained by MOKE. For N = 1, the data is multiplied by a factor of 2. For $N \leq 4$, the curves show an open hysteresis and are almost rectangular, as magnified in the right inset. For $N > 4$, the slanting of the curves indicates the presence of a three-dimensional magnetic microstructure. The presence of perpendicular domains with d_{avg} ≈ 60 nm was verified by MFM shown in the left inset. (b) Longitudinal remagnetization curve for Pt\(Co$_{4\,nm}$\Pt$_{2\,nm}$)$_8$ with almost rectangular shape with K_{tot} = -606 kJ/m³, indicating easy-plane behavior. (c) Longitudinal remagnetization curves obtained by MOKE for Ir\(Co$_{2\,nm}$\Ir$_{1.75\,nm}$)$_N$. Both curves have a rectangular shape with an open hysteresis indicating easy-plane behavior.

the interfacial layers of a multilayer stack was probed by dichroic scattering in grazing incidence reflection geometry.

In order to experimentally verify the formation of a vortex-state, a series of Pt\(Co2 nm\Pt2 nm)$_N$ samples were prepared with N = 1, 4, 6, and 8. The longitudinal remagnetization curves obtained with MOKE are shown in Fig. 5-7(a). For N = 1 and 4 (black and red), the curves exhibit an open hysteresis of almost rectangular shape and fully saturate for $\mu_0 H > \pm$ 5 mT. For N = 6 (blue), the curve still exhibits an open hysteresis in the range of $\mu_0 H < \pm$ 5 mT (shown in the inset), but for larger fields the curve is slanted and saturation is only reached at $\mu_0 H = \pm$ 80 mT. This effect is even more pronounced for N = 8 (green). The presence of out-of-plane domains in the sample with N = 8 was verified by magnetic force microscopy (MFM) imaging (*NanoScope IIIa, Digital Instruments*)[38], shown as inset in Fig. 5-7(a). The sample exhibits a stripe-like domain pattern with d_{avg} = 58.8 nm, which is randomly aligned. The pattern is in its shape and d_{avg} very similar to Fig. 1 in Ref. (*373*) for Pt\(Co2 nm\Pt2 nm)10 with $d_{\mathrm{avg}} \approx$ 60 nm.

To narrow down the thickness regime in which the vortex state is stable, a sample with t_{Co} = 4 nm was prepared, Pt\(Co4 nm\Pt2 nm)8. The longitudinal remagnetization curve, shown in Fig. 5-7(b), exhibits an almost rectangular shape without slanting and saturates for $\mu_0 H > \pm$ 8 mT. Thus, the ground state changes in the region of t_{Co} = (2– 4) nm from a vortex-state to easy-plane magnetization. This is in accordance with the findings in the previously presented numerical study by Labrune, where they found easy-plane magnetization for stronger easy-plane anisotropy (*388*). Experimental results from the most recent beam time of our group have shown that the transition occurs at $t_{\mathrm{Co}} \approx$ 3.7 nm.

Fig. 5-7(c) shows the longitudinal remagnetization curves for Ir\(Co2 nm\Ir1.75 nm)$_N$ with N = 1 and 8. Both curves exhibit an almost rectangular shape, indicating easy-plane behavior. Thus in this system, the transition to easy-plane magnetization occurs much earlier for $t_{\mathrm{Co}} <$ 2 nm. This system exhibits stronger easy-plane anisotropy of $K_{\mathrm{tot}} =$ -390 kJ/m³ for t_{Co} = 2 nm compared to Pt\(Co2 nm\Pt2 nm)$_N$ with $K_{\mathrm{tot}} =$ -285 kJ/m³. Thus, this earlier transition can be attributed to the stronger easy-plane anisotropy.

In the following, micromagnetic simulations were carried out using MicroMagnum (*394*) to qualitatively verify the formation of the vortex-structure for the prevalent magnetic properties, stacking geometry, e.g. number of layers N and spacer layer thickness t_{NM}. First, the underlying principle of the simulation is briefly introduced.

[38] The lift height was 30 nm. The used system has a resolution of ~ 30 nm, thus the domain pattern was barely resolvable. For more information about MFM, the interested reader is referred to (*72, 393*).

5.2.1 Micromagnetic simulation

For a given magnetic microstructure $\mathbf{M}(\mathbf{r})$, the various energy terms of Eq. 1-1 can be calculated with more or less effort. Stationary states $\mathbf{M}_{\mathrm{stat}}(\mathbf{r})$ correspond to minima in the energy landscape. For any domain configuration the total energy can be calculated in order to find the one which has the lowest energy (*117*); the risk is to ignore further configurations and the history of the applied field. In order to bypass these risks, Brown developed a variational principle with the goal that $\mathbf{M}_{\mathrm{stat}}(\mathbf{r})$ would be obtained without requiring any presumptions. The result of this principle are the so-called Brown's differential equations (*117, 395*), which are in vector notation:

$$\mathbf{N}_{\mathrm{eff}} = \mathbf{M}_{\mathrm{stat}}(\mathbf{r}) \times \mathbf{H}_{\mathbf{eff}} = 0\,, \qquad \text{Eq. 5-4}$$

with the so-called effective field $\mathbf{H}_{\mathrm{eff}}$, and the effective torque $\mathbf{N}_{\mathrm{eff}}$. $\mathbf{H}_{\mathrm{eff}}$ is related to the total energy density of Eq. 1-1 by (*395, 396*):

$$\mathbf{H}_{\mathbf{eff}} = \frac{1}{\mu_0}\nabla_{\mathbf{M}}E = \frac{2A_{\mathrm{Ex}}}{\mu_0 M_{\mathrm{S}}^2}\nabla^2\mathbf{M} - \frac{1}{\mu_0}\frac{\partial(E/V)_{\mathrm{mca}}}{\partial\mathbf{M}} + \mathbf{H}_{\mathrm{a}} + \mathbf{H}_{\mathrm{d}}. \qquad \text{Eq. 5-5}$$

Brown's equations show that for an energy minimum there is no effective torque $\mathbf{N}_{\mathrm{eff}}$ acting on the magnetization so that the magnetization is oriented parallel to the effective field. In order to describe the dynamical evolution of the magnetization the Landau-Lifschitz-Gilbert (LLG) equation is often used (Eq. **4-1**).

Micromagnetic simulations, like MicroMagnum (*394*) used in this thesis, solve the LLG numerically by dividing the ferromagnetic sample with volume V in small portions, in which the magnetization is assumed to be homogeneous (*397*). A cuboid mesh is used with the cell dimension (l_{x}, l_y, l_{z}). The choice of the cell dimension is critical. One the one hand, the sample is split into n cells, which correspond to $V/(l_{\mathrm{x}}l_y l_{\mathrm{z}})$, and the calculation time is proportional to n^2, thus choosing the cells too small will drag out the calculation forever. On the other hand, the discretization must be fine enough to calculate the magnetic microstructure, e.g. the domain wall, in a good approximation. The length scale below which the magnetization of such objects can be regarded spatially homogenous are the so-called exchange lengths (*396, 397*)

$$\delta_{\mathrm{ms}} = \sqrt{\frac{2A_{\mathrm{Ex}}}{\mu_0 M_{\mathrm{S}}^2}}, \quad \delta_{\mathrm{mca}} = \sqrt{\frac{A_{\mathrm{Ex}}}{K_{\mathrm{tot}}}}\,. \qquad \text{Eq. 5-6}$$

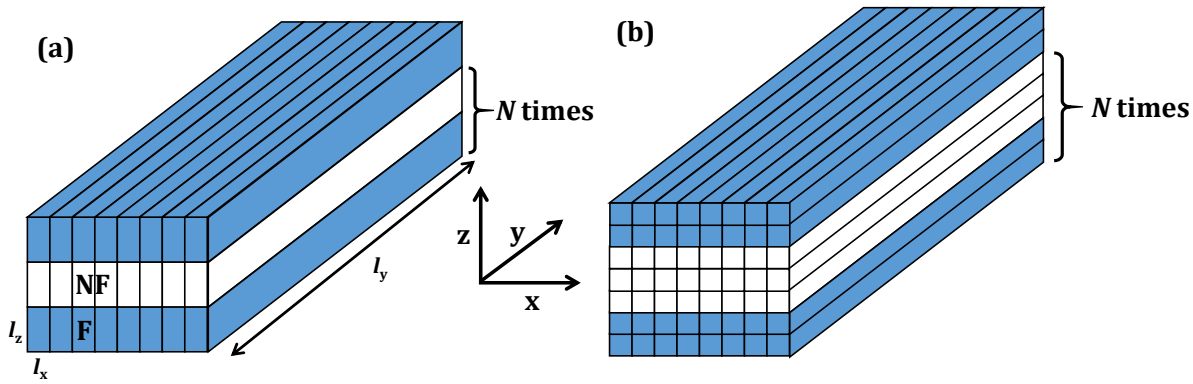

Figure 5-8: Unit-cell geometry used in the simulations. The elongation of the rod-shaped unit cells along the y-axis to the whole extent of the sample inhibits a variation of the magnetization along this axis. Along the x-axis, the cells have a fixed length of 1 nm. Along the z-axis, several cells are stacked with periodically varying magnetic properties to form the multilayers with N repetitions. If the layer thickness is a multiple of two, the unit cells have a length of 2 nm along the z-axis (a), otherwise 1 nm (b).

Depending on the dominating energy term that competes with the exchange energy (*398, 399*). δ_{ms} is the magnetostatic and δ_{mca} the magnetocrystalline exchange length. Realistic results of the calculations of the microstructure can be expected for cell sizes with $l_i \leq \delta_{ms}$ (or $l_i \leq \delta_{mca}$). Starting from an arbitrary configuration of $\mathbf{M}(\mathbf{r})$, MicroMagnum solves the LLG equation iteratively until the angle between $\mathbf{H}_{eff}(\mathbf{r})$ and $\mathbf{M}(\mathbf{r})$ everywhere in the sample is typically below 10^{-5} rad. The resulting microstructure $\mathbf{M}_{stat}(\mathbf{r})$ corresponds to a minimum in the energy landscape.

For more information about state of the art micromagnetic simulations, the interested reader is referred to the reviews (*400–402*).

Next, the simulation parameters are introduced. With the magnetic parameters M_S = 1.4 MA/m (see chapter 4.2) and A_{ex} = 23.3 pJ/m for bulk Co (*327*), follows the magnetostatic exchange length of δ_{ms} = 4.3 nm. With a strongly reduced value of A_{ex} = 10 pJ/m, follows δ_{ms} = 2.8 nm. Thus, choosing a cell size smaller than these length scales will ensure that realistic results can be obtained. To study the formation and stability of vortex-states in multilayers with easy-plane anisotropy, a similar approach to studies found in literature was adopted (*381, 389, 390*). Here, the simulation is limited to stripe-like vortex states in multilayers with t_{Co} = 2 nm and t_{NM} = 2 nm. The stripe geometry is achieved by choosing a rod-shaped unit cell as sketched in Fig. 5-8, with l_y equal to the full length of the sample along this axis (2500 nm). This inhibits a variation of $\mathbf{M}$ along l_y. The cell dimension along l_z was set to l_z = 2 nm for t_{NM} and t_{Co} equal to an even number (a), otherwise

l_z = 1 nm (b) (only used for the simulations shown in appendix A.1. The last dimension was set to l_x = 1 nm and n_x = 2500 cells were used. It should be noted that the stray field of $\mathbf{M}(\mathbf{r})$ is numerically calculated, thus the anisotropy parameter should not include the shape anisotropy that is caused from the stray-field. Thus,

$$K_u = K_{tot} + K_d, \qquad \text{Eq. 5-7}$$

is used in the simulations (see chapters 1.1.2 and 1.1.3). Interlayer exchange coupling was not considered and the initial state was a homogeneous magnetization along the x-axis. To verify that identical solutions for $\mathbf{M}_{stat}(\mathbf{r})$ are obtained with this geometry, the results for the vortex sizes reported in Ref. (*381*) were successfully reproduced for the cases $(Co_{2\,nm}\backslash NM_{3\,nm})_N$ with N = 12 and 24.

In the following, a sample with similar parameters compared to the one shown in Fig. 5-6(a) is simulated. The sample has N = 6 magnetic layers that are separated by spacer layers of thickness t_{NM} = 2 nm, M_S = 1.4 MA/m, A_{ex} = 18 pJ/m, and K_u = 960 kJ/m³ (K_{tot} = -270 kJ/m³). The dimensions of the unit cell are (l_x, l_y, l_z) = (1 nm, 2.5 µm, 2 nm) and a total number of (n_x, n_y, n_z) = (2500, 1, 11) cells were used. Fig. 5-9 depicts the obtained $\mathbf{M}_{stat}(\mathbf{r})$, exhibiting a vortex state highly similar to Fig. 5-6(c).

In Fig. 5-9(a– c), the three magnetizations components along the z-, x-, and y-axes are indicated by the red and blue color-coding. The arrows represent the magnetization direction of every second unit cell within the xz-plane, thus two arrows are separated by 2 nm in x-direction. Regions with perpendicular magnetization throughout the stack of alternating direction with a size of d_{vort} = (46 ± 1) nm are shown in (a), which are called domains throughout this section. In the regions in-between the domains, shown in (b), the magnetization in the upper and lower layers have opposite rotational sense. The upper three layers resemble Néel walls with clockwise rotational sense, the lower three with counterclockwise rotation. The structure is similar to a vortex without its core with a size identical to the domain size. As can be seen from (c), the inner and outer layers exhibit a mixture of Néel and Bloch like walls with a magnetization component along the y-axis. The y-components of the two outer layers (1 and 6) are always opposite with respect to one another; the same is true for the two inner layers (3 and 4). A fixed relation between the component of the inner and outer layers does not exist, e.g. layers 1 and 6 switch the direction of their magnetization at the position marked by [1] while layers 3 and 4 retain their respective signs. The same behavior is found for the inner layers switching their respective directions while the outer

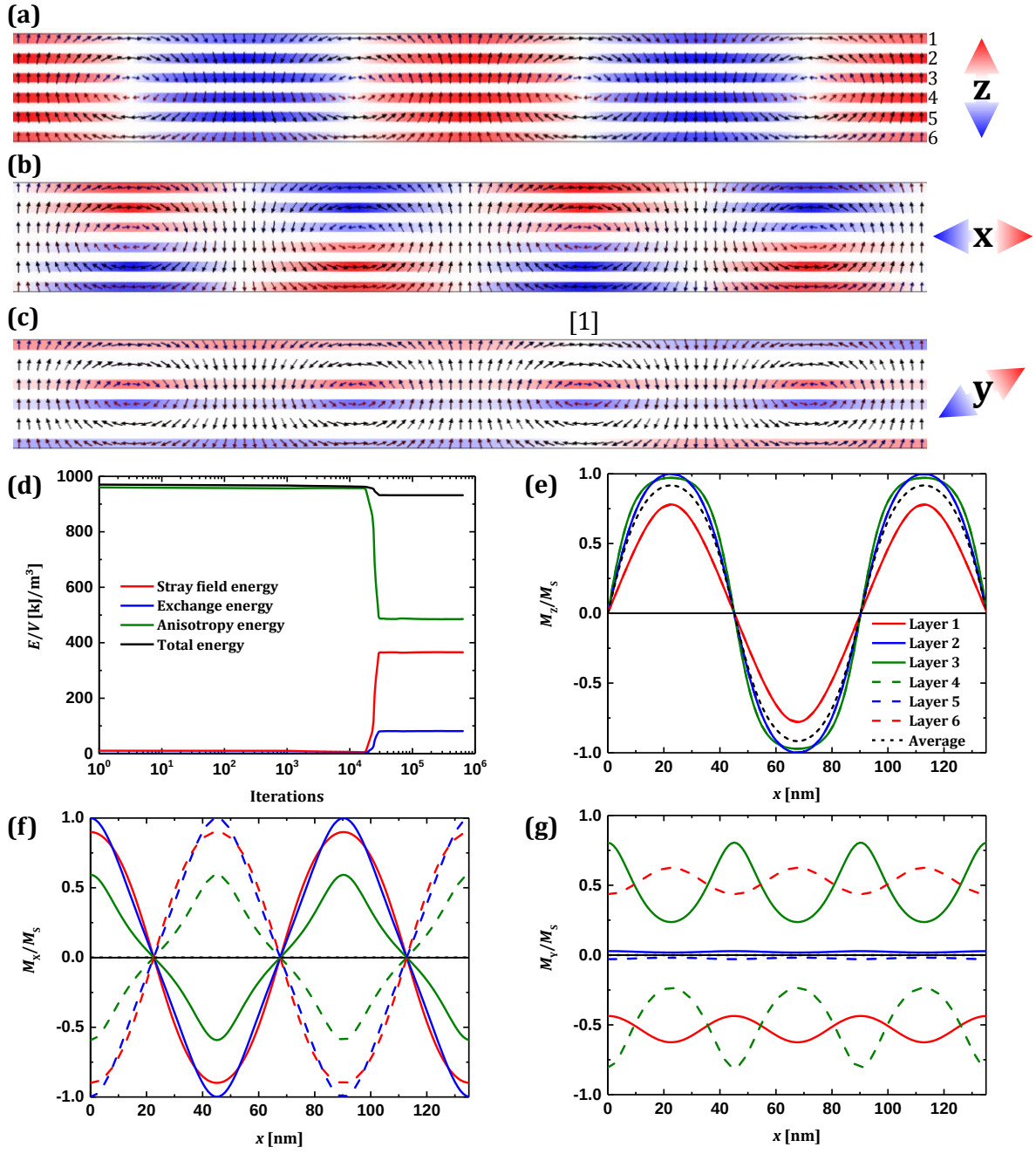

Figure 5-9: Simulated magnetization distribution for a $(Co_{2\,nm}\backslash NM_{2\,nm})_6$ sample with M_S = 1.4 MA/m, A_{ex} = 18 pJ/m, and K_u = 960 kJ/m³. In (a-c), the arrows indicate the magnetization direction within the xz-plane of every second unit cell, the component along the respective axes are color-coded in red and blue. At the position marked with [1], the magnetization direction in the outer layers switches. (d) The individual energy contributions and the total energy are plotted over the number of iterations during the simulation. (e- f) Magnetization profiles for the individual layers.

ones remain unchanged. In (e– g) the magnetization profiles of the individual layers are shown. In (e), the well-defined up and down stripe pattern is visible with the zero-crossing of all layers at the same position. The magnetization profile changes from the outer to inner layers from a sinusoidal to a more rectangular profile. The average magnetization profile has a sinusoidal shape (c.f. Fig. 5-6(b)). In-between the domains, as can be seen in (f, g), layers 1, 2, 5, and 6 represent almost pure Néel walls, while layers 3 and 4 are a mix of Bloch and Néel walls.

In (d) the individual energy contributions, normalized to the total magnetic volume, are plotted over the number of calculated iterations. In the initial homogeneous in-plane magnetized state, the total energy of the samples consists almost exclusively of the uniaxial anisotropy energy. The anisotropy energy drops, once the vortices start to move in from both edges of the sample around iteration 150,000. This is accompanied by an increase of both stray field and exchange energy that is in sum lower than the decrease of anisotropy energy. Thus, the total energy[39] decreases from $E_{\mathrm{tot}}/V = 970\,\mathrm{kJ/m^3}$ in the initial state to $932\,\mathrm{kJ/m^3}$ in the final state, or by 4 %.

It should be noted that by applying periodic boundary conditions along the x- and y-axes an almost identical result is obtained with less than 2 % difference in d_{vort}. However, when doing so an initially homogeneous state inhibits the formation of the vortex state because the magnetization cannot start to rotate anywhere. It forms however by inducing any kind of imperfection, e.g. one non-magnetic cell in the layer, or an initially arbitrary inhomogeneous magnetization state. Furthermore, the same simulation was conducted with varying n_{x} to ensure the length of the sample along the x-axis does not introduce any quantization of d_{vort}. For n_{x} = 2400, 2480, 2500, 2510, 2520, 2600, 2700, and 5000 identical results with less than 5 % deviation were obtained.

The qualitative formation of the vortex state as the energetically favorable state and the out-of-plane magnetization profile could be reproduced with the prevalent magnetic parameters and sample geometry. However, the simulated domain size is with $d_{\mathrm{vort}} = (46 \pm 1)\,\mathrm{nm}$ considerably smaller than the experimentally observed one with $d_{\mathrm{avg}} = (73 \pm 4)\,\mathrm{nm}$. One possible reason for the discrepancy is the non-consideration of the interlayer exchange coupling. Ferromagnetic IEC favors the parallel alignment of the magnetization of adjacent layers, which is in the vortex-state prevalent in the domains but not the vortices. Thus, IEC would likely cause an increase of the domain size while decreasing the vortices. Another possible reason is the geometry of the domain structure. In

[39] In literature, the decrease of the total energy is sometimes falsely accounted to a reduction of the stray field energy (*381, 388*).

the experiment, the sample hosted maze-like domains while the simulated ones are stripe domains, thus larger domains in the experiment are expected.

An analogous simulation has been performed for a sample with $N = 8$ but otherwise identical parameters. From the obtained $\mathbf{M}_{\mathrm{stat}}(\mathbf{r})$ follows a domain size of $d_{\mathrm{vort}} = (57 \pm 1)$ nm and a reduction of the energy from $E_{\mathrm{tot}}/V = 968\,\mathrm{kJ/m^3}$ to $E_{\mathrm{tot}}/V = 895\,\mathrm{kJ/m^3}$or a reduction of 7.5 %. The sample exhibits qualitatively the same features as shown in Fig. 5-9 for the sample with $N = 6$. The two additional layers behave closely like layers 2 and 5 in Fig. 5-9 (e– g). Furthermore, the layers 1 and 8 do not exhibit a y-component of significant magnitude. The calculated domain size is very close to the one obtained in a sample with similar magnetic properties of $d_{\mathrm{avg}} \approx 60\,\mathrm{nm}$ (c.f. inset of Fig. 5-7(a)). Unlike the previously discussed sample, this one hosted stripe domains, indicating again the importance of the geometry of the domain structure on the resulting domain size. On the other hand, the resemblance should not be overestimated, as e.g. the IEC has not been included in the calculation.

Further micromagnetic simulations, studying the influence of various parameters on the stability and size of the vortex-state can be found in appendix A.1.

5.3 Domain spacing models and iDMI

In this chapter, two domain spacing models are employed to calculate the minimum-free-energy domain size in the multilayer systems from the measured magnetic properties. The obtained results are then compared to the obtained average domain sizes from XRMS. Finally, it is shown that the extraction of the iDMI constant using this method remains highly unreliable.

The wall-energy model

One widely used domain spacing model for multilayers was proposed by Draaisma and de Jonge in 1987 (*403*). It is based on previous works by Kittel (*404*), Malek and Kambersky (*379*), Kooy and Enz (*405*) and Suna (*378*). In recent literature, it is frequently called wall-energy model. Within the model, the total energy consists of the domain-wall energy γ_{w} and the stray field energy E_{d}. The latter is numerically calculated from the sample geometry in dependence of the domain period $2d_{\mathrm{calc}}$ under the assumption of infinitely thin ($d_{\mathrm{calc}} \gg \Delta_{\mathrm{w}}$) and freely mobile domain walls and strongly coupled magnetic layers. Subsequently, the total energy is minimized with respect to d_{calc}, yielding the domain size for which the sample is in its lowest energy state. The stray field energy for the stripe phase is calculated from the poles at the interface between the ferromagnetic and nonmagnetic layers to:

$$E_\mathrm{d} = 1 + \sum_{n=1}^{\infty} \frac{4}{(n\pi)^3} \cdot \frac{d_\mathrm{calc}}{t_\mathrm{Co}} \cdot \sin^2\left(\frac{1}{2} n\pi\right) \cdot f_n(d_\mathrm{calc}), \text{ with}$$

$$f_n(d_\mathrm{calc}) = 1 - \exp\left(-2n\pi \frac{t_\mathrm{Co}}{d_\mathrm{calc}}\right) + \frac{\sinh^2\left(n\pi(t_\mathrm{Co}/d_\mathrm{calc})\right)}{\sinh^2\left(n\pi(t_\mathrm{N}/d_\mathrm{calc})\right)} \cdot \left[\frac{1}{N}\left(1 - \exp\left(-2n\pi \frac{N t_\mathrm{N}}{d_\mathrm{calc}}\right)\right) - \left(1 - \exp\left(-2n\pi \frac{t_\mathrm{N}}{d_\mathrm{calc}}\right)\right)\right], \quad \text{Eq. 5-8}$$

with the thickness of a multilayer period $t_\mathrm{N} = t_\mathrm{Co} + t_\mathrm{NM}$. Typically, the domain wall energy per unit area is calculated following the ansatz by Speckmann et al. for ultrathin uniaxial samples to (*375*):

$$\gamma_\mathrm{w} = 4\sqrt{A_\mathrm{Ex} K_\mathrm{tot}}\,. \quad \text{Eq. 5-9}$$

The domain wall energy density in the model follows using Eq. 5-9 to

$$E_\mathrm{w} = \frac{2\gamma_\mathrm{w}}{d_\mathrm{calc}} = \frac{8\sqrt{A_\mathrm{ex} K_\mathrm{tot}}}{d_\mathrm{calc}}. \quad \text{Eq. 5-10}$$

Kisielewski et al. (*406*) proposed another form of γ_w, where they claim that the real domain wall energy ranges in-between that of a, what they call, fully demagnetized wall (Eq. 5-9) and that of a bulk wall (Eq. 5-9 but with K_u instead of K_tot), which disregards all demagnetizing contributions. By taking into account the influence of the finite width of the domain wall and from comparison to micromagnetic simulations they, they end up with (*406*):

$$\gamma_\mathrm{w} = 4\sqrt{A_\mathrm{ex} K_\mathrm{u}} \cdot \left(1 - \frac{1}{4Q\sqrt{1 - Q^{-1}}}\right). \quad \text{Eq. 5-11}$$

In the final step for all models, itis taken into account that in the presence of DMI the domain wall energy is lowered by forming Néel walls of the proper rotational sense (*37*) and thus the DMI can be estimated by comparing experimentally observed average domain sizes d_calc to ones calculated by domain spacing models (*192*). The domain wall energy in the presence of DMI follows to (*37*):

$$\gamma_\mathrm{w,DMI} = \gamma_\mathrm{w} - \pi|D_\mathrm{DMI}|. \quad \text{Eq. 5-12}$$

In the following, this model is called "DJ1 model" for $\gamma_\mathrm{w,DMI}$ following the definition in Eq. 5-9 and "DJ2 model" for Eq. 5-11.

Volume and surface charge model

Over the years, several corrections of the wall energy model have been suggested to account for the surface charges by assuming linear (*407*) and sine domain wall profiles (*408*) in single layers. Recently, a numerical model has been suggested by Lemesh et al. that assumes a domain wall profile

following Lilley's definition (*188*) (c.f. Fig. 1-4) and takes surface and volume charges of domain walls into account. The model makes use of the average medium approach, first proposed by Suna (*378*), which treats the multilayer as a single magnetic layer with thickness $t' = N \cdot t_\mathrm{N}$ with rescaled magnetic properties. Thus, strong ferromagnetic interlayer coupling is assumed. The rescaling factor f is given by (*378*)

$$f = \frac{t_\mathrm{Co}}{t_\mathrm{N}}, \qquad \text{Eq. 5-13}$$

and the rescaled properties follow to (*71, 192, 378*)

$$A'_\mathrm{ex} = fA_\mathrm{ex}, \;\; M'_\mathrm{S} = fM_\mathrm{S}, \;\; K'_\mathrm{tot} = fK_\mathrm{tot}, \;\; D'_\mathrm{DMI} = fD_\mathrm{DMI}\,, \qquad K'_\mathrm{u} = fK_\mathrm{u} - (f - f^2)\frac{\mu_0}{2}M_\mathrm{S}^2\,. \qquad \text{Eq. 5-14}$$

The effective medium model is applicable within the limits of the domains being large with respect to the domain wall width parameter Δ_w, which is similar to the infinitely thin walls assumed in the wall energy model. Furthermore, the multilayer period t_N has to be small with respect to the domain walls and domains (*71*):

$$d_\mathrm{calc} \gg \Delta_\mathrm{w} = \frac{\delta_\mathrm{w}}{\pi}, \qquad d_\mathrm{calc} \gg t_\mathrm{N}, \qquad 2\delta_\mathrm{w} \gg t_\mathrm{N}. \qquad \text{Eq. 5-15}$$

The total energy density of a multilayer sample with stripe domains follows after a lengthy calculation, which is not reproduced here, to[40]:

$$\frac{E^N_\mathrm{tot}}{V'} = \frac{1}{d_\mathrm{calc}}\left(\frac{2A'_\mathrm{ex}}{\Delta_\mathrm{w}(t')} + 2K'_\mathrm{u}\cdot\Delta_\mathrm{w}(t') - \pi|D'_\mathrm{DMI}|\sin\varphi\right) + \frac{E^1_\mathrm{d,s}}{V'} + \frac{E^1_\mathrm{d,v}}{V'} + C\,. \qquad \text{Eq. 5-16}$$

Here, the stray field energy density that originates from surface charges is given by

$$\frac{E^1_\mathrm{d,s}}{V'} = \frac{\pi\mu_0 M'^2_\mathrm{S}\cdot\Delta^2_\mathrm{w}(t')}{d_\mathrm{calc}t'}\cdot\sum_{n=1}^{\infty}\frac{\sin^2\left(\frac{\pi n}{2}\right)}{n}\cdot\frac{1-\exp\left(-\frac{\pi n t'}{d_\mathrm{calc}}\right)}{\sinh^2\left(\frac{\pi^2 n\cdot\Delta_\mathrm{w}(t')}{2d_\mathrm{calc}}\right)}, \qquad \text{Eq. 5-17}$$

and the one from volume charges by

[40] Please note that Eq. 5-16 is originally given in Ref. (*71*) in dependence of external fields and in terms of the domain period with minor and majority domains (favored and unfavored domains). In the version given here, the field term is omitted and all domains are of equal size.

$$\frac{E^1_{\mathrm{d,v}}}{V'} = \frac{\pi\mu_0 M'^2_{\mathrm{S}} \cdot \Delta^2_{\mathrm{w}}(t') \cdot \sin^2\varphi}{d_{\mathrm{calc}} t'} \cdot \sum_{n=1}^{\infty} \frac{\sin^2\left(\frac{\pi n}{2}\right)}{n} \cdot \frac{\exp\left(-\frac{\pi n t'}{d_{\mathrm{calc}}}\right) + \frac{\pi n t'}{d_{\mathrm{calc}}} - 1}{\cosh^2\left(\frac{\pi^2 n \cdot \Delta_{\mathrm{w}}(t')}{2 d_{\mathrm{calc}}}\right)}. \qquad \text{Eq. 5-18}$$

The constant C in Eq. 5-16 is generated by the application of the effective medium approach to the surface stray field energy and is equivalent to a constant term found by Suna (*378*) with:

$$C = (f - f^2)\frac{\mu_0}{2} M_{\mathrm{S}}^2. \qquad \text{Eq. 5-19}$$

The angle φ in Eq. 5-16 is the domain wall angle introduced in chapter 1.2.2 and is calculated by

$$\sin\varphi = \begin{cases} -D'_{\mathrm{DMI}}/D'_{\mathrm{thr}}, & |D'_{\mathrm{DMI}}| < D'_{\mathrm{thr}} \\ -\mathrm{sgn}(D'_{\mathrm{DMI}}), & |D'_{\mathrm{DMI}}| \geq D'_{\mathrm{thr}} \end{cases}, \qquad \text{Eq. 5-20}$$

with convention is chosen that for domain wall angle $\sin\varphi < 0$, $D_{\mathrm{DMI}} > 0$ and the threshold DMI D_{thr} required to fully rotate the domain wall into the Néel type (c.f. chapter 1.2.2) here defined in dependence of the rescaled film thickness t' by

$$D'_{\mathrm{thr}} = \frac{2\mu_0 M'^2_{\mathrm{S}}}{\frac{\pi^2}{t' \ln(2)} + \pi\sqrt{\frac{K'_{\mathrm{u}} + K'_{\mathrm{d}}}{A'_{\mathrm{ex}}}}}. \qquad \text{Eq. 5-21}$$

Finally, the domain wall width parameter is found to exhibit a dependence on the thickness of the magnetic layer for which Eq. 1-33 (divided by π) represents the ultrathin limit. However, as within the effective medium model the thickness of the entire multilayer stack is considered to be the thickness of the effective magnetic layer, the ultrathin limit is not applicable. An explicit solution can be derived for the case of thick and ultrathin samples:

$$\Delta_{\mathrm{w}}(t' \to \infty) = \Delta_\infty = \sqrt{\frac{A'_{\mathrm{ex}}}{K'_{\mathrm{u}} + K'_{\mathrm{d}} \cdot \sin^2\varphi}},$$
$$\Delta_{\mathrm{w}}(t' \to 0) = \Delta_0 - \frac{\mu_0 M'^2_{\mathrm{S}}}{4\pi K'_{\mathrm{tot}}} t', \qquad \text{Eq. 5-22}$$

with

$$\Delta_0 = \sqrt{\frac{A'_{\mathrm{ex}}}{K'_{\mathrm{tot}}}}. \qquad \text{Eq. 5-23}$$

For intermediate t', Δ_{w} is approximately extrapolated from the constant for thick t' and the linear function for ultrathin t':

$$\Delta_w(t') = \Delta_0 - \frac{1}{\frac{2\pi(Q'-1)}{t'} + \frac{1}{\Delta_0 - \Delta_\infty}}, \qquad \text{Eq. 5-24}$$

with the quality factor Q' for the rescaled parameters. Eq. 5-24 is exact for thin and thick samples; for intermediate t', the relative error is below 10% for $Q' \geq 1.2$.

Subsequently, the total energy in Eq. 5-16 is minimized with respect to d_{calc}, yielding the domain size of the magnetic ground state for a given set of magnetic parameters. In the following, this model is called "VSC model".

Calculation of the average domain size and extraction of D_{DMI}

In this section, the average domain size is calculated from measured magnetic parameters and compared with experimental data. Because the models are derived for stripe domains and strong ferromagnetic coupling, only the two samples are addressed that were investigated in the stripe geometry and exhibit FIC (c.f. Fig. 5-4(b)), namely Pt\(Co$_{0-1.5\,nm}$\Pt$_{2\,nm}$)$_8$ and (Pt$_{1\,nm}$\Co$_{0-1.5\,nm}$\Ir$_{1.1\,nm}$)$_8$.

Fig. 5-10 shows the dependency of the total energy density E_{tot}/V on the domain size d_{calc} for all models for (Pt$_{1\,nm}$\Co$_{0-1.5\,nm}$\Ir$_{1.1\,nm}$)$_8$ with t_{Co} = 1.31 nm, t_{NM} = 2.1 nm, M_S = 1.4 MA/m, K_{tot} = 180 kJ/m³, A_{ex} = 12.4 pJ/m, and D_{DMI} = 0 mJ/m². The indicated parameters are varied. In (a, c, e), the DJ1 model is indicated by the solid line while the dashed line represents the DJ2 model; (b, d, f) shows the VSC model. The dots indicate the domain size d_{calc} for which the lowest energy density is obtained. The reduction or increase of a given parameter has the same effect for all models on the total energy density and d_{calc}. Striking is, however, that E_{tot}/V obtained from the VSC model is much smaller than for both DJ models. The difference is caused by the effective medium approach, which treats the entire stack as a single layer with rescaled (reduced) magnetic parameters. The variation of M_S, shown in (a, b), has the strongest influence on the calculated E_{tot}/V and d_{calc}. A reduction of M_S strongly decreases the stray field energy and the domain wall energy dominates E_{tot}/V already for larger values of d_{calc}. It is noteworthy that the energy minimas are very shallow, therefore only weak torques drive the system into its minimum making it highly susceptible to the influence of effects such as pinning. A reduction of A_{ex}, shown in (c, d), has the opposite effect, as it decreases the domain wall energy, making the implementation of additional walls energetically cheaper. The same is true for D_{DMI}, shown in (e, f). Here, however, a special case has to be considered, which is shown in (e) for D_{DMI} = 2 mJ/m² as green lines. For sufficiently large values of D_{DMI} (or sufficiently small domain wall energies), the domain wall energy becomes nega-

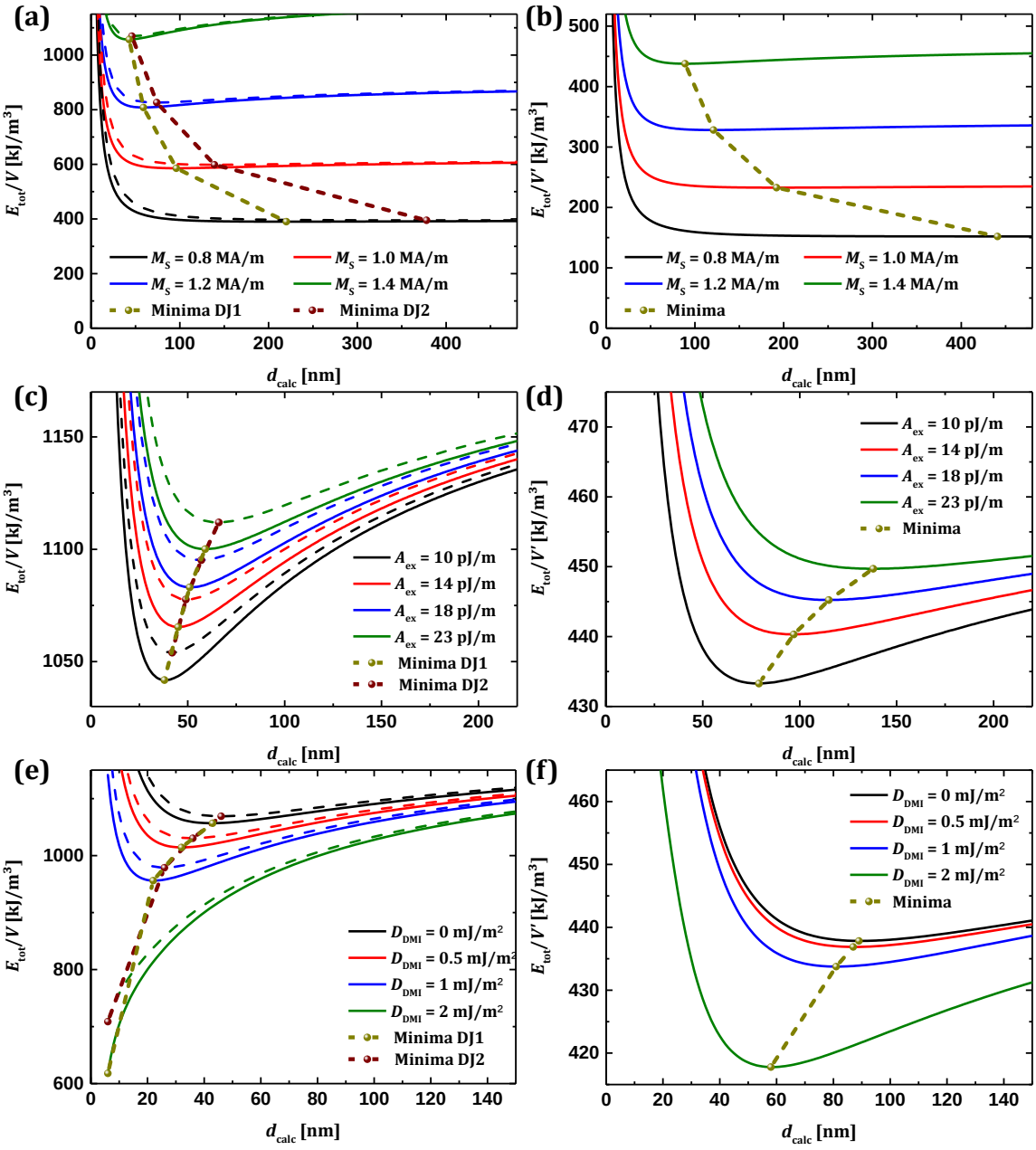

Figure 5-10: Total energy density plotted over the domain size d_{calc} in dependence of M_S, A_{ex}, and D_{DMI} calculated with the DJ1 (solid line) and DJ2 (dashed line) (a, c, e), and the VSC models (b, d, f). The minimas, which are very shallow, are the domain sizes for the energetic ground state of the system. The effective medium approach used in the VSC model rescales the magnetic parameters to a larger volume V' including the spacer layers, reducing the energy densities. In (a, b) M_S is varied. Lower values of M_S strongly reduce the calculated energy densities, while shifting the minimum to larger domains. In (c, d), a reduction of A_{ex} also decreases E_{tot}/V and its minimum, albeit much less pronounced than for M_S. (e, f) Increased values of D_{DMI} reduce the E_{tot}/V and shift the minimas to smaller d_{calc}. For the large values of D_{DMI} (green lines) in (e), the domain wall energy becomes negative.

tive, favoring the implementation of ever more domain walls, causing a collapse of d_{calc} and leading to the formation of a Skyrmion lattice.

In the following, average domain sizes are calculated for $(Pt_{1\,nm}\backslash Co_{0-1.5\,nm}\backslash Ir_{1.1\,nm})_8$ for the Co-layer thicknesses at which scattering data was recorded using M_S = 1.4 MA/m and D_{DMI} = 0 mJ/m². The corresponding values for K_{tot} in dependence of t_{Co} were calculated using the values K_V = 0.23 MJ/m³ and $2K_S$ = 1.55 mJ/m² for $t_{Co} \geq 1$ nm (taken from Tab. 4.3) and linearly interpolated for t_{Co} < 1 nm from the values plotted in Fig. 4-13(e, f) (see section4.3.3). A_{ex} was interpolated from the values shown in Fig. 4-22(a), obtained by the model introduced in chapter 4.4 using σ = 0.5 nm and X_{cut} = 0.375. The obtained d_{calc} are plotted in Fig. 5-11(a) over t_{Co} together with the experimental data from Fig. 5-4(b). The calculated values qualitatively resemble the measured ones to a certain degree. However, especially for $t_{Co} \geq 0.9$ nm both DJ models yield too small values for d_{calc}. On the contrary, the values obtained from the VSC model resemble the measured data in this regime quite well. For $t_{Co} < 0.9$ nm, all models reproduce the collapse observed in the experimental data.

This qualitatively good reproduction of the data is actually surprising. The domain sizes are calculated using D_{DMI} = 0 mJ/m² while the antisymmetric system is expected to host considerable D_{DMI}. In literature, values[41] of $D_{DMI} \cdot t_{Co}$ = 0.84– 2.05 mJ/m are frequently reported (*69*). For $t_{Co} \geq 0.9$ nm, the experimentally obtained domain sizes are already larger than the ones predicted by the models; any additional D_{DMI} would only further reduce the calculated values. Consequently, no D_{DMI} should be expected in the sample. For $t_{Co} < 0.9$ nm, non-vanishing D_{DMI} can be extracted using the DJ2 and VSC model. The obtained values are plotted in Fig. 5-11(c) over t_{Co} as open symbols and vary from one model to the other by a factor of approximately two. Since the DMI is expected to originate from the interfaces, a $1/t_{Co}$ behavior should be expected. Such behaviors are indicated by the dashed lines for various values of atomistic DMI strength D_{at}, given as energy per interface Co atom bond (*409*):

$$D_{DMI} = \frac{3\sqrt{2} \cdot D_{at}}{a^2 \cdot t_{ML} \cdot c}, \qquad \text{Eq. 5-25}$$

[41] This representation of the values for D_{DMI} is analogous to the one used for the anisotropy to account for the expected $1/t_{Co}$ behavior of K_S. Using this representation a single value describes the value of D_{DMI} independent of t_{Co}.

With t_{ML}, the thickness of the magnetic layer in ML, $c = 6.252 \cdot 10^{18}$ J/eV, the conversion factor from eV to J, and the lattice constant $a = 0.39$ nm, measured by XRD for ultrathin Pt\Co\Pt samples prepared under similar conditions in our group (*127*). It is obvious that the data do not exhibit a $1/t_{Co}$ behavior. It is unphysical that a sample hosts no D_{DMI} for $t_{Co} \geq 1$ nm, while for $t_{Co} < 1$ nm D_{DMI} a $1/t_{Co}$ behavior is found. Consequently, the extracted values of D_{DMI} are not meaningful. This may be caused by a variety of reasons. E.g., pinning of the domain walls can inhibit the samples from reaching its energetic ground state, the input values for the magnetic parameters in the models are incorrect, or the prerequisites for the application of the models are not met.

Concerning the magnetic parameters, it is worth mentioning that reduced values of M_S are expected for $t_{Co} < 1.2$ nm, which will increase the calculated domain sizes in this region and lead to an apparent increased D_{DMI} in this region when evaluating the model. Yet the unphysical transition from zero to non-zero would D_{DMI} still occur, only at a different t_{Co}.

Next, we turn to the prerequisites of the models. The prerequisites of the DJ models are infinitely thin ($d_{calc} \gg \Delta_w$), freely mobile domain walls and strongly coupled layers. Assuming that the domain wall can be considered sufficiently thin if the domains are 10 times larger (*71*) than the domain wall parameter, this first prerequisite is met for $t_{Co} < 1.15$ nm. The second prerequisite of freely mobile domain walls is probably not met, as considerable pinning of the domain walls is known to occur in Pt\Co layered systems. Finally, the third prerequisite of rigidly coupled multilayers is at the very least violated within the domain walls. Multilayers with a large number of repetitions generally host hybrid domain walls (*302, 391*) that are a combination of Bloch and Néel type walls and exhibit lower domain wall energies than either of the fundamental types (c.f. chapter 5.2), from which even smaller domains would follow. The same prerequisite applies to the VSC model with some additional ones from the effective medium approach, which are summarized in Eq. 5-15. These additional prerequisites are met (with a ratio of the corresponding parameters of at least 10) and $Q' > 1.2$ for all t_{Co} in this multilayer system. Altogether, concerning the prerequisites the models are only partially applicable as considerable pinning might be present and the magnetic layers are not rigidly coupled.

Turning to the results for Pt\(Co$_{0\text{–}1.5\,nm}$\Pt$_{2\,nm}$)$_8$, shown in Fig. 5-11(b) using $M_S = 1.4$ MA/m and $D_{DMI} = 0$ mJ/m². The corresponding values for K_{tot} and A_{ex} were obtained analogously to the Pt\Co\Ir samples, using $K_V = 0.22$ MJ/m³, $2K_S = 1.43$ mJ/m² (see Tab. 4.3 and Fig. 4-13(a, b)),

σ = 0.5 nm, and X_{cut} = 0.15 (see Fig. 4-22(a)). It is evident, that the experimentally observed behavior cannot be well reproduced with the used parameters. Again, both DJ models predict too small values at large t_{Co}, while the calculated domain sizes cross the experimental ones for smaller t_{Co} and subsequently predict larger values. On the other hand, the VSC model predicts matching domain sizes for large t_{Co} while they considerably exceed the experimental ones for smaller Co layer thicknesses. This would indicate significant DMI in the sample. Again, this is surprising, as no DMI should be expected in a symmetrical system. However, small values of D_{DMI} have been reported (*410, 411*) and were attributed to different interface morphologies at the upper and lower interface with respect to the Co-layers. The extracted values for D_{DMI} are plotted in Fig. 5-11(c) as solid symbols. For both DJ models, non-zero D_{DMI} emerges below specific t_{Co} and increases thereafter, similar to Pt\Co\Ir. For the VSC model and starting from large t_{Co}, the extracted values first rapidly decline. Subsequently, for t_{Co} = 1– 1.3 nm the data follows an $1/t_{Co}$ behavior of D_{at} = 1.5 meV. For t_{Co} < 1 nm, the D_{DMI} deviates from the expected behavior and remains more or less constant (one might argue that the values of D_{DMI} remain almost constant for all t_{Co}, which is again unphysical, of course).

In the region of the decline, $t_{Co} >$ 1.3 nm, the prerequisites, given in Eq. 5-15, are not met and the model is not applicable. One might argue that the values extracted for t_{Co} = 1– 1.3 nm are credible and the deviation from the behavior for t_{Co} < 1 nm is caused by the reduction of M_S expected in this thickness regime (see chapter 4.2.2). However, the value of D_{at} = 1.5 meV is very large considering that it can only originate from varying interface qualities. Calculations by Dupé et al. suggest for a perfect Pt\Co interface D_{at} = 1.8 meV (*412*). Consequently, one interface would have to contribute the full D_{at} of a perfect interface while the second interface, which would have an opposite sign due to inversion, contributed almost nothing. It should be noted that the interfaces of the investigated samples are not expected to be perfect.

It is apparent that the extraction of plausible D_{DMI} values from the average domain sizes in the Pt-Co-Ir system is not feasible. While it is certainly possible to formally extract individual D_{DMI} values for samples using specific models, even careful investigation of all parameters involved does not guarantee that the extracted data in a systematic approach follow a physically meaningful behavior. In literature, deviations from the predicted behavior by domain spacing models are usually attributed to pinning (*71*). This may very well be the cause for the extraction of zero DMI for the antisymmetrical system, for which strong DMI should be expected, as well as for the strong DMI of D_{at} = 1.5 meV for the symmetric system, for which at most a weak DMI should be expected. A

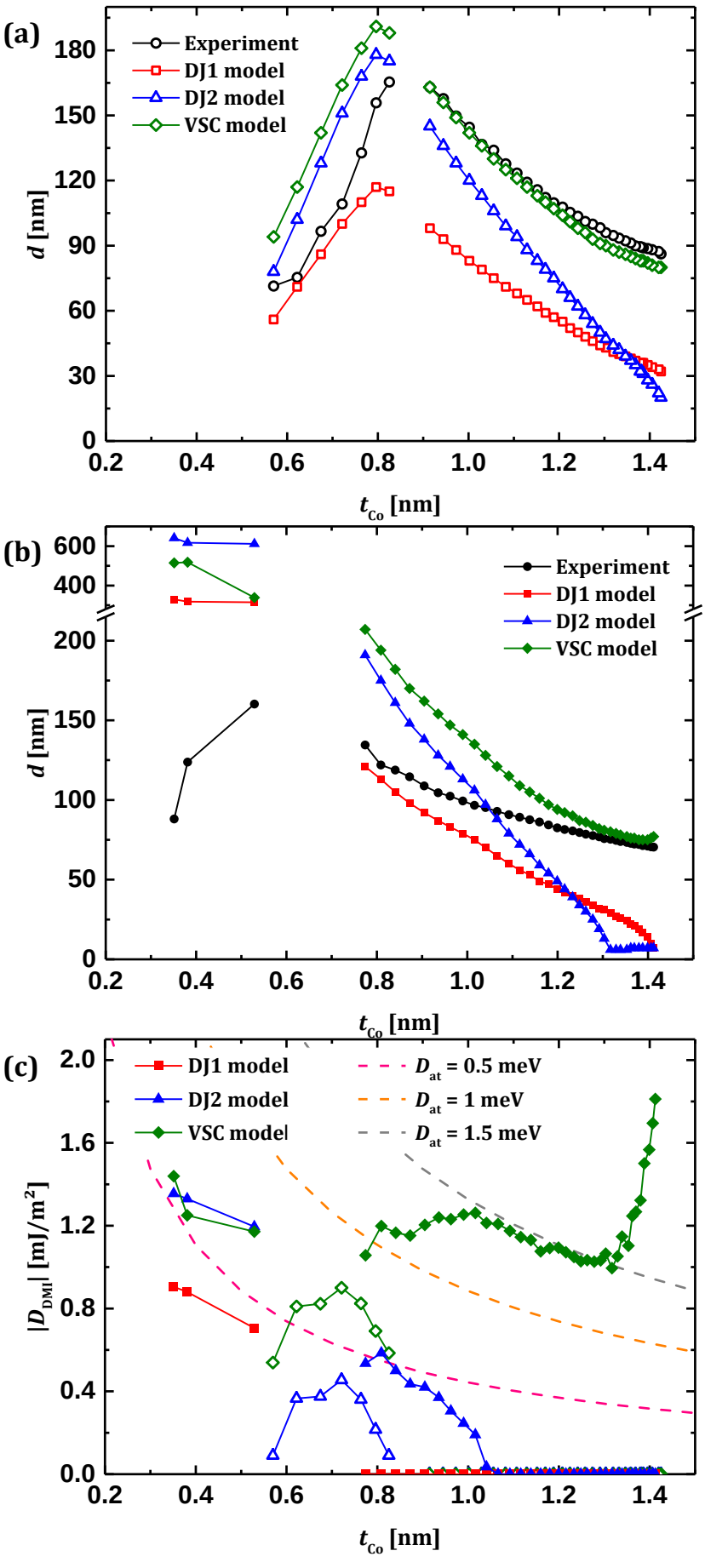
(a)
Experiment
DJ1 model
DJ2 model
VSC model
d [nm]
t_Co [nm]
(b)
Experiment
DJ1 model
DJ2 model
VSC model
d [nm]
t_Co [nm]
(c)
DJ1 model
DJ2 model
VSC model
D_at = 0.5 meV
D_at = 1 meV
D_at = 1.5 meV
|D_DMI| [mJ/m²]
t_Co [nm]

Figure 5-11: (a) Comparison of experimental domain sizes d_{avg}, obtained by XRMS (see chapter 5.1), and calculated d_{calc} using domain spacing models for $(Pt_{1\,nm}\backslash Co_t\backslash Ir_{1.1\,nm})_8$ (a) and $Pt\backslash(Co_t\backslash Pt_{2\,nm})_8$ (b) in stripe geometry plotted over t_{Co}. (c) Extracted values of D_{DMI} using the three domain spacing models plotted over t_{Co} for $(Pt_{1\,nm}\backslash Co_t\backslash Ir_{1.1\,nm})_8$ (open symbols) and $Pt\backslash(Co_t\backslash Pt_{2\,nm})_8$ (filled symbols). The dashed lines represent expected $1/t_{Co}$ behavior for various D_{at}.

systematic study proving the feasibility of this method for the extraction of DMI with the expected $1/t_{Co}$ behavior remains yet to be published. Thus, even the individually extracted values remain sketchy at best. Furthermore, varying results between the different models seriously hamper the comparison of extracted values between groups.

In conclusion, the dependence of the average domain size d_{avg} on t_{Co} was investigated by means of XRMS in both maze and stripe geometry. For all samples with FIC, four distinct regimes were identified. In the first regime for the smallest t_{Co}, d_{avg} increases linearly. Interestingly, a linear fit to the data from the initial increase intercepts the abscissa close to the onset of dichroic signal obtained from XAS measurements for Pt\Co\Pt and Pt\Co\Ir. The intercepts vary from system to system, and the differences appear to originate from interdiffusion at the interfaces and correspondingly a stronger reduction of T_C at Co-Ir compared to Co-Pt interfaces. In the second regime, large domains are observed that are, except for Ir\Co\Ir, too large to be measured with our setup. Subsequently in the third regime, d_{avg} decreases, which is the typically observed behavior described by domain spacing models. It was shown that no fixed ratio between the domain sizes in maze and stripe geometry exists; it rather is dependent on the system and t_{Co}. In the fourth regime, the samples exhibit negative effective anisotropy, yet continue to host perpendicular domains. The domains form three-dimensional magnetic microstructures, the so-called vortex states, where hybrid domain walls separate regions of perpendicular magnetization, with both being of equal size. Hybrid domain walls, the prevalent wall type in typical multilayers, are a combination of Néel- and Bloch-like walls, where the outer layers are of Néel type while the "bulk" layers host Bloch-like walls. The formation of the vortex state reduces the total energy of the sample by reducing the anisotropy energy at the expense of stray field and exchange energy. From MOKE measurements of the longitudinal remagnetization behavior of $Pt\backslash(Co_{2\,nm}\backslash Pt_{2\,nm})_N$ samples, it is shown that the vortex state is the ground state for samples with intermediate Co-layer thicknesses and $N \geq 6$. For $N = 8$ the transition to fully easy-plane magnetization occurs at a Co-layer thickness below 4 nm. A recent experiment has shown that the vortex state is stable up to $t_{Co} \approx 3.7$ nm. Micromagnetic

simulations were used to verify the formation of the vortex state using the magnetic parameters and geometry of the samples. Furthermore, existing domain spacing models for stripe domains were tested to calculate the domain size from the sample parameters and geometries in the first three regimes. The obtained equilibrium domain sizes were subsequently compared to the measured ones in order to extract the strength of D_{DMI}. However, large values of D_{DMI} were found for symmetrical Pt\Co\Pt, while zero or small values were obtained for the antisymmetrical Pt\Co\Ir, which is the opposite of what was expected. The values strongly differ, depending on which domain spacing model is used. Furthermore, the extracted values of D_{DMI} did not follow the expected $1/t_{\mathrm{Co}}$ behavior expected for interface effects. Instead transitions from zero to non-zero D_{DMI} were found on the same sample upon changing t_{Co}, or D_{DMI} remained constant over wide ranges of t_{Co}. These findings reveal that this method for extracting D_{DMI} does not yield reliable results. Finally, in a sample with AIC, magnetic domains were observed within two regimes. In the first regime, domains appear starting from a specific t_{Co} that is much larger than for samples with FIC, and decrease in size. The specific t_{Co} represents the transition from a strong-anisotropy state in which the formation of domains is suppressed to one with weak anisotropy with a ground state of antiferromagnetic domains (*385*). In the second regime, the samples exhibit negative anisotropy and yet perpendicular domains are again observed. This regime was not subject of any study in literature so far and may be attributed to the formation of a vortex-state similar to the samples with FIC.

Brillouin light scattering (BLS) measurements should be conducted for various t_{Co} to measure the prevalent strength of the DMI in each system. Furthermore, the parameter space (t_{Co}, t_{NM}, N, K_{tot}) for which the vortex state is the energetic ground state should be investigated using XRMS and XHM.

6 Conclusion

The magnetic properties of ultrathin Co-based multilayer systems have been systematically studied, where the Co layers were sandwiched either symmetrically or antisymmetrically between layers of Pt and/or Ir. The samples were prepared by sputtering techniques and the investigated properties are the saturation magnetization M_S, anisotropy K_{tot}, exchange stiffness A_{ex}, interlayer exchange coupling J_{IEC}, and the average domain size d_{avg}.

The saturation magnetization was investigated using ferromagnetic resonance spectroscopy (FMR) on samples with intermediate Co thicknesses of t_{Co} = 2 and 4 nm. For all investigated samples, M_S values that closely resemble the bulk values for fcc Co of M_S = 1.44 MA/m (*125*) were obtained. One important result is that, unlike frequently reported for Co\Ir interfaces (*182, 300, 301*), no indication for the formation of a magnetically dead layer was found in the systems containing Ir. Thinner Co layers with $t_{Co} \leq 2$ nm were investigated using the magneto-optic Kerr effect (MOKE) to measure the Kerr rotation in polar geometry in saturation Θ_{sat}. The scatter of the data and an insufficient experimentally accessible thickness range inhibited a clear identification of the regime in which Θ_{sat} depends linearly on t_{Co} that would indicate a constant M_S. By reviewing the literature addressing M_S in the four systems and comparing the reported values to the FMR measurements, the onsets for the regimes of constant M_S are estimated to $t_{Co} \geq 0.9$ nm in Pt\Co\Pt, $t_{Co} \geq 1.3$ nm in Ir\Co\Ir, $t_{Co} \geq 1.2$ nm in Pt\Co\Ir, and $t_{Co} \geq 1.1$ nm in Ir\Co\Pt. A corresponding proposal to verify the regimes of constant M_S and measure its reduction for thinner samples using polarized neutron reflectivity has been submitted.

The anisotropy was studied by measuring the remagnetization behavior using MOKE and the anomalous Hall Effect[42] (AHE). Two methods were applied to extract the anisotropy constant K_{tot} from the remagnetization loops. The first method extracts K_{tot} by fitting a model to the hard-axis remagnetization loops assuming that all magnetic layers act as a single macrospin and that coherent rotation of the magnetization is the dominant process. The second method is free of prerequisites and extracts K_{tot} from the difference between the energy densities required to fully saturate a sample along its hard and easy axis. Both methods yield comparable results for single layers. It is shown that the prerequisites of the first method are not met for multilayers with larger number of repetitions $N \gtrsim 4$ and erroneous results are obtained. Furthermore, the dependence of K_{tot} on t_{Co} was investigated in all four systems for single- and multilayers. For multilayers, spacer layer thicknesses

[42] The AHE measurements were performed by S. Ziesmann as part of his master thesis (*307*).

were chosen in the regime where comparable K_{tot} are obtained independent of N. For all three systems containing Pt (Pt\Co\Pt, Pt\Co\Ir, and Ir\Co\Pt), three distinct thickness regimes with different dependencies of $K_{tot} \cdot t_{Co}$ on t_{Co} were observed, with transitions around $t_{Co} \approx 1\,\text{nm}$ and 4 nm. For $t_{Co} \geq 4\,\text{nm}$ a linear dependency is found, with a very small $K_V \leq 0.09\,\text{MJ/m}^3$. Within the region of $t_{Co} = 1-4\,\text{nm}$, a second linear regime is observed with a smaller slope indicating values of $K_V = 0.16-0.23\,\text{MJ/m}^3$. For $t_{Co} < 1\,\text{nm}$, a bending towards the abscissa is observed, which is attributed to interdiffusion at the interfaces. The relaxation of residual stress, which affects the anisotropy via magneto-elastic coupling, is probably the origin of the second transition around $t_{Co} \approx 4\,\text{nm}$. For the system not containing Pt, (Ir\Co\Ir), only one linear regime for $t_{Co} > 1\,\text{nm}$ with $K_V \approx 0$ was found and a bending of $K_{tot} \cdot t_{Co}$ towards the abscissa for $t_{Co} < 1\,\text{nm}$. The single transition here is also attributed to interdiffusion at the interfaces. The absence of the second linear regime in the absence of Pt is surprising, together with the fact that a single interface with Pt is sufficient to cause it. Structural investigations are required to link the transitions between regimes of differing dependence of the anisotropy on t_{Co} to structural changes. A corresponding proposal for XRD measurements in ultrathin samples has been submitted to PETRA III.

The exchange stiffness was extracted from domain wall profiles in ultrathin Co layers imaged with soft X-ray holographic microscopy (XHM). In order to provide sufficient lateral resolution to resolve the domain walls accurately, the fabrication process of the X-ray optics in the microscope was improved and a lateral resolution of sub 12 nm experimentally verified. Subsequently, an exchange stiffness of $A_{ex} = (13 \pm 6)\,\text{pJ/m}$ ($(11 \pm 4)\,\text{pJ/m}$) for $t_{Co} = 1.28\,\text{nm}$ (1.41 nm) was extracted from the domain-wall profiles. The obtained values are strongly reduced compared to the bulk value for fcc Co of $A_{ex} = 23.3\,\text{pJ/m}$ (*327*). Qualitatively similar reductions of A_{ex} in ultrathin films are found in literature for DC-sputtered samples, but not for epitaxially prepared ones. For epitaxial samples bulk-like values are obtained down to $t_{Co} = 0.8\,\text{nm}$. As the difference is only found in ultrathin samples, it originates most likely from structural differences at the interfaces, namely interdiffusion. Consequently, a model was developed which estimates the reduction of A_{ex} in dependence of one easily accessible parameter, the width of the interdiffusion zone σ, and the sample geometry. Furthermore, the influence of T_C is incorporated into the model, which gives rise to a different onset of ferromagnetic order depending on the interface materials. The model successfully reproduces the experimentally obtained values of A_{ex} and the ones found in literature for CoPt alloys. Furthermore, the predicted offsets along t_{Co} are in line with measurements of the onset of the dichroic signal in X-ray absorption measurements. A_{ex} values reported in literature for ultrathin

Co films are partially reproduced; others show quantitative deviations from the model, yet the reported reduction can be explained qualitatively. Further measurements of domain patterns in various systems should be conducted to extract the domain wall profiles and A_{ex} to verify the predictions of the model.

The interlayer exchange coupling has been investigated by measuring the remagnetization loops using MOKE. For both symmetric systems, Pt\Co\Pt and Ir\Co\Ir, the behavior found in literature is well reproduced. Co layers couple ferromagnetically through Pt spacer layers. Via Ir, J_{IEC} oscillates with the spacer layer thickness and changes its sign periodically. The peak values are strongly damped with increasing spacer thickness and an oscillation period of $\lambda \approx 0.9\,\text{nm}$ is found. In the antisymmetric systems, the interlayer exchange coupling is dependent on the stacking order and composition of the interlayer. The coupling in Co\Pt\Ir\Co (the stacking for Ir\Co\Pt) is qualitatively similar to the one found in Co\Ir\Co, but depends on both, spacer layer thickness and composition. For a constant Ir-layer thickness of $t_{Ir} = 1.1\,\text{nm}$, an oscillation of J_{IEC} with respect to t_{Pt} is observed with an oscillation period of $\lambda \approx 2.2\,\text{nm}$. Ab initio calculations suggest that a similar increase of the period length can be caused by alloying in the spacer layer. In the inversely stacked Pt\Co\Ir system, the Co layers couple always ferromagnetically. An oscillation of the coupling strength with a short period of $\lambda \approx (0.3–0.6)\,\text{nm}$ is observed, but no sign change of J_{IEC}. A similar behavior was reported for Pt\Co\Pt. The parameter space for both systems should be explored in more detail, over a wider range of both, thickness and composition of the spacer layers. Furthermore, structural investigations of the interfaces are required to investigate the widths of the interdiffusion zones at the interfaces and to which extent Pt and Ir form alloys. Such a dependence of the IEC on the stacking order has not been reported in literature so far.

The dependence of the average domain size d_{avg} on t_{Co} was investigated by means of XRMS in both maze and stripe geometry. For all samples with FIC, four distinct regimes were identified. In the first regime for the smallest t_{Co}, d_{avg} increases linearly. Interestingly, a linear fit to the data from the initial increase intercepts the abscissa close to the onset of dichroic signal obtained from XAS measurements for Pt\Co\Pt and Pt\Co\Ir. The intercepts vary from system to system, and the differences appear to originate from interdiffusion at the interfaces and correspondingly a stronger reduction of T_C at Co-Ir compared to Co-Pt interfaces. In the second regime, large domains are observed that are, except for Ir\Co\Ir, too large to be measured with our setup. Subsequently in the third regime, d_{avg} decreases, which is the typically observed behavior described by domain spacing models. It was shown that no fixed ratio between the domain sizes in maze and stripe

geometry exists; it rather is dependent on the system and t_{Co}. In the fourth regime, the samples exhibit negative effective anisotropy, yet continue to host perpendicular domains. The domains form three-dimensional magnetic microstructures, the so-called vortex states, where hybrid domain walls separate regions of perpendicular magnetization, with both being of equal size. Hybrid domain walls, the prevalent wall type in typical multilayers, are a combination of Néel- and Bloch-like walls, where the outer layers are of Néel type while the "bulk" layers host Bloch-like walls. The formation of the vortex state reduces the total energy of the sample by reducing the anisotropy energy at the expense of stray field and exchange energy. From MOKE measurements of the longitudinal remagnetization behavior of Pt\(Co2 nm\Pt2 nm)$_N$ samples, it is shown that the vortex state is the ground state for samples with intermediate Co-layer thicknesses and $N \geq 6$. For $N = 8$ the transition to fully easy-plane magnetization occurs at a Co-layer thickness below 4 nm. A recent experiment has shown that the vortex state is stable up to $t_{Co} \approx 3.7$ nm. Micromagnetic simulations were used to verify the formation of the vortex state using the magnetic parameters and geometry of the samples. Furthermore, existing domain spacing models for stripe domains were tested to calculate the domain size from the sample parameters and geometries in the first three regimes. The obtained equilibrium domain sizes were subsequently compared to the measured ones in order to extract the strength of D_{DMI}. However, large values of D_{DMI} were found for symmetrical Pt\Co\Pt, while zero or small values were obtained for the antisymmetrical Pt\Co\Ir, which is the opposite of what was expected. The values strongly differ, depending on which domain spacing model is used. Furthermore, the extracted values of D_{DMI} did not follow the expected $1/t_{Co}$ behavior expected for interface effects. Instead transitions from zero to non-zero D_{DMI} were found on the same sample upon changing t_{Co}, or D_{DMI} remained constant over wide ranges of t_{Co}. These findings reveal that this method for extracting D_{DMI} does not yield reliable results. Finally, in a sample with AIC, magnetic domains were observed within two regimes. In the first regime, domains appear starting from a specific t_{Co} that is much larger than for samples with FIC, and decrease in size. The specific t_{Co} represents the transition from a strong-anisotropy state in which the formation of domains is suppressed to one with weak anisotropy with a ground state of antiferromagnetic domains (*385*). In the second regime, the samples exhibit negative anisotropy and yet perpendicular domains are again observed. This regime was not subject of any study in literature so far and may be attributed to the formation of a vortex-state similar to the samples with FIC.

Brillouin light scattering (BLS) measurements should be conducted for various t_{Co} to measure the prevalent strength of the DMI in each system. Furthermore, the parameter space (t_{Co}, t_{NM}, N, K_{tot})

for which the vortex state is the energetic ground state should be investigated using XRMS and XHM.

The results presented in this thesis illustrate the importance of the interface morphology and the non-magnetic spacer-materials for the magnetic properties of ultrathin layered structures. The properties are strongly influenced by interdiffusion and a description within the framework of sharp layers is questionable. In-depth studies, such as this thesis, are required in order to understand the evolution of the parameters and enable the development of tailored materials that satisfy the demands of potential future data-storage technologies, such as the racetrack memory with its variety of designs.

A Appendix

A.1 Micromagnetic simulations

This section presents the results of micromagnetic simulations and is a continuation of chapter 5.2.1. Here, the stability and size of the vortex-states are briefly studied, in dependence of the magnetic parameters K_{tot} and A_{ex} as well as the sample geometry in form of t_{NM} and N.

First, the sample geometry is addressed. The influence of the number of multilayer repetitions on the size and stability of vortex-state domains in dependence of N is studied in $(Co_{2\,nm}\backslash NM_{2\,nm})_N$ samples with the magnetic parameters M_S = 1.4 MA/m, A_{ex} = 18 pJ/m, and K_u = 968 kJ/m³ (K_{tot} = -262 kJ/m³). The initial state of the simulations was a homogeneous magnetization along the x-axis. The results for d_{vort} (black circles) and E_{tot}/V (red squares) obtained from the stationary solution $\mathbf{M}_{stat}(\mathbf{r})$ are plotted over N in Fig. A-1(a). For small numbers of repetition, $N < 4$, no perpendicular magnetization is observed in the samples and thus no domain size can be extracted. For these sample geometries, the reduction of anisotropy energy is not sufficient to compensate for the increase in stray-field and exchange energies, thus E_{tot}/V remains practically constant and consists almost exclusively of the anisotropy energy. The small reduction in of E_{tot}/V is caused by the formation of in-plane domains. For $N > 4$, the formation of vortex-domains reduces the total energy. The domain size appears to increase more or less linearly with N while E_{tot}/V decreases asymptotically. Thus, the vortex state becomes more and more stable with increasing N. This is caused by the increasing number of "bulk" layers, where the magnetization for the most part well-aligned with the magnetocrystalline easy axis of the system (c.f. Fig. 5-9(e)) layers 3 and 4). The anisotropy energy for these layers is strongly reduced while the "surface" layers still maintain the flux closure keeping the stray-field energy small.

The simulation for N = 4 is a special case, as the energy of the vortex state is identical to that of a homogenous magnetization. Seeding a homogenous magnetization yields a homogenous final state while the same is true for the vortex state. Thus, with the prevalent magnetic parameters and t_{NM}, the vortex state is stable for $N > 4$, and becomes more and more stable with increasing N. A similar linear increase of d_{vort} with N was reported in an experimental study by Tekielak et al. (*389*) in $Au\backslash(Co_{2\,nm}\backslash Au_{3\,nm})_N$ samples for $N > 12$.

It should be mentioned that the origin of the fluctuations superimposed on the linear increase of d_{vort} is unknown. They are, however, most probably not an artifact of the quantization used in the simulation, i.e. due to the chosen dimensions of the sample along the x-axis, or the choice of too

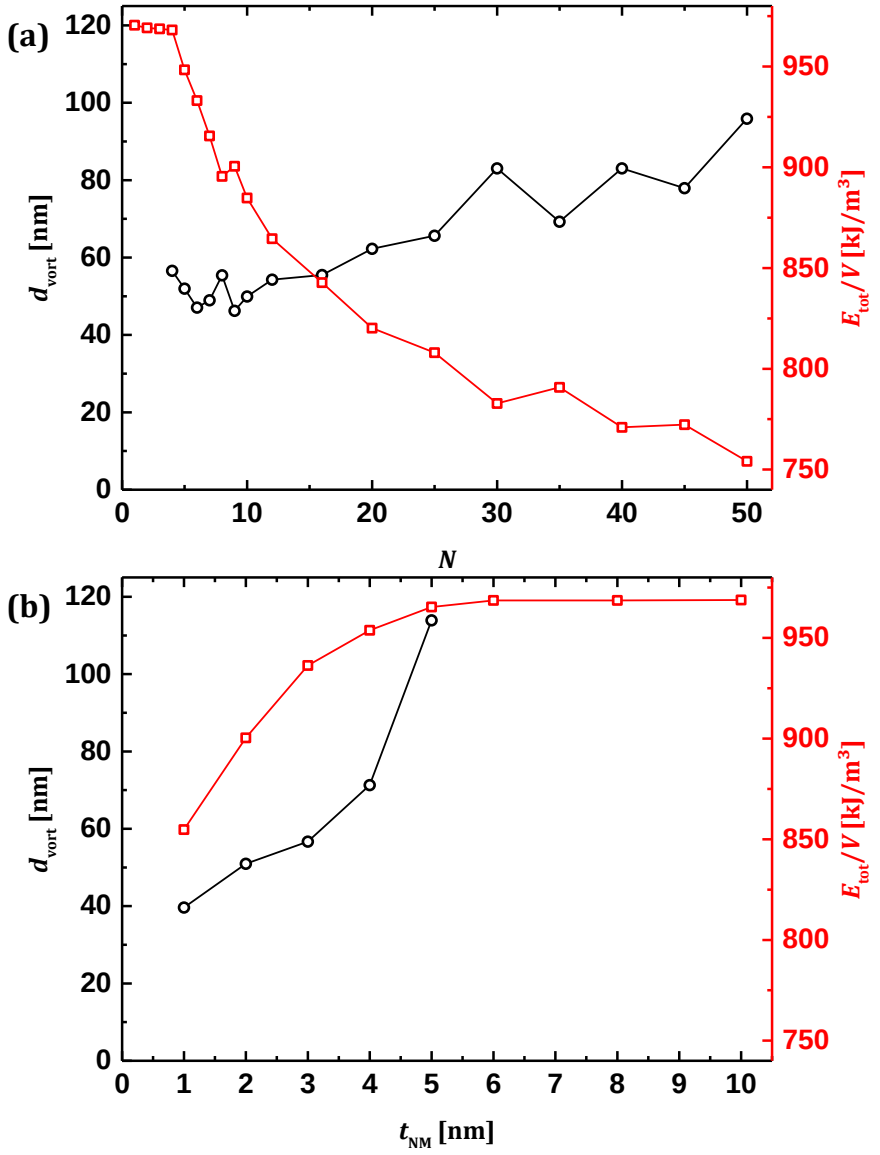

Figure A-1: (a) The domain size (black) and energy (red) of the vortex state in dependence of the number of repetitions N. For $N > 4$, the vortex state has a lower energy than a state of homogeneous easy-plane magnetization. The total energy density decreases with N. The domain size increases with N. For $N = 4$, the homogeneous and the vortex state have the same energy and the initially seeded magnetization state is retained. (b) The domain size (black) and energy (red) of the vortex state in $(Co_{2\,nm}\backslash NM_t)_8$ in dependence of the thickness of the non-magnetic spacer layer t_{NM}. The vortex state is the stable ground state up to $t_{NM} = 5$ nm; for larger values a homogeneous state has the lower energy and no vortex state is obtained. The domain size increases with t_{NM}.

large unit cells. The first was tested by increasing n_x and the latter by decreasing l_x and l_z, nevertheless, the fluctuations persisted.

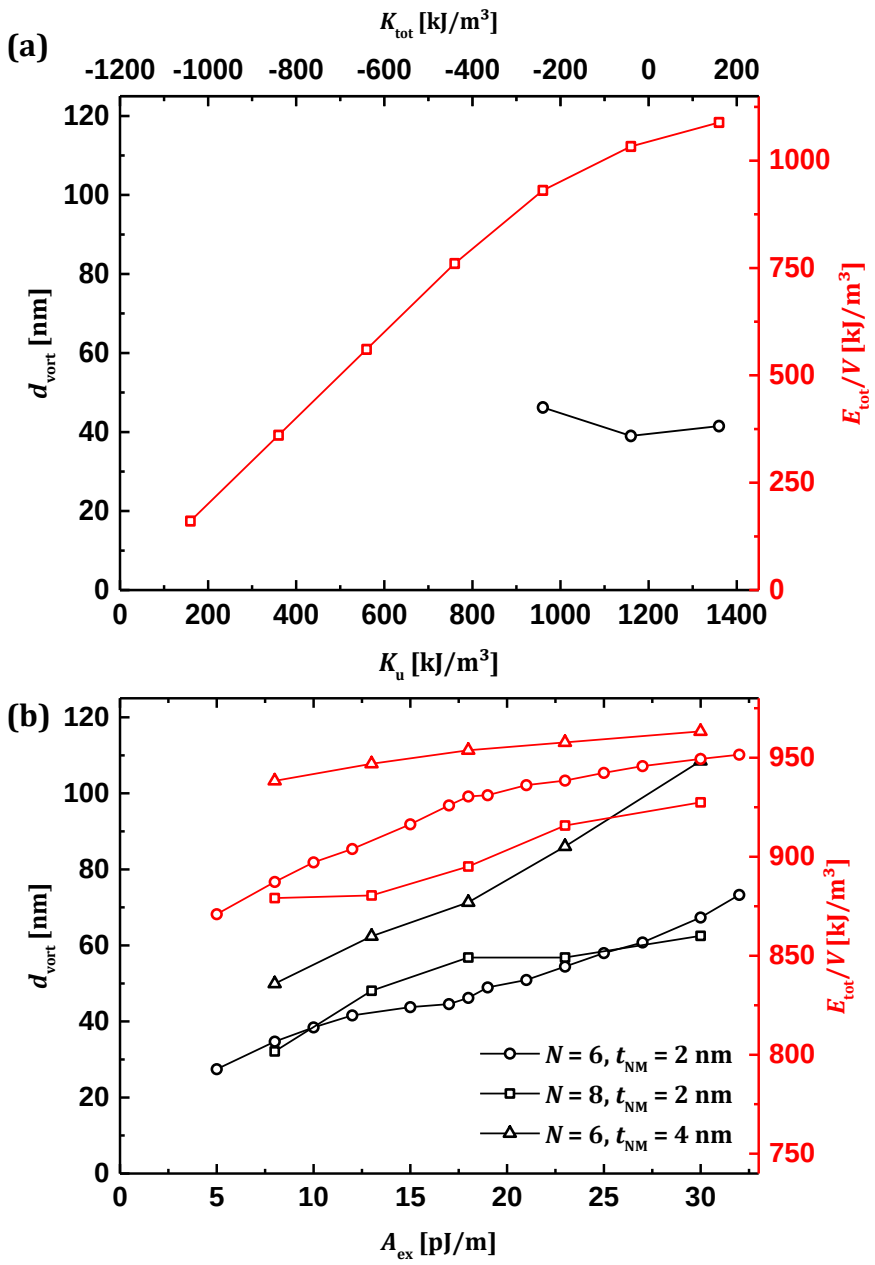

Figure A-2: (a) The domain size (black) and energy density (red) of the vortex state in dependence of the uniaxial anisotropy K_u (lower abscissa) and K_{tot} (upper abscissa) using M_S = 1.4 MA/m. For small values of K_u, the possible reduction of the anisotropy energy by the formation of a vortex state is too small to account for the increased stray-field and exchange energies and a state with in-plane magnetization is obtained. For values of $K_u \geq 970\,kJ/m^3$, the vortex state is energetically favorable. For $K_{tot} > 0\,kJ/m^3$, a "normal" domain pattern forms. (b) The domain size (black) and energy (red) of the vortex state in dependence of A_{ex} for stacks with N = 6 or 8 and t_{NM} = 2 nm and 4 nm. The domain size and the energy density of the vortex state linearly increase with A_{ex}.

Next, the influence of the spacer layer thickness is addressed. In Fig. A-1(b), the dependence of d_{vort} (black circles) and E_{tot}/V (red squares) on t_{NM} is shown for (Co2 nm\NM$t$)8 samples with identical magnetic properties to the samples shown in (a). For $t_{NM} > 5$ nm no formation of vortex states was found and a constant value of E_{tot}/V is obtained, while for $t_{NM} \leq 5$ nm both, d_{vort} and E_{tot}/V rapidly decrease with reduced t_{NM}. As all other sample parameters remain unaltered, the mutual compensation of surface charges in adjacent layers probably plays an important role in reducing the total energy, which is reduced at increasing spacer thickness. It should be stressed that these calculations do not include the interlayer exchange coupling, which becomes increasingly important for thin spacer layers and inhibits the variation of magnetization between adjacent layers that occurs in the vortex regions.

In the following, the influence of the magnetic parameters is addressed. Fig. A-2(a) shows d_{vort} (black circles) and E_{tot}/V (red squares) plotted over K_u for (Co2 nm\NM2 nm)6 samples with M_S = 1.4 MA/m and A_{ex} = 18 pJ/m. It should be noted that these samples have a smaller number of repetitions compared the previously discussed and furthermore, the change in anisotropy is not accompanied by a change of the thickness of the magnetic layers. For strong easy-plane anisotropies, no vortex-state is found and E_{tot}/V increases linearly, and is almost equal to the anisotropy energy K_u. While approaching $K_u = K_d$ (or $K_{tot} = 0$), the energy density deviates from the linear behavior, which is accompanied by the formation of vortex states. For $K_u > K_d$, a continuous transition to a perpendicular domain pattern with hybrid domain walls takes place, which exhibits the same domain size. Since the reduction of the total energy stems from the reduction of the anisotropy energy, not much energy can be gained if K_u is small to begin with. A similar result was obtained by Labrune et al. (*388*).

Finally, the dependence of d_{vort} (black) and E_{tot}/V (red) on the exchange stiffness is shown in Fig. A-2(b) for (Co2 nm\NM$t$)N samples with M_S = 1.4 MA/m and K_u = 968 kJ/m³ (K_{tot} = -262 kJ/m³). For all samples, the domain size and energy density increase more or less linearly with A_{ex}. This is not surprising as the exchange energy favors parallel alignment of adjacent spins, or unit cells in this context. Thus, for smaller values of A_{ex} the energy penalty for smaller domains, in which neighboring cells are more strongly misaligned, is reduced.

In conclusion, the stability of the vortex-state and the resulting domain sizes are, similar to "normal" domains, strongly dependent on the sample geometry and the magnetic parameters.

References

1. C. Sun, J. S. H. Lee, M. Zhang, Magnetic nanoparticles in MR imaging and drug delivery. *Adv. Drug Deliv. Rev.* **60**, 1252 (2008), doi:10.1016/j.addr.2008.03.018.

2. J. Heremans, Solid state magnetic field sensors and applications. *J. Phys. D: Appl. Phys.* **26**, 1149 (1993), doi:10.1088/0022-3727/26/8/001.

3. M. H. Kryder, Magnetic thin films for data storage. *Thin Solid Films* **216**, 174 (1992), doi:10.1016/0040-6090(92)90890-N.

4. D. A. Thompson, J. S. Best, The future of magnetic data storage techology. *IBM J. Res. Develop.* **44**, 311 (2000), doi:10.1147/rd.443.0311.

5. D. Niarchos, Magnetic MEMS. *Sens. Actuator A-Phys.* **109**, 166 (2003), doi:10.1016/j.sna.2003.09.010.

6. B. D. Terris, T. Thomson, Nanofabricated and self-assembled magnetic structures as data storage media. *J. Phys. D: Appl. Phys.* **38**, R199 (2005), doi:10.1088/0022-3727/38/12/R01.

7. C. Chappert, A. Fert, F. N. van Dau, in *Nanoscience and Technology*, , Ed.P. Rodgers (Co-Published with Macmillan Publishers Ltd, UK, 2009).

8. N. S. Kiselev, A. N. Bogdanov, R. Schäfer, U. K. Rößler, Chiral skyrmions in thin magnetic films. *J. Phys. D: Appl. Phys.* **44**, 392001 (2011), doi:10.1088/0022-3727/44/39/392001.

9. O. Cugat, J. Delamare, G. Reyne, Magnetic micro-actuators and systems (MAGMAS). *IEEE Trans. Magn.* **39**, 3607 (2003), doi:10.1109/TMAG.2003.816763.

10. E. D. Daniel, C. D. Mee, M. H. Clark, Eds., *Magnetic Recording, the first 100 years* (IEEE Press, Piscataway, NJ, 1999).

11. K. J. Anderson, Magnetic Recording Materials. *MRS Bull.* **15**, 88 (1990), doi:10.1557/S0883769400060267.

12. G. Binasch, P. Grünberg, F. Saurenbach, W. Zinn, Enhanced magnetoresistance in layered magnetic structures with antiferromagnetic interlayer exchange. *Phys. Rev. B* **39**, 4828 (1989), doi:10.1103/PhysRevB.39.4828.

13. M.N. Baibich, J. M. Broto, A. Fert, D. F. van Nguyen, F. Petroff, P. Etienne, G. Creuzet, A. Friederich, J. Chazelas, Giant magnetoresistance of (001)Fe/(001)Cr magnetic superlattices. *Phys. Rev. Lett.* **61**, 2472 (1988), doi:10.1103/PhysRevLett.61.2472.

14. I. K. Schuller, S. Kim, C. Leighton, Magnetic superlattices and multilayers. *J. Magn. Magn. Mater.* **200**, 571 (1999), doi:10.1016/S0304-8853(99)00336-4.

15. B. Dieny, in *Magnetism*, , Eds.É. du Trémolet de Lacheisserie, D. Gignoux, M. Schlenker (Springer New York, New York, NY, 2005).

16. S. D. Bader, S.S.P. Parkin, Spintronics. *Annu. Rev. Condens. Matter Phys.* **1**, 71 (2010), doi:10.1146/annurev-conmatphys-070909-104123.

17. H. Zabel, Progress in spintronics. *Superlattices Microstruct.* **46**, 541 (2009), doi:10.1016/j.spmi.2009.07.008.

18. B. Dieny, R. Sousa, L. Prejbeanu, Spin Electronics. *J. Phys.: Condens. Matt.* **19**, 160301 (2007), doi:10.1088/0953-8984/19/16/160301.

19. G. A. Prinz, Magnetoelectronics. *Science* **282**, 1660 (1998), doi:10.1126/science.282.5394.1660.

20. A. Manchon, A new moment for Berry. *Nat. Phys.* **10**, 340 (2014), doi:10.1038/nphys2957.

21. T. Kuschel, G. Reiss, Charges ride the spin wave. *Nat. Nanotechnol.* **10**, 22 (2014), doi:10.1038/nnano.2014.279.

22. J. S. Moodera, L. R. Kinder, T. M. Wong, R. Meservey, Large magnetoresistance at room temperature in ferromagnetic thin film tunnel junctions. *Phys. Rev. Lett.* **74**, 3273 (1995), doi:10.1103/PhysRevLett.74.3273.

23. J. S. Moodera, J. Nassar, G. Mathon, SPIN-TUNNELING IN FERROMAGNETIC JUNCTIONS. *Annu. Rev. Mater. Sci.* **29**, 381 (1999), doi:10.1146/annurev.matsci.29.1.381.

24. B. Dieny, R. C. Sousa, J. Herault, C. Papusoi, G. Prenat, U. Ebels, D. Houssameddine, B. Rodmacq, S. Auffret, L. B. Prejbeanu, M. C. Cyrille, B. Delaet, O. Redon, C. Ducruet, J. P. Nozieres, I. L. Prejbeanu, Spin-transfer effect and its use in spintronic components. *IEEE Trans. Magn.* **7**, 591 (2010), doi:10.1504/IJNT.2010.031735.

25. S. Parkin, X. Jiang, C. Kaiser, A. Panchula, K. Roche, M. Samant, Magnetically engineered spintronic sensors and memory. *Proc. IEEE* **91**, 661 (2003), doi:10.1109/JPROC.2003.811807.

26. D. Weller, A. Moser, Thermal effect limits in ultrahigh-density magnetic recording. *IEEE Trans. Magn.* **35**, 4423 (1999), doi:10.1109/20.809134.

27. G. Ju, Y. Peng, E. K. C. Chang, Y. Ding, A. Q. Wu, X. Zhu, Y. Kubota, T. J. Klemmer, H. Amini, L. Gao, Z. Fan, T. Rausch, P. Subedi, M. Ma, S. Kalarickal, C. J. Rea, D. V. Dimitrov, P.-W. Huang, K. Wang, X. Chen, C. Peng, W. Chen, J. W. Dykes, M. A. Seigler, E. C. Gage, R. Chantrell, J.-U. Thiele, High Density Heat-Assisted Magnetic Recording Media and Advanced Characterization—Progress and Challenges. *IEEE Trans. Magn.* **51**, 1 (2015), doi:10.1109/TMAG.2015.2439690.

28. R. C. Sousa, I. L. Prejbeanu, Non-volatile magnetic random access memories (MRAM). *C. R. Phys.* **6**, 1013 (2005), doi:10.1016/j.crhy.2005.10.007.

29. S. S. P. Parkin, M. Hayashi, L. Thomas, Magnetic Domain-Wall Racetrack Memory. *Science* **320**, 190 (2008), doi:10.1126/science.1145799.

30. S. S. P. Parkin, S.-H. Yang, Memory on the racetrack. *Nat. Nanotechnol.* **10**, 195 (2015), doi:10.1038/nnano.2015.41.

31. J. C. Slonczewski, Current-driven excitation of magnetic multilayers. *J. Magn. Magn. Mater.* **159**, L1 (1996), doi:10.1016/0304-8853(96)00062-5.

32. L. Berger, Emission of spin waves by a magnetic multilayer traversed by a current. *Phys. Rev. B* **54**, 9353 (1996), doi:10.1103/PhysRevB.54.9353.

33. M. D. Stiles, J. Miltat, in *Spin Dynamics in Confined Magnetic Structures III*, , Eds.B. Hillebrands, A. Thiaville (Springer Berlin Heidelberg, 2006), Vol. **101**.

34. M. Tsoi, A. G.M. Jansen, J. Bass, W.-C. Chiang, M. Seck, V. Tsoi, P. Wyder, Excitation of a magnetic multilayer by an electric current. *Phys. Rev. Lett.* **80**, 4281 (1998), doi:10.1103/PhysRevLett.80.4281.

35. A. Yamaguchi, T. Ono, S. Nasu, K. Miyake, K. Mibu, T. Shinjo, Real-space observation of current-driven domain wall motion in submicron magnetic wires. *Phys. Rev. Lett.* **92**, 77205 (2004), doi:10.1103/PhysRevLett.92.077205.

36. A. Vanhaverbeke, M. Viret, Simple model of current-induced spin torque in domain walls. *Phys. Rev. B* **75**, 24411 (2007), doi:10.1103/PhysRevB.75.024411.

37. A. Thiaville, S. Rohart, É. Jué, V. Cros, A. Fert, Dynamics of Dzyaloshinskii domain walls in ultrathin magnetic films. *Europhys. Lett.* **100**, 57002 (2012), doi:10.1209/0295-5075/100/57002.

38. A. Fert, V. Cros, J. Sampaio, Skyrmions on the track. *Nat. Nanotechnol.* **8**, 152 (2013), doi:10.1038/nnano.2013.29.

39. S.-H. Yang, K.-S. Ryu, S. Parkin, Domain-wall velocities of up to 750 ms−1 driven by exchange-coupling torque in synthetic antiferromagnets. *Nat. Nanotechnol.* **10**, 221 (2015), doi:10.1038/nnano.2014.324.

40. I. E. Dzyaloshinskii. *Sov. Phys. JETP* **5** (1957).

41. T. Moriya, Anisotropic Superexchange Interaction and Weak Ferromagnetism. *Phys. Rev.* **120**, 91 (1960), doi:10.1103/PhysRev.120.91.

42. A. R. Fert, Magnetic and Transport Properties of Metallic Multilayers. *MSF* **59-60**, 439 (1991), doi:10.4028/www.scientific.net/MSF.59-60.439.

43. M. Bode, M. Heide, K. von Bergmann, P. Ferriani, S. Heinze, G. Bihlmayer, A. Kubetzka, O. Pietzsch, S. Blügel, R. Wiesendanger, Chiral magnetic order at surfaces driven by inversion asymmetry. *Nature* **447**, 190 (2007), doi:10.1038/nature05802.

44. T.H.R. Skyrme, A unified field theory of mesons and baryons. *Nucl. Phys.* **31**, 556 (1962), doi:10.1016/0029-5582(62)90775-7.

45. A. N. Bogdanov, D. A. Yablonskii, Thermodynamically stable "vortices" in magnetically ordered crystals. The mixed state of magnets. *Sov. Phys. JETP* **68**, 101 (1989).

46. A. V. Bezvershenko, A. K. Kolezhuk, B. A. Ivanov, Stabilization of magnetic skyrmions by RKKY interactions. *Phys. Rev. B* **97**, 54408 (2018), doi:10.1103/PhysRevB.97.054408.

47. S. A. Montoya, S. Couture, J. J. Chess, J. C. T. Lee, N. Kent, D. Henze, S. K. Sinha, M.-Y. Im, S. D. Kevan, P. Fischer, B. J. McMorran, V. Lomakin, S. Roy, E. E. Fullerton, Tailoring magnetic energies to form dipole skyrmions and skyrmion lattices. *Phys. Rev. B* **95**, 24415 (2017), doi:10.1103/PhysRevB.95.024415.

48. A. O. Leonov, M. Mostovoy, Multiply periodic states and isolated skyrmions in an anisotropic frustrated magnet. *Nat. Commun.* **6**, 8275 (2015), doi:10.1038/ncomms9275.

49. G. Chen, A. Mascaraque, A. T. N'Diaye, A. K. Schmid, Room temperature skyrmion ground state stabilized through interlayer exchange coupling. *Appl. Phys. Lett.* **106**, 242404 (2015), doi:10.1063/1.4922726.

50. S. Rohart, A. Thiaville, Skyrmion confinement in ultrathin film nanostructures in the presence of Dzyaloshinskii-Moriya interaction. *Phys. Rev. B* **88**, 184422 (2013), doi:10.1103/PhysRevB.88.184422.

51. B. F. Miao, L. Sun, Y. W. Wu, X. D. Tao, X. Xiong, Y. Wen, R. X. Cao, P. Wang, D. Wu, Q. F. Zhan, B. You, J. Du, R. W. Li, H. F. Ding, Experimental realization of two-dimensional artificial skyrmion crystals at room temperature. *Phys. Rev. B* **90**, 174411 (2014), doi:10.1103/PhysRevB.90.174411.

52. G. Finocchio, F. Büttner, R. Tomasello, M. Carpentieri, M. Kläui, Magnetic skyrmions. *J. Phys. D: Appl. Phys.* **49**, 423001 (2016), doi:10.1088/0022-3727/49/42/423001.

53. A. N. Bogdanov, U. K. Rössler, Chiral symmetry breaking in magnetic thin films and multilayers. *Phys. Rev. Lett.* **87**, 37203 (2001), doi:10.1103/PhysRevLett.87.037203.

54. S. Mühlbauer, B. Binz, F. Jonietz, C. Pfleiderer, A. Rosch, A. Neubauer, R. Georgii, P. Böni, Skyrmion lattice in a chiral magnet. *Science* **323**, 915 (2009), doi:10.1126/science.1166767.

55. S. Heinze, K. v. Bergmann, M. Menzel, J. Brede, A. Kubetzka, R. Wiesendanger, G. Bihlmayer, S. Blügel, Spontaneous atomic-scale magnetic skyrmion lattice in two dimensions. *Nat. Phys.* **7**, 713 (2011), doi:10.1038/NPHYS2045.

56. W. Jiang, P. Upadhyaya, W. Zhang, G. Yu, M. B. Jungfleisch, F. Y. Fradin, J. E. Pearson, Y. Tserkovnyak, K. L. Wang, O. Heinonen, S. G. E. te Velthuis, A. Hoffmann, Magnetism: Blowing magnetic skyrmion bubbles. *Science* **349**, 283 (2015), doi:10.1126/science.aaa1442.

57. K. Litzius, I. Lemesh, B. Krüger, P. Bassirian, L. Caretta, K. Richter, F. Büttner, K. Sato, O. A. Tretiakov, J. Förster, R. M. Reeve, M. Weigand, I. Bykova, H. Stoll, G. Schütz, G. S. D. Beach, M. Kläui, Skyrmion Hall effect revealed by direct time-resolved X-ray microscopy. *Nat. Phys.* **13**, 170 (2016), doi:10.1038/nphys4000.

58. W. Jiang, X. Zhang, G. Yu, W. Zhang, X. Wang, M. Benjamin Jungfleisch, J. E. Pearson, X. Cheng, O. Heinonen, K. L. Wang, Y. Zhou, A. Hoffmann, S. G. E. te Velthuis, Direct observation of the skyrmion Hall effect. *Nat. Phys.* **13**, 162 (2017), doi:10.1038/NPHYS3883.

59. S. Woo, K. M. Song, H.-S. Han, M.-S. Jung, M.-Y. Im, K.-S. Lee, K. S. Song, P. Fischer, J.-I. Hong, J. W. Choi, B.-C. Min, H. C. Koo, J. Chang, Spin-orbit torque-driven skyrmion

dynamics revealed by time-resolved X-ray microscopy. *Nat. Commun.* **8**, 15573 (2017), doi:10.1038/ncomms15573.

60. G. Yu, P. Upadhyaya, X. Li, W. Li, S. K. Kim, Y. Fan, K. L. Wong, Y. Tserkovnyak, P. K. Amiri, K. L. Wang, Room-Temperature Creation and Spin-Orbit Torque Manipulation of Skyrmions in Thin Films with Engineered Asymmetry. *Nano letters* **16**, 1981 (2016), doi:10.1021/acs.nanolett.5b05257.

61. F. Büttner, I. Lemesh, M. Schneider, B. Pfau, C. M. Günther, P. Hessing, J. Geilhufe, L. Caretta, D. Engel, B. Krüger, J. Viefhaus, S. Eisebitt, G. S. D. Beach, Field-free deterministic ultrafast creation of magnetic skyrmions by spin-orbit torques. *Nat. Nanotechnol.* **12**, 1040 (2017), doi:10.1038/nnano.2017.178.

62. W. Legrand, D. Maccariello, N. Reyren, K. Garcia, C. Moutafis, C. Moreau-Luchaire, S. Collin, K. Bouzehouane, V. Cros, A. Fert, Room-Temperature Current-Induced Generation and Motion of sub-100 nm Skyrmions. *Nano letters* **17**, 2703 (2017), doi:10.1021/acs.nanolett.7b00649.

63. J. Iwasaki, M. Mochizuki, N. Nagaosa, Current-induced skyrmion dynamics in constricted geometries. *Nat. Nanotechnol.* **8**, 742 (2013), doi:10.1038/nnano.2013.176.

64. S. Woo, K. M. Song, X. Zhang, Y. Zhou, M. Ezawa, X. Liu, S. Finizio, J. Raabe, N. J. Lee, S.-I. Kim, S.-Y. Park, Y. Kim, J.-Y. Kim, D. Lee, O. Lee, J. W. Choi, B.-C. Min, H. C. Koo, J. Chang, Current-driven dynamics and inhibition of the skyrmion Hall effect of ferrimagnetic skyrmions in GdFeCo films. *Nat. Commun.* **9**, 959 (2018), doi:10.1038/s41467-018-03378-7.

65. X. Zhang, Y. Zhou, M. Ezawa, Magnetic bilayer-skyrmions without skyrmion Hall effect. *Nat. Commun.* **7**, 10293 (2016), doi:10.1038/ncomms10293.

66. M. Belmeguenai, J.-P. Adam, Y. Roussigné, S. Eimer, T. Devolder, J.-V. Kim, S. M. Cherif, A. Stashkevich, A. Thiaville, Interfacial Dzyaloshinskii-Moriya interaction in perpendicularly magnetized Pt/Co/AlOx ultrathin films measured by Brillouin light spectroscopy. *Phys. Rev. B* **91**, 180405 (2015), doi:10.1103/PhysRevB.91.180405.

67. J. Torrejon, J. Kim, J. Sinha, S. Mitani, M. Hayashi, M. Yamanouchi, H. Ohno, Interface control of the magnetic chirality in CoFeB/MgO heterostructures with heavy-metal underlayers. *Nat. Commun.* **5**, 4655 (2014), doi:10.1038/ncomms5655.

68. A. Hrabec, N. A. Porter, A. Wells, M. J. Benitez, G. Burnell, S. McVitie, D. McGrouther, T. A. Moore, C. H. Marrows, Measuring and tailoring the Dzyaloshinskii-Moriya interaction in perpendicularly magnetized thin films. *Phys. Rev. B* **90**, 20402 (2014), doi:10.1103/PhysRevB.90.020402.

69. D.-S. Han, N.-H. Kim, J.-S. Kim, Y. Yin, J.-W. Koo, J. Cho, S. Lee, M. Kläui, H. J. M. Swagten, B. Koopmans, C.-Y. You, Asymmetric Hysteresis for Probing Dzyaloshinskii-Moriya Interaction. *Nano letters* **16**, 4438 (2016), doi:10.1021/acs.nanolett.6b01593.

70. C. Moreau-Luchaire, C. Mouta S, N. Reyren, J. Sampaio, C. A. F. Vaz, N. van Horne, K. Bouzehouane, K. Garcia, C. Deranlot, P. Warnicke, P. Wohlhüter, J.-M. George, M. Weigand, J. Raabe, V. Cros, A. Fert, Additive interfacial chiral interaction in multilayers for stabilization of small individual skyrmions at room temperature. *Nat. Nanotechnol.* **11**, 444 (2016), doi:10.1038/nnano.2015.313.

71. I. Lemesh, F. Büttner, G. S. D. Beach, Accurate model of the stripe domain phase of perpendicularly magnetized multilayers. *Phys. Rev. B* **95**, 174423 (2017), doi:10.1103/PhysRevB.95.174423.

72. P. C. D. Hobbs, D. W. Abraham, H. K. Wickramasinghe, Magnetic force microscopy with 25 nm resolution. *Appl. Phys. Lett.* **55**, 2357 (1989).

73. G. N. Phillips, M. Siekman, L. Abelmann, J. C. Lodder, High resolution magnetic force microscopy using focused ion beam modified tips. *Appl. Phys. Lett.* **81**, 865 (2002).

74. M. Futamoto, T. Hagami, S. Ishihara, K. Soneta, M. Ohtake, Improvement of magnetic force microscope resolution and application to high-density recording media. *IEEE Trans. Magn.* **49**, 2748 (2013).

75. K. Nagano, K. Tobari, M. Ohtake, M. Futamoto, Effect of Magnetic Film Thickness on the Spatial Resolution of Magnetic Force Microscope Tips. *J. Phys.: Conf. Ser.* **303**, 12014 (2011), doi:10.1088/1742-6596/303/1/012014.

76. R. Wiesendanger, Spin mapping at the nanoscale and atomic scale. *Rev. Mod. Phys.* **81**, 1495 (2009), doi:10.1103/RevModPhys.81.1495.

77. M. R. Scheinfein, J. Unguris, M. H. Kelley, D. T. Pierce, R. J. Celotta, Scanning electron microscopy with polarization analysis (SEMPA). *Rev. Sci. Instrum.* **61**, 2501 (1990), doi:10.1063/1.1141908.

78. H. Kronmüller, S. S. P. Parkin, *Handbook of magnetism and advanced magnetic materials*, *Micromagnetism* (John Wiley & Sons, Hoboken, N.J., 2007).

79. K. Koike, Spin-polarized scanning electron microscopy. *Microscopy* **62**, 177 (2013), doi:10.1093/jmicro/dfs092.

80. R. Frömter, F. Kloodt, S. Rößler, A. Frauen, P. Staeck, D. R. Cavicchia, L. Bocklage, V. Röbisch, E. Quandt, H. P. Oepen, Time-resolved scanning electron microscopy with polarization analysis. *Appl. Phys. Lett.* **108**, 142401 (2016), doi:10.1063/1.4945053.

81. E. C. Corredor, S. Kuhrau, F. Kloodt-Twesten, R. Frömter, H. P. Oepen, SEMPA investigation of the Dzyaloshinskii-Moriya interaction in the single, ideally grown Co/Pt(111) interface. *Phys. Rev. B* **96**, 60410 (2017), doi:10.1103/PhysRevB.96.060410.

82. H. Hopster, H. P. Oepen, *Magnetic microscopy of nanostructures* (Springer, Berlin, New York, ed. 1, 2010).

83. C. Phatak, A. K. Petford-Long, M. de Graef, Recent advances in Lorentz microscopy. *Curr. Opin. Solid. St. M. (Current Opinion in Solid State and Materials Science)* **20**, 107 (2016), doi:10.1016/j.cossms.2016.01.002.

84. S. McVitie, D. McGrouther, S. McFadzean, D. A. MacLaren, K. J. O'Shea, M. J. Benitez, Aberration corrected Lorentz scanning transmission electron microscopy. *Ultramicroscopy* **152**, 57 (2015), doi:10.1016/j.ultramic.2015.01.003.

85. H. S. Park, J. S. Baskin, A. H. Zewail, 4D Lorentz electron microscopy imaging. *Nano letters* **10**, 3796 (2010), doi:10.1021/nl102861e.

86. Z. Q. Qiu, S. D. Bader, Surface magneto-optic Kerr effect. *Rev. Sci. Instrum.* **71**, 1243 (2000), doi:10.1063/1.1150496.

87. F. Schmidt, W. Rave, A. Hubert, Enhancement of magneto-optical domain observation by digital image processing. *IEEE Trans. Magn.* **21**, 1596 (1985), doi:10.1109/TMAG.1985.1064048.

88. J. McCord, A. Hubert, Normalized differential Kerr microscopy an advanced method for magnetic imaging. *Phys. Status Solidi A* **171**, 555 (1999), doi:10.1002/(SICI)1521-396X(199902)171:2<555::AID-PSSA555>3.0.CO;2-G.

89. E. Abbe, Beiträge zur Theorie des Mikroskops und der mikroskopischen Wahrnehmung. *Archiv f. mikrosk. Anatomie* **9**, 413 (1873), doi:10.1007/BF02956173.

90. A. Laraoui, M. Albrecht, J.-Y. Bigot, Femtosecond magneto-optical Kerr microscopy. *Opt. Lett.* **32**, 936 (2007), doi:10.1364/OL.32.000936.

91. G. Schmahl, D. Rudolph, B. Niemann, O. Christ, Zone-plate X-ray microscopy. *Q. Rev. Biophys.* **13**, 297 (1980), doi:10.1017/S0033583500001700.

92. J. Kirz, C. Jacobsen, M. Howells, Soft X-ray microscopes and their biological applications. *Q. Rev. Biophys.* **28**, 33 (1995), doi:10.1017/S0033583500003139.

93. W. Chao, J. Kim, S. Rekawa, P. Fischer, E. H. Anderson, Demonstration of 12 nm resolution Fresnel zone plate lens based soft x-ray microscopy. *Opt. Express* **17**, 17669 (2009), doi:10.1364/OE.17.017669.

94. T. Warwick, K. Franck, J. B. Kortright, G. Meigs, M. Moronne, S. Myneni, E. Rotenberg, S. Seal, W. F. Steele, H. Ade, A scanning transmission x-ray microscope for materials science spectromicroscopy at the advanced light source. *Rev. Sci. Instrum.* **69**, 2964 (1998), doi:10.1063/1.1149041.

95. B. Rösner, F. Koch, F. Döring, V. A. Guzenko, M. Meyer, J. L. Ornelas, A. Späth, R. H. Fink, S. Stanescu, S. Swaraj, R. Belkhou, B. Watts, J. Raabe, C. David, 7 nm Spatial Resolution in Soft X-ray Microscopy. *Microsc. Microanal. (Microscopy and Microanalysis)* **24**, 272 (2018), doi:10.1017/S1431927618013697.

96. S. Kasai, P. Fischer, M.-Y. Im, K. Yamada, Y. Nakatani, K. Kobayashi, H. Kohno, T. Ono, Probing the spin polarization of current by soft X-ray imaging of current-induced magnetic vortex dynamics. *Phys. Rev. Lett.* **101**, 237203 (2008), doi:10.1103/PhysRevLett.101.237203.

97. M. Bolte, G. Meier, B. Krüger, A. Drews, R. Eiselt, L. Bocklage, S. Bohlens, T. Tyliszczak, A. Vansteenkiste, B. van Waeyenberge, Time-resolved x-ray microscopy of spin-torque-induced magnetic vortex gyration. *Phys. Rev. Lett.* **100**, 176601 (2008), doi:10.1103/PhysRevLett.100.176601.

98. T. Kinoshita, K. Arai, K. Fukumoto, T. Ohkochi, M. Kotsugi, F. Guo, T. Muro, T. Nakamura, H. Osawa, T. Matsushita, Observation of micro-magnetic structures by synchrotron radiation photoelectron emission microscopy. *J. Phys. Soc. Jpn.* **82**, 21005 (2012).

99. C. M. Schneider, A. Krasyuk, S. A. Nepijko, A. Oelsner, G. Schönhense, Accessing fast magnetization dynamics by XPEEM. *J. Magn. Magn. Mater.* **304**, 6 (2006), doi:10.1016/j.jmmm.2006.02.013.

100. E. Beaurepaire, J.-C. Merle, A. Daunois, J.-Y. Bigot, Ultrafast spin dynamics in ferromagnetic nickel. *Phys. Rev. Lett.* **76**, 4250 (1996), doi:10.1103/PhysRevLett.76.4250.

101. J. Hohlfeld, E. Matthias, R. Knorren, K. H. Bennemann, Nonequilibrium magnetization dynamics of nickel. *Phys. Rev. Lett.* **78**, 4861 (1997), doi:10.1103/PhysRevLett.78.4861.

102. B. Koopmans, M. van Kampen, J. T. Kohlhepp, W. J. M. de Jonge, Ultrafast magneto-optics in nickel. *Phys. Rev. Lett.* **85**, 844 (2000), doi:10.1103/PhysRevLett.85.844.

103. L. Müller, C. Gutt, B. Pfau, S. Schaffert, J. Geilhufe, F. Büttner, J. Mohanty, S. Flewett, R. Treusch, S. Düsterer, H. Redlin, A. Al-Shemmary, M. Hille, A. Kobs, R. Frömter, H. P. Oepen, B. Ziaja, N. Medvedev, S.-K. Son, R. Thiele, R. Santra, B. Vodungbo, J. Lüning, S. Eisebitt, G. Grübel, Breakdown of the x-ray resonant magnetic scattering signal during intense pulses of extreme ultraviolet free-electron-laser radiation. *Phys. Rev. Lett.* **110**, 234801 (2013), doi:10.1103/PhysRevLett.110.234801.

104. L. Müller, S. Schleitzer, C. Gutt, B. Pfau, S. Schaffert, J. Geilhufe, C. von Korff Schmising, M. Schneider, C. M. Günther, F. Büttner, F. Capotondi, E. Pedersoli, S. Düsterer, H. Redlin, A. Al-Shemmary, R. Treusch, J. Bach, R. Frömter, B. Vodungbo, J. Gautier, P. Zeitoun, H. Popescu, V. Lopez-Flores, N. Beaulieu, F. Sirotti, N. Jaouen, G. Malinowski, B. Tudu, K. Li, J. Lüning, H. P. Oepen, M. Kiskinova, S. Eisebitt, G. Grübel, Ultrafast Dynamics of Magnetic Domain Structures Probed by Coherent Free-Electron Laser Light. *Synchrotron Radiat. News* **26**, 27 (2013), doi:10.1080/08940886.2013.850384.

105. X. Shi, P. Fischer, V. Neu, D. Elefant, J. C. T. Lee, D. A. Shapiro, M. Farmand, T. Tyliszczak, H.-W. Shiu, S. Marchesini, S. Roy, S. D. Kevan, Soft x-ray ptychography studies of nanoscale magnetic and structural correlations in thin SmCo5 films. *Appl. Phys. Lett.* **108**, 94103 (2016), doi:10.1063/1.4942776.

106. Y.-S. Yu, R. Celestre, B. Enders, K. Nowrouzi, H. Padmore, T. Warwick, J.-R. Jeong, D. A. Shapiro, Nanoscale Visualization of Magnetic Contrasts with Soft X-ray Spectro-Ptychography at the Advanced Light Source. *Microsc. Microanal. (Microscopy and Microanalysis)* **24**, 530 (2018), doi:10.1017/S143192761801485X.

107. O. M. Yefanov, A. V. Zozulya, I. A. Vartanyants, J. Stangl, C. Mocuta, T. H. Metzger, G. Bauer, T. Boeck, M. Schmidbauer, Coherent diffraction tomography of nanoislands from grazing-incidence small-angle X-ray scattering. *Appl. Phys. Lett.* **94**, 123104 (2009), doi:10.1063/1.3103246.

108. C. Donnelly, M. Guizar-Sicairos, V. Scagnoli, S. Gliga, M. Holler, J. Raabe, L. J. Heyderman, Three-dimensional magnetization structures revealed with X-ray vector nanotomography. *Nature* **547**, 328 (2017), doi:10.1038/nature23006.

109. D. Stickler, Doctoral dissertation, Universität Hamburg (2010).

110. T. Wang, D. Zhu, B. Wu, C. Graves, S. Schaffert, T. Rander, L. Müller, B. Vodungbo, C. Baumier, D. P. Bernstein, Femtosecond single-shot imaging of nanoscale ferromagnetic order in Co/Pd multilayers using resonant x-ray holography. *Phys. Rev. Lett.* **108**, 267403 (2012), doi:10.1103/PhysRevLett.108.267403.

111. C. von Korff Schmising, B. Pfau, M. Schneider, C. M. Günther, M. Giovannella, J. Perron, B. Vodungbo, L. Müller, F. Capotondi, E. Pedersoli, Imaging ultrafast demagnetization dynamics after a spatially localized optical excitation. *Phys. Rev. Lett.* **112**, 217203 (2014), doi:10.1103/PhysRevLett.112.217203.

112. L. D. Landau, E. M. Lifšic, *Electrodynamics of continuous media* (Pergamon Press, Oxford, 1960).

113. S. Blundell, *Magnetism in condensed matter* (Oxford University Press, Oxford, New York, 2012).

114. R. C. O'Handley, *Modern magnetic materials*, *Principles and applications* (John Wiley, New York, 2000).

115. C. Kittel, C.-Y. Fong, *Quantum theory of solids* (Wiley, New York, ed. 2, 2010).

116. L. D. Landau, E. Lifshits, On the theory of the dispersion of magnetic permeabiliy in ferromagnetic bodies. *Phys. Z.* **8**, 153 (1935).

117. A. Aharoni, *Introduction to the theory of ferromagnetism* (Clarendon Press, Oxford, 1996).

118. T. Maeda, H. Yamauchi, H. Watanabe, Spin Wave Resonance and Exchange Parameters in fcc Fe-Ni Alloys. *J. Phys. Soc. Jpn.* **35**, 1635 (1973), doi:10.1143/JPSJ.35.1635.

119. M. D. Kuz'min, Shape of temperature dependence of spontaneous magnetization of ferromagnets. *Phys. Rev. Lett.* **94**, 107204 (2005), doi:10.1103/PhysRevLett.94.107204.

120. R. Moreno, R. F. L. Evans, S. Khmelevskyi, M. C. Muñoz, R. W. Chantrell, O. Chubykalo-Fesenko, Temperature-dependent exchange stiffness and domain wall width in Co. *Phys. Rev. B* **94**, 104433 (2016), doi:10.1103/PhysRevB.94.104433.

121. A. Hubert, R. Schäfer, *Magnetic domains*, *The analysis of magnetic microstructures* (Springer, Berlin, 2011).

122. J. A. Osborn, Demagnetizing Factors of the General Ellipsoid. *Phys. Rev.* **67**, 351 (1945), doi:10.1103/PhysRev.67.351.

123. C. Kittel, *Einführung in die Festkörperphysik* (Oldenbourg Verlag, München, ed. 15, 2013).

124. T. Suzuki, D. Weller, C.-A. Chang, R. Savoy, T. Huang, B. A. Gurney, V. Speriosu, Magnetic and magneto-optic properties of thick face-centered-cubic Co single-crystal films. *Appl. Phys. Lett.* **64**, 2736 (1994), doi:10.1063/1.111946.

125. M. Stearns, *Landolt-Börnstein: Numerical Data and Functional Relationships in Science and Technology*, *New Series* (Springer, 1986).

126. M. T. Johnson, P. J. H. Bloemen, F. J. A. den Broeder, J.J. de Vries, Magnetic anisotropy in metallic multilayer. *Rep. Prog. Phys.* **59**, 1409 (1996), doi:10.1088/0034-4885/59/11/002.

127. A. Kobs, Doctoral dissertation, Universität Hamburg (2013).

128. A. Kobs, S. Hesse, W. Kreuzpaintner, G. Winkler, D. Lott, P. Weinberger, A. Schreyer, H. P. Oepen, Anisotropic interface magnetoresistance in Pt/Co/Pt sandwiches. *Phys. Rev. Lett.* **106**, 217207 (2011), doi:10.1103/PhysRevLett.106.217207.

129. G. Winkler, A. Kobs, A. Chuvilin, D. Lott, A. Schreyer, H. P. Oepen, On the variation of magnetic anisotropy in Co/Pt(111) on silicon oxide. *J. Appl. Phys.* **117**, 105306 (2015), doi:10.1063/1.4914039.

130. G. Winkler, Doctoral dissertation, Universität Hamburg (2015).

131. M. Kisielewski, A. Maziewski, M. Tekielak, J. Ferré, S. Lemerle, V. Mathet, C. Chappert, Magnetic anisotropy and magnetization reversal processes in Pt/Co/Pt films. *J. Magn. Magn. Mater.* **260**, 231 (2003), doi:10.1016/S0304-8853(02)01333-1.

132. L. Néel, Anisotropie magnétique superficielle et surstructures d'orientation. *J. Phys. Radium* **15**, 225 (1954), doi:10.1051/jphysrad:01954001504022500.

133. L. Néel, N. Kurti, *The selected works of Louis Néel*, *Translations from the first French edition* (Gordon and Breach, New York, 1988).

134. U. Gradmann, J. Müller, Flat Ferromagnetic, Epitaxial 48Ni/52Fe(111) Films of few Atomic Layers. *Phys. Status Solidi B* **27**, 313 (1968), doi:10.1002/pssb.19680270133.

135. P. F. Carcia, A. D. Meinhaldt, A. Suna, Perpendicular magnetic anisotropy in Pd/Co thin film layered structures. *Appl. Phys. Lett.* **47**, 178 (1985), doi:10.1063/1.96254.

136. P. F. Carcia, Perpendicular magnetic anisotropy in Pd/Co and Pt/Co thin-film layered structures. *J. Appl. Phys.* **63**, 5066 (1988), doi:10.1063/1.340404.

137. F.J.A. den Broeder, W. Hoving, P.J.H. Bloemen, Magnetic anisotropy of multilayers. *J. Magn. Magn. Mater.* **93**, 562 (1991), doi:10.1016/0304-8853(91)90404-X.

138. T. Kingetsu, Molecular-beam-epitaxial growth and magnetic properties of (111)Pt/Co/Ag, Pt/Co, and Ag/Co/Pt superlattices. *J. Appl. Phys.* **76**, 4267 (1994), doi:10.1063/1.357311.

139. O. Fruchart, A. Thiaville, Magnetism in reduced dimensions. *C. R. Phys.* **6**, 921 (2005), doi:10.1016/j.crhy.2005.10.011.

140. P. Bruno, Tight-binding approach to the orbital magnetic moment and magnetocrystalline anisotropy of transition-metal monolayers. *Phys. Rev. B* **39**, 865 (1989), doi:10.1103/PhysRevB.39.865.

141. J. M. MacLaren, R. H. Victora, Theoretical predictions for magnetic interface anisotropy. *IEEE Trans. Magn.* **29**, 3034 (1993), doi:10.1109/20.281110.

142. R. H. Victora, J. M. MacLaren, Theory of anisotropy in strained superlattices. *J. Appl. Phys.* **73**, 6415 (1993), doi:10.1063/1.352617.

143. J. A. C. Bland, B. Heinrich, Eds., *Ultrathin Magnetic Structures I*, *An Introduction to the Electronic, Magnetic and Structural Properties* (Springer-Verlag Berlin Heidelberg, Berlin, Heidelberg, 2005).

144. Y. Luo, M. Moske, K. Samwer, Interlayer coupling and magnetoresistance in Ir/Co multilayers. *Europhys. Lett.* **42**, 565 (1998), doi:10.1209/epl/i1998-00288-6.

145. F. C. Frank, J. H. van der Merwe, One-Dimensional Dislocations. I. Static Theory. *Proc. Royal Soc. A* **198**, 205 (1949), doi:10.1098/rspa.1949.0095.

146. P. Bruno, Magnetic surface anisotropy of cobalt and surface roughness effects within Neel's model. *J. Phys. F: Met. Phys.* **18**, 1291 (1988), doi:10.1088/0305-4608/18/6/029.

147. H. Stillrich, C. Menk, R. Frömter, H. P. Oepen, Magnetic anisotropy and the cone state in Co/Pt multilayer films. *J. Appl. Phys.* **105**, 07C308 (2009), doi:10.1063/1.3070644.

148. R. Frömter, H. Stillrich, C. Menk, H. P. Oepen, Imaging the cone state of the spin reorientation transition. *Phys. Rev. Lett.* **100**, 207202 (2008), doi:10.1103/PhysRevLett.100.207202.

149. L. Louail, K. Ounadjela, R. L. Stamps, Temperature-dependent thin-film cone states in epitaxial Co/Pt multilayers. *J. Magn. Magn. Mater.* **167**, L189-L199 (1997), doi:10.1016/S0304-8853(96)00724-X.

150. P. Jensen, K. H. Bennemann, Magnetic structure of films. *Surf. Sci. Rep.* **61**, 129 (2006), doi:10.1016/j.surfrep.2006.02.001.

151. R. Frömter, C. Menk, H. Stillrich, H. Peter Oepen, Imaging the domain pattern of the canted magnetization state in Co/Pt multilayer films. *Vacuum* **82**, 395 (2007), doi:10.1016/j.vacuum.2007.07.064.

152. Y. Millev, J. Kirschner, Reorientation transitions in ultrathin ferromagnetic films by thickness- and temperature-driven anisotropy flows. *Phys. Rev. B* **54**, 4137 (1996), doi:10.1103/PhysRevB.54.4137.

153. E. Y. Vedmedenko, H. P. Oepen, J. Kirschner, Microstructure of the spin reorientation transition in second-order approximation of magnetic anisotropy. *Phys. Rev. B* **66**, 214401 (2002), doi:10.1103/PhysRevB.66.214401.

154. E. Y. Vedmedenko, H. P. Oepen, J. Kirschner, Magnetic microstructure of the spin reorientation transition. *J. Appl. Phys.* **89**, 7145 (2001), doi:10.1063/1.1357154.

155. A. Fert, P. M. Levy, Role of Anisotropic Exchange Interactions in Determining the Properties of Spin-Glasses. *Phys. Rev. Lett.* **44**, 1538 (1980), doi:10.1103/PhysRevLett.44.1538.

156. O. Boulle, S. Rohart, L. D. Buda-Prejbeanu, É. Jué, I. M. Miron, S. Pizzini, J. Vogel, G. Gaudin, A. Thiaville, Domain wall tilting in the presence of the Dzyaloshinskii-Moriya interaction in out-of-plane magnetized magnetic nanotracks. *Phys. Rev. Lett.* **111**, 217203 (2013), doi:10.1103/PhysRevLett.111.217203.

157. P. Grünberg, R. Schreiber, Y. Pang, M. B. Brodsky, H. Sowers, Layered magnetic structures. *Phys. Rev. Lett.* **57**, 2442 (1986), doi:10.1103/PhysRevLett.57.2442.

158. C.F. Majkrzak, J.W. Cable, J. Kwo, M. Hong, McWhan D. B., Y. Yafet, J.V. Waszczak, C. Vettier, Observation of a magnetic antiphase domain structure with long-range order in a

synthetic Gd-Y superlattice. *Phys. Rev. Lett.* **56**, 2700 (1986), doi:10.1103/PhysRevLett.56.2700.

159. Salamonm M. B., S. Sinha, J. J. Rhyne, Cunningham J. E., R. W. Erwin, J. Borchers, C. P. Flynn, Long-range incommensurate magnetic order in a Dy-Y multilayer. *Phys. Rev. Lett.* **56**, 259 (1986), doi:10.1103/PhysRevLett.56.259.

160. S. S. P. Parkin, N. More, K. P. Roche, Oscillations in exchange coupling and magnetoresistance in metallic superlattice structures. *Phys. Rev. Lett.* **64**, 2304 (1990), doi:10.1103/PhysRevLett.64.2304.

161. J. Unguris, R. J. Celotta, D. T. Pierce, Oscillatory exchange coupling in Fe/Au/Fe(100). *J. Appl. Phys.* **75**, 6437 (1994), doi:10.1063/1.356954.

162. S. S. P. Parkin, Systematic variation of the strength and oscillation period of indirect magnetic exchange coupling through the 3d, 4d, and 5d transition metals. *Phys. Rev. Lett.* **67**, 3598 (1991), doi:10.1103/PhysRevLett.67.3598.

163. F. Petroff, A. Barthélemy, D. H. Mosca, D. K. Lottis, A. Fert, P. A. Schroeder, W. P. Pratt, R. Loloee, S. Lequien, Oscillatory interlayer exchange and magnetoresistance in Fe/Cu multilayers. *Phys. Rev. B* **44**, 5355 (1991), doi:10.1103/PhysRevB.44.5355.

164. J. Fassbender, F. Nörtemann, R. L. Stamps, R. E. Camley, B. Hillebrands, G. Güntherodt, S. S. P. Parkin, Oscillatory interlayer exchange coupling of Co/Ru multilayers investigated by Brillouin light scattering. *Phys. Rev. B* **46**, 5810 (1992), doi:10.1103/PhysRevB.46.5810.

165. K. Ounadjela, D. Muller, A. Dinia, A. Arbaoui, P. Panissod, G. Suran, Perpendicular anisotropy and antiferromagnetic coupling in Co/Ru strained superlattices. *Phys. Rev. B* **45**, 7768 (1992), doi:10.1103/PhysRevB.45.7768.

166. Y. Huai, R. W. Cochrane, Oscillatory magnetic coupling and magnetoresistance in Co/Re superlattices. *J. Appl. Phys.* **72**, 2523 (1992), doi:10.1063/1.351549.

167. P.J.H. Bloemen, W. J. M. de Jonge, R. Coehoorn, Interlayer coupling in Co/Os multilayers. *J. Magn. Magn. Mater.* **121**, 306 (1993), doi:10.1016/0304-8853(93)91209-P.

168. Z. Q. Qiu, J. Pearson, S. D. Bader, Oscillatory interlayer magnetic coupling of wedged Co/Cu/Co sandwiches grown on Cu(100) by molecular beam epitaxy. *Phys. Rev. B* **46**, 8659 (1992), doi:10.1103/PhysRevB.46.8659.

169. P. Bruno, Interlayer exchange coupling. *J. Magn. Magn. Mater.* **121**, 248 (1993), doi:10.1016/0304-8853(93)91197-F.

170. P. Bruno, Theory of interlayer magnetic coupling. *Phys. Rev. B* **52**, 411 (1995), doi:10.1103/PhysRevB.52.411.

171. M. D. Stiles, Exchange coupling in magnetic heterostructures. *Phys. Rev. B* **48**, 7238 (1993), doi:10.1103/PhysRevB.48.7238.

172. M. D. Stiles, in *Ultrathin Magnetic Structures III*, , Eds.J. A. C. Bland, B. Heinrich (Springer-Verlag, Berlin/Heidelberg, 2005).

173. P. Bruno, Theory of interlayer exchange interactions in magnetic multilayers. *J. Phys.: Condens. Matt.* **11**, 9403 (1999), doi:10.1088/0953-8984/11/48/305.

174. P. Bruno, Oscillations of Interlayer Exchange Coupling vs. Ferromagnetic-Layers Thickness. *Europhys. Lett.* **23**, 615 (1993), doi:10.1209/0295-5075/23/8/013.

175. J. W. Knepper, F. Y. Yang, Oscillatory interlayer coupling in Co/Pt multilayers with perpendicular anisotropy. *Phys. Rev. B* **71**, 224403 (2005), doi:10.1103/PhysRevB.71.224403.

176. J. Moritz, F. Garcia, J. C. Toussaint, B. Dieny, J. P. Nozières, Orange peel coupling in multilayers with perpendicular magnetic anisotropy. *Europhys. Lett.* **65**, 123 (2004), doi:10.1209/epl/i2003-10063-9.

177. X.-X. Li, J. Bao, L.-Y. Lu, X.-G. Xu, Y. Jiang, Oscillatory antiferromagnetic interlayer coupling in Co/Pt multilayer with perpendicular anisotropy. *Solid State Commun.* **148**, 209 (2008), doi:10.1016/j.ssc.2008.08.017.

178. Z. Y. Liu, F. Zhang, H. L. Chen, B. Xu, D. L. Yu, J. L. He, Y. J. Tian, Antiferromagnetic interlayer coupling in Pt/Co multilayers with perpendicular anisotropy. *Phys. Rev. B* **79**, 24427 (2009), doi:10.1103/PhysRevB.79.024427.

179. Z. Y. Liu, F. Zhang, B. Xu, D. L. Yu, J. L. He, Y. J. Tian, Thermally induced antiferromagnetic interlayer coupling and its oscillatory dependence on repetition number in spin-valve Co/Pt multilayers. *J. Phys. D: Appl. Phys.* **42**, 35010 (2009), doi:10.1088/0022-3727/42/3/035010.

180. P. Lang, L. Nordström, R. Zeller, P. H. Dederichs, Ab initio calculations of the exchange coupling of Fe and Co monolayers in Cu. *Phys. Rev. Lett.* **71**, 1927 (1993), doi:10.1103/PhysRevLett.71.1927.

181. P. J. H. Bloemen, H. W. van Kesteren, H. J. M. Swagten, W. J. M. de Jonge, Oscillatory interlayer exchange coupling in Co/Ru multilayers and bilayers. *Phys. Rev. B* **50**, 13505 (1994), doi:10.1103/PhysRevB.50.13505.

182. M. S. Gabor, T. Petrisor, R. B. Mos, M. Nasui, C. Tiusan, Interlayer exchange coupling in perpendicularly magnetized Pt/Co/Ir/Co/Pt structures. *J. Phys. D: Appl. Phys.* **50**, 465004 (2017), doi:10.1088/1361-6463/aa8ece.

183. S. S. P. Parkin, A. Mansour, G. P. Felcher, Antiferromagnetic interlayer exchange coupling in sputtered Fe/Cr multilayers. *Appl. Phys. Lett.* **58**, 1473 (1991), doi:10.1063/1.105201.

184. B. Dieny, J. P. Gavigan, J. P. Rebouillat, Magnetisation processes, hysteresis and finite-size effects in model multilayer systems of cubic or uniaxial anisotropy with antiferromagnetic coupling between adjacent ferromagnetic layers. *J. Phys.: Condens. Matt.* **2**, 159 (1990), doi:10.1088/0953-8984/2/1/013.

185. H. Itoh, H. Yanagihara, K. Suzuki, E. Kita, Coexistence of the uniaxial anisotropy and the antiferromagnetic coupling in Co/Ir(111) superlattices. *J. Magn. Magn. Mater.* **257**, 184 (2003), doi:10.1016/S0304-8853(02)01167-8.

186. B. Kaplan, G. A. Gehring, The domain structure in ultrathin magnetic films. *J. Magn. Magn. Mater.* **128**, 111 (1993), doi:10.1016/0304-8853(93)90863-W.

187. Y. Millev, Bose - Einstein integrals and domain morphology in ultrathin ferromagnetic films with perpendicular magnetization. *J. Phys.: Condens. Matt.* **8**, 3671 (1996), doi:10.1088/0953-8984/8/20/013.

188. B. A. Lilley, LXXI. Energies and widths of domain boundaries in ferromagnetics. *Philos. Mag.* **41**, 792 (2010), doi:10.1080/14786445008561011.

189. H. Träuble, O. Boster, H. Kronmüller, A. Seeger, Ferromagnetische Eigenschaften hexagonaler Kobalt-Einkristalle. *Phys. Status Solidi B* **10**, 283 (1965), doi:10.1002/pssb.19650100127.

190. S. V. Tarasenko, A. Stankiewicz, V. V. Tarasenko, J. Ferré, Bloch wall dynamics in ultrathin ferromagnetic films. *J. Magn. Magn. Mater.* **189**, 19 (1998), doi:10.1016/S0304-8853(98)00230-3.

191. H. Yang, A. Thiaville, S. Rohart, A. Fert, M. Chshiev, Anatomy of Dzyaloshinskii-Moriya Interaction at Co/Pt Interfaces. *Phys. Rev. Lett.* **115**, 267210 (2015), doi:10.1103/PhysRevLett.115.267210.

192. S. Woo, K. Litzius, B. Krüger, M.-Y. Im, L. Caretta, K. Richter, M. Mann, A. Krone, R. M. Reeve, M. Weigand, P. Agrawal, I. Lemesh, M.-A. Mawass, P. Fischer, M. Kläui, G. S. D. Beach, Observation of room-temperature magnetic skyrmions and their current-driven dynamics in ultrathin metallic ferromagnets. *Nat. Mater.* **15**, 501 (2016), doi:10.1038/nmat4593.

193. J. Stöhr, H. C. Siegmann, Eds., *Magnetism*, *From fundamentals to nanoscale dynamics* (Springer, 2016).

194. J. Als-Nielsen, Des McMorrow, Eds., *Elements of modern X-ray physics* (Wiley, Chichester, 2011).

195. E. C. Stoner, Collective Electron Ferromagnetism. II. Energy and Specific Heat. *Proc. Royal Soc. A* **169**, 339 (1939), doi:10.1098/rspa.1939.0003.

196. J. Stöhr, Exploring the microscopic origin of magnetic anisotropies with X-ray magnetic circular dichroism (XMCD) spectroscopy. *J. Magn. Magn. Mater.* **200**, 470 (1999), doi:10.1016/S0304-8853(99)00407-2.

197. S. W. Lovesey, S. P. Collins, Eds., *X-ray scattering and absorption by magnetic materials* (Clarendon Press, Oxford, 1996).

198. J.P. Hannon, G.T. Trammell, M. Blume, D. Gibbs, X-ray resonance exchange scattering. *Phys. Rev. Lett.* **61**, 1245 (1988), doi:10.1103/PhysRevLett.61.1245.

199. N.-T. D. Loh, S. Eisebitt, S. Flewett, V. Elser, Recovering magnetization distributions from their noisy diffraction data. *Phys. Rev. E* **82**, 61128 (2010), doi:10.1103/PhysRevE.82.061128.

200. J. L. Erskine, E. A. Stern, Calculation of the M23 magneto-optical absorption spectrum of ferromagnetic nickel. *Phys. Rev. B* **12**, 5016 (1975), doi:10.1103/PhysRevB.12.5016.

201. G. Schütz, W. Wagner, W. Wilhelm, P. Kienle, R. Zeller, R. Frahm, G. Materlik, Absorption of Circularly Polarized X Rays in Iron. *Phys. Rev. Lett.* **58**, 737 (1987), doi:10.1103/PhysRevLett.58.737.

202. J. B. Kortright, S.-K. Kim, G. P. Denbeaux, G. Zeltzer, K. Takano, E. E. Fullerton, Soft-x-ray small-angle scattering as a sensitive probe of magnetic and charge heterogeneity. *Phys. Rev. B* **64**, 92401 (2001), doi:10.1103/PhysRevB.64.092401.

203. G. van der Laan, B. T. Thole, G. A. Sawatzky, J. B. Goedkoop, J. C. Fuggle, J.-M. Esteva, R. Karnatak, J. P. Remeika, H. A. Dabkowska, Experimental proof of magnetic x-ray dichroism. *Phys. Rev. B* **34**, 6529 (1986), doi:10.1103/PhysRevB.34.6529.

204. E. Arenholz, G. van der Laan, R. V. Chopdekar, Y. Suzuki, Anisotropic x-ray magnetic linear dichroism at the Fe L2,3 edges in Fe3O4. *Phys. Rev. B* **74**, 94407 (2006), doi:10.1103/PhysRevB.74.094407.

205. S. Streit-Nierobisch, D. Stickler, C. Gutt, L.-M. Stadler, H. Stillrich, C. Menk, R. Frömter, C. Tieg, O. Leupold, H. P. Oepen, G. Grübel, Magnetic soft x-ray holography study of focused ion beam-patterned Co/Pt multilayers. *J. Appl. Phys.* **106**, 83909 (2009), doi:10.1063/1.3246724.

206. C. Gutt, S. Streit-Nierobisch, L.-M. Stadler, B. Pfau, C. M. Günther, R. Könnecke, R. Frömter, A. Kobs, D. Stickler, H. P. Oepen, R. R. Fäustlin, R. Treusch, J. Feldhaus, E. Weckert, I. A. Vartanyants, M. Grunze, A. Rosenhahn, T. Wilhein, S. Eisebitt, G. Grübel, Single-pulse resonant magnetic scattering using a soft x-ray free-electron laser. *Phys. Rev. B* **81**, 100401 (2010), doi:10.1103/PhysRevB.81.100401.

207. T. O. Menteş, C. Sánchez-Hanke, C. C. Kao, Reconstruction of magnetization density in two-dimensional samples from soft X-ray speckle patterns using the multiple-wavelength anomalous diffraction method. *J. Synchrotron Radiat.* **9**, 90 (2002), doi:10.1107/S0909049502001310.

208. K. Bagschik, Doctoral dissertation, Universität Hamburg (2017).

209. K. Bagschik, R. Frömter, J. Bach, B. Beyersdorff, L. Müller, S. Schleitzer, M. H. Berntsen, C. Weier, R. Adam, J. Viefhaus, C. M. Schneider, G. Grübel, H. P. Oepen, Employing soft x-ray resonant magnetic scattering to study domain sizes and anisotropy in Co/Pd multilayers. *Phys. Rev. B* **94**, 134413 (2016), doi:10.1103/PhysRevB.94.134413.

210. D. Nolle, M. Weigand, P. Audehm, E. Goering, U. Wiesemann, C. Wolter, E. Nolle, G. Schütz, Note. *Rev. Sci. Instrum.* **83**, 46112 (2012), doi:10.1063/1.4707747.

211. W. Chao, B. D. Harteneck, J. A. Liddle, E. H. Anderson, D. T. Attwood, Soft X-ray microscopy at a spatial resolution better than 15 nm. *Nature* **435**, 1210 (2005), doi:10.1038/nature03719.

212. B. Pfau, S. Eisebitt, in *Synchrotron Light Sources and Free-Electron Lasers*, , Eds.E. Jaeschke, S. Khan, J. R. Schneider, J. B. Hastings (Springer International Publishing, Cham, 2014).

213. D. Gabor, W. E. Kock, G. W. Stroke, Holography. *Science* **173**, 11 (1971), doi:10.1126/science.173.3991.11.

214. G. K. Ackermann, J. Eichler, *Holography*, *A practical approach* (John Wiley distributor, Weinheim, Chichester, 2007).

215. G. W. Stroke, D. G. Falconer, Attainment of high resolutions in wavefront-reconstruction imaging. *Phys. Lett.* **13**, 306 (1964), doi:10.1016/0031-9163(64)90022-8.

216. G. W. Stroke, LENSLESS FOURIER-TRANSFORM METHOD FOR OPTICAL HOLOGRAPHY. *Appl. Phys. Lett.* **6**, 201 (1965), doi:10.1063/1.1754131.

217. S. Aoki, Y. Ichihara, S. Kikuta, X-Ray Hologram Obtained by Using Synchrotron Radiation. *Jpn. J. Appl. Phys.* **11**, 1857 (1972), doi:10.1143/JJAP.11.1857.

218. I. McNulty, J. Kirz, C. Jacobsen, E. H. Anderson, M. Howells, D. P. Kern, High-Resolution Imaging by Fourier Transform X-ray Holography. *Science* **256**, 1009 (1992), doi:10.1126/science.256.5059.1009.

219. S. Eisebitt, J. Lüning, W. F. Schlotter, M. Lörgen, O. Hellwig, W. Eberhardt, J. Stöhr, Lensless imaging of magnetic nanostructures by X-ray spectro-holography. *Nature* **432**, 885 (2004), doi:10.1038/nature03139.

220. D. Stickler, R. Frömter, H. Stillrich, C. Menk, C. Tieg, S. Streit-Nierobisch, M. Sprung, C. Gutt, L.-M. Stadler, O. Leupold, G. Grübel, H. P. Oepen, Soft x-ray holographic microscopy. *Appl. Phys. Lett.* **96**, 42501 (2010), doi:10.1063/1.3291942.

221. E. Guehrs, C. M. Günther, B. Pfau, T. Rander, S. Schaffert, W. F. Schlotter, S. Eisebitt, Wavefield back-propagation in high-resolution X-ray holography with a movable field of view. *Opt. Express* **18**, 18922 (2010), doi:10.1364/OE.18.018922.

222. J. W. Goodman, Ed., *Introduction to Fourier optics* (Roberts & Company, Englewood, Colorado, 2005).

223. D. M. Paganin, Ed., *Coherent X-ray optics* (Oxford University Press, Oxford, 2013).

224. W. F. Schlotter, Doctoral dissertation, Stanford University (2007).

225. T. Butz, *Fouriertransformation für Fußgänger* (Vieweg+Teubner Verlag / Springer Fachmedien Wiesbaden GmbH Wiesbaden, Wiesbaden, 2012).

226. W. F. Schlotter, R. Rick, K. Chen, A. Scherz, J. Stöhr, J. Lüning, S. Eisebitt, C. Günther, W. Eberhardt, O. Hellwig, I. McNulty, Multiple reference Fourier transform holography with soft x rays. *Appl. Phys. Lett.* **89**, 163112 (2006), doi:10.1063/1.2364259.

227. P. C. Mehta, C. Bhan, R. Hradaynath, Multiple imaging by lensless Fourier transform holography. *J. Opt.* **10**, 133 (1979), doi:10.1088/0150-536X/10/3/006.

228. J. D. Gaskill, J. W. Goodman, Use of multiple reference sources to increase the effective field of view in lensless Fourier-transform holography. *Proc. IEEE* **57**, 823 (1969), doi:10.1109/PROC.1969.7099.

229. B. Pfau, Doctoral dissertation, TU Berlin (2013).

230. W. F. Schlotter, J. Lüning, R. Rick, K. Chen, A. Scherz, S. Eisebitt, C. M. Günther, W. Eberhardt, O. Hellwig, J. Stöhr, Extended field of view soft x-ray Fourier transform holography. *Opt. Lett.* **32**, 3110 (2007), doi:10.1364/OL.32.003110.

231. B. Pfau, C. M. Günther, R. Könnecke, E. Guehrs, O. Hellwig, W. F. Schlotter, S. Eisebitt, Magnetic imaging at linearly polarized x-ray sources. *Opt. Express* **18**, 13608 (2010), doi:10.1364/OE.18.013608.

232. H. D. Luke, The origins of the sampling theorem. *IEEE Commun. Mag.* **37**, 106 (1999), doi:10.1109/35.755459.

233. D. Attwood, A. Sakdinawat, Eds., *X-rays and Extreme Ultraviolet Radiation*, *Principles and Applications* (Cambridge University Press, 2017).

234. O. Kfir, S. Zayko, C. Nolte, M. Sivis, M. Möller, B. Hebler, S. S. P. K. Arekapudi, D. Steil, S. Schäfer, M. Albrecht, O. Cohen, S. Mathias, C. Ropers, Nanoscale magnetic imaging using circularly polarized high-harmonic radiation. *Sci. Adv.* **3**, eaao4641 (2017), doi:10.1126/sciadv.aao4641.

235. L.-M. Stadler, C. Gutt, T. Autenrieth, O. Leupold, S. Rehbein, Y. Chushkin, G. Grübel, Hard X ray Holographic Diffraction Imaging. *Phys. Rev. Lett.* **100**, 245503 (2008), doi:10.1103/PhysRevLett.100.245503.

236. E. Gührs, Doctoral dissertation, TU Berlin (2013).

237. T. Itō, Ed., *Ion beam assisted film growth* (Elsevier, Amsterdam, 1989).

238. J. A. Thornton, Magnetron sputtering. *J. Vac. Sci. Technol.* **15**, 171 (1978), doi:10.1116/1.569448.

239. H. Stillrich, C. Menk, R. Frömter, H. P. Oepen, Magnetic anisotropy and spin reorientation in Co/Pt multilayers. *J. Magn. Magn. Mater.* **322**, 1353 (2010), doi:10.1016/j.jmmm.2009.09.039.

240. H.F. Ding, S. Pütter, H.P. Oepen, J. Kirschner, Experimental method for separating longitudinal and polar Kerr signals. *J. Magn. Magn. Mater.* **212**, 5 (2000), doi:10.1016/S0304-8853(99)00790-8.

241. D. Stickler, R. Frömter, W. Li, A. Kobs, H. P. Oepen, Integrated setup for the fabrication and measurement of magnetoresistive nanoconstrictions in ultrahigh vacuum. *Rev. Sci. Instrum.* **79**, 103901 (2008), doi:10.1063/1.2981693.

242. J. Orloff, Ed., *Handbook of charged particle optics* (CRC Press, Boca Raton, FL, ed. 2, 2009).

243. J. Orloff, M. Utlaut, L. Swanson, *High Resolution Focused Ion Beams: FIB and its Applications*, *The Physics of Liquid Metal Ion Sources and Ion Optics and Their Application to Focused Ion Beam Technology* (Springer US, Boston, MA, s.l., 2003).

244. L. A. Giannuzzi, F. A. Stevie, Eds., *Introduction to focused ion beams*, *Instrumentation, theory, techniques and practice* (Springer Science+Business Media Inc, Boston, MA, 2005).

245. J. Viefhaus, F. Scholz, S. Deinert, L. Glaser, M. Ilchen, J. Seltmann, P. Walter, F. Siewert, The Variable Polarization XUV Beamline P04 at PETRA III. *Nucl. Instrum. Methods Phys. Res. A* **710**, 151 (2013), doi:10.1016/j.nima.2012.10.110.

246. D. L. Abernathy, G. Grübel, S. Brauer, I. McNulty, G. B. Stephenson, S. G. Mochrie, A. R. Sandy, N. Mulders, M. Sutton, Small-angle X-ray scattering using coherent undulator radiation at the ESRF. *J. Synchrotron Radiat.* **5**, 37 (1998), doi:10.1107/S0909049597015835.

247. E. Dufresne, Doctoral dissertation, Centre for the Physics of Materials.

248. M. Gilbert, H.-C. Mertins, M. Tesch, O. Berges, H. Feilbach, C. M. Schneider, TetraMag. *Rev. Sci. Instrum.* **83**, 25109 (2012), doi:10.1063/1.3684877.

249. K. Bagschik, R. Frömter, L. Müller, W. Roseker, J. Bach, P. Staeck, C. Thönnißen, S. Schleitzer, M. H. Berntsen, C. Weier, R. Adam, J. Viefhaus, C. M. Schneider, G. Grübel, H.

P. Oepen, Spatial coherence determination from the Fourier analysis of a resonant soft X-ray magnetic speckle pattern. *Opt. Express* **24**, 23162 (2016), doi:10.1364/OE.24.023162.

250. J. Geilhufe, Doctoral dissertation, TU Berlin (2015).

251. C. M. Günther, B. Pfau, R. Mitzner, B. Siemer, S. Roling, H. Zacharias, O. Kutz, I. Rudolph, D. Schondelmaier, R. Treusch, S. Eisebitt, Sequential femtosecond X-ray imaging. *Nat. Photonics* **5**, 99 (2011), doi:10.1038/nphoton.2010.287.

252. D. Weder, C. von Korff Schmising, F. Willems, C. M. Gunther, M. Schneider, B. Pfau, A. E. D. Merhe, E. Jal, B. Vodungbo, J. Luning, B. Mahieu, F. Capotondi, E. Pedersoli, S. Eisebitt, Multi-Color Imaging of Magnetic Co/Pt Multilayers. *IEEE Trans. Magn.* **53**, 1 (2017), doi:10.1109/TMAG.2017.2699560.

253. F. Willems, C. von Korff Schmising, D. Weder, C. M. Günther, M. Schneider, B. Pfau, S. Meise, E. Guehrs, J. Geilhufe, A. E. D. Merhe, E. Jal, B. Vodungbo, J. Lüning, B. Mahieu, F. Capotondi, E. Pedersoli, D. Gauthier, M. Manfredda, S. Eisebitt, Multi-color imaging of magnetic Co/Pt heterostructures. *Struct. Dyn.* **4**, 14301 (2017), doi:10.1063/1.4976004.

254. Z. Xin, S. Xiao-Hui, Z. Dian-Lin, Thickness dependence of grain size and surface roughness for dc magnetron sputtered Au films. *Chin. Phys. B* **19**, 86802 (2010), doi:10.1088/1674-1056/19/8/086802.

255. M. T. Robinson, O. S. Oen, The Chanelling of Energetic Atoms in Crystal Lattices. *Appl. Phys. Lett.* **2**, 30 (1963), doi:10.1063/1.1753757.

256. G. R. Piercy, F. Brown, J. A. Davies, M. McCargo, Experimental Evidence for the Increase of Heavy Ion Ranges by Channeling in Crystalline Structure. *Phys. Rev. Lett.* **10**, 399 (1963), doi:10.1103/PhysRevLett.10.399.

257. D. Onderdelinden, The Influence of Channeling on Cu Single-Crystal Sputtering. *Appl. Phys. Lett.* **8**, 189 (1966), doi:10.1063/1.1754548.

258. Y. Stark, R. Frömter, D. Stickler, H. P. Oepen, Sputter yields of single- and polycrystalline metals for application in focused ion beam technology. *J. Appl. Phys.* **105**, 13542 (2009), doi:10.1063/1.3056161.

259. M. T. Robinson, O. S. Oen, THE CHANNELING OF ENERGETIC ATOMS IN CRYSTAL LATTICES. *Appl. Phys. Lett.* **2**, 30 (1963), doi:10.1063/1.1753757.

260. J. Xu, T. White, P. Li, C. He, J. Yu, W. Yuan, Y.-F. Han, Biphasic Pd-Au alloy catalyst for low-temperature CO oxidation. *J. Am. Chem. Soc.* **132**, 10398 (2010), doi:10.1021/ja102617r.

261. Micro to Nano V.O.F, *Target material selection for coating SEM samples using an SEM sputter coater* (2018) (available at https://www.microtonano.com/TIN-Target-material-selection-for-coating-SEM-samples-using-an-SEM-sputter-coater.php).

262. A. Neumann, C. Thönnissen, A. Frauen, S. Hesse, A. Meyer, H. P. Oepen, Probing the magnetic behavior of single nanodots. *Nano letters* **13**, 2199 (2013), doi:10.1021/nl400728r.

263. A. S. Wills, R. Ballou, C. Lacroix, Model of localized highly frustrated ferromagnetism. *Phys. Rev. B* **66**, 144407 (2002), doi:10.1103/PhysRevB.66.144407.

264. B. Canals, I.-A. Chioar, V.-D. Nguyen, M. Hehn, D. Lacour, F. Montaigne, A. Locatelli, T. O. Menteş, B. S. Burgos, N. Rougemaille, Fragmentation of magnetism in artificial kagome dipolar spin ice. *Nat. Commun.* **7**, 11446 (2016), doi:10.1038/ncomms11446.

265. S. Zhang, J. Li, I. Gilbert, J. Bartell, M. J. Erickson, Y. Pan, P. E. Lammert, C. Nisoli, K. K. Kohli, R. Misra, V. H. Crespi, N. Samarth, C. Leighton, P. Schiffer, Perpendicular magnetization and generic realization of the Ising model in artificial spin ice. *Phys. Rev. Lett.* **109**, 87201 (2012), doi:10.1103/PhysRevLett.109.087201.

266. E. Mengotti, L. J. Heyderman, A. Bisig, A. Fraile Rodríguez, L. Le Guyader, F. Nolting, H. B. Braun, Dipolar energy states in clusters of perpendicular magnetic nanoislands. *J. Appl. Phys.* **105**, 113113 (2009), doi:10.1063/1.3133202.

267. D. Stickler, R. Frömter, H. Stillrich, C. Menk, H. P. Oepen, C. Gutt, S. Streit-Nierobisch, L.-M. Stadler, G. Grübel, C. Tieg, F. Yakhou-Harris, Domain size in systems with canted magnetization. *Phys. Rev. B* **84**, 104412 (2011), doi:10.1103/PhysRevB.84.104412.

268. M. Wellhöfer, M. Weißenborn, R. Anton, S. Pütter, H. P. Oepen, Morphology and magnetic properties of ECR ion beam sputtered Co/Pt films. *J. Magn. Magn. Mater.* **292**, 345 (2005), doi:10.1016/j.jmmm.2004.11.150.

269. S. Kuhrau, F. Kloodt-Twesten, C. Heyn, H. P. Oepen, R. Frömter, Cap-layer-dependent oxidation of ultrathin cobalt films and its effect on the magnetic contrast in scanning electron microscopy with polarization analysis. *submitted* (2018).

270. H. Yanagihara, E. Kita, M. B. Salamon, Aperiodical oscillation of interlayer coupling in epitaxial Co/Ir(001) superlattices. *Phys. Rev. B* **60**, 12957 (1999), doi:10.1103/PhysRevB.60.12957.

271. S. Colis, A. Dinia, C. Mény, P. Panissod, C. Ulhaq-Bouillet, G. Schmerber, Magnetic, transport, and structural properties of Fe/Co/Cu/[Co/Ir/Co] sandwiches and Fe/Co/Cu/[Co/Ir] multilayers prepared by ion-beam sputtering. *Phys. Rev. B* **62**, 11709 (2000), doi:10.1103/PhysRevB.62.11709.

272. C. Kittel, Interpretation of Anomalous Larmor Frequencies in Ferromagnetic Resonance Experiment. *Phys. Rev.* **71**, 270 (1947), doi:10.1103/PhysRev.71.270.2.

273. C. Kittel, On the Theory of Ferromagnetic Resonance Absorption. *Phys. Rev.* **73**, 155 (1948), doi:10.1103/PhysRev.73.155.

274. M. Farle, Ferromagnetic resonance of ultrathin metallic layers. *Rep. Prog. Phys.* **61**, 755 (1998), doi:10.1088/0034-4885/61/7/001.

275. S. V. von Sovskii, Ed., *Ferromagnetic Resonance*, *The phenomenon of resonance absorption of HF electromagnetic field energy in ferromagnetic materials* (Elsevier, 2016).

276. L. Bocklage, S. Motl-Ziegler, J. Topp, T. Matsuyama, G. Meier, Spin waves and domain wall modes in curved magnetic nanowires. *J. Phys. Condens. Matter* **26**, 266003 (2014), doi:10.1088/0953-8984/26/26/266003.

277. F. Balhorn, Diploma thesis, Universität Hamburg (2009).

278. J. Lindner, *Ferromagnetische Resonanz an ultradünnen magnetischen Einfach- und Mehrfachlagen der 3d-Übergangsmetalle - Statik und Dynamik*, Zugl.: Berlin, Freie Univ., Diss., 2002 (dissertation.de - Verl. im Internet GmbH, Berlin, 2003).

279. U. Wiedwald, M. Spasova, M. Farle, M. Hilgendorff, M. Giersig, Ferromagnetic resonance of monodisperse Co particles. *J. Vac. Sci. Technol.* **19**, 1773 (2001), doi:10.1116/1.1345906.

280. M. Farle, B. Mirwald-Schulz, A. N. Anisimov, W. Platow, K. Baberschke, Higher-order magnetic anisotropies and the nature of the spin-reorientation transition in face-centered-tetragonal Ni(001)/Cu(001). *Phys. Rev. B* **55**, 3708 (1997), doi:10.1103/PhysRevB.55.3708.

281. W. Platow, A. N. Anisimov, G. L. Dunifer, M. Farle, K. Baberschke, Correlations between ferromagnetic-resonance linewidths and sample quality in the study of metallic ultrathin films. *Phys. Rev. B* **58**, 5611 (1998), doi:10.1103/PhysRevB.58.5611.

282. J. Kim, J.-W. Lee, J.-R. Jeong, S.-C. Shin, Y. H. Ha, Y. Park, D. W. Moon, Ultrathin Co films on Pt(111) and the Co-Pt interface investigated by surface magneto-optical Kerr effect and medium-energy ion scattering spectroscopy. *Phys. Rev. B* **65**, 104428 (2002), doi:10.1103/PhysRevB.65.104428.

283. G. Winkler, Diploma thesis, Universität Hamburg (2010).

284. N. Mikuszeit, S. Pütter, R. Frömter, H. P. Oepen, Magneto-optic Kerr effect. *J. Appl. Phys.* **97**, 103107 (2005), doi:10.1063/1.1904722.

285. S. Fiedler, H. Stillrich, H. P. Oepen, Magneto-optic properties of electron cyclotron resonance ion beam sputtered and magnetron sputtered Co/Pt multilayers. *J. Appl. Phys.* **102**, 83906 (2007), doi:10.1063/1.2794713.

286. N. W. E. McGee, M. T. Johnson, J. J. de Vries, J. aan de Stegge, Localized Kerr study of the magnetic properties of an ultrathin epitaxial Co wedge grown on Pt(111). *J. Appl. Phys.* **73**, 3418 (1993), doi:10.1063/1.352943.

287. C. L. Canedy, X. W. Li, G. Xiao, Large magnetic moment enhancement and extraordinary Hall effect in Co/Pt superlattices. *Phys. Rev. B* **62**, 508 (2000), doi:10.1103/PhysRevB.62.508.

288. P. Poulopoulos, M. Angelakeris, E. T. Papaioannou, N. K. Flevaris, D. Niarchos, M. Nyvlt, V. Prosser, S. Visnovsky, C. Mueller, P. Fumagalli, F. Wilhelm, A. Rogalev, Structural, magnetic, and spectroscopic magneto-optical properties aspects of Pt–Co multilayers with intentionally alloyed layers. *J. Appl. Phys.* **94**, 7662 (2003), doi:10.1063/1.1629156.

289. J. Crangle, W. R. Scott, Dilute Ferromagnetic Alloys. *J. Appl. Phys.* **36**, 921 (1965), doi:10.1063/1.1714264.

290. Z. S. Shan, J. X. Shen, R. D. Kirby, D. J. Sellmyer, Y. J. Wang, Temperature-dependent interface magnetism and magnetization reversal in Co/Pt multilayers. *J. Appl. Phys.* **75**, 6418 (1994), doi:10.1063/1.355370.

291. H. W. van Kesteren, W. B. Zeper, Controlling the Curie temperature of Co/Pt multilayer magneto-optical recording media. *J. Magn. Magn. Mater.* **120**, 271 (1993), doi:10.1016/0304-8853(93)91339-9.

292. C. A. F. Vaz, J. A. C. Bland, G. Lauhoff, Magnetism in ultrathin film structures. *Rep. Prog. Phys.* **71**, 56501 (2008), doi:10.1088/0034-4885/71/5/056501.

293. M. Bersweiler, K. Dumesnil, D. Lacour, M. Hehn, Impact of buffer layer and Pt thickness on the interface structure and magnetic properties in (Co/Pt) multilayers. *J. Phys. Condens. Matter* **28**, 336005 (2016), doi:10.1088/0953-8984/28/33/336005.

294. R. T. Heap, S. J. Greaves, The magnetic structure of platinum-cobalt multilayers. *J. Phys. D: Appl. Phys.* **27**, 1343 (1994), doi:10.1088/0022-3727/27/7/001.

295. S. Bandiera, R. C. Sousa, B. Rodmacq, B. Dieny, Enhancement of perpendicular magnetic anisotropy through reduction of Co-Pt interdiffusion in (Co/Pt) multilayers. *Appl. Phys. Lett.* **100**, 142410 (2012), doi:10.1063/1.3701585.

296. S. Bandiera, R. R. Sousa, B. B. Rodmacq, B. Dieny, Asymmetric Interfacial Perpendicular Magnetic Anisotropy in Pt/Co/Pt Trilayers. *IEEE Magn. Lett.* **2**, 3000504 (2011), doi:10.1109/LMAG.2011.2174032.

297. R. Lavrijsen, D. M. F. Hartmann, A. van den Brink, Y. Yin, B. Barcones, R. A. Duine, M. A. Verheijen, H. J. M. Swagten, B. Koopmans, Asymmetric magnetic bubble expansion under in-plane field in Pt/Co/Pt. *Phys. Rev. B* **91**, 104414 (2015), doi:10.1103/PhysRevB.91.104414.

298. P. J. Metaxas, J. P. Jamet, A. Mougin, M. Cormier, J. Ferré, V. Baltz, B. Rodmacq, B. Dieny, R. L. Stamps, Creep and flow regimes of magnetic domain-wall motion in ultrathin Pt/Co/Pt films with perpendicular anisotropy. *Phys. Rev. Lett.* **99**, 217208 (2007), doi:10.1103/PhysRevLett.99.217208.

299. W. B. Zeper, F. J. A. M. Greidanus, P. F. Carcia, C. R. Fincher, Perpendicular magnetic anisotropy and magneto-optical Kerr effect of vapor-deposited Co/Pt-layered structures. *J. Appl. Phys.* **65**, 4971 (1989), doi:10.1063/1.343189.

300. A. Dinia, M. Stoeffel, K. Rahmouni, D. Stoeffler, H. A. M. van den Berg, Exchange coupling and magnetoresistance in Co/Ir multilayers prepared by ion beam sputtering. *Europhys. Lett.* **42**, 331 (1998), doi:10.1209/epl/i1998-00251-7.

301. H. Yanagihara, K. Pettit, M. B. Salamon, E. Kita, S. S. P. Parkin, Magnetoresistance and magnetic properties of Co/Ir multilayers on MgO(110) substrates. *J. Appl. Phys.* **81**, 5197 (1997), doi:10.1063/1.364464.

302. W. Legrand, J.-Y. Chauleau, D. Maccariello, N. Reyren, S. Collin, K. Bouzehouane, N. Jaouen, V. Cros, A. Fert, Hybrid chiral domain walls and skyrmions in magnetic multilayers. *Sci. Adv.* **4**, eaat0415 (2018), doi:10.1126/sciadv.aat0415.

303. P. M. Shepley, H. Tunnicliffe, K. Shahbazi, G. Burnell, T. A. Moore, Magnetic properties, domain-wall creep motion, and the Dzyaloshinskii-Moriya interaction in Pt/Co/Ir thin films. *Phys. Rev. B* **97**, 134417 (2018), doi:10.1103/PhysRevB.97.134417.

304. K. Zeissler, M. Mruczkiewicz, S. Finizio, J. Raabe, P. M. Shepley, A. V. Sadovnikov, S. A. Nikitov, K. Fallon, S. McFadzean, S. McVitie, T. A. Moore, G. Burnell, C. H. Marrows, Pinning and hysteresis in the field dependent diameter evolution of skyrmions in Pt/Co/Ir superlattice stacks. *Sci. Rep.* **7**, 15125 (2017), doi:10.1038/s41598-017-15262-3.

305. J. Lucassen, F. Kloodt-Twesten, R. Frömter, H. P. Oepen, R. A. Duine, H. J. M. Swagten, B. Koopmans, R. Lavrijsen, Scanning electron microscopy with polarization analysis for multilayered chiral spin textures. *Appl. Phys. Lett.* **111**, 132403 (2017), doi:10.1063/1.4998535.

306. J. Kötzler, W. Gil, Anomalous Hall resistivity of cobalt films. *Phys. Rev. B* **72**, 60412 (2005), doi:10.1103/PhysRevB.72.060412.

307. S. Ziesmann, M.Sc. Thesis, Universität Hamburg (2018).

308. C. M. Hurd, Ed., *The Hall Effect in Metals and Alloys* (Springer US, Boston, MA, 1972).

309. S. P. McAlister, C. M. Hurd, Hall effect in 3d-transition metals and alloys (invited). *J. Appl. Phys.* **50**, 7526 (1979), doi:10.1063/1.326888.

310. M. Bubek, Doctoral dissertation, Universität Hamburg (2011).

311. S. J. Greaves, A. K. Petford-Long, Y.-H. Kim, R. J. Pollard, P. J. Grundy, J. P. Jakubovics, A magnetic and high resolution structural investigation of Pt/Co multilayers. *J. Magn. Magn. Mater.* **113**, 63 (1992), doi:10.1016/0304-8853(92)91247-Q.

312. D. Weller, A. Carl, R. Savoy, T. C. Huang, M. F. Toney, C. Chappert, Structural transitions and magnetic anisotropy in ultrathin Co wedges on Pt(111) investigated with the magneto-optical Kerr effect. *J. Phys. Chem. Solids* **56**, 1563 (1995), doi:10.1016/0022-3697(95)00129-8.

313. S. Hashimoto, Y. Ochiai, K. Aso, Perpendicular magnetic anisotropy and magnetostriction of sputtered Co/Pd and Co/Pt multilayered films. *J. Appl. Phys.* **66**, 4909 (1989), doi:10.1063/1.343760.

314. E. A. M. van Alphen, H. A. M. de Gronckel, P. J. H. Bloemen, A. S. van Steenbergen, W. J. M. de Jonge, Structural dependence of the magnetic anisotropy of Co films. *J. Magn. Magn. Mater.* **121**, 77 (1993), doi:10.1016/0304-8853(93)91153-X.

315. J. V. Harzer, B. Hillebrands, I. S. Pogosova, M. Herrmann, G. Güntherodt, D. Weller, Structural and Magnetic Properties of e-Beam Prepared CoxPt1-x Alloy Films. *MRS Proc.* **313**, 7 (1993), doi:10.1557/PROC-313-387.

316. H. Masumoto, K. Watanabe, K. Inagawa, Magnetic Properties of Hexagonal Close-Packed Structure Type Co-Ir Binary Alloys*. *Trans. Jpn. Inst. Met.* **17**, 592 (1976).

317. J. Crangle, D. Parsons, The Magnetization of Ferromagnetic Binary Alloys of Cobalt or Nickel with Elements of the Palladium and Platinum Groups. *Proc. Royal Soc. A* **255**, 509 (1960), doi:10.1098/rspa.1960.0083.

318. Z. Zhang, P. E. Wigen, S. S. P. Parkin, Pt layer thickness dependence of magnetic properties in Co/Pt multilayers. *J. Appl. Phys.* **69**, 5649 (1991), doi:10.1063/1.347924.

319. H. Kronmüller, M. Fähnle, Eds., *Micromagnetism and the Microstructure of Ferromagnetic Solids* (Cambridge University Press, Cambridge, 2009).

320. X. Liu, M. M. Steiner, R. Sooryakumar, G. A. Prinz, R. F. C. Farrow, G. Harp, Exchange stiffness, magnetization, and spin waves in cubic and hexagonal phases of cobalt. *Phys. Rev. B* **53**, 12166 (1996), doi:10.1103/PhysRevB.53.12166.

321. R. H. Brown, D. M. C. Nicholson, X. Wang, T. C. Schulthess, First principles theory of spin waves in Fe, Co, and Ni. *J. Appl. Phys.* **85**, 4830 (1999), doi:10.1063/1.370035.

322. R. Pauthenet, Experimental verification of spin-wave theory in high fields (invited). *J. Appl. Phys.* **53**, 8187 (1982), doi:10.1063/1.330287.

323. A. Michels, J. Weissmüller, A. Wiedenmann, J. S. Pedersen, J. G. Barker, Measuring the exchange-stiffness constant of nanocrystalline solids by elastic small-angle neutron scattering. *Philos. Mag.* **80**, 785 (2000), doi:10.1080/09500830010001805.

324. J. Weissmüller, A. Michels, J. G. Barker, A. Wiedenmann, U. Erb, R. D. Shull, Analysis of the small-angle neutron scattering of nanocrystalline ferromagnets using a micromagnetics model. *Phys. Rev. B* **63**, 840 (2001), doi:10.1103/PhysRevB.63.214414.

325. S. J. Pickart, H. A. Alperin, V. J. Minkiewicz, R. Nathans, G. Shirane, O. Steinsvoll, Spin-Wave Dispersion in Ferromagnetic Ni and fcc Co. *Phys. Rev.* **156**, 623 (1967), doi:10.1103/PhysRev.156.623.

326. G. Shirane, V. J. Minkiewicz, R. Nathans, Spin Waves in 3d Metals. *J. Appl. Phys.* **39**, 383 (1968), doi:10.1063/1.2163453.

327. H. A. Alperin, O. Steinsvoll, G. Shirane, R. Nathans, Observation of the Dispersion Relation for Spin Waves in Hexagonal Cobalt. *J. Appl. Phys.* **37**, 1052 (1966), doi:10.1063/1.1708330.

328. M. Grimsditch, E. E. Fullerton, R. L. Stamps, Exchange and anisotropy effects on spin waves in epitaxial Co films. *Phys. Rev. B* **56**, 2617 (1997), doi:10.1103/PhysRevB.56.2617.

329. A. Yoshihara, H. Sato, J.-i. Mawatari, K. Yoshida, O. Kitakami, Y. Shimada, Brillouin light scattering from spin waves in Co100−xCrx alloy films. *J. Magn. Magn. Mater.* **221**, 261 (2000), doi:10.1016/S0304-8853(00)00495-9.

330. J. G. Kim, K. H. Han, J. H. Cho, S. Lee, Brillouin light scattering characterizations in thin cobalt films. *Phys. Status Solidi B* **241**, 1718 (2004), doi:10.1002/pssb.200304535.

331. J. M. Karanikas, R. Sooryakumar, G. A. Prinz, B. T. Jonker, Thermal magnons in bcc cobalt-itinerancy and exchange stiffness (invited). *J. Appl. Phys.* **69**, 6120 (1991), doi:10.1063/1.348778.

332. C. Eyrich, A. Zamani, W. Huttema, M. Arora, D. Harrison, F. Rashidi, D. Broun, B. Heinrich, O. Mryasov, M. Ahlberg, O. Karis, P. E. Jönsson, M. From, X. Zhu, E. Girt, Effects of substitution on the exchange stiffness and magnetization of Co films. *Phys. Rev. B* **90**, 235408 (2014), doi:10.1103/PhysRevB.90.235408.

333. S. P. Vernon, S. M. Lindsay, M. B. Stearns, Brillouin scattering from thermal magnons in a thin Co film. *Phys. Rev. B* **29**, 4439 (1984), doi:10.1103/PhysRevB.29.4439.

334. E.P. Wohlfarth, Ed., *Handbook of Ferromagnetic Materials* (Elsevier, 1980).

335. R. Vollmer, M. Etzkorn, P. S. A. Kumar, H. Ibach, J. Kirschner, Spin-polarized electron energy loss spectroscopy of high energy, large wave vector spin waves in ultrathin fcc Co films on Cu(001). *Phys. Rev. Lett.* **91**, 147201 (2003), doi:10.1103/PhysRevLett.91.147201.

336. R. Vollmer, M. Etzkorn, P. S. A. Kumar, H. Ibach, J. Kirschner, Spin-wave excitation in ultrathin Co and Fe films on Cu(001) by spin-polarized electron energy loss spectroscopy (invited). *J. Appl. Phys.* **95**, 7435 (2004), doi:10.1063/1.1689774.

337. M. Etzkorn, P. S. Anil Kumar, W. Tang, Y. Zhang, J. Kirschner, High-wave-vector spin waves in ultrathin Co films on W(110). *Phys. Rev. B* **72**, 184420 (2005), doi:10.1103/PhysRevB.72.184420.

338. J. I. Goldstein, Ed., *Scanning electron microscopy and x-ray microanalysis* (Springer, New York, 2009).

339. N. Nakajima, T. Koide, T. Shidara, H. Miyauchi, H. Fukutani, A. Fujimori, K. Iio, T. Katayama, M. Nývlt, Y. Suzuki, Perpendicular Magnetic Anisotropy Caused by Interfacial Hybridization via Enhanced Orbital Moment in Co/Pt Multilayers. *Phys. Rev. Lett.* **81**, 5229 (1998), doi:10.1103/PhysRevLett.81.5229.

340. S. Ferrer, J. Alvarez, E. Lundgren, X. Torrelles, P. Fajardo, F. Boscherini, Surface x-ray diffraction from Co/Pt(111) ultrathin films and alloys. *Phys. Rev. B* **56**, 9848 (1997), doi:10.1103/PhysRevB.56.9848.

341. P. Bruno, Magnetization and Curie Temperature of Ferromagnetic Ultrathin Films. *MRS Proc.* **231**, 127 (1991), doi:10.1557/PROC-231-299.

342. P. Neilinger, T. Ščepka, M. Mruczkiewicz, J. Dérer, D. Manca, E. Dobročka, A. S. Samardak, M. Grajcar, V. Cambel, Ferromagnetic resonance study of sputtered Pt/Co/Pt multilayers. *Appl. Surf. Sci.*, in press (2018), doi:10.1016/j.apsusc.2018.06.172.

343. H. T. Nembach, J. M. Shaw, M. Weiler, É. Jué, T. J. Silva, Linear relation between Heisenberg exchange and interfacial Dzyaloshinskii–Moriya interaction in metal films. *Nat. Phys.* **11**, 825 (2015), doi:10.1038/nphysS3418.

344. S. I. Kiselev, J. C. Sankey, I. N. Krivorotov, N. C. Emley, A. G. F. Garcia, R. A. Buhrman, D. C. Ralph, Spin-transfer excitations of permalloy nanopillars for large applied currents. *Phys. Rev. B* **72**, L261 (2005), doi:10.1103/PhysRevB.72.064430.

345. J. Rajeswari, H. Ibach, C. M. Schneider, A. T. Costa, D. L. R. Santos, D. L. Mills, Surface spin waves of fcc cobalt films on Cu(100). *Phys. Rev. B* **86**, 165436 (2012), doi:10.1103/PhysRevB.86.165436.

346. T. Devolder, S. Pizzini, J. Vogel, H. Bernas, C. Chappert, V. Mathet, M. Borowski, X-ray absorption analysis of sputter-grown Co/Pt stackings before and after helium irradiation. *Eur. Phys. J. B* **22**, 193 (2001), doi:10.1007/s100510170127.

347. C. Vieu, J. Gierak, H. Launois, T. Aign, P. Meyer, J. P. Jamet, J. Ferré, C. Chappert, T. Devolder, V. Mathet, H. Bernas, Modifications of magnetic properties of Pt/Co/Pt thin layers by focused gallium ion beam irradiation. *J. Appl. Phys.* **91**, 3103 (2002), doi:10.1063/1.1427144.

348. T. McGuire, J. Aboaf, E. Klokholm, Negative anisotropic magnetoresistance in 3d metals and alloys containing iridium. *IEEE Trans. Magn.* **20**, 972 (1984), doi:10.1109/TMAG.1984.1063188.

349. A. Murayama, M. Miyamura, K. Nishiyama, K. Miyata, Y. Oka, Brillouin spectroscopy of spin waves in sputtered CoPt alloy films and Co/Pt/Co multilayered films. *J. Appl. Phys.* **69**, 5661 (1991), doi:10.1063/1.347928.

350. C. M. Schneider, P. Bressler, P. Schuster, J. Kirschner, J. J. de Miguel, and R. Miranda, Curie temperature of ultrathin films of fcc-cobalt epitaxially grown on atomically flat Cu(100) surfaces. *Phys. Rev. Lett.* **64**, 1059 (1990), doi:10.1103/PhysRevLett.64.1059.

351. J. Kimling, A. Philippi-Kobs, J. Jacobsohn, H. P. Oepen, D. G. Cahill, Thermal conductance of interfaces with amorphous SiO2 measured by time-resolved magneto-optic Kerr-effect thermometry. *Phys. Rev. B* **95**, 184305 (2017), doi:10.1103/PhysRevB.95.184305.

352. M. Matczak, B. Szymański, M. Urbaniak, M. Nowicki, H. Głowiński, P. Kuświk, M. Schmidt, J. Aleksiejew, J. Dubowik, F. Stobiecki, Antiferromagnetic magnetostatic coupling in Co/Au/Co films with perpendicular anisotropy. *J. Appl. Phys.* **114**, 93911 (2013), doi:10.1063/1.4819380.

353. O. Hellwig, A. Berger, J. B. Kortright, E. E. Fullerton, Domain structure and magnetization reversal of antiferromagnetically coupled perpendicular anisotropy films. *J. Magn. Magn. Mater.* **319**, 13 (2007), doi:10.1016/j.jmmm.2007.04.035.

354. R. Morgunov, A. Hamadeh, T. Fache, G. Lvova, O. Koplak, A. Talantsev, S. Mangin, Magnetic field and temperature control over Pt/Co/Ir/Co/Pt multistate magnetic logic device. *Superlattices Microstruct.* **104**, 509 (2017), doi:10.1016/j.spmi.2017.02.033.

355. S. S. P. Parkin, D. Mauri, Spin engineering. *Phys. Rev. B* **44**, 7131 (1991), doi:10.1103/PhysRevB.44.7131.

356. S. N. Okuno, K. Inomata, Oscillatory Behavior of the Interlayer Exchange Coupling as a Function of Au Cap Layer Thickness in Au/Fe/Au/Fe/Au(001). *J. Phys. Soc. Jpn.* **64**, 3631 (1995), doi:10.1143/jpsj.64.3631.

357. D. C. Parks, P. J. Chen, W. F. Egelhoff, R. D. Gomez, Interfacial roughness effects on interlayer coupling in spin valves grown on different seed layers. *J. Appl. Phys.* **87**, 3023 (2000), doi:10.1063/1.372390.

358. J. Kudrnovský, V. Drchal, P. Bruno, I. Turek, P. Weinberger, Interlayer exchange coupling. *Phys. Rev. B* **56**, 8919 (1997), doi:10.1103/PhysRevB.56.8919.

359. J. Pommier, P. Meyer, G. Pénissard, Ferré J., Bruno P., D. Renard, Magnetization reversal in ultrathin ferromagnetic films with perpendicular anistropy. *Phys. Rev. Lett.* **65**, 2054 (1990), doi:10.1103/PhysRevLett.65.2054.

360. V. Grolier, D. Renard, B. Bartenlian, P. Beauvillain, C. Chappert, C. Dupas, J. Ferre, M. Galtier, E. Kolb, M. Mulloy, J. P. Renard, and P. Veillet, Unambiguous evidence of oscillatory magnetic coupling between Co layers in ultrahigh vacuum grown Co/Au(111)/Co trilayers. *Phys. Rev. Lett.* **71**, 3023 (1993), doi:10.1103/PhysRevLett.71.3023.

361. P. Bruno, J. Kudrnovský, V. Drchal, I. Turek, Interlayer exchange coupling through ordered and disordered alloy spacers. *J. Magn. Magn. Mater.* **165**, 128 (1997), doi:10.1016/S0304-8853(96)00487-8.

362. J. Kudrnovský, V. Drchal, P. Bruno, I. Turek, P. Weinberger, Interlayer magnetic coupling. *Phys. Rev. B* **54**, R3738 (1996), doi:10.1103/PhysRevB.54.R3738.

363. S. S. P. Parkin, C. Chappert, F. Herman, Oscillatory Exchange Coupling and Giant Magnetoresistance via Cu-X Alloys (X = Au, Fe, Ni). *Europhys. Lett.* **24**, 71 (1993), doi:10.1209/0295-5075/24/1/012.

364. Q. Leng, V. Cros, R. Schäfer, A. Fuss, P. Grünberg, W. Zinn, Interlayer coupling across noble metal spacers. *J. Magn. Magn. Mater.* **126**, 367 (1993), doi:10.1016/0304-8853(93)90629-G.

365. M. S. Ferreira, J. d'Albuquerque e Castro, R. B. Muniz, L. C. Lopes, Exponential behavior of the interlayer exchange coupling across nonmagnetic metallic superlattices. *Phys. Rev. B* **58**, 8198 (1998), doi:10.1103/PhysRevB.58.8198.

366. N. N. Lathiotakis, B. L. Györffy, J. B. Staunton, B. Újfalussy, Periods and damping of the oscillatory exchange coupling across Cu(1−x)Nix alloy spacers. *J. Magn. Magn. Mater.* **185**, 293 (1998), doi:10.1016/S0304-8853(98)00041-9.

367. J. J. de Vries, A. A. P. Schudelaro, R. Jungblut, P. J. H. Bloemen, A. Reinders, J. T. Kohlhepp, R. Coehoorn, W. J. M. de Jonge, Oscillatory Interlayer Exchange Coupling with the Cu Cap Layer Thickness in Co/Cu/Co/Cu(100). *Phys. Rev. Lett.* **75**, 4306 (1995), doi:10.1103/PhysRevLett.75.4306.

368. L. Li, Y. Lu, Z. Liu, Y. Lv, Y. Zhang, S. Liu, C. Hao, W. Lv, Interlayer exchange coupling and magnetic reversal in Co/Pt multilayers. *J. Magn. Magn. Mater.* **325**, 117 (2013), doi:10.1016/j.jmmm.2012.08.018.

369. S. N. Okuno, K. Inomata, Two oscillatory behaviors as functions of ferromagnetic layer thickness in Fe/Cr(100) multilayers. *Phys. Rev. Lett.* **72**, 1553 (1994), doi:10.1103/PhysRevLett.72.1553.

370. S. N. Okuno, K. Inomata, Oscillatory exchange coupling with a period of two Fe monolayers in Au/Fe/Au/Fe/Au(001). *Phys. Rev. B* **51**, 6139 (1995), doi:10.1103/PhysRevB.51.6139.

371. J. C. S. Kools, A. J. Devasahayam, K. Rook, C.-L. Lee, M. Mao, Effect of microstructure on the oscillating interlayer coupling in spin-valve structures. *J. Appl. Phys.* **93**, 7921 (2003), doi:10.1063/1.1555798.

372. O. Glatter, O. Kratky, Eds., *Small angle x-ray scattering* (Academic Press, London, New York, 1983).

373. L. Belliard, J. Miltat, V. Kottler, V. Mathet, C. Chappert, T. Valet, Stripe domains morphology versus layers thickness in CoPt multilayers. *J. Appl. Phys.* **81**, 5315 (1997), doi:10.1063/1.364531.

374. T. N. G. Meier, M. Kronseder, C. H. Back, Domain-width model for perpendicularly magnetized systems with Dzyaloshinskii-Moriya interaction. *Phys. Rev. B* **96**, 144408 (2017), doi:10.1103/PhysRevB.96.144408.

375. M. Speckmann, H. P. Oepen, and H. Ibach, Magnetic Domain Structures in Ultrathin Co/Au(111): On the Influence of Film Morphology. *Phys. Rev. Lett.* **75**, 2035 (1995), doi:10.1103/PhysRevLett.75.2035.

376. M. Kronseder, T. N. G. Meier, M. Zimmermann, M. Buchner, M. Vogel, C. H. Back, Real-time observation of domain fluctuations in a two-dimensional magnetic model system. *Nat. Commun.* **6**, 6832 (2015), doi:10.1038/ncomms7832.

377. V. Baltz, A. Marty, B. Rodmacq, B. Dieny, Magnetic domain replication in interacting bilayers with out-of-plane anisotropy. *Phys. Rev. B* **75**, 14406 (2007), doi:10.1103/PhysRevB.75.014406.

378. A. Suna, Perpendicular magnetic ground state of a multilayer film. *J. Appl. Phys.* **59**, 313 (1986), doi:10.1063/1.336684.

379. Z. Málek, V. Kamberský, On the theory of the domain structure of thin films of magnetically uni-axial materials. *Czech. J. Phys. (Czechoslovak Journal of Physics)* **8**, 416 (1958), doi:10.1007/BF01612066.

380. C. T. Chen, Y. U. Idzerda, H.-J. Lin, N. V. Smith, G. Meigs, E. Chaban, G. H. Ho, E. Pellegrin, F. Sette, Experimental confirmation of the X-ray magnetic circular dichroism sum rules for iron and cobalt. *Phys. Rev. Lett.* **75**, 152 (1995), doi:10.1103/PhysRevLett.75.152.

381. M. Tekielak, R. Gieniusz, M. Kisielewski, P. Mazalski, A. Maziewski, V. Zablotskii, F. Stobiecki, B. Szymański, R. Schäfer, The effect of magnetostatic coupling on spin configurations in ultrathin multilayers. *J. Appl. Phys.* **110**, 43924 (2011), doi:10.1063/1.3626747.

382. O. Hellwig, T. L. Kirk, J. B. Kortright, A. Berger, E. E. Fullerton, A new phase diagram for layered antiferromagnetic films. *Nat. Mater.* **2**, 112 (2003), doi:10.1038/nmat806.

383. C. Bran, A. B. Butenko, N. S. Kiselev, U. Wolff, L. Schultz, O. Hellwig, U. K. Rößler, A. N. Bogdanov, V. Neu, Evolution of stripe and bubble domains in antiferromagnetically coupled [(Co/Pt)8/Co/Ru]18 multilayers. *Phys. Rev. B* **79**, 24430 (2009), doi:10.1103/PhysRevB.79.024430.

384. N. S. Kiselev, C. Bran, U. Wolff, L. Schultz, A. N. Bogdanov, O. Hellwig, V. Neu, U. K. Rößler, Metamagnetic domains in antiferromagnetically coupled multilayers with perpendicular anisotropy. *Phys. Rev. B* **81**, 54409 (2010), doi:10.1103/PhysRevB.81.054409.

385. U. K. Rößler, A. N. Bogdanov, Synthetic metamagnetism — magnetic switching of perpendicular antiferromagnetic superlattices. *J. Magn. Magn. Mater.* **269**, L287 (2004), doi:10.1016/j.jmmm.2003.10.006.

386. O. Hellwig, G. P. Denbeaux, J. B. Kortright, E. E. Fullerton, X-ray studies of aligned magnetic stripe domains in perpendicular multilayers. *Physica B Condens. Matter* **336**, 136 (2003), doi:10.1016/S0921-4526(03)00282-5.

387. J. Miguel, J. F. Peters, O. M. Toulemonde, S. S. Dhesi, N. B. Brookes, J. B. Goedkoop, X-ray resonant magnetic scattering study of magnetic stripe domains in a−GdFe thin films. *Phys. Rev. B* **74**, 94437 (2006), doi:10.1103/PhysRevB.74.094437.

388. M. Labrune, L. Belliard, Stripe Domains in Multilayers: Micromagnetic Simulations. *Phys. Status Solidi A* **174**, 483 (1999), doi:10.1002/(SICI)1521-396X(199908)174:2%3C483::AID-PSSA483%3E3.0.CO;2-7.

389. M. Tekielak, P. Mazalski, A. Maziewski, R. Schafer, J. McCord, B. Szymanski, M. Urbaniak, F. Stobiecki, Creation of Out-of-Plane Magnetization Ordering by Increasing the Repetitions Number N in (Co/Au)N Multilayers. *IEEE Trans. Magn.* **44**, 2850 (2008), doi:10.1109/TMAG.2008.2001813.

390. V. Kamberský, P. de Haan, J. Šimšová, S. Porthun, R. Gemperle, J. C. Lodder, Domain wall theory and exchange stiffness in Co/Pd multilayers. *J. Magn. Magn. Mater.* **157/158**, 301 (1996), doi:10.1016/0304-8853(95)01162-5.

391. V. Kamberský, DOMAINS IN CoPd MULTILAYERS AND THEORETICAL MODELS. *J. Magn. Soc. Jpn.* **19**, 37 (1995), doi:10.3379/jmsjmag.19.S1_37.

392. J.-Y. Chauleau, W. Legrand, N. Reyren, D. Maccariello, S. Collin, H. Popescu, K. Bouzehouane, V. Cros, N. Jaouen, A. Fert, Chirality in Magnetic Multilayers Probed by the Symmetry and the Amplitude of Dichroism in X-Ray Resonant Magnetic Scattering. *Phys. Rev. Lett.* **120**, 37202 (2018), doi:10.1103/PhysRevLett.120.037202.

393. U. Hartmann, MAGNETIC FORCE MICROSCOPY. *Annu. Rev. Mater. Sci.* **29**, 53 (1999), doi:10.1146/annurev.matsci.29.1.53.

394. *MicroMagnum*, *Fast Micromagnetic Simulator for Computations on CPU and Graphics Processing Unit (GPU)* (http://micromagnum.informatik.uni-hamburg.de).

395. W. F. Brown, Ed., *Micromagnetics* (Interscience Publishers, New York, N.Y., 1963).

396. R. Hertel, *Micromagnetism-Lecture Notes of the 40th Spring School 2009-Spintronics*, *From GMR to Quantum Information* (2009).

397. G. S. Abo, Y.-K. Hong, J. Park, J. Lee, W. Lee, B.-C. Choi, Definition of Magnetic Exchange Length. *IEEE Trans. Magn.* **49**, 4937 (2013), doi:10.1109/TMAG.2013.2258028.

398. G.-W. Chern, H. Youk, O. Tchernyshyov, Topological defects in flat nanomagnets. *J. Appl. Phys.* **99**, 08Q505 (2006), doi:10.1063/1.2168439.

399. A. Thiaville, J. M. García, R. Dittrich, J. Miltat, T. Schrefl, Micromagnetic study of Bloch-point-mediated vortex core reversal. *Phys. Rev. B* **67**, 94410 (2003), doi:10.1103/PhysRevB.67.094410.

400. J. Fidler, T. Schrefl, Micromagnetic modelling - the current state of the art. *J. Phys. D: Appl. Phys.* **33**, R135 (2000), doi:10.1088/0022-3727/33/15/201.

401. A. Aharoni, Micromagnetics. *Physica B Condens. Matter* **306**, 1 (2001), doi:10.1016/S0921-4526(01)00954-1.

402. M. Kruzík, A. Prohl, Recent Developments in the Modeling, Analysis, and Numerics of Ferromagnetism. *SIAM Rev.* **48**, 439 (2006), doi:10.1137/S0036144504446187.

403. H. J. G. Draaisma, W. J. M. de Jonge, Magnetization curves of Pd/Co multilayers with perpendicular anisotropy. *J. Appl. Phys.* **62**, 3318 (1987), doi:10.1063/1.339345.

404. C. Kittel, Theory of the Structure of Ferromagnetic Domains in Films and Small Particles. *Phys. Rev.* **70**, 965 (1946), doi:10.1103/PhysRev.70.965.

405. C. Kooy, U. Enz, Experimental and theoretical study of the domain conguration in thin layers of BaFe12O19. *Philips Res. Rep.* **15**, 7 (1960).

406. M. Kisielewski, A. Maziewski, T. Polyakova, V. Zablotskii, Wide-scale evolution of magnetization distribution in ultrathin films. *Phys. Rev. B* **69**, 184419 (2004), doi:10.1103/PhysRevB.69.184419.

407. G.-P. Zhao, L. Chen, J. Wang, A modified scaling law for 180° stripe domains in ferroic thin films. *J. Appl. Phys.* **105**, 61601 (2009), doi:10.1063/1.3055355.

408. F. Virot, L. Favre, R. Hayn, M. D. Kuz'min, Theory of magnetic domains in uniaxial thin films. *J. Phys. D: Appl. Phys.* **45**, 405003 (2012), doi:10.1088/0022-3727/45/40/405003.

409. F. Kloodt-Twesten, personal communication.

410. A. W. J. Wells, P. M. Shepley, C. H. Marrows, T. A. Moore, Effect of interfacial intermixing on the Dzyaloshinskii-Moriya interaction in Pt/Co/Pt. *Phys. Rev. B* **95**, 54428 (2017), doi:10.1103/PhysRevB.95.054428.

411. C. Florin, M.Sc. Thesis, Universität Hamburg (2016).

412. B. Dupé, M. Hoffmann, C. Paillard, S. Heinze, Tailoring magnetic skyrmions in ultra-thin transition metal films. *Nat. Commun.* **5**, 4030 (2014), doi:10.1038/ncomms5030.

B Publications

Published

P1. Raimund Schneider, Thomas Mehringer, Giuseppe Mercurio, Lukas Wenthaus, Anton Classen, Günter Brenner, Oleg Gorobtsov, Adrian Benz, Daniel Bhatti, Lars Bocklage, Birgit Fischer, Sergey Lazarev, Yuri Obukhov, Kai Schlage, Petr Skopintsev, Jochen Wagner, Felix Waldmann, Svenja Willing, Ivan Zaluzhnyy, Wilfried Wurth, Ivan A. Vartanyants, Ralf Röhlsberger, and Joachim von Zanthier,
Quantum imaging with incoherently scattered light from a free-electron laser,
Nature Physics **14**, 126 EP (2017), doi:10.1038/nphys4301.

P2. Simon Hettler, Jochen Wagner, Manuel Dries, Marco Oster, Christian Wacker, Rasmus R. Schröder, Dagmar Gerthsen,
On the role of inelastic scattering in phase-plate transmission electron microscopy,
Ultramicroscopy **155**, 27 (2015), doi:10.1016/j.ultramic.2015.04.001.

Conference contributions as presenter

C1. Jochen Wagner, Kai Bagschik, Judith Bach, Robert Frömter, Leonard Müller, Stefan Schleitzer, Jens Viefhaus, Christian Weier, Roman Adam, Claus Michael Schneider, Gerhard Grübel, and Hans Peter Oepen.
High-Resolution Soft X-ray Holographic Microscope,
Talk at DPG-Frühjahrstagung 2015, Berlin (Germany).

C2. Jochen Wagner, Kai Bagschik, Stefan Freercks, André Kobs, Robert Frömter, Leonard Müller, Magnus Hardensson Berntsen, Gerhard Grübel, and Hans Peter Oepen,
Imaging of magnetic nanodots utilizing soft X-ray holograpic microscopy,
Talk at DPG-Frühjahrstagung 2016, Regensburg (Germany).

C3. Jochen Wagner, Kai Bagschik, Robert Frömter, Stefan Freercks, Carsten Thönnißen, André Kobs, Leonard Müller, Magnus Hardensson Berntsen, Jens Viefhaus, Gerhard Grübel, and Hans Peter Oepen,
Imaging of magnetic nanodots utilizing soft X-ray holograpic microscopy,
Poster at PETRA III Variable Polarization XUV Beamline P04 User Meeting 2016, Hamburg (Germany).

C4. Jochen Wagner, Robert Frömter, Kai Bagschik, Stefan Freercks, Carsten Thönnißen, Björn Beyersdorff, Leonard Müller, Stefan Schleitzer, Magnus Hardensson Berntsen, Jens Viefhaus, Gerhard Grübel, and Hans Peter Oepen,
Arrays of magnetic nanodots studied by X-ray holographic microscopy and scattering,
Poster at DESY Photon Science User Meeting 2017, Hamburg (Germany).

C5. Jochen Wagner, Robert Frömter, Kai Bagschik, Stefan Freercks, Carsten Thönnißen, Björn Beyersdorff, Ralph Buss, Matthias Riepp, André. Philippi-Kobs, Leonard Müller, Stefan Schleitzer, Magnus Hardensson Berntsen, Jens Viefhaus, Gerhard Grübel, and Hans Peter Oepen,
Arrays of magnetic Nanodots studied by X-ray holographic Microscopy and Scattering,
Poster DPG-Frühjahrstagung 2017, Dresden (Germany).

C6. Jochen Wagner, Robert Frömter, Kai Bagschik, André Philippi-Kobs, Rustam Rysov, Leonard Müller, Magnus Hardensson Berntsen, Gerhard Grübel, Hans Peter Oepen,
Magnetic skyrmions in Pt/Co/Ir at zero field,
Talk DPG-Frühjahrstagung 2017, Dresden (Germany).

C7. Jochen Wagner, Robert Frömter, Kai Bagschik, André Philippi-Kobs, Rustam Rysov, Leonard Müller, Magnus Hardensson Berntsen, Gerhard Grübel, Hans Peter Oepen,
Magnetic skyrmions in Pt/Co/Ir at zero field,
Poster at MMM 2017, Pittsburgh (USA).

C8. Jochen Wagner, Robert Frömter, Kai Bagschik, Ralph Buß, André Philippi-Kobs, Matthias Riepp, Rustam Rysov, Leonard Müller, Magnus Hardensson Berntsen, Jens Viefhaus, Gerhard Grübel, Hans Peter Oepen,
Magnetic skyrmions in Pt/Co/Ir at zero field,
Poster at DESY Photon Science User Meeting 2018, Hamburg (Germany).

C Acknowledgement

At this point, I would like to thank all the people without whose support I would have never finished this thesis:

Foremost, I would like to sincerely thank Prof. Hans Peter Oepen for giving me the opportunity to write this thesis under his supportive and patient supervision, and his open-door policy. The many critical and humorous discussions about physics, and many other things, taught me a lot about scientific work, critical thinking, and greatly shaped the outcome of this thesis.

Furthermore, many thanks are due to Prof. Ralf Röhlsberger for refereeing this thesis as second assessor and the fruitful collaboration. I am very grateful.

I owe a great debt of gratitude to Dr. Robert Frömter for his constant scientific support, in-depth knowledge about the various experimental setups, numerous ideas that were of great help in improving the data analysis and results, shouldering most of the review of this thesis, and the fun night outs on various occasions.

I would like to thank Dr. Kai Bagschik for the many hours shared in the lab, at beamtimes, discussing physics, running around the Alster, and in pubs. Your uplifting spirit, great support during the writing of this thesis, and reviewing it are greatly appreciated.

Many thanks are also due to Dr. Àndrè Philippi-Kobs for the numerous helpful discussions about physics that provided great insights and for reviewing this thesis.

A heartful cheers to my office mates Dr. Carsten Thönnißen, Daniel Riebesehl, Dr. Axel Frauen, Jonathan Jacobsohn, and Fabian Kloodt-Twesten for sharing the daily nonsense, much laughter, some beers, and every now and then discussions regarding work.

Susanne Kuhrau deserves a special mentioning for introducing me to the weirdness of the internet and my cherished giraffe.

Special thanks go to Sonja Hesselmann for the hundreds of layers we sputtered together while talking about anything and everything.

I would like to thank Ralph Buß for the easy-going joint work in the lab, providing useful programs for data evaluation and helping me fix my buggy code.

My thanks go to the entire beamtime crew, Matthias Riepp, Dr. Leonard Müller, Dr. Magnus H. Berntsen, Dr. Wojciech Roseker, Rustam Rysov, and the entire P04 staff who were indispensable for performing the experiments at Petra III and made the many hours during weekend and night shifts enjoyable.

Many thanks are due to Dr. Lars Bocklage for providing the FMR setup, helping with the data analysis and interpretation.

Thanks are also due to Stefan Freercks for providing nanodots for experiments at P04.

Furthermore, my thanks go to all members of Group G, current and former, who made the past years in Hamburg as enjoyable as they were with the lighthearted and cooperative atmosphere.

Neben meinen Arbeitskollegen möchte ich noch ganz besonders meiner Familie danken für die immense Unterstützung über all die Jahre und dafür, dass sie immer an mich geglaubt haben. Meiner Mutter Katharina für die vielen aufmunternden Worte wann immer sie nötig waren, meinem Vater Victor für die vielen hilfreichen Ratschläge zu allen möglichen Lebenslagen und meinem Bruder Frank für die unterhaltsame, gemeinsame WG-Zeit in Hamburg.

D Eidesstattliche Erklärung/Declaration on oath

Hiermit versichere ich an Eides statt, die vorliegende Dissertationsschrift selbst verfasst und keine anderen als die angegebenen Hilfsmittel und Quellen benutzt zu haben.

Die eingereichte schriftliche Fassung entspricht der auf dem elektronischen Speichermedium.

Die Dissertation wurde in der vorgelegten oder einer ähnlichen Form nicht schon einmal in einem früheren Promotionsverfahren angenommen oder als ungenügend beurteilt.

I hereby declare on oath that I have written the present dissertation myself and have not used any other than the acknowledged resources and aids.

Hamburg, den 08.08.2019

Jochen Wagner